Evaluation of Stability for Different Stoping Sequences through the use of Numerical Modelling.

Case Study - Cavanacaw Gold Mine, Northern Ireland

Mr. David William Monteith

European Mining Course (MSc.)

TU Delft

Evaluation of Stability for Different Stoping Sequences through the use of Numerical Modelling.

Case Study - Cavanacaw Gold Mine, Northern Ireland

by

Mr. David William Monteith

to obtain the degree of Master of Science

at the Delft University of Technology,

to be defended publicly on Tuesday August 18, 2020 at 13:30.

Student number:	4736184	
Project duration:	May 1, 2019 – August 18, 2020	
Thesis committee:	Dr. M. W. N. Buxton,	TU Delft, supervisor
	Dr. A. A. M. Dieudonné,	TU Delft, supervisor
	Dr. R. B. J. Brinkgreve,	TU Delft, supervisor
	Dr. M. Rinne,	Aalto University, supervisor
	Prof. B. G. Lottermoser,	RWTH Aachen University, supervisor

TU Delft

Abstract

The current plan of bottom to top bottom sublevel stoping for the Kearney gold vein at the Cavanacaw mine, Omagh, Northern Ireland may not be the most effective in terms of stability. The Kearney ore body is a narrow vein gold deposit, which has been previously exploited through an open pit and is currently being developed as an underground operation using sublevel stoping (modified Avoca mining method). Stability within the mine is one of the key factors to be considered when it comes to hard rock mining. It should be considered equally as important from a safety and economic point of view. The extraction sequence plays an important role when considering the stability of a designed mine. This thesis aims to establish if the current planned sequence of extraction of bottom to top sublevel stoping is the most effective in terms of overall rock stability, or whether an alternative plan would be better? In the context of this thesis, the modified Avoca mining method is a form of sublevel stoping where material is extracted (stoped) between two drives (blind tunnels) and then backfilled.

The project addressed, a conceptual study, field testing and laboratory testing in order to yield the information required to build several numerical models. The numerical modelling was carried out on several different stoping orders which met the constraints set out by Galantas, using the Hoek-Brown model within Plaxis2D. The analysis was conducted on the total displacements, phase displacements, predicted failure points and safety factors. The analysis of the different models showed that an alternative stoping method of middle to top bottom to middle sublevel stoping peformed better in terms of stability. This improvement in stability was shown by an increase in the minimum safety factor from 3.20 to 3.50, over the current plan. There is further evidence in the reduction of the total number of predicted failure point by 25%.

Mr. David William Monteith
Delft, August 2020

Contents

List of Figures

List of Tables

Acronyms

ASTM American Society for Testing and Materials

D disturbance factor

GSI Geological Strength Index

GSI(Q) GSI value determined from Q-value parameters

J_a Degree of Joint Alteration

J_n Number of Joint Sets

J_r Roughness of Joints

J_w Water Inflow

$JCond_{89}$ Joint Condition

m_b reduced material constant

m_i Hoek-Brown Material Constant

ODN ore drive north

ODS ore drive south

Q-value Rock Mass Quality

RMi Rock Mass Index

RMR Rock Mass Rating

RQD Rock Quality Designation

SRF stress reduction factor

UCS Unconfined Compressive Strength

1

Introduction

The extractive proportion of mining consists of two phases, the development and the production phase. The development consists of the construction of drives and the establishment of amenities. Drives can be described as blind tunnels, as they only have a singular access. The main excavation within the production phase is known as stoping. Stoping is the step-like removal of ore. The design and extraction sequence of stopes, occurs through a complex analysis, which consists of many factors, with the key ones being the geometry of the ore body, the grade, the geology, the mechanical behaviour of the rock masses, and the time scale. These factors allow for the design of different approaches to the mining method. The determination of the viability of a method, is dependent on dilution, the time value of money, supporting method cost, stability, and experience of the mining team. A particular solution for a mine design and sequence may be the most optimal in one aspect, but in other aspects, it may perform significantly worse. A balance should be reached in order to maximise the economic value, whilst maintaining the highest level of safety.

The Cavanacaw mine, located in Omagh, County Tyrone, Northern Ireland, is owned and operated by Galantas Gold Corporation. The deposit is orogenic gold hosted within several shear zones. The mine was in operation between 2007 and 2012 as an open pit operation. Since 2017 it has been continued as an underground mine. The ore body is planned to be exploited through the modified Avoca mining method, a form of sublevel stoping. Currently, the mine is in its development phase with decline and multiple ore drives being constructed within the Kearney ore body.

1.1. Problem Statement

The extraction sequence of the Kearney ore body at the Cavanacaw, has been determined to be bottom to top sublevel stoping based on the analysis mentioned above. This approach maximises the recovery of the ore, however, this may not maximise the other characteristics.

This thesis will look specifically at the stability of the mine and therefore the problem statement will be to establish which stoping order will be most effective in terms of rock stability, whilst meeting the mines requirement. The stoping orders are as follows:

1. The original plan of building the development to the base of the deposit and then stoping and backfilling upwards, as can be seen in the red line of Figure 1.1.
2. An alternate plan of building the development to the middle level of the deposit, then stoping and backfilling upwards to the top, followed by a continuation of development to the base of the deposit and then stoping and backfilling upwards towards the middle, as can be seen by the blue line in Figure 1.1.

3. The original extractions sequence (item 1), except without stoping and backfilling the stopes within the zone shown as middle in Figure 1.1.

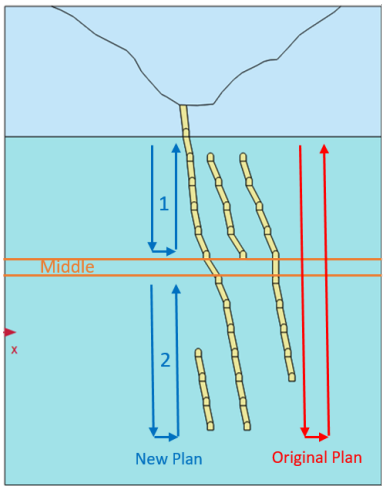

Figure 1.1: The red line shows the original plan for stoping at the mine, whereas the blue line shows a new possible approach

1.2. Objective

The main objective of this thesis will be to establish if the current planned sequence of extraction (item 1 in section 1.1) is the most effective in terms of overall rock stability, or whether an alternative plan would be better.

A secondary objective will be to identify correlations between the field and laboratory tests, for future numerical stability studies and to confirm the rock property assumptions with depth.

Major Question: **Is bottom to top sublevel stoping the most stable excavation order or is an alternative method more stable?**

Sub Questions:

1. What alternative stoping orders are available meeting the mines requirements?
2. Can numerical analysis be used to determine the stability of different stoping orders?
3. How can stability be evaluated through the results of the numerical analysis?
4. Can 2D provide an adequate representation of the scenario or is 3D needed?
5. What failure mechanisms are relevant for this application?
6. What constitutive models are relevant for the project? And which will be chosen? What information is needed?
7. What information is necessary to build an accurate numerical model?
8. Which information is currently available and which information should be gathered in order to build a relevant numerical model?
9. How does the rock mass character vary throughout the mine?
10. Is it viable to correlate Q-value to GSI, for the quantification of rock mass at the mine.

11. Can the combination of field observations and laboratory testing generate the necessary input to simulate a representative rock mass in a numerical model?

12. Is intact rock property testing at the mine sufficiently accurate to allow for the generation of an accurate numerical model, or can it be used as a long term proxy to confirm assumption made in this thesis?

13. What are the major factors controlling the stress field around the underground excavations?

14. Why is one stoping sequences more stable than another sequence?

1.3. Methodology

This thesis is in the field of numerical modelling for underground excavations within hard rock, the project was completed using a finite element analysis software (Plaxis2D). This Project will cover the steps from data collection to model generation and analysis. The decision was made to model in 2D for only the Kearney ore body, as it reduces the complexity of the problem in terms of design, computing power and analysis, whist still providing a realistic result. The mining method will be the planned method of sublevel stoping with backfill, so no alternatives will be considered. The backfill characteristics and testing are not within the scope and will be estimated from literature. The rock mass will be treated as unsaturated by water under the advice of the mine.

In order to reach the objective of this thesis, several steps are required, as shown in Figure 1.2. The description of these steps are as follows:

1. Perform **concept study**, consisting of a mine literature review, a subject literature review and preliminary synthesis. In order to propose a plan for data acquisition, modelling method, and model design.

2. Identify **geological variation** which can be used to establish rock units within the numerical model.

3. Determine material properties.

   (a) Define the **rock mass quantification** for the different rock units within the Kearney ore body and host rock.

   (b) Establish the **intact rock properties**, based on laboratory and field testing for the rock units.

4. Identify possible **correlations** between laboratory tests and field tests, which can be used to further refine future models.

5. Determine the **rock mass properties** based on the relationships identified during the concept study, coupled with the data gathered during the field and laboratory work.

6. Determine a 2D representation of the **mine layout**.

7. Establish **multi-stage 2D numerical model** for stoping order based on the rock mass properties, mine layout, and geological variation.

8. Generate the **displacements, stresses, predicted failure points and safety factors** for the different models.

9. **Model Comparison**, in order to determine the most stable stoping order.

10. **Conclude and recommend**, proposing a plan of action for moving forward.

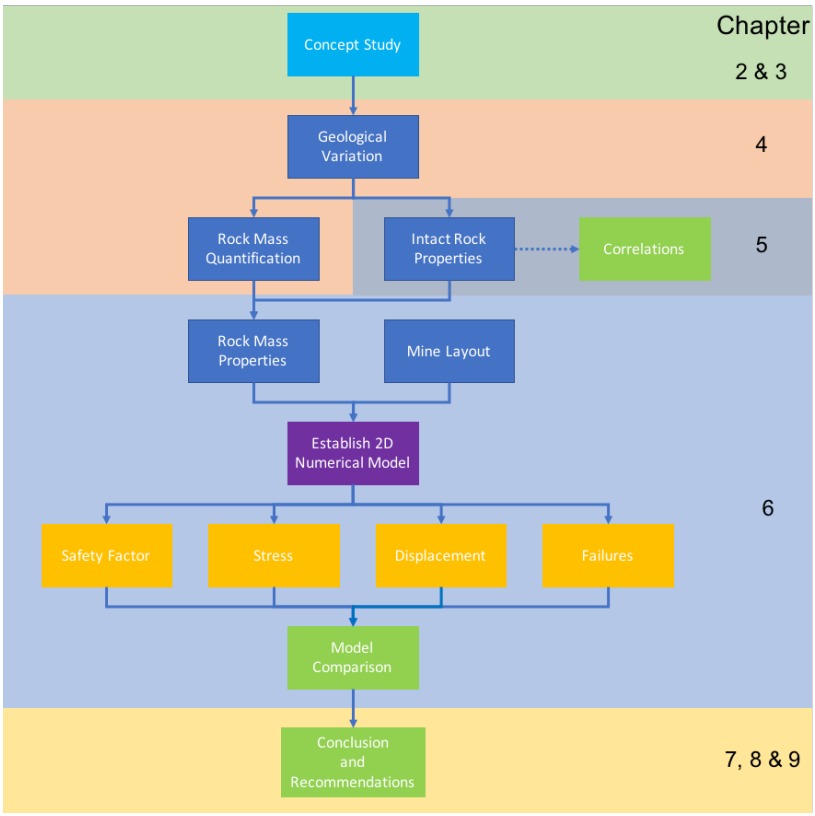

Figure 1.2: Flow diagram for thesis

1.4. Outline of the Thesis

The thesis will be organised into chapters as follows:

2. **Project Background**, this will discuss the background and history of the mine up to the present day. Setting the geological scene for the ore deposit, discuss the development, and the proposed mining method.
3. **Rock Mechanics**, this will discuss the fundamental background information such as the relationship between stress and strain, intact rock properties, rock mass properties, the rock mass quantification and failure mechanisms. The chapter will conclude with a proposed method of data collection and model design.
4. **Field Testing**, will discuss the data gathered within the field for quantifying the geology and rock mass characteristics.
5. **Intact Rock Testing**, will discuss the sampling and testing carried out in order to gather the data identified in the concept study. Additionally the linking of different experimental results will be carried out to allow for future model refinements and the clarification of assumptions with depth.
6. **Numerical Modelling**, will initially present the background to numerical modelling. This will be followed by the model set up and material properties for the rock masses. The permutation of the different stoping order will then be explained. Finally, the result for the different numerical models will be compared and discussed.
7. **Summary**, presents a summary of all of the findings throughout the project.
8. **Conclusion**, presents the final findings of the project.
9. **Limitations & Recommendations**, presents the limitation of this work, and provides recommendations for further work which mitigates these limitations.

2

Project Background

It is important to set the scene within any project, therefore, this chapter will give the reader an understanding of the project background, further this will help contextualise the problem statement and objectives of this thesis. The chapter will be subdivided into project history, geology and mining method.

2.1. Project History

This section will look through the project history for the deposit at Cavanacaw, Omagh. Looking at location, discovery, exploration, feasibility planning, and open pit operation.

2.1.1. Location

The project in question is the Cavanacaw Mine in Omagh, Northern Ireland. The mine is located 5 km west south-west of the town of Omagh, County Tyrone and 100 km west of Belfast the capital of Northern Ireland, as shown in Figure 2.1.

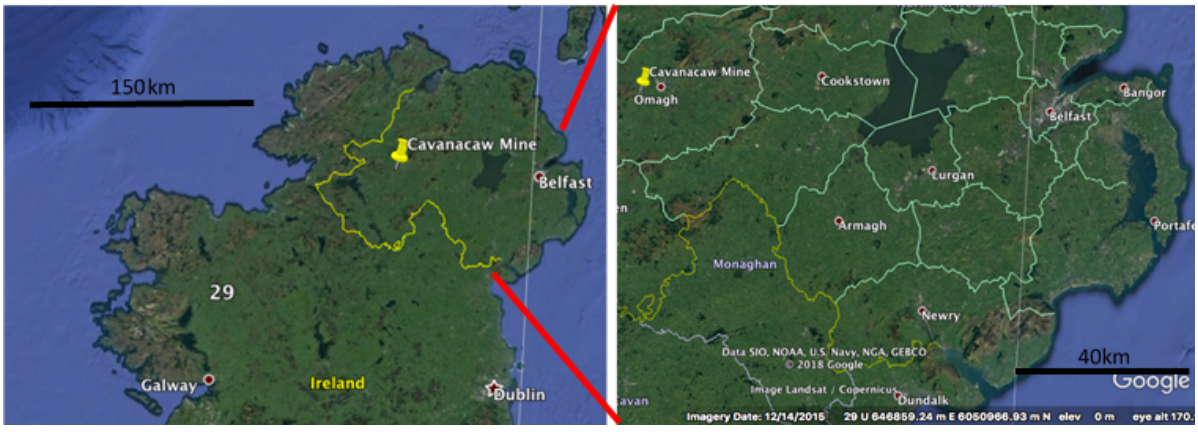

Figure 2.1: Left showing the map of the northern half of the island of Ireland with the location of the mine. Right showing a map of Northern Ireland, and the location of the mine (Google Maps, 2015)

2.1.2. Discovery

The Sperrin Mountains of Northern Ireland have been known to contain gold since the mid 17th century, when Gerrard Boate reported in his Natural History of Ireland, that an occurrence of alluvial gold was found in the Moyola River (Boate, Hartlib, and Boate, 1657).

> *"I believe many will think it very unlikely, that there should be any gold-mines in Ireland, but a credible person hath given me to understand, that one of his acquaintance had several times assured him, that out of a certain rivulet in the county of nether-Tyrone, called Miola (the which rising in the mountains Slew-galen, and passing by the village Maharry, falleth into the northwest corner of Lough Neagh, close by the place where the river Bann cometh out of it) he had gathered about one dram of pure gold, concluding thereby, that in the aforesaid mountains rich gold mines do lye hidden."*
>
> **Gerrard Boate (1657, p.125)**

In the 1970s a regional study by the Geological Survey of Northern Ireland (Arthurs, 1976) drove a new wave of exploration in Dalradian metasedimentary rocks. This new campaign of exploration led to the discovery of shear zones within the metasediments that had the prospect of being associated with gold mineralisations. These discoveries were made at Curraghinalt (Earls, Clifford, and Meldrum, 1989; Clifford et al., 1992), Cavanacaw (Cliff and Wolfenden, 1992) and Golan Burn (Woodham, Finlay, and Holman, 1989).

The Cavanacaw deposit is owned and operated by Galantas Gold Corperation. The discovery of this deposit was through a drilling campaign carried out by Riofinex. This campaign led to the discovery of the Kearney vein structure. The Kearney vein system is the primary target of the current operation of Galantas. Further, the discovery of the surrounding swarm of gold veins occurred during that campaign (ACA Howe, 2008).

2.1.3. Discovery to Development

This section will discuss the road to discovery (ACA Howe, 2008). The timeline for this is as follows:

- 1990 Riofinex project was transferred to Omagh Minerals, who commissioned Kilborn Engineering Ltd. and Knight Piesold to determine the practicalities of mining and the metalogical recovery.
- 1992 Wardell Armstrong carried out an environmental impact assessment.
- 1993 The Crown Estate Commissioners awarded a Lease of Rights to work gold and silver for a 10-year initial period, with effect of one month of planning permission being granted.
- 1995 Conditional planning permission was granted.
- 1997 A further exploration through channel cut was carried out by Omagh minerals.
- 2000 and 2001, Omagh minerals carried out selective mining trials.
- 2003 ACA Howe carried out a compilation of all exploration data.
- 2005 Financing was granted and recruitment began.
- 2006 Open pit development started.

2.1.4. The Open Pit Operation

Open pit mining beyond the restriction of bulk sampling commenced in 2006. During the operation of the open pit, a selective mining method was employed, by utilising a narrow bucket excavator with a bucket width of 30 cm to a depth of 1.5 m. This was possible due to the nature of the mineralised fault breccia being incompetent due to the clay fault gouge matrix. The removal of the country rock occurred using a single tooth ripper driven by a dozer or tracked excavator. Thus, no explosives were in use during the open pit operation.

Figure 2.2: Kearney Pit post vein extraction (looking south, Volvo A40 for scale) (Phelps et al., 2014).

In 2012 the mining operation, as shown in Figure 2.2 was predominantly in the northern end of the open pit, as most of the operation had reached the limits determined based on the stripping ratio, the property boundary, the road to the east and rock stockpiles to the west. During the later phases of this operation a consultation addressing the viability of underground mining was conducted, which concluded underground mining to be viable.

2.1.5. Final Pit Limits

At the termination of the open operation in 2012, an open pit survey was conducted. This survey can be seen in two 2-dimensional cross sections in Figure 2.3. These show a height profile from 160 m on the region around the open pit to a base depth of 116 m. The pit is around 800 m long and 200 m wide at its extremities.

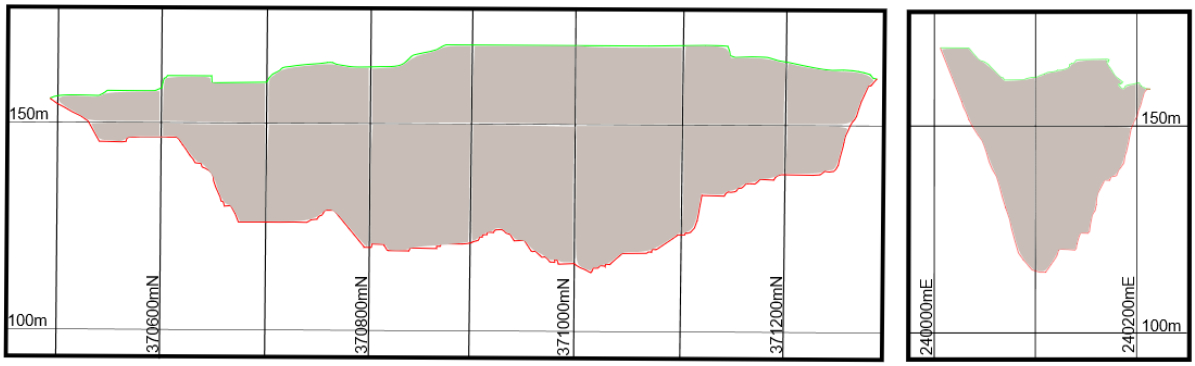

Figure 2.3: Shadow profiles of the open pit. Left north-south orientated, right east-west orientated.

2.1.6. Summary

The key points for the project history would be that the deposit is located in Omagh, Northern Ireland, with the first indication of such a deposit existing being made by Gerrard Boate in 1657. The project was first explored in the 1980s, eventually materialising as an open pit project in 2006, which was in operation till 2012, where it was terminated as it reached its limits. At the termination point for the deposit, it concluded that the operation could move underground. Both operation would not exist if the geology did not contain an economically viable gold deposit.

2.2. Geology

Throughout this section, the regional, local and deposit geological setting will be discussed in order to contextualise the mine, and planned exploitation that will follow.

2.2.1. Regional Geology

The geology of the Sperrin Mountains is composed of several key rock terranes. These terranes are the Central Inlier basement, the Tyrone Ophiolite, the Tyrone Igneous complex, the Dalradian metatamorphosed clastics, and the post-Silurian sedimentary cover (Parnell et al., 2000).

The mineralisation is predominantly located within the Neoproterozoic age Dalradian Supergroup. The protolith for the Dalradian Supergroup consists of a sequence of marine clastic sediments, with a small degree of volcanic units (ACA Howe, 2008). These units are suggested to have been deposited within a passive-margin rift basin system on the eastern margin of Laurentia. The rifting is believed to have lasted from 800 Ma to 550 Ma to during the break up of the supercontinent of Rodinia, which led to the formation of the Iapetus Ocean (ACA Howe, 2008; Strachan et al., 2002).

The protolith for the Dalradian Supergroup collided with the block containing the Central Inlier basement, the Tyrone Ophiolite, and the Tyrone Igneous Group during the Caledonian Orogeny. This block may be considered as a possible source of mineralisation (Lusty et al., 2009). The block is as follows, the basement material of the central inlier, which is composed of sillimanite-grade paragneiss and greenstones. Uncomformably above lies the Tyrone ophiolite. The ophiolite is composed of gabbros, sheeted dykes, and Mid Ocean Ridge back-arc affinity pillow lavas. This ophiolite formed contemporaneously with the Caledonian orogeny. This is then unconformably overlain to the north by the Tyrone Igneous Complex, composed of volcanic and granitoid rocks. This final complex has been intruded by tonalite porphyry bodies and calk-alkaline granites during the latter stages of deformation (Parnell et al., 2000).

The collision led to crustal thickening and the formation of the Sperrin Nappe, overthrusting of the Dalradian Supergroup, as well as the greenschist facies metamorphism of the Dalradian protolith. The deformation also introduced the necessary heat for the solution of gold-hosting sulphides from the source rocks. The gold-hosting sulphide solution the perculated through the rock mass and was precipitated in voids and due to a decreases in pressure. The metamorphic grade is between biotite and garnet, with the predominant rock types found to be of psammites, siltstones and shales (Parnell et al., 2000).

The Sperrin Nappe is interpreted as the lower limb of low angle north-west dipping major overturned recumbent tight isoclinal fold, which is considered part of the Caledonian Orogenic belt (ACA Howe, 2008).

The Caledonian Orogenic belt has been of great interest for mineral exploration over the last four decades. This exploration has led to the discovery of several significant ore deposits, which include Cavanacaw, Curraghinalt and Cononish, all within the United Kingdom. The location of these deposits can be seen in Figure 2.4. The extent of the Caledonian orogeny extends into Scandinavia and North America where geologically similar major deposits exist (Hollis et al., 2014).

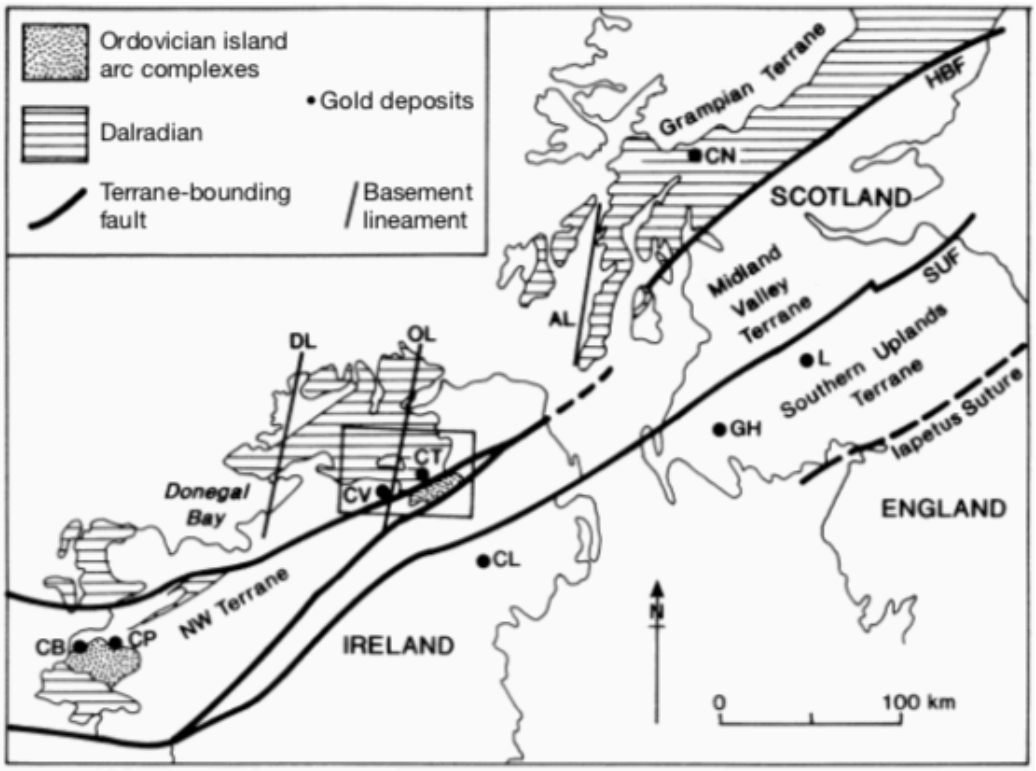

Figure 2.4: Map of region of northern British Isles, showing Caledonian terranes, outcrop of Dalradian (Neoproterozoic) rocks, prominent northeast-southwest lineaments (HBF = Highland Boundary fault, SUF = Southern Uplands fault), north-northeast-south-southwest basement lineaments (AL = Argyll lineament, DL = Donegal lineament, and OL = Omagh lineament;, and location of gold deposits (CB = Cregganbaun, CL = Clontibret, CN = Cononish, CP = Croagh Patrick, CT = Curraghinalt, CV = Cavanacaw, GH = Glenhead, L = Leadhills)(Parnell et al., 2000).

Parnell et al. (2000) state that the regional mineralisation is controlled by two dominant structures, the north-south Omagh lineament and the east-southeast trending Curraghinalt lateral ramp within the footwall of the northeast-trending Omagh thrust. Both of these structures caused mineralisation post-peak metamorphism, but are believed to be pre-Caledonian Orogeny structures (Tanner, 2014; Parnell et al., 2000).

The work of Tanner (2014) however stipulates ”Curraghinalt, appears to have developed as a result of space problems caused by an oblique footwall ramp on the S-directed Omagh Thrust (Parnell et al., 2000), but there is insufficient published information with which to analyse the structures at Cavanacaw and Cregganbaun.” This suggests the control being the lateral ramp at Curraghinalt. At Cavanacaw, Parnell et al. (2000) infers the location of the Omagh Lineament to run directly through the deposit and is cited by Lusty et al. (2009) as one of the key controls on mineralisation.

The uplift and erosion related to the Caledonian orogeny allowed for the generation of material. This material then formed the sediments of the Devonian and Carboniferous that overlie much of the region. Late Tertiary dykes were intruded in relation to an extensional regime. The youngest units are extensive Quaternary glacial and fluvioglacials. These deposits vary in thickness from a thin coating to more than 20 m thick (Cliff and Wolfenden, 1992).

The work on the regional geology, sets the scene that there is a great deal of complexity to the genesis of the region. It does, however, confirm that the formation of the ore body is most probably through the re-concentration of gold in zones of structural weakness during orogenesis.

2.2.2. Local Geology

This section will move from regional to local geology in order to provide further refinement on the genesis of gold and the rocks it exists within. The localised area is known as the Lack inlier, with its geology shown in Figure 2.5.

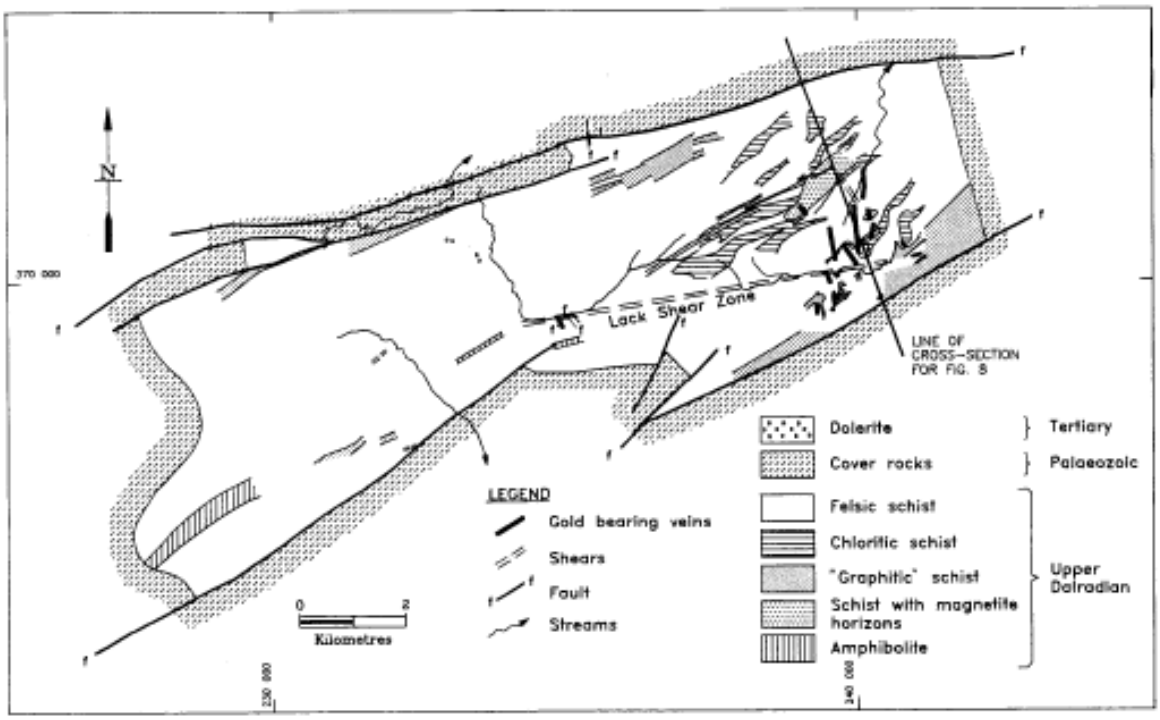

Figure 2.5: Geological Map of the Lack Inlier (Cliff and Wolfenden, 1992).

The majority of work carried out in the region from an exploration standpoint is within the eastern half of the Lack inlier. The dominant rock is Dalradian quartz-feldspar-muscovite-chlorite schist. The fabric within the schists tends to dip at low angles to the north-northwest.

The Dalradian rocks of the Lack inlier are fault-bounded in the north and south by the Cool Fault and Omagh Thrust respectively. Carboniferous sedimentary rocks unconformably overlie the Dalradian rocks on the north, east and west boundaries. These sedimentary sequences are predominantly Old Red Sandstone of Devonian age.

The localised metamorphism is linked to the deformation during the Caladonian orogenic event. These deformations resulted in folding. The minor fold axis in the western half of the inlier plunge between 6 and 40° towards the west-southwest. Within the north-central region, the fold axis is plunging to the east-northeast with a dip of around 20°. The schistosity generally trends towards the north-northwest with dips generally 20 to 65° (ACA Howe, 2008).

Cliff and Wolfenden (1992) subdivides the local geology into 7 rock types. Felsic schist, chloritic schist, graphitic schist, amphibolites, magnetite-bearing schist, diorite dykes and glacial deposits (cover rocks). The geological map of these rock units can be seen in Figure 2.5.

The Lack Inlier is composed of predominantly Mullaghcarn formation. The schematic cross-section in Figure 2.6, shows a section running northwest-southeast. It shows the suggested relation with the Tyrone Igneous Group, the ophiolite and the Central Inlier, however, this contact is not exposed at any point. Further, it shows the 3 main rock units within the Lack Inlier, the felsic schist, graphitic schist and chloritic schist (Cliff and Wolfenden, 1992). The interpretation taken from the work of McFarlane, Cooper, and Chew (2009) suggests that the graphitic schist is part of the Glengawna formation rather than the Mullaghcarn.

The rocks observed within the mine are the Mullaghcarn formations, which are of sedimentary origin in the form of semi-pelites, psammites and pelites (ACA Howe, 2008). There are localised amphibolite lenses, which are hypothesised to be a sequence of basic volcanic and igneous rocks which have undergone metamorphism.

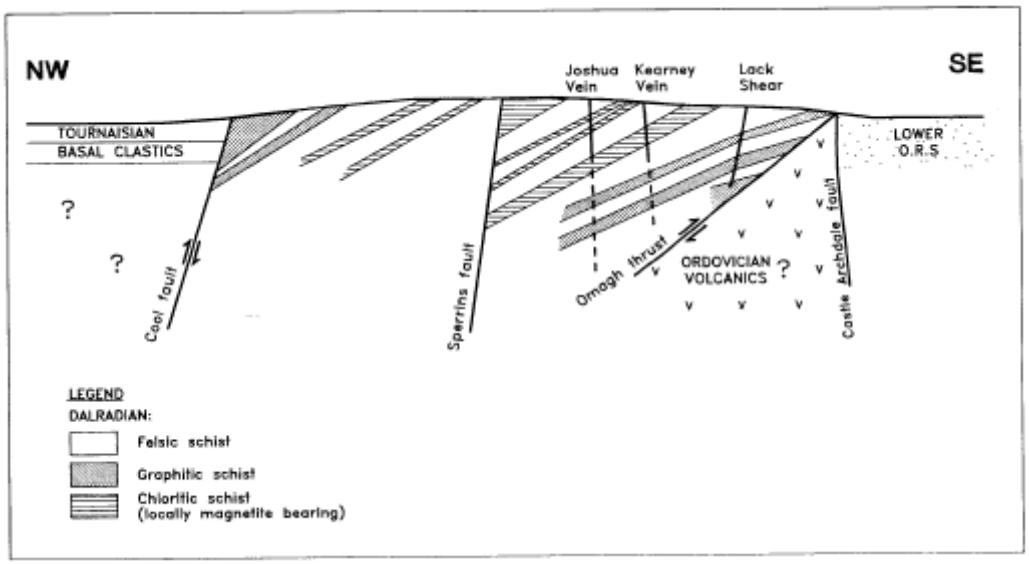

Figure 2.6: Schematic cross section of the Lack Inlier (Cliff and Wolfenden, 1992).

The Figure 2.6 shows 3 zones of mineralisation: The Joshua and Kearney veins and the Lack Shear. Joshua and Kearney strike approximately north-south with dips between vertical and 65° to the east. These mineralised zones have an average thickness of 1.5 m , with a maximum thickness of 5 m (Cliff and Wolfenden, 1992). The region around the Joshua and Kearney mineralisation is actually composed of 16 named vein structures over a 6 km ^{2} area (ACA Howe, 2008). Figure 2.6 shows the orientation of the named mineralised structures. The Lack Shear is a fractured zone over 150 - 200 m which strikes 80° and dips to the north (Cliff and Wolfenden, 1992).

The mineralised zones within the Joshua Kearney vicinity all share similar characteristics with the host rocks. These mineralised zones tend to follow shear zones and precipitated from the mineralising fluid. This is due to the nature of mineralising fluids preferentially flowing along these regions of weakness. These fluids percolating through the rocks have resulted in an alteration halo around the mineralised zone of up to several meters. This alteration is metasomatic and predominantly altering feldspars through sericitisation (Cliff and Wolfenden, 1992).

The current information known at the mine about the in situ stress is rather limited. There is a known positive anomaly within the centre of the Lack inlier, known in the Dromore High. This is suggested to be connected to a intruded granodioritic body. This body is suggested to have induced a significant factor into local tectonic stress field. The report suggest that major faulting within the region caused by the previously mentioned intrusion.

The significant occurrence of these mineralised fault zones indicates that the stress environment is strongly influenced by the local tectonic movement. It is anticipated that the stress field will be oriented parallel to the faulting. Observational methods will be initially used to verify the assumptions. For design purposes the horizontal to vertical stress (K) ratio of 2.0 is extrapolated from ore bodies in similar setting. The orientation of maximum principal stress is assumed to be NNE-SSW i.e. parallel to the faults system and the shear zone. The horizontal stress component normal to the principal is substantially lower given that many of the major structures display displacement and extensive cavity/infill development (Burke, 2017).

The local restriction for the generation of mineralisiation further confirms that, it is extremely structurally controlled. This structural control has a significant impact on the in situ stress of the mine. It is further determined that the deposit type is narrow vein, which is confirmed extensively over an area 6 km^2 in the form of 16 veins.

2.2.3. Kearney Geology

The geology is further required to be distilled one further step, so as to look at one specific vein structure. This structure is the Kearney ore body, which is the predominant region of exploitation for the mine.

The mineralisation of the Kearney is hosted within a shear zone. The country-rock of the region is predominantly psammite, which is coarsely bedded, with thicknesses from 5 cm to 100 cm. The mineralogy is predominantly of quartz, with lesser feldspars and micas, although the composition is variable throughout. The psammite is interbedded with pelite layers with a higher abundance of mica, which vary in thickness from 1 to 20 cm (Marshall and Brown, 2011).

A structural mapping project was conducted by SRK Consulting in 2011 within the open pit, during the design phase of the underground mine. During this, structural data was collected for bedding planes and joint sets as well as joint conditions. The data for a bedding plane and 4 joint sets was determined, which can be seen in Table 2.1. This was calculated through 233 points, however, there is a bias within the data due to 126 points gathered within the southern outcrops, 94 in the central section and 13 in the north (Marshall and Brown, 2011). There is no justification for this bias, however this may be a result of the lack of observable surfaces.

Table 2.1: Data for the bedding and joint orientation from (Marshall and Brown, 2011)

Joint Set	Dip (°)	Dip Direction (°)	Confidence (°)*
Bedding	26	317	15
JS2	40	59	11
JS3	66	85	8
JS4	81	255	11
JS5	63	155	8

Further mapping of the Kearney was conducted by Cliff and Wolfenden (1992). This was carried out through trench mapping. The generated map is shown in Figure 2.7, which splits the trench into 3 rock types: Felsic schist rock, quartz vein and altered schist. The latter two are both mineralised with sulphides. The map shows that the zone is heavily faulted and fractured. This section is only 20 m, however, it is of the authors' opinion that this is relatively representative of the behaviour observed within the ore body. The structural data is difficult to decipher due to the joint and shear measurement having an identical symbol.

Cliff and Wolfenden (1992) further subdivides the mineralised structures into 4 units. Brecciated quartz veining, which contains a matrix of pyrite and galena with a ratio of (5:1). Massive or semi-massive pyrite and galena (2:1) within veins and veinlets of quartz, which are locally brecciated. Stringers and veinlets with pyrite and galena, within the heavily altered schists. Black sulphidic clay gouge which develops as part of the alteration halo due to grain size reduction in shearing.

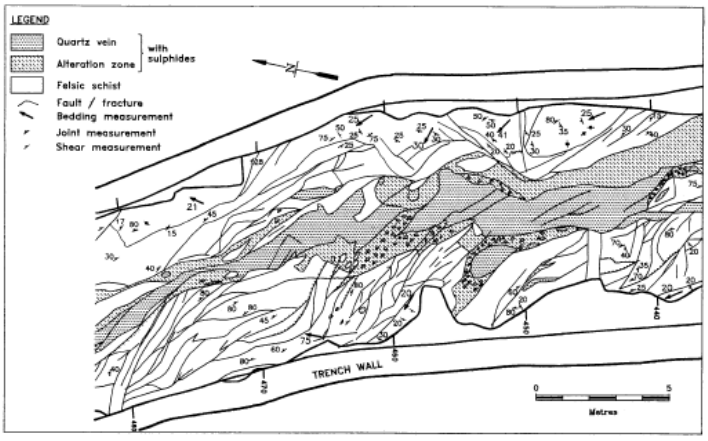

Figure 2.7: Geological map of the Kearney Trench (Cliff and Wolfenden, 1992).

A key discussion point from the literature must be the geometry of the ore body in 3D space. It is already known that the ore body is narrow between 1 to 5 m in width, further the suggestion is that the ore body dips vertically to sub-vertically to the east. The early exploratory work of Cliff and Wolfenden (1992) in terms of the trench shown in Figure 2.7 and a single drill hole known as BH55, are used to generate a preliminary structure for the Kearney vein. This is shown in Figure 2.8, where the trench section suggests a single mineralised quartz vein, but at depth there is the suggestion of 3 to 4 veins. This is an indication that the ore body is more complex than a single vein structure. The vein structures are believe to be hosted in an altered schist which exists as a halo around the veins. This halo is then surrounded by the felsic schist in the same manner as the trench cut. This can only be confirmed by further exploration work, as a result, a thorough exploration campaign was carried out over the next decade in order to generate a resource and reserve block model.

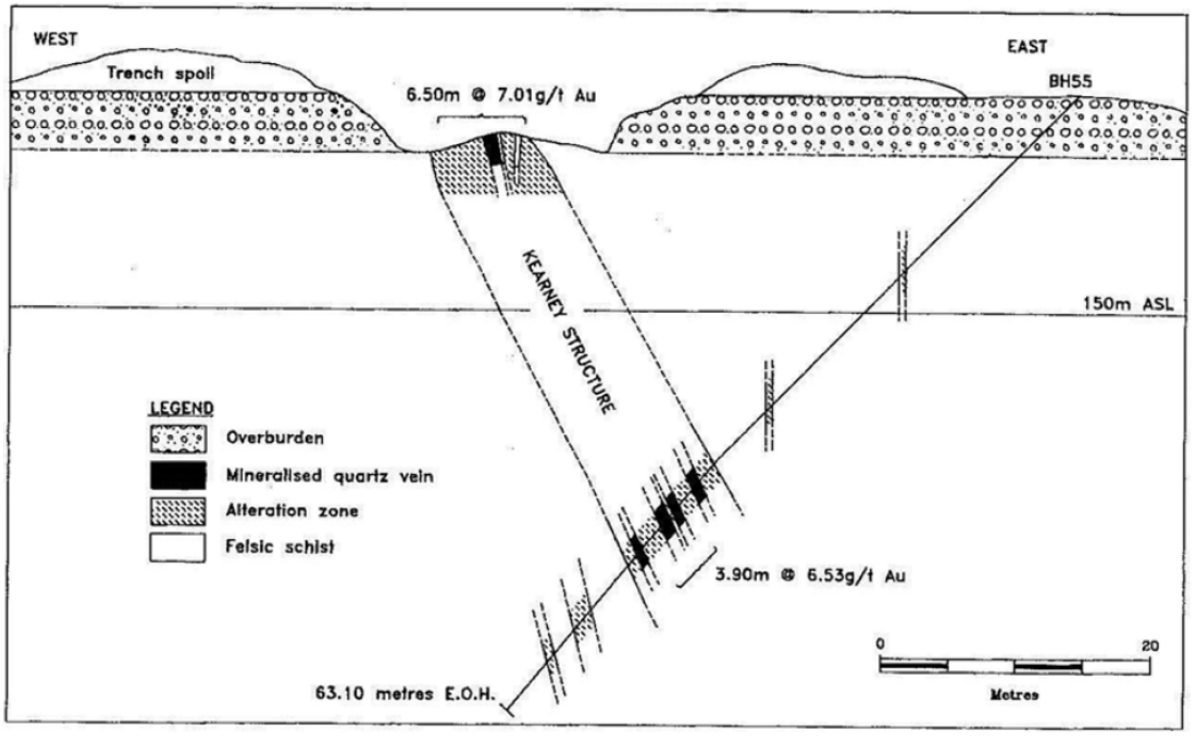

Figure 2.8: A cross sectional interpretation based on the trench and drillhole BH55, shows an ore body dipping 65° to the east. BH55 intersects the ore body at a depth of aproximately 30 m below the trench (Cliff and Wolfenden, 1992).

The block model of the mine based on the exploration drillholes shows this exact behaviour. The block model also shows the extent along strike is to be expected to be 800m to a depth of around 70 m from the base of the pit, with a vein continuity of 30-450 m. The vein structure for the Kearney, is suggested to be made up of a several pinching and swelling vein, with in the southern section the vein splays into several discontinuous vein structures. This is shown by the block model in Figure 2.9, generated for the resource estimate in Phelps et al. (2014).

The generation of a resource and reserve block model, is a useful data set, it provides the basis for the decision to mine or not to mine. This decision is complicated, but in reality is based on an economic decision determined by the feasible mining method based on the geometry and disparity of the ore. This is however a block model which is established with limited data, as drill holes only intersect a small section of the deposit and from that a large amount of information is estimated. Further refinement of the models occurs during the development of the ore drives coupled with further underground exploration drilling. This refinement may result in a direct change in the method of mining or the decision to mine or not.

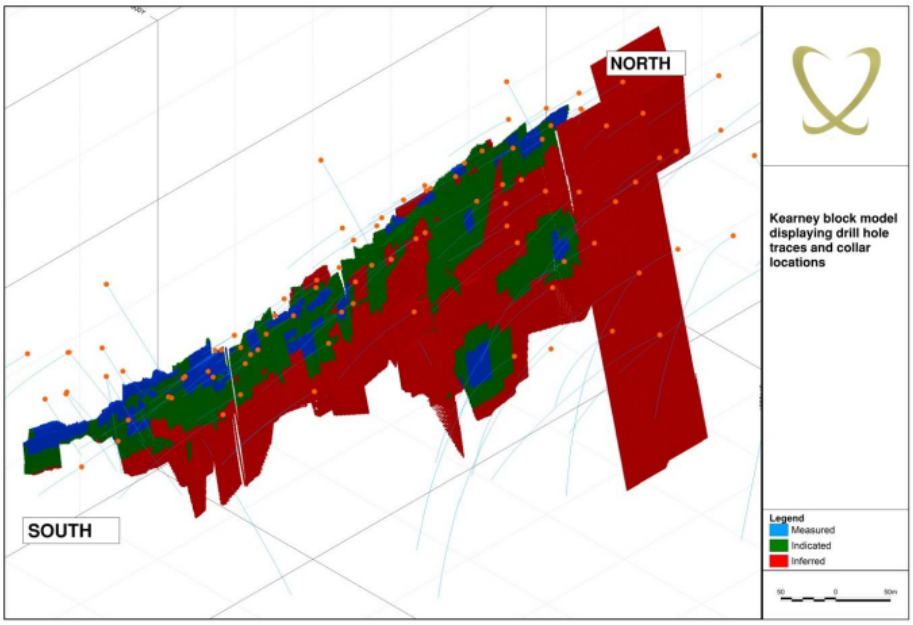

Figure 2.9: A block model showing the measured, indicated and inferred blocks, for the Kearney ore body (Phelps et al., 2014).

2.2.4. Material Properties (Estimate)

The final piece before moving to the mining method is to have some indication of the material properties for the rocks contained within the mine. An explanation for these properties will follow in chapter 3. Within the documentation for the mine, there is a ground control management plan, which contains estimations of material properties from the geotechnical work carried out (Burke, 2017). This data is estimations based on field observations and therefore is not accurate enough to be used to build the numerical model, but provides some indications on what can be expected and what data is possible to gather. The results of this work can be seen in Table 2.2. These results indicate that the hanging wall is the weakest material by a significant amount based on the Unconfined Compressive Strength (UCS). The elastic modulus is considered fairly similar, however it is not clear from the results whether they refer to the intact rock or rock mass.

Table 2.2: Estimated rock properties from the Cavanacaw (Burke, 2017)

Rock	UCS (MPa)	Elastic Modulus (GPa)	Poisson's Ratio
Footwall	100	6.9	0.25
Orebody	94	7.5	0.2
Hanging Wall	55	6.5	0.27

2.3. Mining Method

The mining method is controlled predominantly by the geology, however the geology consists of several different components. The key components for determining the mining method are the geometry, the orientation, and the variability and strength of the ore and host rock. As discussed in the previous section we have a narrow steeply dipping deposit, with little known about the internal variability, with host rock which is similar in strength if not weaker than the ore. These factors culminated in the decision for Galantas to design a mine based on the modified Avoca mining method, a sublevel stoping mining method, which will be explained in due course (Phelps et al., 2014).

This section will discuss the methodology for mining the Kearney ore body starting with a summary of the design protocol and explanation of key components of the mine. Then development will be discussed in the form of the decline, the access tunnels and ore drives and finally the stoping method.

2.3.1. Mining Method Design

The work to determine viable solutions for mining method was carried out by SRK Consulting, this work consisted of the geological logs, downhole surveys and core photographs, for the exploration drill holes, with a particular focus on the intersections with ore body. The work carried out during the open pit operation was used as further information for this study (Phelps et al., 2014)

The results yielded that a combination of sublevel longhole stoping and shrinkage stoping would be used, this would be dependent on the width of the orebody coupled with the localised geotechnical properties. The use of paste fill was suggested throughout, in order to maximise extraction and stability, whilst minimising the tailings disposal footprint (Phelps et al., 2014).

The initial design of stoping was carried out using a traditional stope dimension technique developed by Potvin (1988). As a result stope dimensions of 30 m in strike length, with a height of 35 m and a width of 3 m is determined (Phelps et al., 2014)

There are many different iteration of sublevel longhole stoping, however later studies within the mine (Burke, 2017), have ruled out man entry stoping due to anticipated poor ground conditions. These poor ground conditions are the driving factor behind this thesis, as it has raised concern for the overal stability of the mine. A reduction in the height between levels to 12 m from floor to roof was also decided within Burke (2017). This report suggests that the most viable solution based on the current understanding of the deposit is to use the modified Avoca mining method. This method will be explained in a subsequent subsection.

Thus far only the mining method design has been discussed, however an important factor to consider is how to get from the surface to the ore body. A labelled diagram for the mine is shown in Figure 2.10, note that all the access drives are not labelled. The key features to note are the crown pillar, adit, the decline, the access and the ore drives. The later 4 are all excavations considered part of the mine development, rather than the mining operation. These features will all be explained within a subsequent subsection to describe and explain their importance.

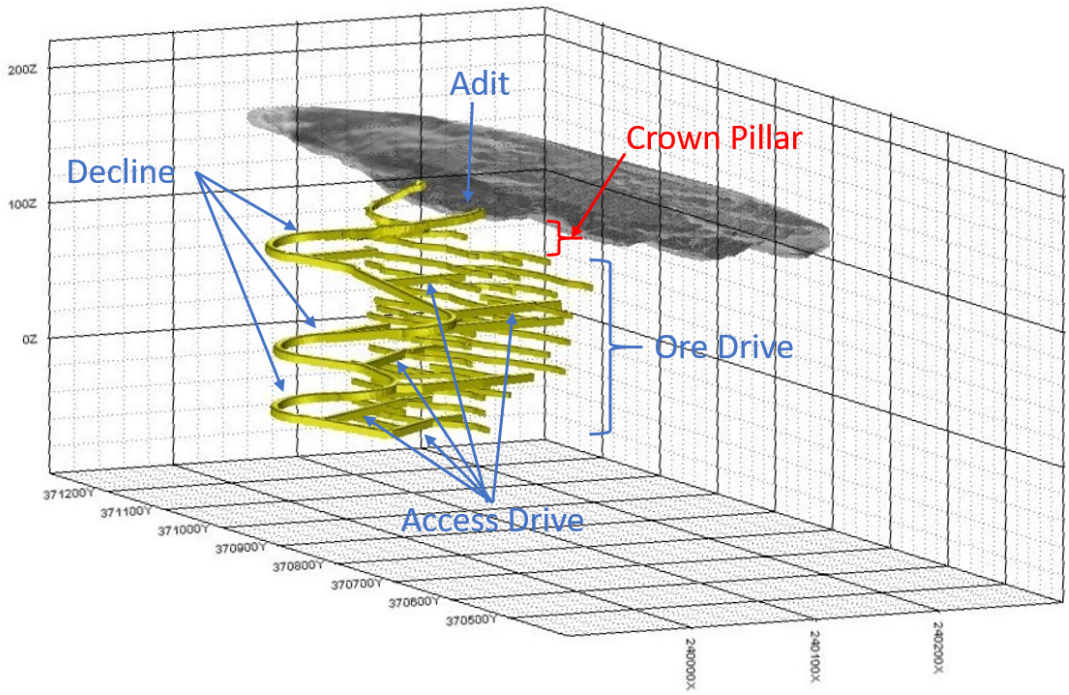

Figure 2.10: Diagram of the development within the Kearney ore body looking north west. Scale small boxes are 20 x 20 m.

2.3.2. Development

The definition of an adit is a sub-horizontal opening which leads to the mine from the surface. This is the direct connection from the preexisting open pit to the decline which it is connected to. This section is one of the more complex points for excavations, as it is directly at the surface, thus a concrete reinforced arch is used to reinforce it. The initial opening of the adit can be seen in Figure 2.11, which began on 25th of April, 2017. The dimension is 6 m wide with a height of 5m, this narrows after the first 20 m, where it can be described as the decline.

Figure 2.11: The initial work when the adit was first being opened.

Development is typically conducted as drill and blast following the methodology proscribed in Figure 2.12, which is a feedback loop. First a region must be surveyed in order to determine if the region is adequately stable. Secondly if that test is passed, the face is drilled, then charged and blasted. Post blasting it is essential to remove dust and toxic gases, which may have been produced during blasting, this is done through actively ventilating the region. The blasted region is then checked and scaled to remove any loose blocks which are unstable. Blasted material on the floor is then mucked, to its storage place or final destination. Once the excavation is clear of rubble, the support required is then added. The region is then surveyed again to make sure that it is safe to proceed with the next blast. If it is not safe then it is reverted back to scaling, supporting or abandoned. This method has been used in all the development excavations within the mine from the initial development of the adit, to the development drives that will follow.

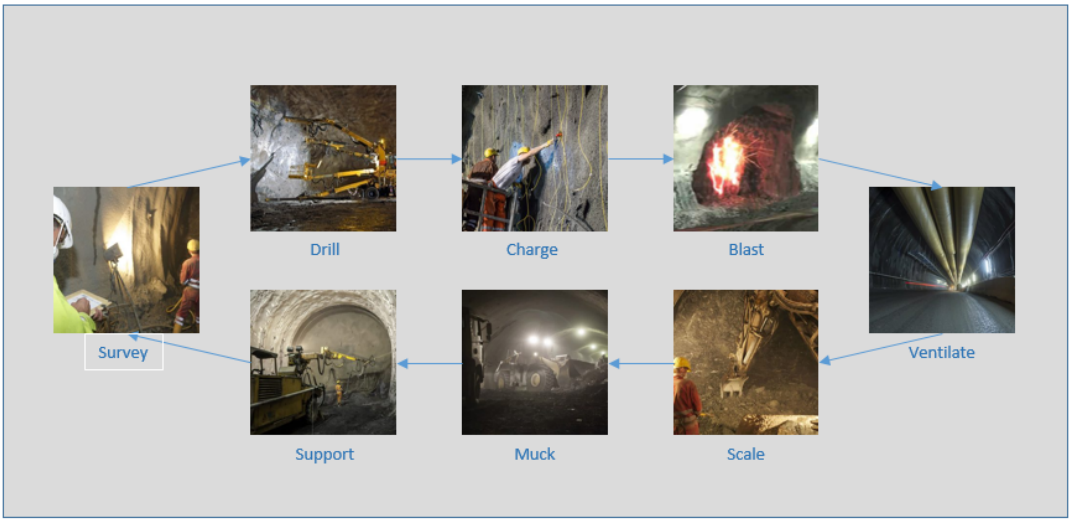

Figure 2.12: This shows a typical drill and blast cycle within the mine adapted from (RailSystem, 2019)

Decline

The decline is the ramp that descends with a 1 in 7 gradient through the host rock, in the hanging wall of the deposit, in a corkscrew pattern with 5 180° turns. Starting at the adit, the decline descends to below the ore body. The dimensions of the ramp are designed to be arched excavations, which are 4.5 m in both width and height, however the reality is they are around 5 m. As discussed the method of excavation is drill and blast, with a typical cycle progressing 2.5 to 3 m further forward. A typical supporting method for the decline is a mixture of galvinised rock bolts, mesh and shotcrete, except at drive intersections where cable bolts are used. These intersection points are the locations in which the decline has reached the location, which are the proposed points for gaining access to the ore body. These points are the beginning of the access drives.

Access Drives

Access drives are essentially excavations which go from the main development (decline) to the ore body. The planned development, which is currently in progress is to develop 13 different access drives. These drives are at 12 m vertical increments, the method of defining heights within the mine is K1000 equates to sea level, so the top drive is K1096 (96 m above sea level) and the bottom drive is K0952 (48 m below sea level).

The specification for these drives is identical to decline other than the dip. The dip of these drives is 1 in 100 in the direction of the decline, to allow for water drainage. The supporting method is the same as for the decline, and can be observed in Figure 2.13. Here the walls can be seen, with mesh held on by rock bolts, which has been sprayed with shotcrete. Also within the access drives the intersections with the ore body requires cable bolts.

Figure 2.13: K1060 access support method of split sets and rock bolts with mesh as well as 75 mm of shotcrete. Field of view is 5 m.

There is one fundamental difference between the development drives for the decline and access drives, and those for the ore drives, which is the end location of the excavated material. The material from the first two is destined fro the waste rock piles, however the development within the ore drives can be processed and sold to raise revenue.

Ore Drives

The ore drives are dissimilar to the other development drives, they exist as two separate drives; drives in a southern direction known as ore drive south (ODS) and those in a northern (ore drive north (ODN)). The length of the drives in a north or south direction, are dependent on where the access drive intersects the ore body. The ore drives dip towards the access in both direction with a gradient of 1 to 100. The

exact direction of the ore drives is variable throughout, as the objective aims to follow the ore body as best as possible without making major deviations. Both drives are specified as 2.7 m wide and 3.8 m high, however in reality they are 3 m wide and 4 m high. The excavations are carried out with the drill and blast procedure, with a typical progression rate of 2.5 to 3 m per blast. The support method is different, with the use of split set bolts and shotcrete as shown in Figure 2.14, this is partially because the regions where the support is going, will be stoped in the future which causes the required time of stable standing to be reduced. Localised refinement of the supporting method, is carried out in areas where the geologist has identified weakness.

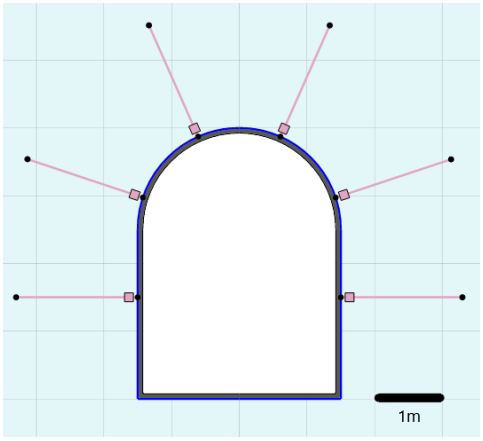

Figure 2.14: Typical support method for an ore drive. The bolts are 1.8 m long split sets, with a shotcrete layer of up to 75 mm.

It is important to take away how the development fits together to understand the current operation. First the adit was opened, which is then progressed to the decline. The decline is continued to be focused on until the development is around 10m beyond the intersection point with the first access drive, at this point the cut for the access is made. Development continues in both, until either the ore body is passed by the access drive or the decline passes its next access intersection point. Once one of these is reached either an ore drive will be opened or a new access. All the drives that are opened are continued until they reach their termination length determined by the mine design. A timeline of the key underground steps are shown in the list below:

- The opening of the adit took place on 25th of April, 2017.
- The mine opened an ore drive in the south and north directions (K1096 ODS and K1096 ODN) on 5th of July 2018 and 10th of July 2018. The operation on the 1096 level was brought to a halt due to stability reasons on the 23rd of October 2018 and 18th of April 2019 respectively.
- The K1084 level access was opened on 3rd December 2018. An ore drive in the southern direction was opened on 25th of January 2019. This drive is known as K1084 ODS. The drive has been brought to a halt on the 4th of July 2019, with a length of 138 m. The pausing is due to reaching the end of the known deposit based on the block model and there being several blasts of low quality ore, as well as the occurrence of a highly evident fault. This location however, has been identified as a location for probe drilling to establish whether there are indications that mineralised rock occurs further within the drive. Due to the identification of mineralised material in undefined regions of the block model, the decision was taken to open an ore drive in a northern direction. K1084 ODN was opened on the 18th of July 2019.
- The K1072 level access was opened on 20th of March 2019. An ore drive to the south and north were opened on 16th of May 2019 and 3rd of June 2019 respectively. These drives are known as K1072 ODS and ODN.
- The K1060 level access was opened on the 18th of June 2019, and at the time of writing is still under construction, however, the ore drives south and north were both reached on the 8th of July 2019. Work on opening these drives is still yet to commence.

A key note to be taken from the timeline above is the abandonment of the highest level of ore drives within the mine. This decision was made to terminate the expansion on this level was particularly important, as the region above this level was the crown pillar between the open pit and the underground operation.

2.3.3. Overall Ground Stability Improvement Methods

The overall ground stability can be improve by two methods, first naturally by not excavating material and secondly artificially by adding material to excavated regions. Before looking at the mining method, it is important to address two key methods in detail. The first of these methods is the leaving of pillars, this might seem counter intuitive, but this is a well practised technique in mining. The second method is to introduce backfill into large voids in order to generate artificial pillars.

The natural pillars method can be subdivided into several specific pillar types, which are based on their location. These pillars are known as the crown pillar, sill pillar and the rib pillar.

The crown pillar is the material between the surface and the highest subsurface excavation. The crown pillar must be specified correctly in order to prevent instability in the mine and prevent the inflow of water, something which is particularly important when under an open pit.

A sill pillar is the material where a whole level between two ore drives is left unmined. The introduction of such a pillar at the mine would be in the aim of increasing stability or to allow for the splitting of the ore to start at a different location. This will become apparent in the subsequent chapters.

The final type of pillar is a rib pillar, this is a section of material which is left in a region where stoping is occurring. This is done to increase overall stability, and would preferentially occur in areas which contain low grade ore or are barren.

The artificial pillars of backfill can take the form of several different types; rockfill, cemented rockfill, paste fill and hydraulic backfill. The introduction of such material removes the open voids which exist, meaning that excavations cannot collapse upon themselves. Further it can be an excellent method for reducing the amount of waste rock or tailings which needs to be stored on the surface.

2.3.4. Stoping

The mining method and stope dimensions have already been determined in Phelps et al. (2014) and Burke (2017). The method of mining will be the modified Avoca method with stope dimensions of 12 m in height, 4 m wide and 30 m in length. This subsection will explain the term stoping as well as describe how the modified Avoca method works at the mine.

A stope is an excavation of ore material which is not part of the development process of the mine. Stoping is the mining phase in which the majority of the ore will be excavated. The stoping process is normally as follows:

1. Complete the development drives for above and below the stope.
2. Survey the rock, checking the expected geotechnical rock properties.
3. Drill longholes between the two drives based on the blasting pattern determined for the stope.
4. Charge the holes with explosives.
5. Blast and then allow the area to ventilate.
6. Conduct a safety check.
7. Proceed to muck the blasted material.

The exact methodology of stoping may deviate in shape, orientation and size, but the general order is always as above. The method choosen for stope extraction in the Kearney ore body is the modified Avoca mining method. First the general Avoca method as shown in Figure 2.15 will be explained and followed by the modifications made by the mine.

The Avoca method works on the basis that a tunnel is generated above and below the material that is to be stoped. These tunnels are produced within the ore material. The first step is to create a slot, which is done by stoping a small section within the ore body at one end of the tunnel, this can be seen in Figure 2.15. This material is then mucked. The next step is to follow stoping process listed above for the next section as proscribed by the stope dimensions. After blasting, waste material is then dumped into the void created from the end where the slot was generated. This process is completed for subsequent slices as defined by the stope dimensions. Once a level has been completely stoped the method progresses upwards (Bullock, 2011). The planned operation for the Kearney ore body is a modified version of the Avoca method. The method is modified by having only one opening as the mine is designed with drives, rather than the two openings of a tunnel required for the general method. As a result the mining process must start at the furthest point from the opening of the drive. The operation of creating a slot is removed from the process, so the first step is to stope material as described in the stoping process. As there is only one opening it means that the backfilling will occur from the direction of progression. The mine plans to use cemented rock fill, thus whilst backfilling they must build a barrier, known as a bulkhead to stop the material from flowing into the drives, this can be seen in Figure 2.16.

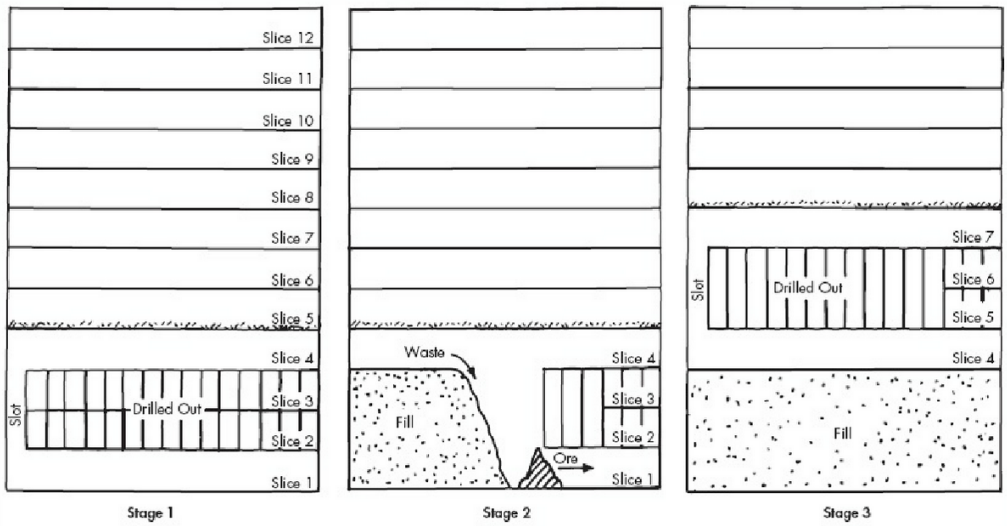

Figure 2.15: Avoca mining method (Bullock, 2011)

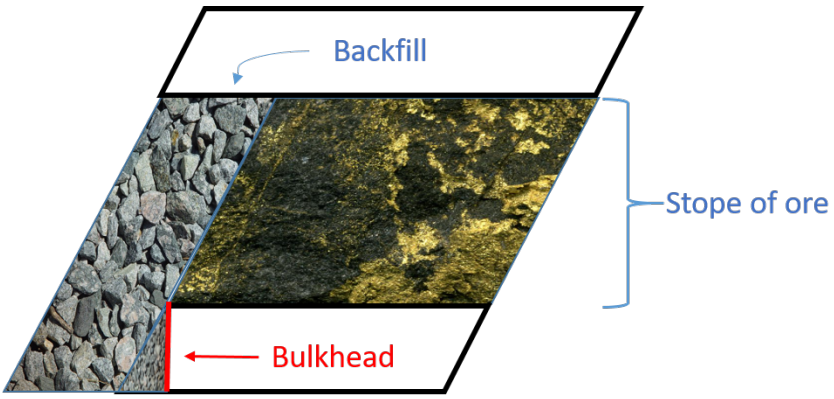

Figure 2.16: The method of backfilling stopes at the mine.

The definitive mining process is not fully confirmed at the mine, as they are still within the development phases, so ground conditions are not fully known with depth. As a result, there is the option that within the mine there will be sill and rib pillars of ore material left to increase the stability. Particularly in the case for low grade ore areas. There is the possibility that a complete level will be left as a sill pillar in the central region of the deposit. This is something that will be seen in the different models within the numerical modelling chapter that will follow.

2.4. Summary

The Kearney ore body is a shear hosted orogenic gold deposit, within the Cavanacaw mine, Omagh, Northern Ireland. Initial indications that there was gold in the Sperrin region was made by Gerrard Boate in the 17^{th} century. It was not until the 1980s that there was an indication that there was gold specifically in Cavanacaw. Between 2006 and 2012, Galantas Gold Corporation exploited the deposit as an open pit, however it has subsequently met its pit limits.

The deposit would not be viable unless the geological conditions were not advantageous. The understanding of the geology based on the literature is that the Kearney ore body is a steeply dipping pinching and swelling vein structure which splays at its southern end. The deposit extends to 800 m along strike reaching a known depth of 70 m below the open pit. The vein and host to the sulphide mineralisation is the quartz breccia which occupies the shear zone.

The Kearney ore body is not the only one that exists on the mine property, it is only 1 of 16 named structures within a $6km^2$ region. These structures are all shear zones which exist in the host rock of psammitic schist with interbedded pelite.

These named structures within the mine property are not the only deposit that exist in the region, within 20 km another significant deposit (Curraghinalt) has planned to exploited by Dalradian Gold Limited and in Scotland, Scotgold are currently in the initial phases of exploiting a deposit in Cononish. The deposits all have several things in common, these are that they are formed within the Dalradian rocks of Scotland and Ireland, and that they were formed with structural regions of weakness during the Caledonian orogeny.

The gold generated during this complex geological and tectonic history is locked within the sulphide mineralisation at the mine. The first step to unlocking the gold must be the excavation of the material from the subsurface. The only viable option now is to exploit the Kearney ore body underground. This is done through the creation of a decline from the open pit to the base of the deposit which descends with a gradient of 1 in 7 in a corkscrew pattern. The next step is to gain access to the ore deposit, this is done at 13 predetermined locations, with a vertical height difference of 12 m. These accesses are in the form of drives, know as the access drives. When the ore body has been reached, drives in the ore body are created in both strike directions.

Once development is at a sufficient level, the ore body is exploited using a modified version of the Avoca mining method. The modification made to this stoping technique is that there is only 1 opening rather than 2, thus the backfilling occurs from the same direction as mining progresses.

The mining method has been designed based on values from a limited amount of data using empirical methods which have been tried and tested over several decades. This project aims to use numerical methods to determine the order of stoping levels. As the mine is currently executing its initial plan of exploitation for the deposit, requirements are therefore fixed by the mine.

The requirements are as follows; the mining method must be the modified avoca method, therefore progression must be upwards; levels must be 12 m apart with identical geometry to that described in this chapter; the crown pillar is to contain all the material above the K1084 level due to the instabilities that occurred in the past; in order to minimise the amount of ore left in situ, the mine will only allow for one sill pillar; rib pillars will be omitted as they will be addressed on a case by case basis when more refined ore grades are known.

These requirements allow for the proposal of several different scenarios, the first is bottom to top sublevel stoping, which is the initially planned case. The second scenario is middle to top bottom to middle sublevel stoping, this would introduce a sill pillar in the middle of the deposit. The final case therefore would be bottom to top sublevel stoping with the introduction of a sill pillar. These cases would meet the requirements. One alternative method that is not discussed within this thesis is single lens stoping. This scenario was not considered as it would be slower due to only one stope level being able to be worked on at a time.

A large amount of information as to the mine design requirement for the model as well as the geological units that can be expected at the mine are now determined. It is now apparent that there is not enough accurate information known on the rock properties to build an accurate numerical model. In order to move forward a well designed campaign of data collection must be conducted. Before this campaign is undertaken an understanding of the data required and why it should be collected needs to be presented.

3

Rock Mechanics

The objective of this project is to determine the most stable stoping order through the use of a numerical model given a specific set of constraints defined by the mine. This type of modelling relies on a firm knowledge of the underlying principles of rock mechanics. These themes coupled with the knowledge from chapter 2, will help to define the data acquisition that is required to build an accurate numerical model in order to determine the best stoping order for the mine based on the stability.

The application of rock mechanics in mining, is based on classical mechanics. Classical mechanics is a branch of physics, which encompasses Newtonian mechanics and Continuum mechanics, which are the key behaviours within this thesis. The topic can be divided into 5 key categories (Brady and Brown, 2007):

1. The behaviour of an intact rock can be described through classical mechanics.
2. A rock mass can be quantified in terms of its discontinuities and related to the intact rock material properties.
3. A rock mass can therefore be described through classical mechanics.
4. Mining produces openings and support elements, which show in principle, behaviour which can be modelled with classical mechanics.
5. Safety and economic performance can be assured or controlled through the ability to predict and control the behaviour of the rock mass.

This chapter will discuss the key themes of rock mechanics in order to model the behaviour of the rock mass. First stress, strain and their relations will be presented. This will then follow on to the material properties of the intact rock. The behaviour of the rock mass will be described. The quantification of the rock mass in order to translate it from the intact rock properties to rock mass properties will then be presented. The final section will talk about possible failure mechanisms, that may be seen within the results of the numerical models.

3.1. Stress

The initial concept of classical mechanics that needs to be understood is stress. Stress is the intensity of internal reaction forces within a body, which counter act the external surface force applied on that body. This is based on Newtons third law, that every force has an equal but opposite reaction. The left

image in Figure 3.1, shows the equilibrium reaction force P_j on a finite body, as reaction to the surface forces $P_{1\text{-}4}$ (Brady and Brown, 2007).

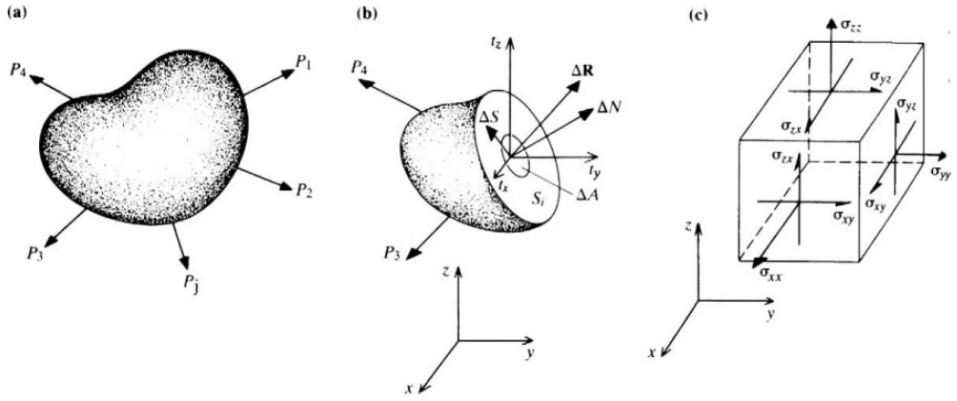

Figure 3.1: Left: A finite body in equilibrium due to a force applied to the surface. Middle: The stress components at a single point. Right: The stress components as traction elements in at a point defined by an orthogonal coordinate system.

To asses the state of stress for a body, it is essential to understand the state of loading within a single plane. This single plane would be S_i in the middle diagram of Figure 3.1. If a single plane is loaded, the reaction force should be equal but opposite to maintain equilibrium of forces. The stress of that single plane can be defined by looking at the load distribution. The surface of the body is given by ΔA, with a reaction force of ΔR. As the stress is the intensity of the internal reaction forces applied over the loaded region, it can be denoted as shown in Equation 3.1 (Brady and Brown, 2007).

$$\sigma_r = \lim_{\Delta A \to 0} \frac{\Delta R}{\Delta A} \tag{3.1}$$

The resultant stress for the rock mass can be broken up into two constituent components, these are the normal stress component and the shear stress component. These stresses are as a result two separate reaction force types, the normal force, which is the force that acts perpendicular to the to the surface. And the shear force, which is the force that acts tangentially to the surface. These can both be seen respectively as ΔN and ΔS in the middle image of Figure 3.1. As the normal and shear stresses are constitutive components of the resultant stress they can be defined over the same surface, thus the equations are as follows in Equation 3.2 and Equation 3.3 (Brady and Brown, 2007).

$$\sigma_n = \lim_{\Delta A \to 0} \frac{\Delta N}{\Delta A} \tag{3.2}$$

$$\tau = \lim_{\Delta A \to 0} \frac{\Delta S}{\Delta A} \tag{3.3}$$

A cube defined in an orthogonal coordinate system, with its sides defined by a two axis plane (for example XY in a cartesian coordinate system), like that shown in the right image of Figure 3.1. The reaction stress on the block can be resolved in to three components, t_1, t_2, and t_3 known as the traction vectors which represents the intensity of reaction force on each of the three co-perpendicular surfaces. These traction components are then divided into a normal stress and two shear stresses on any surface. This generates 3 stress components as can be seen in Equation 3.4 (Brady and Brown, 2007).

$$\sigma_{xx} \quad \sigma_{xy} \quad \sigma_{xz} \tag{3.4}$$

As a result of the body in such an orthogonal coordinate system, the resultant stress can be described in the stress tensor in Equation 3.5 (Brady and Brown, 2007). This suggests that there are 9 independent components, however this is not the case, as the body is not considered to rotate or move, therefore the body is considered to have moment equilibrium, therefore components $\sigma_{xy} = \sigma_{yx}$, thus reducing the matrix to 6 components in symmetric matrix as shown in Equation 3.6, further to define that it is a shear stress, the component is change from σ to τ.

$$\boldsymbol{\sigma} = \begin{bmatrix} \sigma_{xx} & \sigma_{xy} & \sigma_{xz} \\ \sigma_{yx} & \sigma_{yy} & \sigma_{yz} \\ \sigma_{zx} & \sigma_{zy} & \sigma_{zz} \end{bmatrix} \tag{3.5}$$

$$\boldsymbol{\sigma} = \begin{bmatrix} \sigma_{xx} & \tau_{xy} & \tau_{xz} \\ \tau_{xy} & \sigma_{yy} & \tau_{yz} \\ \tau_{xz} & \tau_{yz} & \sigma_{zz} \end{bmatrix} \tag{3.6}$$

The concept of principal stresses is important within the thesis as it is the building block for many failure criterion analyses. The principal stress is defined as the normal stress when the shear stress is equal to zero. The minimum value for this is known as σ_1 and the maximum value is known as σ_3.

Another consideration to the stress is the inclusion of water. Where water is included in the rock mass, either in pore spaces or joint spaces, the water can become pressurised due to hydraulic head (height difference). The pressurisation of the water is known as the pore water pressure (p_w) (Brady and Brown, 2007).

3.1.1. Stresses In Situ and Mining

The pre-mining stress state of a rock mass is defined by its geologically history. This is made up of multiple phases; burial, subduction, techtonics, uplift and erosion, all having their part to play when defining the in situ pre mining stress. At the mine in Cavanacaw, the geology has been metamorphosed and uplifted. The dominant mechanism for the in situ stress is believed to be the shear zone.

The introduction of mining results in a change of the in situ stress within the rocks. Open pit excavations tends to show some form of elastic rebound as material is removed. This elastic rebound is the same that would be seen when you remove a bowling ball from a trampoline, however, the displacements would be substantially lower.

The removal of material in the development and ore drives leads to an alteration in the near stress field for the excavations. This component normally has a low impact on the mine, however, when these excavations are coupled, it has a significant impact on the overall disturbance of the mine. The in situ stress overprinted with the mining induced stresses can lead to stress changes and therefore displacements in the underground. The major mining induced stress will be from the opening of stopes, however, the long term effect of these stresses can be compensated for by the use of backfill.

3.2. Strain

A continuation of classical mechanics is strain. Strain describes the relative displacement of particles within a body that is undergoing deformation. When a stress field is altered by an external force it induces deformations within the body. The deformation of the body, and subsequent displacements of the of the particles, can lead to shape changes, which can be described by strains. An example of the engineering strain, which is the 1-dimensional change in length over the total original length, when a uni-axial external force is applied to a body, which can be seen in the left diagram of Figure 3.2. The relation is shown in Equation 3.7.

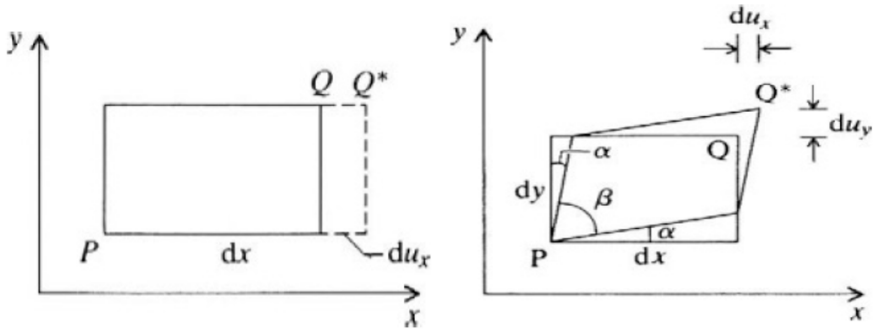

Figure 3.2: Left: A visualisation of engineering strain, where an uniaxial force is applied to a body resulting in a deformation (change in length). Right: A visualisation of strain in two dimensions, as a result of shear stresses.

$$\varepsilon = \frac{\Delta Length}{Length} = \frac{\partial u_x}{\partial x} dx \tag{3.7}$$

This example above only deals with the normal strain, but in reality the shape can change in inter-plane spaces, resulting in shear strains, see the right diagram in Figure 3.2. The magnitude of the shear is 2α, based on the angle change. As the shear strain is the sense of action for the given surface it is composed of two terms much like that of shear stress.

$$\varepsilon_{xy} = \frac{1}{2}\gamma_{xy} = \frac{1}{2}\left[\frac{\partial u_x}{\partial y} + \frac{\partial u_x}{\partial y}\right] \tag{3.8}$$

As a result of a single surface being composed of a normal strain and two shear components, and the body is considered to have moment equilibrium. The formation of the strain tensor is identical symmetrically to that of the stress tensor. This is shown below in the Equation 3.9.

$$\boldsymbol{\varepsilon} = \begin{bmatrix} \varepsilon_{xx} & \frac{1}{2}\gamma_{xy} & \frac{1}{2}\gamma_{xz} \\ \frac{1}{2}\gamma_{xy} & \varepsilon_{yy} & \frac{1}{2}\gamma_{yz} \\ \frac{1}{2}\gamma_{xz} & \frac{1}{2}\gamma_{yz} & \varepsilon_{zz} \end{bmatrix} \tag{3.9}$$

Strains can be divided into two further types relevant for this thesis, based on the permanence of the deformation. The first is elastic strain which refers to deformation within the rocks which is non-permanent, and when the load is removed the deformed points return to their original locations. The second is plastic strains, these deformed points no longer return to their location when the load is removed due to slip and dislocation at the atomic scale. The total strain on a body is therefore composed of these two types based on the amount of deformation, which will be explained subsequently.

3.3. Stress-Strain relations

The previous two section have introduced the concept of stress and strain, it is now essential to describe how these two are linked. These two are related for a medium by the constitutive relationship.

The constitutive relationship, can describe stress and strain for a medium exhibiting any response, such as elasticity or plasticity. Due to the nature of the stress and strain matrix being symmetric, they can be described by two column vectors, which are related by a stiffness matrix, as shown in Equation 3.10 and Equation 3.11.

$$\begin{bmatrix} \varepsilon_{ii} \\ \varepsilon_{jj} \\ \varepsilon_{kk} \\ \gamma_{ij} \\ \gamma_{ik} \\ \gamma_{jk} \end{bmatrix} = \begin{bmatrix} S_{11} & S_{12} & S_{13} & S_{14} & S_{15} & S_{16} \\ S_{21} & S_{22} & S_{23} & S_{24} & S_{25} & S_{26} \\ S_{31} & S_{32} & S_{33} & S_{34} & S_{35} & S_{36} \\ S_{41} & S_{42} & S_{43} & S_{44} & S_{45} & S_{46} \\ S_{51} & S_{52} & S_{53} & S_{54} & S_{55} & S_{56} \\ S_{61} & S_{62} & S_{63} & S_{64} & S_{65} & S_{66} \end{bmatrix} \begin{bmatrix} \sigma_{ii} \\ \sigma_{jj} \\ \sigma_{kk} \\ \sigma_{ij} \\ \sigma_{ik} \\ \sigma_{jk} \end{bmatrix} \tag{3.10}$$

or

$$\boldsymbol{\epsilon} = \mathbf{S}\boldsymbol{\sigma} \tag{3.11}$$

The stiffness matrix is composed of 21 independent stiffnesses, due to the symetric nature. These stiffnesses are defined by a function that describes the rocks reaction to being deformed.

3.3.1. Linearly Elastic Perfectly Plastic Model

Linearly elastic perfectly plastic model, is a constitutive model for replicating the stress-strain relationship. This model is split into the linear elastic stress-strain relationship following Hooke's law until reaching the yield strength. Upon reaching the yield strength, the stress induced by deformation is constant at the yield strength and the model behaves perfectly-plastic, producing plastic strains.

3.4. Rock Response

The previous three sections have introduced the reaction behaviour of materials to applied loads. This thesis is only addressing rocks and backfill as material, thus a specific description with respect to these materials should be made.

A generalised rock response when a uniaxial load is applied is shown in Figure 3.3. The rock responds in the direction of loading (axial strain) and in the perpendicular to loading direction (radial strain). The graph can be divided into several behaviour types as follows.

1. Crack closing, during this phase the material behaves non-linearly as the pre-exisiting discontinuities with the material are closed.

2. Linear elastic, the material behaves elastically meaning that all strains generated, will disappear when the load is removed. During this phase the material will behave according to Hooke's law, which will subsequently be explained.

3. Crack initiation, at this point existing and new fractures begin to propagate marking the change from elastic to elastoplastic.

4. Elastic + Plastic or elastoplastic, at this point the material is behaving as a mixture of elastic, as some of the deformations will disappear when the load is removed. However the deformation caused by the growth of new and existing fracture will not disappear after unloading.

5. Crack coalescence, is the convergence of different fractures which have been generated.

6. Failure or yield strength or Unconfined Compressive Strength (UCS), is the maximum stress in which the sample can maintain.

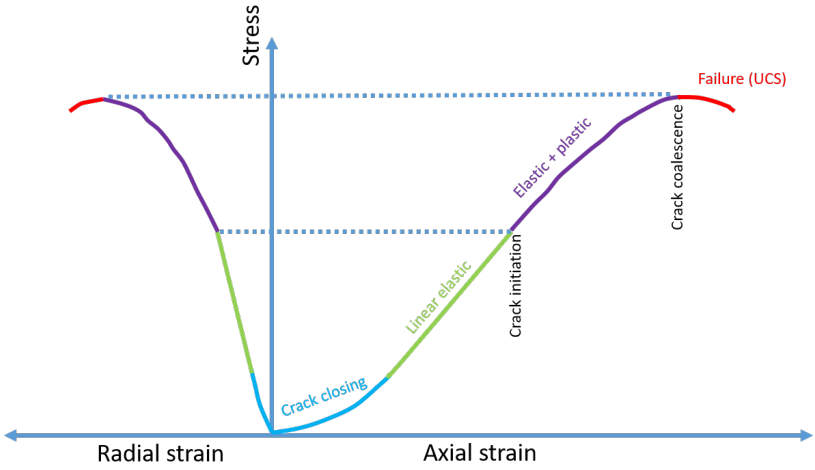

Figure 3.3: The typical stress strain curve for a rock, adapted from Stöckhert (2015).

3.4.1. Hooke's Law

The elastic response of the rock material is of particular interest as it can be approximated by Hooke's Law. Hooke's law is that an elastic medium will deform linearly when a force is applied to it. This linear deformation is defined by a stiffness constant, which is defined within the stiffness matrix addressed in Equation 3.10.

Two separate relationships are important to be defined within the stiffness matrix, those of normal and those of shear. The normal stresses and strains are related through a combination of the Poison's ratio and Young's Modulus as shown in Equation 3.12, whereas the shear stresses and strains are related through the shear modulus, which can be described in term of the Young's modulus and Poisson's ratio as shown in Equation 3.13.

$$\varepsilon_{ii} = \frac{1}{E}[\sigma_{ii} - \nu(\sigma_{jj} + \sigma_{kk})] \tag{3.12}$$

$$\gamma_{ij} = \frac{1}{G}\sigma_{ij} = \frac{2(1+\nu)}{E}\sigma_{ij} \tag{3.13}$$

As all stiffness values can be described by two constants, the Poisson's ratio and Young's modulus, it allows for the generation of an elasticity matrix as shown in Equation 3.14.

$$\begin{bmatrix} \varepsilon_{xx} \\ \varepsilon_{yy} \\ \varepsilon_{zz} \\ \gamma_{xy} \\ \gamma_{xz} \\ \gamma_{yz} \end{bmatrix} = \frac{1}{E} \begin{bmatrix} 1 & -\nu & -\nu & 0 & 0 & 0 \\ -\nu & 1 & -\nu & 0 & 0 & 0 \\ -\nu & -\nu & 1 & 0 & 0 & 0 \\ 0 & 0 & 0 & 2(1+\nu) & 0 & 0 \\ 0 & 0 & 0 & 0 & 2(1+\nu) & 0 \\ 0 & 0 & 0 & 0 & 0 & 2(1+\nu) \end{bmatrix} \begin{bmatrix} \sigma_{xx} \\ \sigma_{yy} \\ \sigma_{zz} \\ \sigma_{xy} \\ \sigma_{xz} \\ \sigma_{yz} \end{bmatrix} \tag{3.14}$$

This thesis plans to use numerical modelling, hence it is important to establish the inverse relationship of this as shown in Equation 3.15. The software determines displacements with the model, which can be used to determine the strain and therefore the stresses at stress points. This will further be explained within chapter 6.

$$\begin{bmatrix}\sigma_{xx}\\ \sigma_{yy}\\ \sigma_{zz}\\ \sigma_{xy}\\ \sigma_{xz}\\ \sigma_{yz}\end{bmatrix} = \frac{E(1-\nu)}{(1+\nu)(1-2\nu)}\begin{bmatrix} 1 & \frac{\nu}{(1-\nu)} & \frac{\nu}{(1-\nu)} & 0 & 0 & 0\\ \frac{\nu}{(1-\nu)} & 1 & \frac{\nu}{(1-\nu)} & 0 & 0 & 0\\ \frac{\nu}{(1-\nu)} & \frac{\nu}{(1-\nu)} & 1 & 0 & 0 & 0\\ 0 & 0 & 0 & \frac{(1-2\nu)}{2(1-\nu)} & 0 & 0\\ 0 & 0 & 0 & 0 & \frac{(1-2\nu)}{2(1-\nu)} & 0\\ 0 & 0 & 0 & 0 & 0 & \frac{(1-2\nu)}{2(1-\nu)}\end{bmatrix}\begin{bmatrix}\varepsilon_{xx}\\ \varepsilon_{yy}\\ \varepsilon_{zz}\\ \gamma_{xy}\\ \gamma_{xz}\\ \gamma_{yz}\end{bmatrix} \tag{3.15}$$

3.4.2. Young's Modulus

The Young's modulus is the elastic response to being loaded uniaxialy, i.e. the gradient of the axial stress over the axial strain as shown in Equation 3.16. This gradient can be defined in many different ways, however for this thesis the consideration is to use the average Young's Modulus. This is done by calculating the average slope of the linear section of the graph generated from UCS tests, as shown by the linear elastic section of Figure 3.3.

$$E = \frac{\Delta\sigma_{axial}}{\Delta\varepsilon_{axial}} \tag{3.16}$$

3.4.3. Poisson's Ratio

A further parameter that is required for the stiffness matrix is the Poisson's ratio. As has been already defined, the loading of a material axially results in deformation in the axial and radial planes. The Poisson's ratio, is the relationship between the axial and radial elastic modulus. The values recorded in this thesis are defined as the ratio between the gradients for the linearly elastic portions as shown in Figure 3.3 and defined in Equation 3.17.

$$\nu = \frac{\Delta\sigma_{axial}/\Delta\varepsilon_{axial}}{\Delta\sigma_{axial}/\Delta\varepsilon_{radial}} \tag{3.17}$$

3.4.4. Anisotropy

The concept of anisotropy is extremely important when describing rocks, as rocks are non-homogeneous material. Anisotropy means that the physical properties of a medium will be different in differing planes. Schist, which is the main material expected to be encountered within this thesis, is by definition an anisotropic rock due to the existence of foliations within. Anisotopy can be in terms of strength or elastic response.

3.4.5. Mohr-Coulomb

Mohr-Coulomb is a failure criterion for soil or rock (intact rock or rock mass), depending on the material tested. But before looking at the failure criterion, it is important to explain the Mohr circle, which is a graphical representation of the shear and normal stresses in arbitrary plane. The vertical axis is shear stress, horizontal is normal stress. The magnitudes of the known principle stress σ_1 and σ_3 are plotted on the effective normal stress axis and the centre of the circle is located half way between the two points. This can be seen in figure Figure 3.4 (Weijermars, 1997).

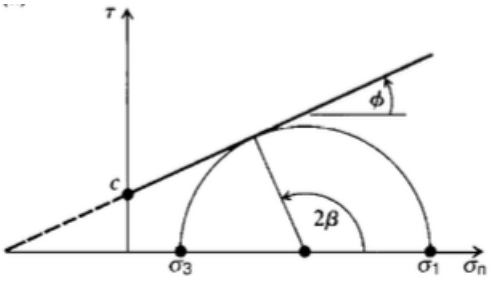

Figure 3.4: Examples of the Mohr circle (Weijermars, 1997).

The Mohr-Coulomb failure criterion, only represents the material tested, thus it can be used to represent both intact and rock mass behaviours. In order to represent the rock mass, a larger sample must be selected in order to account for the discontinuities. The intact rock, however can be represented with a smaller sample, which will return much higher strengths for the most part.

The Mohr-Coulomb failure criterion is the failure envelope defined by multiple triaxial tests. The model works by plotting multiple triaxial tests in terms of their σ_3 and σ_1 as a Mohr circle. The circles are connected using a linear best fit line, as shown in Figure 3.4.

The linear best fit line is the Mohr-Coulomb failure criterion. The equation of the line is shown in Equation 3.18 (Weijermars, 1997). This line represents the relationship between the normal stress and shear stress, there can be no points that exist above that line as they would have exceeded failure. The symbol c represents the cohesion, and ϕ is the internal angle of friction for the rock.

$$\tau = c + \sigma_N tan(\phi) \tag{3.18}$$

The visualisation of a sample should be made to make sense of the data from the graph. This can be seen in Figure 3.5, this shows an inclined shear failure, with an angle of β. This data from a single test could be used to determine a failure curve, by using the fracture angle coupled with the normal stress. As the failure curve is the tangent to where the Mohr circle and the 2β intersect.

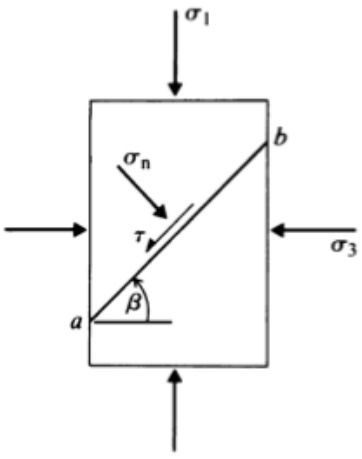

Figure 3.5: A visualisation of the data that is acquired from a triaxial test, which can be used for Mohr-Coulomb.

Mohr-Coloumb is an effect method of modelling the failure criterion of the material tested, however issues occur when the tested material does not represent that of the overall material. A translation

between the intact rock and the rock mass must be established in order to provide a representative model.

An additional mechanism to the Mohr-Coulomb failure criterion is the tensile cut-off. This is a vertical line which intersects the failure curve at a specific tensile stress. If the tensile stress is to exceed that value, the material will reach localised failure.

3.5. Rock Mass Response

Having shown the behaviour exhibited by the intact rock, it is now important to show the methods which can be used to replicate the rock mass behaviour. Rocks exhibit different behaviours on different scales, a good analogy would be a box of gravel. When a load is applied to a single piece of gravel, it may require a significantly large load to break it. However if a load is applied to a pile of gravel, the failure would happen at lower value. This is due to discontinuities, i.e. the gaps between the individual pieces of gravel. This section will look at both the strength, and elastic modulus modification which allows for the generation of rock mass response.

3.5.1. Hoek-Brown Failure Criterion

A failure criterion, that allows the translation of intact rock properties to rock mass properties is the Hoek-Brown failure criterion established in Hoek and Brown (1980). The objective of the criterion was to provide input information to allow for the design of underground excavations, as at the time there was the lack of a suitable method for estimating the rock mass strength, thus their efforts focused on transforming geological information into equations. The original equation was identical to that of an equation that had been used since the 1930s for describing failures within concrete (Hoek and Marinos, 2007).

What Hoek and Brown did, however, was link this equation to geological observations. A framework existed for the classification of geological information in terms of rock mechanics, this was Rock Mass Rating (RMR) developed by Bieniawski (1974) (Hoek and Marinos, 2007). The issue arose that RMR was hard to apply to rock masses of very poor quality. As a result GSI was developed. This then became the key input data for the Hoek-Brown failure criterion, and will be subsequently described in section 3.6 (Hoek and Marinos, 2007).

One of the current accepted models for the estimation of rock mass strength is considered to be the generalised Hoek-Brown failure criterion. This is an empirical method which can be used to estimate the rock mass strength. This equation is shown in Equation 3.19, the terms of the reduced material constant (m_b), s and a are explained and calculated in the equations that follow. Equation 3.19 determines the equation of the line that relates the σ_1 to σ_3, and is based on input values calculated in Equation 3.20 to Equation 3.22.

$$\sigma_1 = \sigma_3 - UCS(m_b \frac{\sigma_3}{UCS} + s)^a \tag{3.19}$$

The m_b, as shown in Equation 3.20, is the reduced material constant. This value is the Hoek-Brown material constant (m_i) reduced by the GSI and disturbance factor (D), which will be explained subsequently.

$$m_b = m_i\left(exp\left[\frac{GSI - 100}{28 - 14D}\right]\right) \tag{3.20}$$

The terms of s and a are shown in Equation 3.21 and Equation 3.22, these terms are Hoek-Brown constants, which are dependent on the characteristics of the rock mass, i.e. the GSI and D.

$$s = exp\left[\frac{GSI - 100}{9 - 3D}\right] \tag{3.21}$$

$$a = \frac{1}{2} + \frac{1}{6}\left(e^{\frac{-GSI}{15}} - e^{\frac{-20}{3}}\right) \tag{3.22}$$

Figure 3.6 shows the resulting failure criterion for a sample based on the laboratory data (blue line), whereas the orange line shows the profile of the failure criterion of the same data with a reduction in strength through the use of the Hoek Brown failure criterion.

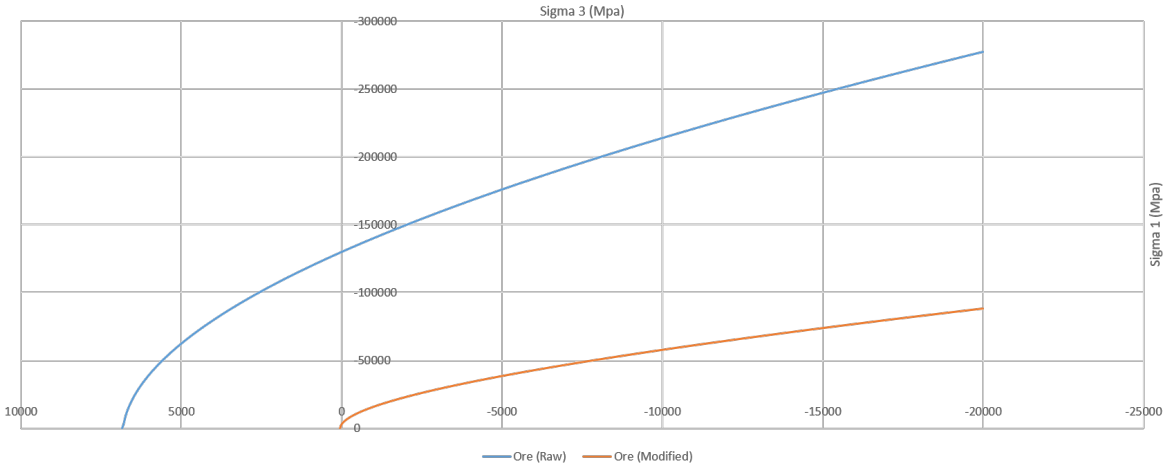

Figure 3.6: Raw data for Hoek-Brown failure criterion compared to the result of the failure criterion modified by GSI

3.5.2. Hoek-Diederichs Rock Mass Modulus

Having established a methodology for the estimation of the rock mass strength, it is equally as important to do this for the elastic behaviour of the rock mass. Using the same terms mentioned previously this is possible through the Hoek-Diederichs empirical estimation of rock mass modulus. This formula reduces the Young's modulus of the intact rock (E_i) to the Young's Modulus of the rock mass (E_{rm}). The equation for this is shown in Equation 3.23 Hoek and Diederichs (2006).

$$E_{rm} = E_i\left(0.02 + \left[\frac{1 - D/2}{1 + e^{((60+15D-GSI)/11)}}\right]\right) \tag{3.23}$$

3.5.3. Jointed Rock Model

Another method for modelling the rock mass is the jointed rock model. The jointed rock model is a model which allows for the modelling of anisotropic behaviour in the rock. This is in terms of both the elastic and plastic stiffness of the the material. The jointed rock model has the ability to replicate a rock mass well when there are defined sets of joints with specific orientations. The model however does require the orientation of the joint sets to be known accurately. This method requires the elastic properties of the rock mass to be known in the parallel and perpendicular orientation to the primary joint set. Further the method requires the strength parameters for each joint orientation to be defined in the same way as the isotropic Mohr-Coulomb method. This means that the results of testing, must represent the rock mass properties in each joint plane.

3.5.4. Influence of Water

As mentioned in section 3.1, the pore pressure alters the effective stress within the rock mass. The response to the water in a homogeneous porous rock rock is to reduce the ultimate yield strength of the rock. The result in jointed rocks is that the pore pressure within the joints, leads to a reduction in friction mobilised shear resistance, due to a reduction in the normal effective stress in the block contact. A further effect related to water within specifically jointed rocks may be the strength reduction due to the softening of infill material. The softening of the infill material, leads to an increase in the ease of deformation. Further the density of the rock mass will increase with the addition of water, as a saturated rock mass is more dense than a dry rock mass, this will lead to an increase in the loading.

3.6. Rock Mass Quantification

A continuation of the previously mentioned Hoek-Brown and Hoek-Diederichs rock mass modulus, is the quantification of the rock mass. This rock mass quantification is then used to convert the intact rock properties to the the rock mass properties. This section will additionally address the quantification method the mine uses for rock mass, which can be translated to the information required to generate both the constitutive models.

3.6.1. Norwegian Geotechnical Institute Tunnelling Q-System

The Norwegian Geotechnical Institute developed the Q-system in 1974 based on over 200 tunnel histories (Barton, Lien, and Lunde, 1974). Grimstad and Barton (1993) updated the system using the data from more than 1,000 cases.

The Q-system gives numerical values to six descriptive features of the rock mass. These values can then be used to assess the requirements for tunnel support. The six parameters are as follows:

- Rock Quality Designation (RQD) originates from a procedure proposed by Deere and Deere (1964) as a measure of the quality of borehole rock. The procedure proposed that RQD is the ratio of the total length of core greater than 10 cm to the total run length of the core.
- Number of Joint Sets (J_n), this is based on the number of joints of differing orientation present in a rock mass. Orientations are counted if they are pervasive throughout the rock otherwise they are treated as random in orientation.
- Roughness of Joints (J_r), the measure of the undulation of the overall joint, coupled with the roughness of the joint surface.
- Degree of Joint Alteration (J_a), describes the alteration product of any joint infill as well as its pervasiveness. It is important to establish the alteration fill, as materials such as clay can have significantly different properties to that of sand.
- Water Inflow (J_w), the rate of inflow of water from the rock surface. This has an impact as the higher the flow the higher the possible pore pressure, which has a significant impact on the resulting stress field.
- Stress condition given as the stress reduction factor (SRF). This is a quantification of how the rock has adapted to the stress regime surrounding it.

For further information on this index for tunnel stability, it would be best practice to consult the Norwegian Geotechnical Institute (2015).

These values are grouped into 3 fractions to generate a Rock Mass Quality (Q-value). This equation is shown in Equation 3.24. The first fraction represents the structure of the rock mass. The second

fraction is representative of the shear strength between blocks. The third fraction describes the current stress conditions.

$$Q = \frac{RQD}{J_n} x \frac{J_r}{J_1} x \frac{J_w}{SRF} \tag{3.24}$$

3.6.2. Rock Mass Rating (RMR)

Rock Mass Rating (RMR) was the alternative method for the quantification of the rock mass, which was proposed in Bieniawski (1974). This method did see a refinement in Bieniawski (1989), which is the method that will be discussed here.

The method for quantification by Bieniawski (1989) is composed of 6 components.

- UCS of the rock material, as explained above.
- RQD, as above
- Spacing of discontinuities, this is the distance between joints.
- Joint Condition ($JCond_{89}$), this is composed of the joint roughness, separation and infill material.
- Groundwater, the amount of water inflow from the rock.
- Orientation adjustment, this adjusts the score based on the favourability of the joint orientations based on the direction of tunnelling.

These 6 components produce values which can be seen in Bieniawski (1989). These components are then combined to give a RMR for the tunnel, which generates a quality for the rock mass as shown in Table 3.1

Table 3.1: Rock quality based on the RMR system (Bieniawski, 1989).

RMR	Rock quality
0 - 20	Very Poor
21 - 40	Poor
41 - 60	Fair
61 - 80	Good
81 - 100	Very good

3.6.3. Geological Strength Index (GSI)

The final method of quantify the rock mass required for this thesis is the Geological Strength Index (GSI). This was developed in Hoek (1994), as a quantification of the rock mass for the Hoek-Brown failure criterion. The GSI graph was later modified in Hoek and Brown (1997) and is based on a relationship between the RQD and the joint condition developed by Bieniawski (1989). This can be seen in Equation 3.25.

$$GSI = 1.5JCond_{89} + RQD/2 \tag{3.25}$$

The most up to date GSI for jointed rocks, is that of Hoek and Marinos (2000). However, jointed rocks do not represent all rocks, therefore Marinos and Hoek (2000) developed an alternative graph for quantifying GSI, which was updated in Marinos, Marinos, and Hoek (2007). These can both be found in Figure A.1 and Figure A.2.

3.6.4. Material Constant

The Hoek-Brown Material Constant (m_i) is dependent on the material, and is used to correlate the relationship between σ_3 and σ_1. Experimental practice for the determination of m_i would be to conduct several triaxial tests. However, where there is no triaxial data, there is an established chart of test data as shown in Figure A.3 (Hoek, 2001).

3.6.5. Disturbance Factor

During mining there will be the removal of material, which provides stress relief to the surrounding rock. This stress relief allows for the surrounding rock to relax and contract into the created void. These relaxations and contractions cause displacements in the remaining rock mass. In order to minimise these effects good excavation design should be applied, in terms of excavation shape, method and application of support and reinforcement.

It should be taken into account that only a localised region will experience damage due to the excavation. This region can reach up to 3 m into the surrounding rock. The damage caused by an explosion is said to be somewhat linear over this 3 m region (Hoek and Brown, 2019), and thus the value can be treated as such. A visualisation of the high to low damage intensity is shown in Figure 3.7.

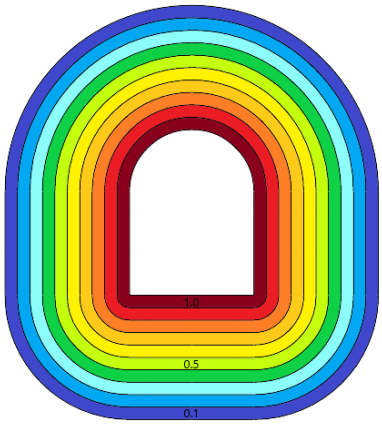

Figure 3.7: Blast damage gradient for a tunnel, gradient generated with 0.3 m intervals where the disturbance factor was reduced by 0.1 from 1 at the boundry of the excavation. Field of view 9 m in the horizontal and 10 m in the vertical

3.7. Failure Mechanisms

The mine consists of two types of excavations, the open pit and underground excavations. It is important to discuss the possible failure mechanisms that exist within the underground openings, the impact they have on the subsurface and the possible impacts on the open pit.

3.7.1. Behaviour Types in Underground Openings

This subsection will discuss the behaviour and failures of underground openings, based on the work of Palmstrom and Stille (2007) and references therein. Currently there is only limited information on the behaviour of the underground excavations at depth within the mine, therefore all possible mechanisms will be presented.

Failures within underground openings occur through several mechanisms, these are gravity driven, stress induced and water influenced. The mechanisms are as follows:

- Stable, which can be seen in box 1 of Figure 3.8. This mode is defined as standing for several days or longer without support.
- Block falls are gravity induced failures, which typically occur along discontinuities. These can occur as single block or multiple blocks falling or sliding out of the surrounding rock mass. Box 2 of Figure 3.8 shows a block failure.
- Caving is a specific case of multiple block falling, where the volume exceeds 10 m^3. This will occur due to gravity and discontinuities. The degree of discontinuity will normally be more pervasive, than in single block falls. This can be seen in box 3 of Figure 3.8.
- Buckling is when rock fragments begin to loosen and fall off along the internal structures such as bedding and foliation. This occurs in rock masses which are anisotropic and brittle, when the deflection is sufficient.
- Rupturing is the breakdown of the tunnel surface over time into pieces, flakes or fragments. This is a time dependent result of the redistribution of stress within the rock mass.
- Slabbing is a brittle failure in which thin rock slabs are detached from the tunnel surfaces in a violent and sudden manner. Slabbing also encompasses popping and spalling, which is a result of moderate to high overstressing of a brittle massive rock.
- Rock bursts are similar to slabbing, however, they have more energy and thus are more violent. Further, rock burst can produce much larger volumes, with some of the large ones registering as seismic events. The cause for rock bursts is a brittle massive rock mass being highly overstressed.
- Plastic behaviour is the permanent deformations of the rock mass due to operstressing. It is shown in Box 8 of Figure 3.8.
- Squeezing and swelling are two behaviours that are regularly mistaken for each other. Squeezing is a time dependent deformation of the overstressed plastic rock, which results in the reduction in the size of the tunnel. It occurs in rock masses with a high percentage of clay minerals with a low swelling capacity. Swelling on the other hand is the reduction in tunnel size due to water absorption. This will occur in rock masses with a large proportion of hydrophilic constituents such as evaporites and swelling clays.
- Swelling clay is when the clay occurs in seams specifically. The introduction of water leads to reduced cohesion and therefore the loosening of blocks. This will only occur where there is water ingress and the occurrence of swelling clays in lenses, bands or seams.

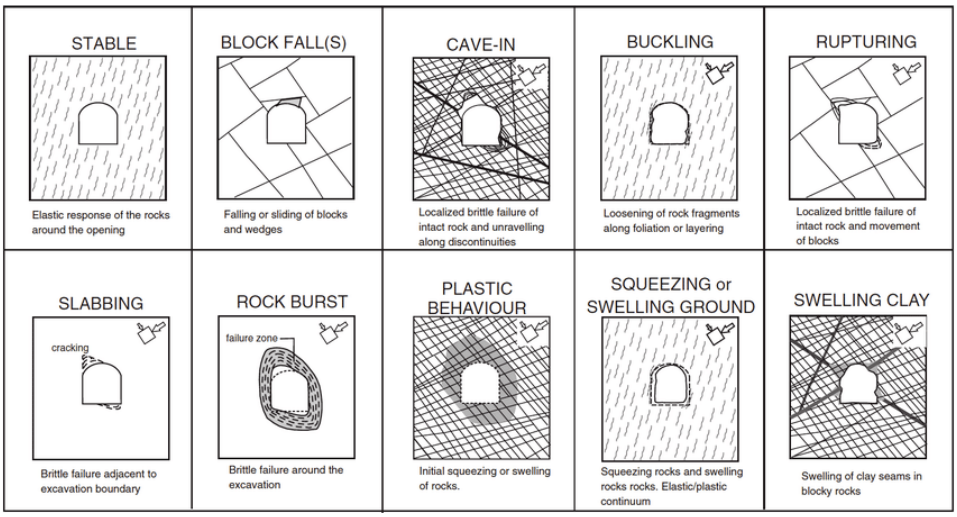

Figure 3.8: The behaviour of underground openings (Palmstrom and Stille, 2007)

3.7.2. Subsidence

Subsidence is the reduction in the ground level due to mining related activities. These activities can be in the form of stress redistribution or a change in the pore pressure due to de-watering. Subsidence in terms of mining can be considered in two ways: Continuous and discontinuous.

Continuous subsidence is a smooth subsidence profile, without any defined steps. This is normally related to tabular horizontal deposits overlain by non-brittle weak rock.

Discontinuous subsidence is a stepped subsidence profile focused on a specific location. These steps are normally large in comparison with the regional subsidence profile. Discontinuous subsidence is more likely to be seen at the mine due to the jointed nature of the rock mass, coupled with the narrow steeply dipping ore body.

Discontinuous subsidence can be caused by two mechanisms: Pillar collapse and caving.

Pillar collapse normally occurs when the stresses contained within the pillar exceed the failure criterion. An unconfined pillar in a mine can be considered in the same manner as a rock mass undergoing a UCS test. Confinement can be achieved through several support techniques such as strapping, rock bolts and backfill. Further, over time a pillar can deteriorate, which leads to a reduction in the strength, which may reduce the strength to below the yield strength. The failure of a pillar, if coupled to further support pillars, can lead to a chain reaction in pillar failure, due to the reduction in the overall support surface area.

Caving is another cause for discontinuous subsidence. This can be split into 3 different categories: Chimney caving, piping and funnelling. Chimney caving occurs in rock which is altered, weak or has previously caved. The caving is a progressive mechanism which occurs in the roof and/or hanging wall, when a stable self supporting arch cannot form. The upper surface of the failing excavation, will continue to progress upwards until enough material has collapsed to fill the void and support the roof. To avoid this unravelling of the rock, confining support methods are used, such as rock bolts, mesh and shotcrete.

A particular concern within chimney caving is the case of crown holes, which are holes within the crown pillar (the top layer of the mine). The crown pillar is extremely important as it generates stability for the mine. At a mine that is progressing from open pit to underground it is important to have analysed the crown pillar correctly. This is due to the mining induced stress field due to the isostatic rebound from the open pit. Isostatic rebound, is the elastic response of the rock mass due to the removal of overburden. This has been discussed in more detail in subsection 3.1.1.

3.7.3. Slope Stability

This section will look at the failure mechanisms which occur within an open pit mine. The mine's open pit is currently stable with no evidence of extensive failure. However, the introduction of the underground mining, may lead to significant changes in induced stresses. Failures within the open pit are dominated by slope stability. Further, alternative mechanisms for slope failure are erosion, rainfall, earthquakes, external loading, and rapid subsidence. Slope stability here will be split into 4 categories: Plane failure, wedge failure, and circular failure, and toppling failure.

Plane failure occurs when 3 criteria are met: The plane of the discontinuity must be parallel or sub-parallel to the plane of the slope face. The discontinuity plane must have a dip shallower than that of the slope and the discontinuity plane must be steeper than that of the friction angle for the discontinuity.

Wedge failure occurs when 3 criteria are met: Two intersecting discontinuities must have trending intersection lines of parallel to sub parallel to the direction dip of the slope. The plunge of the intersection line must be less than the dip of the slope but, steeper than the friction angle for the discontinuities.

Circular failure occurs when 2 criteria are met: The material of the slope, which is either made of soil or

rock, is several orders of magnitude smaller than the slope. The material is not interlocked, and thus behaves in a manner similar to soil. Circular failure can be further divided into 3 distinct categories: Slope failure, toe failure, and base failure. Slope failure occurs when the failure plane meets the slope above the toe. Toe failure occurs when the failure surface meets the toe of the slope. Base failure is where the failure plane extends to below the toe into the base of the surface.

Toppling failure is the overturning or rotation of rock masses, the criteria that are required to be met are: They must contain closely spaced joint sets which dip out of the slope surface. The centre of gravity must fall outside of the dimensions of its base. It should be noted that the removal of overburden (adjusting the in situ stress) can lead to deconfinement and partial stress relief, which may result in toppling failure.

The generation of the open pit has massively influenced the in situ stress within the region. Hence why the discussion about slope failure mechanics has been proposed. It is noted that the introduction of underground operations, specifically stoping, may induce subsidence at the surface and therefore could result in any of the failures mentioned above.

3.8. Initial Synthesis

In order to generate an accurate numerical model it is essential to be able to present a realistic scenario. The scenario must contain a representative geometry, boundary conditions and rock mass properties. Numerical models relies on deformations, strains, and stresses and how they relate through the stiffness matrix. In addition numerical modelling relies on the ability to predict failures based on the chosen constitutive model.

The choice of numerical modelling for scenario based analysis is particularly useful, as it will provide a unique solution for each scenario. These unique solution will provide insight into the the induced stresses, displacements and failure at a local and global scale. This type of testing and analysis cannot be replicated in the field, due to the cost and the inability to create several scenarios in the same location.

3.8.1. Available data

As discussed in chapter 2, the decision regarding the mining method and design has all ready been determined by previous work carried out by the mine. Further discussion was had with the mine as to what further information currently existed that could be used to create an informed decision for modelling.

As mentioned previously the material characteristic for the rocks were available (Burke, 2017), however these results are only estimates and therefore in the authors opinion these were not scientifically robust enough for a master thesis. This means that a method for quantifying the rock mass properties through testing or empirical relationships must be chosen.

The current process at the mine is to work using Q-value in order to determine the stability. This data cannot be used directly within Hoek-Brown or Hoek-Diederichs, to provide the reduction in strength caused by discontinuities. This issue can be resolved as Hoek, Carter, and Diederichs (2013) proposes that GSI can be related to the parameters determined in Barton, Lien, and Lunde (1974) for the rock quality designation for tunnelling. The results of the correlation from Hoek, Carter, and Diederichs (2013) are shown in Figure 3.9.

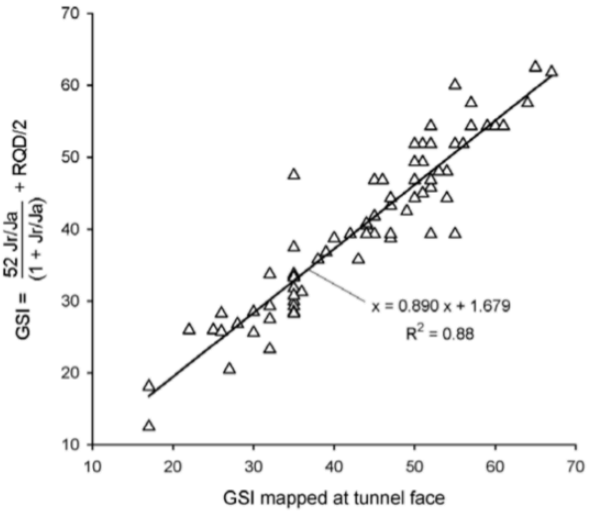

Figure 3.9: GSI Correlation between GSI and GSI data calculated using the parameters from the NGI Q-system (Hoek, Carter, and Diederichs, 2013).

The formula can be seen in Equation 3.26, allowing for the rapid conversion of the Q-value to GSI value determined from Q-value parameters (GSI(Q)).

$$GSI = 52(J_r/J_a)/(1 + J_r/J_a) + RQD/2 \tag{3.26}$$

To determine if this is a viable method, field observations have to be made at several faces to determine the GSI and compare it to the calculated GSI(Q). The mine results should be compared with the correlation observed by Hoek, Carter, and Diederichs (2013).

Currently the understanding of the ground water at the mine is extremely limited. This is in terms of the water table and the ingress of water. The information that is currently available comes from the J_w included within the Q-values, which is discussed in chapter 4.

3.8.2. Relevant Failure mechanisms

The scenario at the mine is that the majority of the host rock is schist with multiple defined joint sets. This means that multiple different failure mechanisms may be exhibited around the underground excavation, such as cave in, buckling, rupturing, slabbing and rock burst, further there is the presence of clay (however it is unknown whether this is swelling or not). These mechanisms mention add levels of complexity to the model in terms of the information required. This project has the objective of looking at the overall stability of the mine so it is therefore possible to omit this complexity to focus on the larger picture. The key failure mechanism that needs to be observed is the plastic behaviour of the rock. Models indicating plastic failures, give an indication to the locations that may be considered for further more complex analysis in the future.

3.8.3. Constitutive models

Several constitutive models have been addressed within this chapter but it is essential to determine a which model offers a good representation of the rock mass, whilst being viable in terms of cost and availability of data. The first proposed model would be Mohr-Coulomb which offers a method to estimate the rock mass failure criterion through multiple tri-axial tests. The second proposed method is the Hoek-Brown model, which allows for the transformation of the intact rock properties to the the rock mass properties through the quantification of rock mass characteristics. Both the Mohr-Coulomb

and Hoek Brown are linearly elastic perfectly plastic constitutive models. The final method presented is the jointed rock model, this method allows for the anisotropic elastic and plastic behaviour of a rock mass to be presented. This method relies on the ability to quantify the rock mass properties through triaxial testing, as well as well as quantifying the joint orientation within the rock mass.

The decision as to constitutive model chosen for the rock mass is difficult as each method has its limitation. The limitations of both Mohr-Coulomb and the jointed rock model is they require the results to be for the rock mass. This means that the testing conducted must be triaxial, and the sample must represent the rock mass. As a result a larger size of sample is required as well as a more expensive and complex testing. Further for the jointed rock model the orientation of the joint sets must be known, this is something that is difficult to quantify in a folded ore body where measurements in unsupported locations are not allowed due to safety concerns. The Hoek-Brown failure criterion and Hoek-Diederichs rock mass modulus, are based upon empirical relationships for the estimation of the rock mass, which is a limitation. Both these methods are well supported within the mining industry and are modelling methods available within multiple numerical modelling softwares such as Plaxis, RS2 and Flac. The availability of rock mass characteristics for almost all of the mine in the form of Q-value, has already been presented as something that can be converted to GSI, is an import consideration as it provides a significant amount of data. The testing of the intact rock properties is also simpler than testing of rock mass properties, as it can be done through several non-destructive test methods as well as UCS testing.

The requirements for the Hoek-Brown model is to establish properties for the intact rock and characteristics for the rock mass. The properties of the intact rock need to be the UCS, the Young's modulus and the Poisson's ratio. The rock mass is quantified by the GSI, the m_i and the disturbance factor.

3.8.4. Planned Data Collection

The data that needs to be collected is the GSI and Q-value during the field campaign, to determine whether it is a viable to use the existing data. During the field work the geology should be looked at to determine m_i, and if there is further refinement on the rock units which would make sense for modelling. Finally the disturbance factor will be addressed and discussed.

During the lab testing it is essential to gather data for UCS, Young's modulus and Poisson's ratio. The mine agreed to allow for the conducting of point load testing, however this does not yield enough information. The decision was then made that TU Delft, would allow for the use of Equotip and acoustic emissions, as well as several UCS tests. As a result of this enough information could be gathered to build an accurate numerical model.

4

Field Testing

In order to build a numerical model, data must be acquired for the geology and rock mass quantification, as detailed at the end of of chapter 3. The checking of the hypothesised relationship between the Q-value and GSI is essential in order to validate the use of preexisting data. Finally analysis should carried out to identify any geological trends within the deposit which may be beneficial for model refinement.

This chapter will review the data collected in the field for the development of the model. Three types were collected: the geology, the Q-value and the GSI. The data collected is a mixture of data collected by the author and the mine geologists. This was due to time constraints when visiting the mine, and due to the protocol that all faces are shotcreted, making it impossible to observe any geological features.

The chapter will divide the mine into 4 domains, which progress with depth. The 4 domains are: the open pit, the decline, the access drives and the ore drives, where the geology and rock mass quantification are discussed.

4.1. The Open Pit

The open pit was observed by the author to identify relevant information for the refinement of the model, this was carried out after the development of the underground workings had commenced. Currently, the open pit has several faces which can still be observed. However, a large amount of scree and backfill cover the majority of the open pit surfaces, this can be seen in Figure 4.1. Within the pit it is difficult to determine what material is in situ and what material has been displaced during the introduction of the mining induced stresses.

To get an indication of the variation within the ore body region it is possible to look at the geology of the faces which are still exposed in the open pit. However, this may not be representative at depth due to the inhomogeneous nature of the rocks. Two locations were selected for observing the geology: the eastern and western slope of the pit. These slopes straddle either side of the ore body. The north and south slopes could not be analysed as they were used as accesses to the open pit, and showed no clear exposure. It should be noted that rock within the open pit has been exposed to the elements for several years, thus has degraded and weathered.

Figure 4.1: View of the open pit looking to the south, showing the limited faces, due to the scree cover. The arrows mark the location of the two identified locations. Field of view 150m.

The western wall of the open pit, as shown in Figure 4.2, shows a bedded exposure of psammite, with a cover of scree. The beds are 10 to 50 cm in thickness and in some parts are interbedded by pelites of up to 15 cm in thickness. The rock is coherent and considered to have a GSI of 50-60. The scree coating on the slope is composed of angular clasts of the country rocks, however, it is not clear whether the scree was natural or man made as a result of backfilling of the pit.

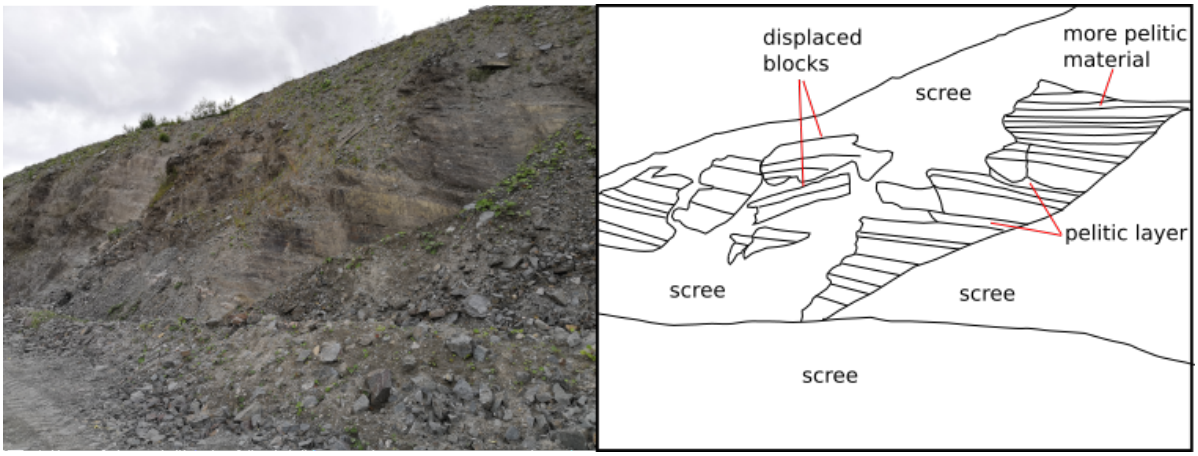

Figure 4.2: Western wall of the open pit. The dip on the bedding is 26|330. Field of view approximately 20 m looking south west.

A closer view of the rock in the western wall can be seen in Figure 4.3. This shows the bedded psammite interbedded with layers of pelite. The psammite is weathered on the surface, also it shows the formation of iron staining. The psamite is a sandy pelite, composed of quartz, feldspar and mica. The pelite, shows the same mineral assemblage, with an increase in mica, which results in a more defined foliation. The joint sets seen in this rock are bedding of 26|330, J1 = 72|168 and J2 = 50|072 as labelled in Figure 4.3.

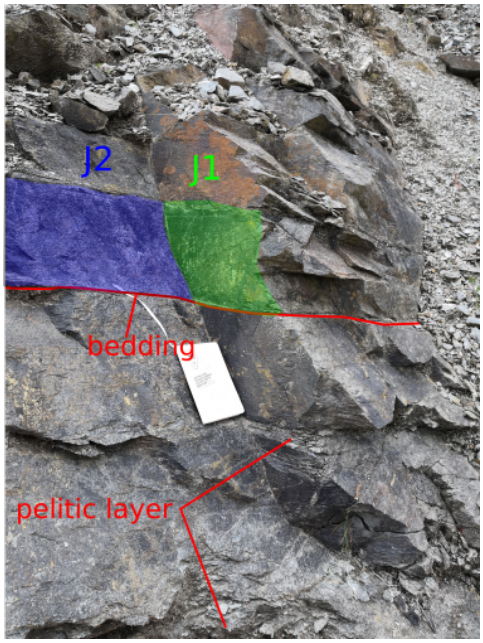

Figure 4.3: Wall rock in the west of the open pit. The diagram shows the pelitic material as well as the bedding and joints. Looking north-west, A5 notebook for scale.

The eastern side of the open pit is also composed of psammite, interbedded with pelites, as shown in Figure 4.4. Evidence of shearing can be observed on this side of the open pit, in the form of boudinaged quartz. The bedding is predominantly thinner than that observed in the western wall, with the bedding being in the range of 5 to 50 cm in thickness. There is also a higher abundance of pelite. These two characteristics lead to a reduction in the GSI, giving a value of 45-55.

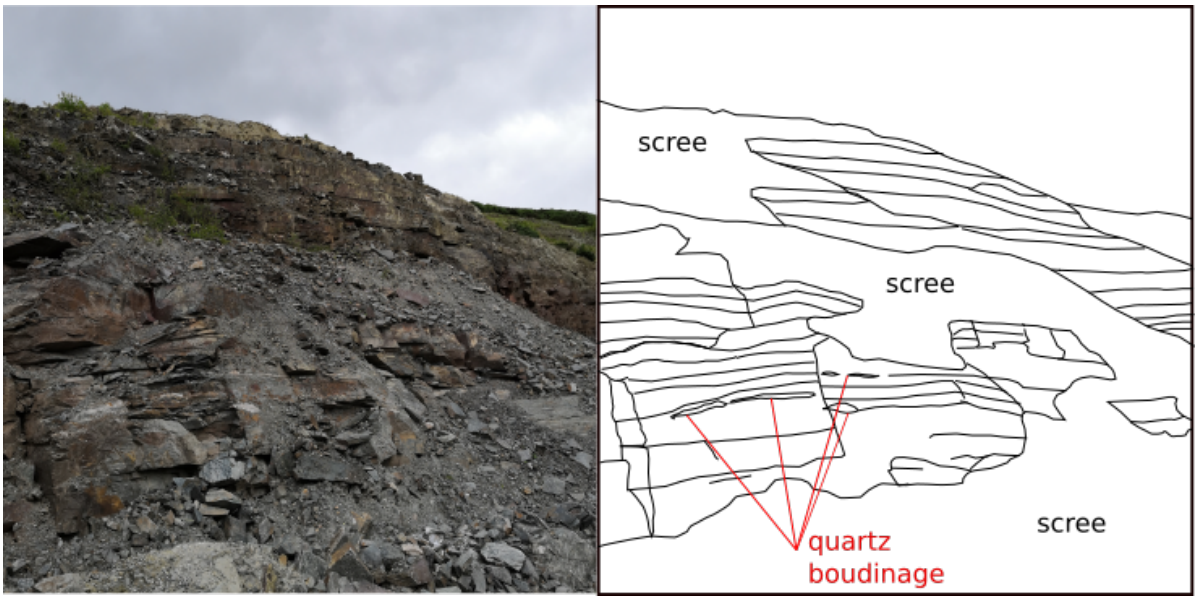

Figure 4.4: Eastern wall of the open pit, showing the bedded nature of the rock mass which dip 10|340, coupled with scree coating. The important shear indicators, the quartz boudins are also labelled. Field of view approximately 20 m, direction of view east.

Figure 4.5 shows a closer view of the eastern wall in the open pit. The resulting bedding plane measured was 10|340, with joint orientations (J1 & J2) of 70|210 and 74|140 respectively. The volume of pelitic material is higher than observed in the western walls.

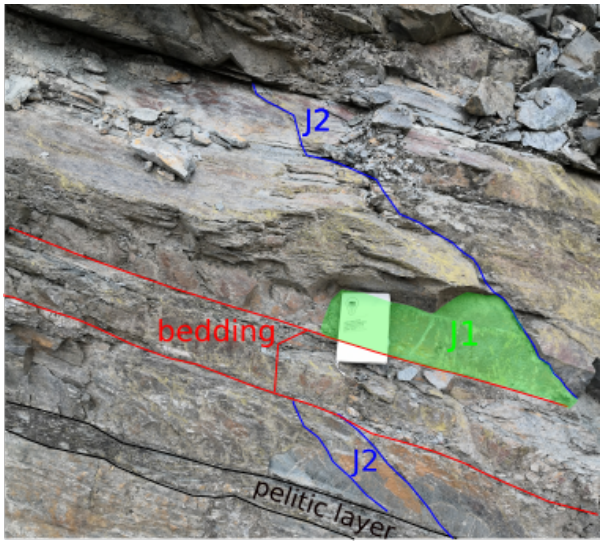

Figure 4.5: Wall rock in the east of the open pit. The diagram shows the pelitic material as well as the bedding and joints. Looking east, A5 notebook for scale.

GSI work was carried out in the early phases of the open pit within McFarlane, Attwood, and Hardie (2009). This data shown in Table 4.1, shows the variation of the GSI within the different faces of the operation. The data gives an average GSI of 50. It should be noted this work was carried out at the surface, where the rock will have experienced more weathering due to fluid percolation and interaction.

Table 4.1: GSI values recorded for the open pit whilst still in operation. (Psam = Psamite and Pel = Pelite)

ID	Easting	Northing	Wall	Locality Info	Rock Type	GSI Rating
1	240169	370850	East	Top of Access into North End	Psam	50
2	240171	370800	East	Old Access Rd. to South End	Psam	63
3	240172	370749	East	Bottom of old Access Rd. to South End	Psam	65
4	240175	370700	East	Along Southern Access Red. Into pit	Psam	56
5	240174	370650	East	Top of Southern Access Rd.	Psam+Pel	36
6	240186	370611	East	Southern Extremity of Exposure	Psam+Pel	30
7	240140	370600	West	North of backfilled area	Psam+Pel	35
8	240114	370650	West	Upper Bench	Psam	61
9	240129	370700	West	2nd Bench	Psam+Pel	57
10	240123	370750	West	2nd Bench	Psam+Pel	40
11	240113	370800	West	Bottom of main access road	Psam+Pel	47.5
12	240089	370850	West	Mid way along Main Haul Road	Psam+Pel	53
13	240106	370900	West	Bench below haul road	Psam+Pel	43
14	240108	370950	West	Bench below haul road	Psam+Pel	40
15	240098	371000	West	NW corner of pit	Psam	70
16	240114	3701000	East	NE corner of pit	Psam+Pel	53
17	240140	370950	East	Access Rd. To North End	Psam+Pel	45
18	240153	370900	East	2nd. Bench/Access Rd. To North End	Psam+Pel	57
					AVERAGE:	50.1

Despite the scree coating, the two available faces help to generate some understanding of the geology that may be encountered underground. Firstly both locations in the open pit were composed of psammitic and pelitic material, however the abundance of each was different on either side of the pit. The western side showed thicker beds and less pelitic material, as a result the GSI was higher. Furthermore, there is the indication of folding within the open pit due to the change in orientation of bedding planes within the east and west walls. The work of McFarlane, Attwood, and Hardie (2009), determined a GSI of 50 for faces within the open pit. This can be linked to the increased fluid peculation and weathering at the surface.

4.2. Decline

The second domain is the decline. The decline is the corkscrew style drive which descends through the country rock to the base of the ore body, its specifications and development process can be found in section 2.3. This section will look at the work carried out in the decline, which is sub-divided into geology, Q-value and then GSI.

4.2.1. Geology of the Decline

The geology of the decline was analysed through face maps produced by the mine geologist, as well as an underground inspection in regions that were not shotcreted. The geology of the decline is predominantly psammite, which is interbedded with minor amounts of pelite. It should be noted that there are quartz veins as well as lenses of fault gouge and chlorite, which occur sporadically throughout the rock mass. Figure 4.6 shows a typical decline face, the face is composed of a uniformly bedded psammite, which exhibits minor folding, localised faulting, and minor pelite interbedding. The bedding of the psammite is typically in the range of 5 to 30cm, whereas the pelite is typically thinner in the range of 1 to 10 cm.

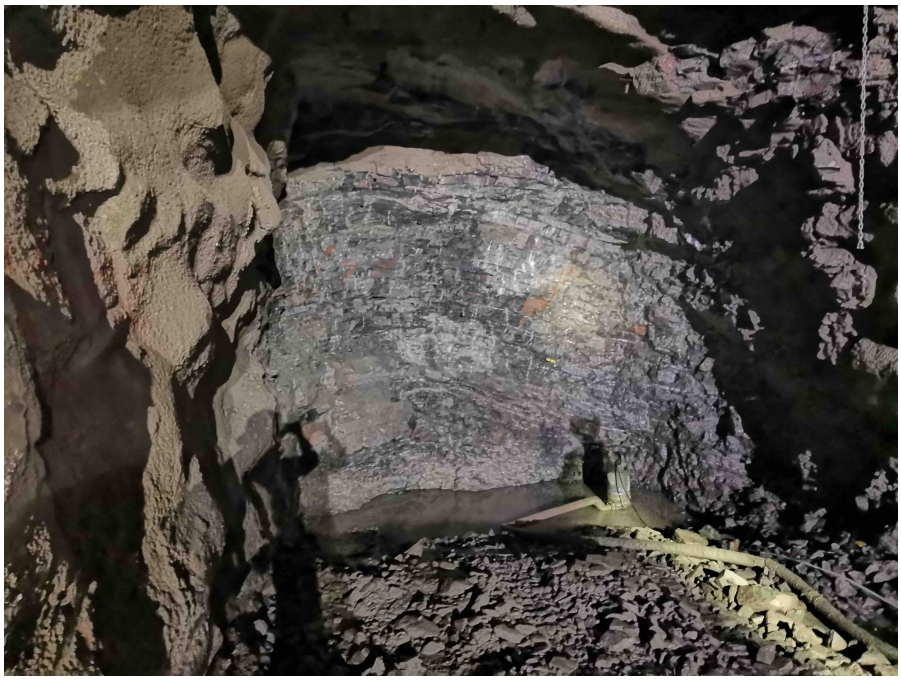

Figure 4.6: Image of the decline face showing slight folding within the bedding. The face is composed of psammite with very little layers of pelitic layers. The field of view is 5 m.

The country rock psammite is composed of quartz, feldspar and mica. There is a defined foliation throughout, however, the degree of foliation is variable. Iron staining is fairly common on the faces of the decline, but to a much lower degree than that seen in the open pit. The pelitic layers are made of the same material, however, the abundance of mica is higher, thus leading to a more defined foliation.

4.2.2. Q-Values of decline

The Q-values of the decline can be seen in Figure 4.7. The data was gathered at the same time as face mapping (approximately 2.5 to 5 m intervals), during the development of the decline. The data was gathered by two separate geologists, with the first covering from the opening of the addit to 150 m, there is then a 62 m gap before the second geologist took over the data acquisition. The graph

shows that the Q-values increased from opening the portal to the current face. Due to the data being collected by two separate geologists the data sets were split into data set A and B. The values seem to have stabilised a little in the second data set, as there is a reduction in the standard deviation from 1.56 to 1.10, as can be seen in Table 4.2. Further, the range of Q-values between the two data sets has decreased from 7.06 to 4.36.

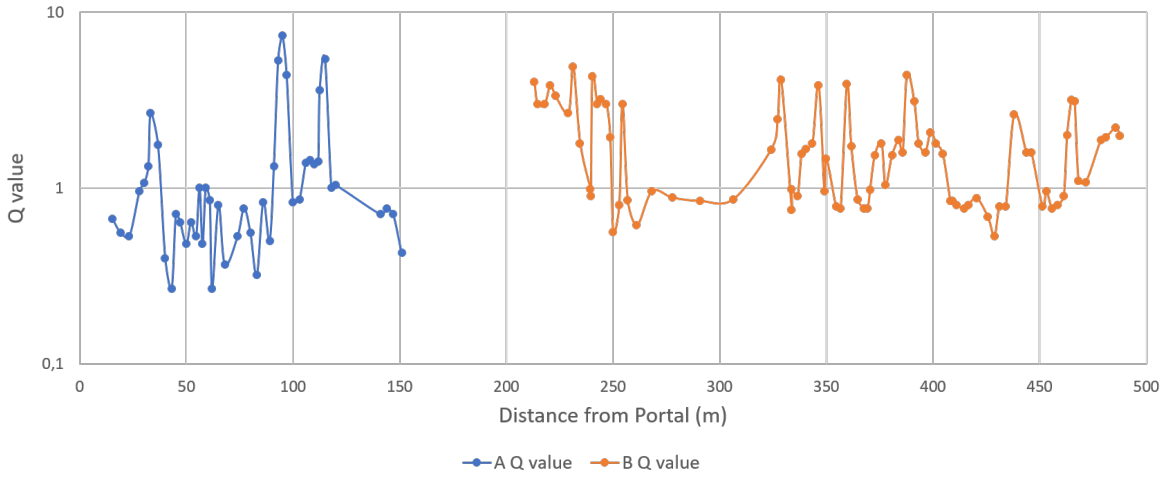

Figure 4.7: Q-value progression as you move further from the portal down the decline. It should be noted there is a 62 m gap between data set A and B

Table 4.2: Statistical analysis of the Q-values data collected from the decline.

	Mean	Mode	Median	Max	Min.	St.Dev.	N
A	1,39	0,53	0,84	7,33	0,27	1,56	42
B	1,76	0,77	1,57	4,89	0,53	1,10	84

4.2.3. GSI of the Decline

Due to the methodology of recording geotechnical information at the mine, only a limited amount of GSI data is available for the decline. These values were collected by the author from 3 consecutive faces, providing a GSI of 60, 56, and 57. A discussion with the team regarding these three consecutive faces, as well as consultation of the previous face maps, concluded that these three faces appeared to be representative of the localised rock within the decline. As discussed previously in subsection 3.8.1, the conversion of Q-value to GSI is theoretically possible, however the viability for this particular case will be discussed in subsection 4.7.2.

4.3. Access

The access drives are those drives which connect the decline to the ore body, the specifications can be found in section 2.3. At time of writing only data for the K1084, K1072 and K1060 accesses were available. The key data that was unavailable was the K1096 access.

4.3.1. Geology of the Access

The geology of the access levels is composed of the same material as the decline up to the point where the ore body is intersected. The faces are composed of psammite, with minor interbedded pelite, with a thickness of 5 to 30 cm, and 1 to 10 cm respectively. When intersecting the ore body the geology changes from the country rock, to quartz breccia and massive sulphides, which contains the

mineralisation. When analysing the facemaps, the transition from country rock to ore occurs over 50 cm to 3 m. This geology and transition are described more thoroughly in subsection 4.4.1. The geology then moves back into the same country rock, the indication from face maps is that the geology is the same either side of the ore body.

4.3.2. Q values of the Access

The Q-values within the ore drives are show in Figure 4.8, these were collected by the mine geologist. It should be noted that the ore drives occur at 38 m for the K1084, 67 m for K1072 and 34 m for the K1060 access. These locations are highlighted with arrows in the figure. The data suggests that the Q-value has improved overall with depth, as the average value for access K1072 is higher by a factor of 2.35 than the K1084 and the value for K1060 is higher by a factor of 1.75 than K1084. The average for the K1084 access is the lowest Q-value of 1.15. The value may have gone down between K1072 and K1060 accesses due to K1072 covering a larger distance without data being collected. There seems to be a dip in the Q-values in the direct vicinity of the ore drives, however there does not seem to be any other distinctive trend within the access drives.

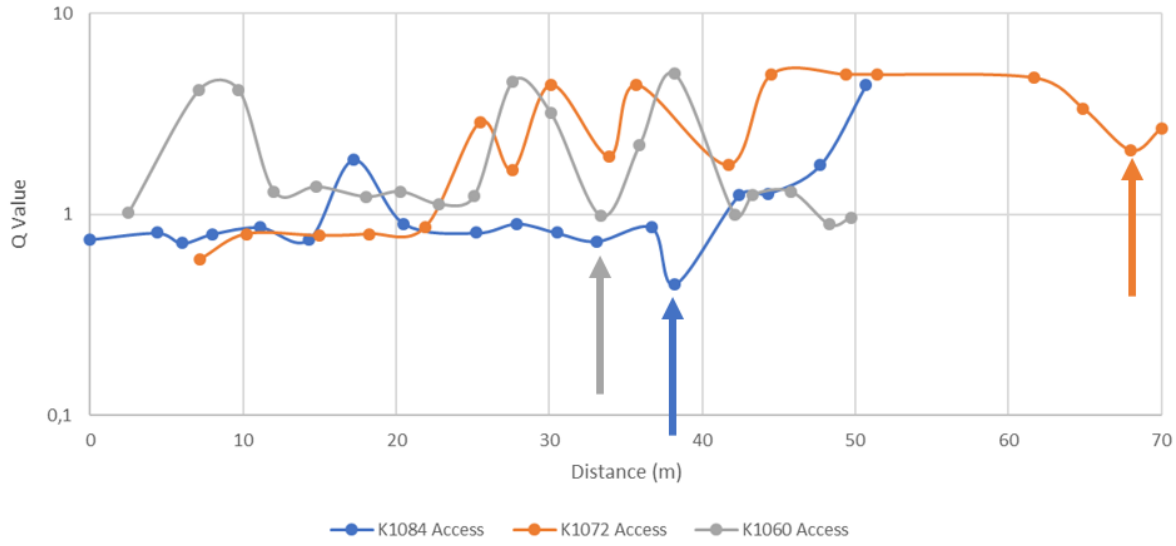

Figure 4.8: Q-values progressing along the access drive towards the ore body. Arrows show location of ore body.

Table 4.3: Statistical analysis of the Q-values data collected from the access levels.

	Mean	Mode	Median	Max	Min.	St.Dev.
K1084	1,15	0,81	0,84	4,40	0,45	0,89
K1072	2,70	4,95	2,37	4,95	0,60	1,67
K1060	2,02	1,30	1,30	5,00	0,89	1,42

4.3.3. GSI of the Access

The values recorded for GSI in the accesses are limited in the same way as the decline. As a result there are 5 consecutive faces in the K1060 level that were recorded for GSI. These faces generated GSI values of 62, 60, 55, 55, and 65. This generates an average GSI of 59.5 with a standard deviation of 3.9. This is comparable with the GSI that was reported for the decline, in the section above.

4.4. Ore Drives

The ore drives could be considered the most important piece of development, due to their financial importance. As stated, these drives aim to follow the ore body as closely as possible. The specifications can be found in section 2.3. This section will discuss the work carried out in the ore drives, consisting of the geology, the Q-value and then the GSI.

4.4.1. Geology of the Ore Drives

At current, the geology is known for 3 levels with confidence. These levels are: The K1096 ODS, K1084 ODS and the K1072 ODN and ODS.

The geology is split into 6 different rock units on a mappable domain. These units are country rock (psammitic schist), altered country rock, mineralised country rock, massive sulphide, quartz breccia, and mineralised fault gouge. There are further quartz veins and grey-green fault gouge , however, these are too narrow and discontinuous to discretise into mappable units. The descriptions that follow are based on the observations of the author and discussions with the mine manager and geologist.

The country rock is a psammite, composed of quartz, feldspar and mica. The rock shows a defined folation, however, this is variable throughout. Within the country rock there are some pods of quartz and layers of pelite. The pelite is composed of the same material as the psammite, however, the abundance of mica is higher and as a result the foliation is more defined.

An altered version of the aforementioned country rock, appears as a localised halo. This rock unit has undergone a form of diagenetic alteration, which has resulted in chloritisation. A hypothesised mechanism for this alteration, would be the peculation of hydrothermal fluids within the shear zone during deformation.

Mineralised country rock occurs locally around the main mineral hosting units, and contains significantly higher percentages of sulphides than the country rock. These sulphides are the same sulphides found within the quartz breccia and massive sulphides.

The ore body is a continuum composed of varying degrees of sulphides and quartz. The two end members of the ore continuum are massive sulphide and quartz breccia. The massive sulphide is composed of mostly sulphides in the form of pyrite, chalcopyrite, sphalerite and galena, whereas the abundance of those minerals is lower in the quartz breccia. The sulphide minerals make up the matrix of both of these rock types, and hosts the gold mineralisation as bound gold. Both rock types contain clasts of quartz, those in the quartz breccia vary in size from 2 to 15 cm. Whereas those within the massive sulphide show higher evidence of techtonic clast reduction, which results in a reduced size of 5 mm to 5 cm.

The mineralised fault gouge (black clay) is the thinnest mapped unit. It is composed of a sulphide-rich fault gouge, which is developed predominantly through the centre of the ore body as a result of shearing. At some points the fault gouge was smaller than the mappable unit, at these points the layer was still mapped as it provided essential information that the direction of drive progression was correct.

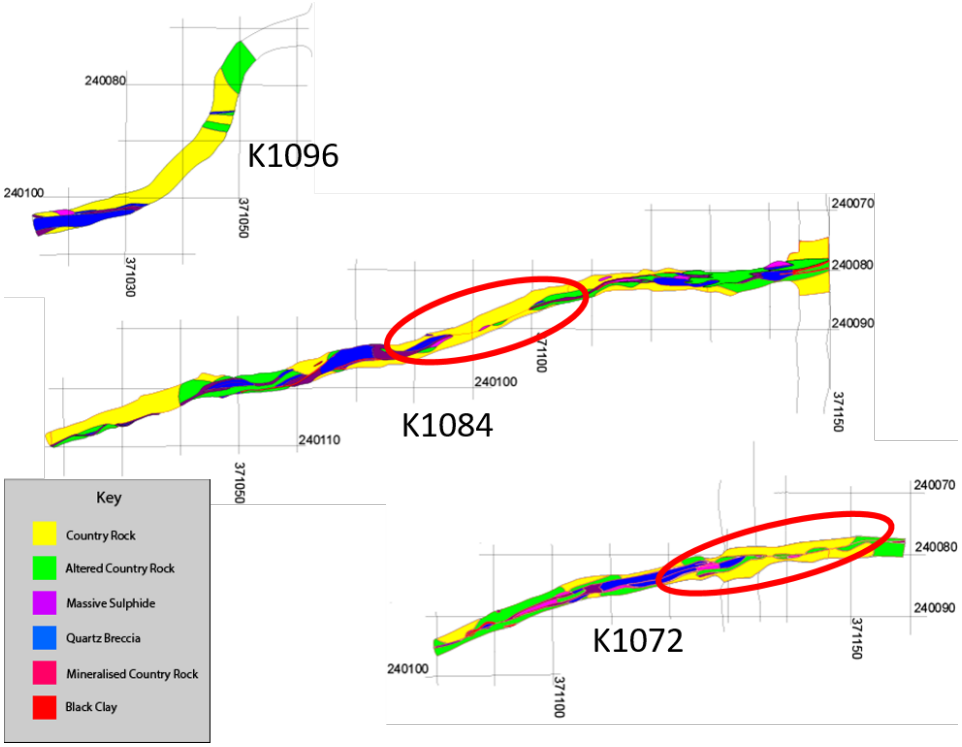

Figure 4.9: A geological plan map of excavation of ore drives based on the face maps. Geological key for the maps that are to follow. Yellow = Country rock, Green = Altered country rock, Purple = Massive sulphide, Blue = Quartz breccia, Pink = Mineralised country rock, Red = Black fault gouge. North to the right.

K1096

The geology of the K1096 ODS drive is shown in the top plan map of Figure 4.9. The map shows a curving drive, which bends in the direction of the ore body. Outwith the ore body, the geology is a mixture of country rock and altered country rock. The ore body starts at around 40 m into the drive where quartz breccia is observed. The known ore body continues for 25 m and is composed of quartz breccia, mineralised country rock, and massive sulphide.

K1084

K1084ODS is currently the longest ore drive within the mine and can be seen in Figure 4.9 as the middle map. The ore drive shows 2 to 3 sheared structures with ore that pinches and swells. There is a known thread of mineralised fault gouge which extends throughout the drive. The ore structure is composed of quartz breccia, massive sulphide and mineralised fault gouge, with very little order. The ore body shows localised halos of altered country rock along its length.

K1072

The K1072 level consists of 2 ore drives in the north and south directions and can be seen in Figure 4.9 as the bottom plan map. There is a higher proportion of ore than seen in the K1084ODS drive. A thin vein of mineralised fault gouge exists laterally in the same manner as the level above (K1084). The ore body is composed of the same material as the level above.

4.4.2. Ore Drive Q-values

The Q-values of the ore drives are the most variable of all of the underground workings. This is due to several factors, the degree of faulting, the geology and the joint alteration. The largest influence on the Q-value for the ore drives is the stress reduction factor, this is high due to the number of faults within the shear zone.

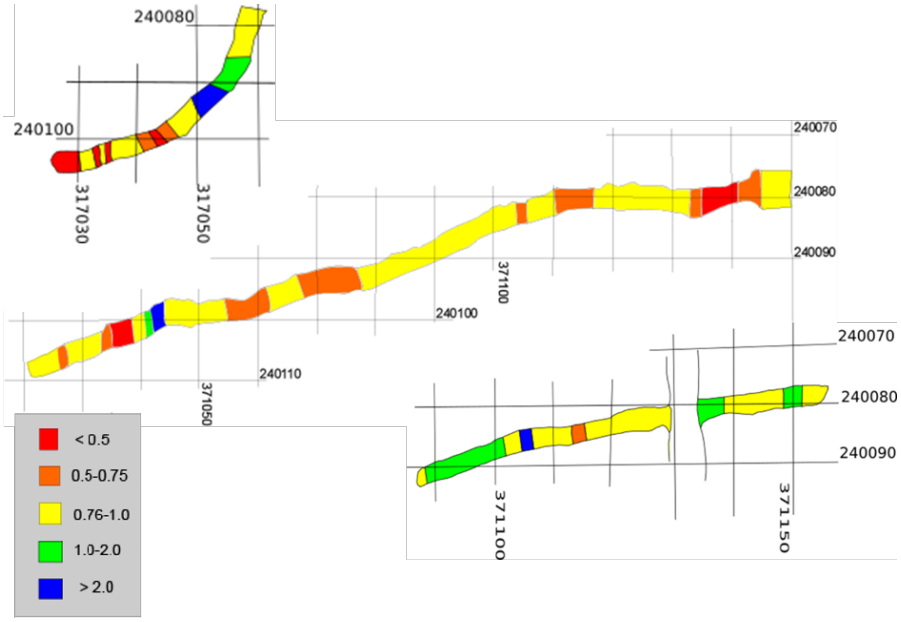

Figure 4.10: Q maps for the ore drives on level K1096, K1084, and K1072.

Table 4.4: Statistical analysis of the Q-values data collected from the ore drive drives

	Mean	Mode	Median	Max	Min.	St.Dev.
K1096	0.6	0.5	0.5	0.9	0.3	0.2
K1084	0.8	0.7	0.8	1.0	0.4	0.2
K1072 ODS	1.0	1.0	1.0	2.1	0.7	0.2
K1072 ODN	0.9	n/a	0.9	1.6	0.7	0.2

K1096

The K1096 drive was abandoned as noted previously because of low Q-values, this can be seen in top plan map within Figure 4.10. It should further be noted that the drive does not start in the ore body but rotates into it, thus the ore body starts at 40 m into the drive. The average Q-value for the ore drive is 0.59, although the Q-value dropped below a critical level 0.5 for over 5 m, as can be seen in Figure 4.11. This was more critical than in any other level as K1096 is the highest level in the mine, thus lies directly beneath the crown pillar, a key component for mine stability.

K1084

The K1084ODS drive also shows reduced Q-values when compared with the development. However, there is a marked improvement from the K1096 drive. The average Q-value is 0.84 which is 42% higher than the K1096 level. The majority of the drive length lies in the domain between 0.76 and 1.0, as can be seen in the middle plan map of Figure 4.10. There are two sections which can be considered on the more dangerous side of the spectrum, with a Q-value of less than 0.5, these can be seen as the two low point in the graph in Figure 4.12 at 5 to 10 m and 114 m.

K1072

The K1072 level is split into 2 ore drives, ODS and ODN respectively. Both of these drives show a marked improvement in the Q-value over the K1084 level. The average Q-value has improved to 0.94 which is a 12% increase on the K1084 level. This can also be seen when doing a visual inspection of Figure 4.10, the proportion of values in the 1-2 Q-value bracket is much higher. When looking at Figure 4.13, it can be seen that the variation has decreased throughout the drive as the majority of the points lie or or are near to 1.0.

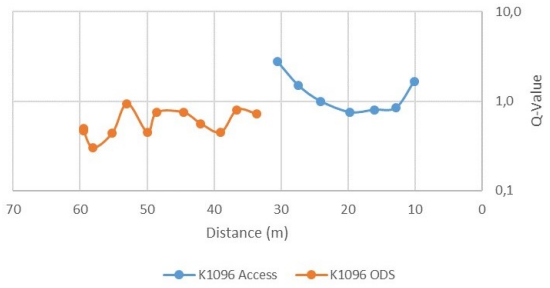

Figure 4.11: A graph of the Q-value as you progress down the K1092 drive. North to the right.

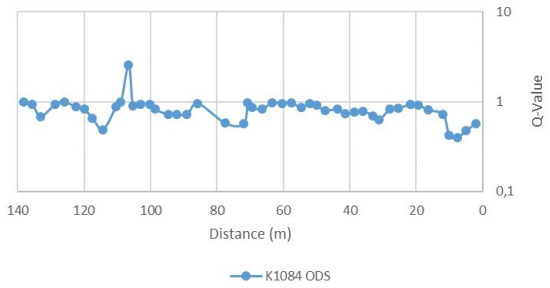

Figure 4.12: A graph of the Q-value as you progress down the drive for the K1084. North to the right.

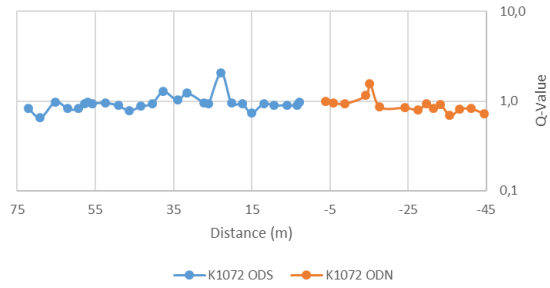

Figure 4.13: A graph of the Q-value as you progress down the drives of K1072 ODS and ODN. North to the right.

4.4.3. Ore Drive GSI

As stated previously, the GSI is not the method used for recording rock mass at the mine. Further, the GSI is easier to associate with specific rock types, rather than a complete face made up of different rock units. The proposed method here will be to take the observations from the field and plot a range on the GSI chart.

The first unit is the country rock (yellow circle in Figure 4.14). Within the ore body there is some indications of enhanced shearing, however, the GSI predominantly lies in the range of 45-60. The same is true of the mineralised country rock, which shows very little reduction in the quality of the

rock mass. The altered country rock does show a reduction in the GSI, resulting in a GSI of between 35 and 50 (green circle in Figure 4.14). The quartz breccia and massive sulphide are heavily broken up rock masses and therefore are represented with a GSI of 30 to 40 (shown by the blue circle in Figure 4.14). The final unit indicated with a red circle in Figure 4.14, is the mineralised fault gouge which is represented with a GSI of between 10 and 15.

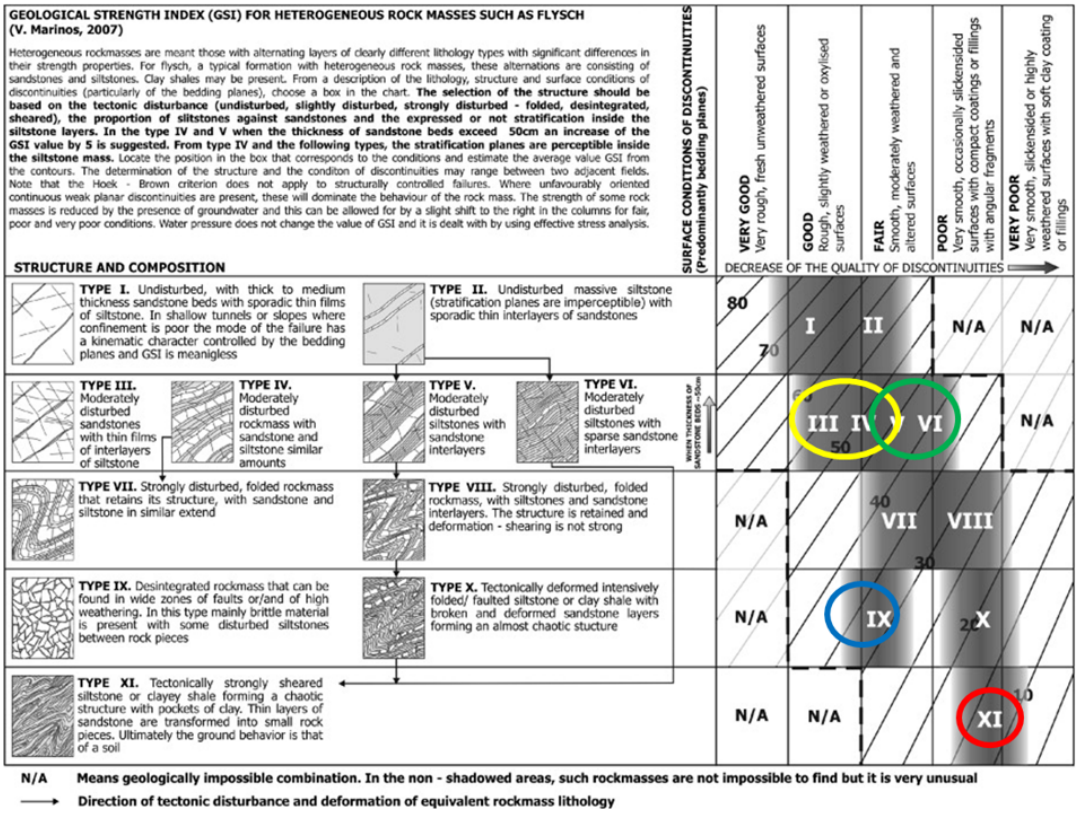

Figure 4.14: Shows the GSI of different rock units plotted on the Flysch GSI chart. Yellow represents the country rock and mineralised country rock, green represents the altered country rock, blue represents the quartz breccia and massive sulphide, and the red represents the black fault gouge (Marinos, Marinos, and Hoek, 2007).

4.5. Ground water

As mentioned in subsection 3.5.4, water can affect the strength and therefore the stability of the rock mass. During the consultation period at the mine, the author observed limited water ingress within all developments. This result is backed up by the J_w from the Q-values for the mine, where the results are predominantly dry to minor inflow. Occasionally within the ore drives there are localised regions with occasional out washing of joint fillings in heavily faulted zones. This tended to be only in periods of extended precipitation at the mine site.

Upon consultation with the mine manager, the decision was taken to exclude water from the study on the basis that there is limited evidence of water egress through the mine walls. This may not be the case with depth as the water table may be encountered before reaching the mine limits.

4.6. Disturbance Factor

As discussed in subsection 3.6.5, the rock will experience a reduction in strength caused by the extraction of material in the immediate vicinity. The extraction by a poorly designed blast has a much larger impact than a well designed blast. At the mine it is difficult to see the extent of the blast damage,

however it is present. The disturbance factor will be excluded from the models due to the fact that the intact rock that will be tested has experienced the highest degree of disturbance, therefore already reducing the strength before testing.

4.7. Analysis

This section will look through the gathered field data in order to extract relationships which are useful in terms of the refinement of the models. This will initially address the geological interpretation of the observations made at the different localities. The rock mass will then be analysed in order to establish viable solutions for quantifying the rock mass within the models.

4.7.1. Geology

To define the model well it is important to understand the geology of the mine. The initial observations made from the geological sections within this chapter is the country rock is a psammite which is interbedded with pelite. These rock units do show localised variation in bed thickness and mineralogy, but for the most part are 10 to 40 cm thick, and composed of quartz, feldspar, and mica.

The geology gets significantly more complex when looking at the ore drives, due to the sheared nature. When considering linking the different plan maps as seen in Figure 4.9, it is difficult to draw a definitive conclusion due to the limited data. Looking at the two levels with the most data, K1084 and K1072, it could be suggested from the geometry that there is a dip of 17° to the north as shown in Figure 4.15. This is based on purely a visual geometric relationship for the geology as shown by the red ellipses in Figure 4.9. In reality the complexity of a shear hosted gold deposit is more complex.

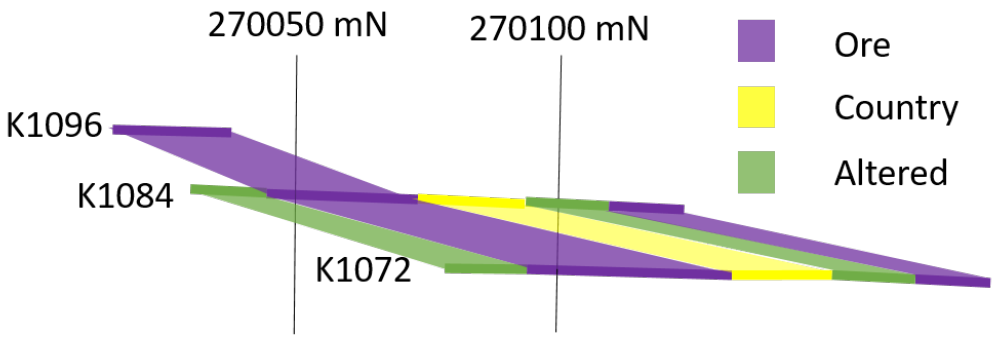

Figure 4.15: Schematic section through the ore body running along strike, connecting the known data.

4.7.2. Rock Mass

This subsection will look at comparing the data that quantifies the rock mass. First the relation between the geology and the Q-value will be presented. Next the results of comparing the Q-value and GSI, to establish if the relationship presented in Figure 3.9 was viable for the mine. If this is successful, then the method will be used to calculate GSI for the rock masses.

Geology and Q

As mentioned previously the mine records rock mass data in the form of Q-value, so the initial comparison will be made between the observed geology and Q-value, specifically that shown in Figure 4.9 and Figure 4.10. Firstly, the proportion of weaker units, such as the altered country rock and fault gouge lead to a reduction in the overall Q-value for a face. Secondly, within the rock units there are variabilities which result in a reduced Q-value, for example the country rock in one section may have a higher

percentage of pelite or the bedding within the psammite may be less than 10 cm. Thirdly, structures such as faults have not been recorded on the geological map, but can result in significant reductions in Q-value. Finally, the geological maps do not take water into account, however some sections within the ore body show more water ingress than in other sections. This is something that Q-value takes into account where as geology does not. The Q-values do on the whole appear to improve with depth, especially within the ore drives.

Q and GSI

As discussed in subsection 3.8.1, there is a formula that can be used to convert the Q-value to GSI. As proof that this conversion is viable for the estimation of GSI, the author calculated the correlation between the GSI and GSI(Q) for the mine, and compared them to the correlation shown in Hoek, Carter, and Diederichs (2013).

This conversion can be done for development faces as they do not show the variation like that of the ore drives. The values compared consisted of 10 data points gathered between the 28th of June and the 10th of July 2019, these values were taken in the decline and K1060 access. The data points and their ranges are shown in Figure 4.16.

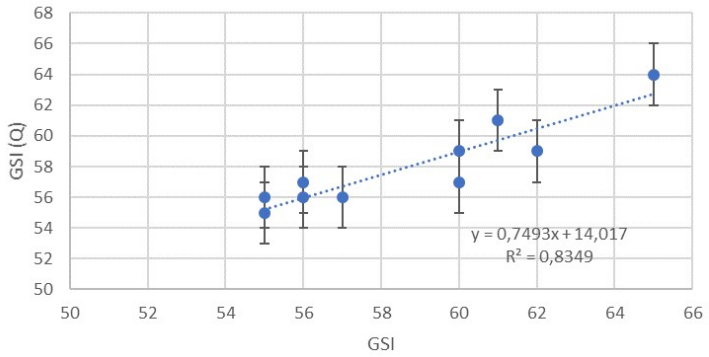

Figure 4.16: GSI vs GSI from the Q-values collected by the mine geologist

The result is that the correlation generated is 0.7493x + 14.017, with a R^2 of 0.8349. This is a shallower linear line than the line reported in Hoek, Carter, and Diederichs (2013), however, it should be noted that the range and number of samples in that example is significantly larger. The decision was made to use correlation suggested by Hoek, Carter, and Diederichs (2013), due to the limited number of sample points for the mine and limited range.

However, the conversion of the Q-value and GSI from the ore drives does not provide good correlation for two reasons. The first reason is that the Q-values are representative of the whole face of the ore drives, whereas the GSI is representative of a single rock type. The second is that within the ore drive there are multiple rock units which make up the face, as can be seen in the maps within Figure 4.9. This is the reason that the author has determined that it is not a feasible method to use the formula to covert the Q-value to the GSI for the ore drives.

The conversion of Q-value was done for each point represented in Figure 4.7. This allowed for an even spread of data distributed down the tunnel, excluding the 62 m gap where no data is available. The data collected from the decline was split into two data sets, decline (0 to 150 m), and decline (213 m to current).

The first set of GSI(Q) data, which represents the addit to the first 150 m, shows 3 data clusters within the histogram as can be seen in Figure 4.17. These clusters are around 45, 50, and 57, and generate a mean of 54, a median of 56, and a standard deviation of 5.1. This information coupled with the data from Table 4.1 allows the selection of a conservative GSI of 50 for the upper part of the ore body.

The second set of GSI data for the decline is from 213 m up until 475 m. The histogram of this data is

visible in Figure 4.18 and is clustered around the values of 53 to 59, where 80 of the 86 points lie. The resulting mean and median value of 56 with a standard deviation of less than 2.4. This gives confidence that a GSI value of 55 is a reasonable assumption based on the available information and the fact that the ground conditions seem to be improving with depth.

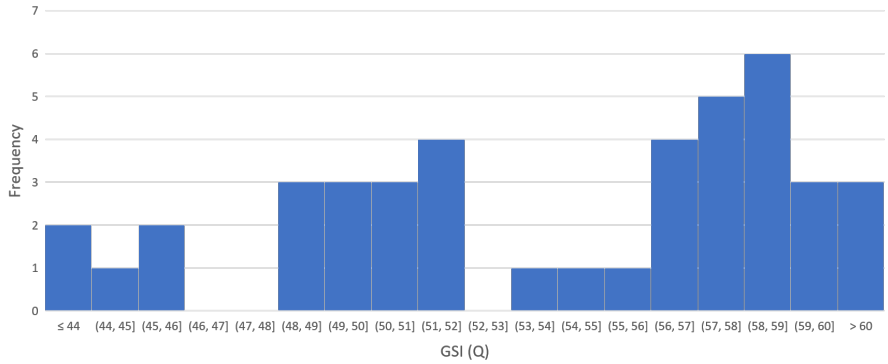

Figure 4.17: A histogram of the values calculated for GSI, starting at the addit and finishing at 150 m.

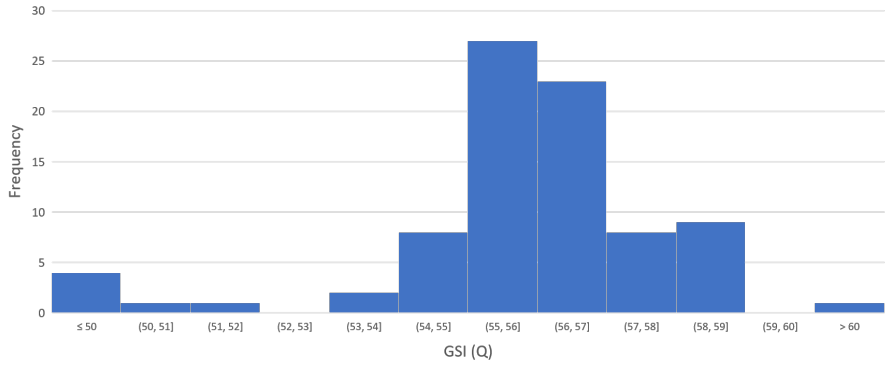

Figure 4.18: A histogram of the values calculated for GSI within the decline. These values start from 213 m into the decline.

Table 4.5: Statistical analysis of the GSI data generated from the decline Q-values.

	Mean	Mode	Median	Max	Min.	St. Dev.	N
A	54	51	56	64	42	5.1	42
B	56	56	56	67	49	2.3	84

The next data set is that of the access drives. When combining all access drive results, this generates a mean of 57, a median of 56 and a standard devation of 1.9, as can be seen in Table 4.5 and Figure 4.19. Further in Table 4.5, it can be seen that the GSI has improved with depth. A reasonable assumption for the GSI is 55, which is identical to that of the decline.

Table 4.6: Statistical analysis of the GSI data generated from the access drives Q-values.

Drive	Mean	St. Dev.	N
K1084	55	1,8	19
K1072	58	1,1	18
K1060	57	1,9	20

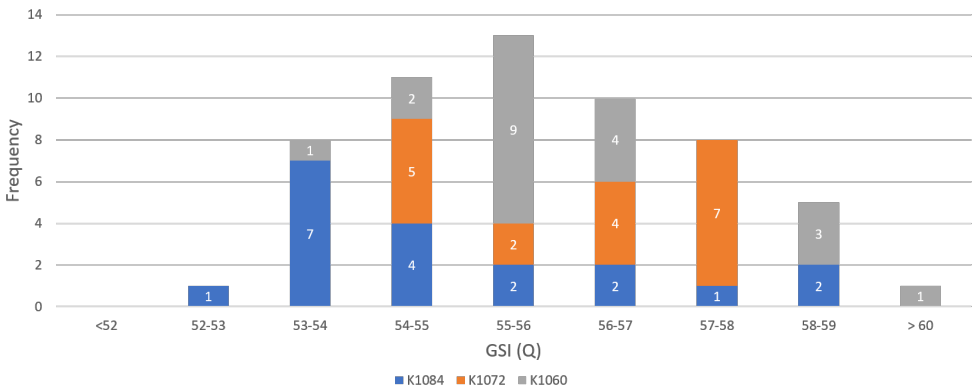

Figure 4.19: A histogram of the values calculated for GSI within the access drives of K1084, K1072 and K1060.

The decision was made by the author for the complete lower section of the country rock to have a GSI of 55. The point in which the change will occur will be at the base of the K1096 level. This is based on the observation that the rock mass has improved in quality with depth.

4.8. Summary

The geology of the material that lies outside the ore body can be described as country rock, there is some localised variation, but this is not on the meter scale which would be relevant for the overall goals of this thesis. Ore drive geology is composed of several units, which are country rock, altered country rock, mineralised country rock, quartz breccia, massive sulphide, and mineralised fault gouge. A possible geological trend was identified, which was the mineralised zone within the ore body dipped dipped 17° to the north. This is perpendicular to the overall ore body strike as shown by the block model in Figure 2.9. A further trend is that the ore body pinches and swells along the ore drives.

The conversion developed in Hoek, Carter, and Diederichs (2013) for the determining the GSI(Q) from the components of Q-value was partially successful. As a result it was possible to use the data collected over the complete development of the underground operation to generate a GSI(Q) of 50 for the upper and 55 for the lower country rock. This method cannot be used within the ore drives, as GSI represents a single material, rather than the multiple materials observed in the ore drives. However, the rock units of the ore drive were plotted independently to determine the GSI on the graph developed in Marinos, Marinos, and Hoek (2007).

When defining water within the model it is difficult due to the limited information gathered at the mine, and a lack of knowledge about the ground water. After consulting the mining team , the decision was taken to exclude water from the study on the basis that there is limited evidence of water egress through the mine walls. This may not be the case with depth as the water table may be encountered before reaching the mine limits. As a result there may be an overestimation of the rock strength. Further as the effective stress which governs the mechanical response of the rock mass, is a function of the applied stress and the pore pressure. This means that an increase in pore pressure would result in the rock mass being nearer to the failure criterion. However the addition of water would lead to an increase in the mass, which would increase the loading stress magnitude. Therefore the net result would dependent on whether the pressure increase or the additional mass was dominant.

Finally, based on the information gathered within the chapter, certain rock units were identified for further testing as they would generate essential information for the development of the numerical model. The collection and preparation of these samples will be discussed in section 5.1.

5

Intact Rock Testing

To build a realistic numerical model it is important to have the material properties for the rock units. Prior to this project only estimations of the rock properties based on visual inspections of the rock were available. The visual inspection of rocks or minerals can only tell limited information, this information is useful, however it can also be misleading. When looking at numerical modelling, the properties which require a reasonable degree of accuracy are impossible to determine by eye. Experienced engineers and geologists can make estimations using simple field assessments, such as comparing to previously seen rocks and the hammer test. However, to create a realistic numerical model, the best practice is to determine accurate rock properties. In terms of the Hoek-Brown and Hoek-Diederichs constitutive models that are planned to be used within this thesis, the properties that are required are the intact rock UCS, Young's modulus, and Poisson's ratio, which are discussed in chapter 3.

The objective of this chapter is to determine the material properties listed above for the rock units which will populate the model. This will be done by conducting Equotip, point load, acoustic emission, and UCS testing. Further to refine future models and confirm the assumptions at depth, it is useful to generate correlations between laboratory tests and tests which can be made at the mine.

This chapter will discuss sampling first and then go onto discuss the background, methodology, and results of the tests conducted within this project. The chapter will be conclude with remarks on the success and possible correlations between the tests.

5.1. Sampling

Sampling is an essential part of any scientific campaign to gain further information for building a realistic numerical model. Based on the knowledge of the geology and the requirements of the numerical model, rock units must be selected. The selected rock units are required to be representative and of a resolution which could be used within the numerical model. Two testing strategies were initial determined, field testing and laboratory testing, which have different resolutions. Field testing consisted of point load testing, these rock units were determined to be country rock, altered country rock and ore. The laboratory testing consisted of point load testing, Equotip, accoustic emision and UCS testing, the rock units tested within this section were country rock, quartz breccia and massive sulphide. This section will first describe the sample acquisition and then follow with sample preparation.

5.1.1. Sample Acquisition

The two testing strategies mentioned above, have different sample acquisition techniques.

Firstly, the field test samples had dimensions of 5 cm to 20 cm and were collect in all drives that had been mucked and supported. These samples had experienced the blast and were collected across the drive face floor. The samples were categorised into: country rock, altered country rock and ore at the surface. Oversized samples were then cut down to size, while undersized samples were discarded.

Secondly, the laboratory test samples consisted of three samples which will be explained subsequently.

The first of these samples was from the raise on the K1084 level. This sample was the closest country rock to the ore body that was possible to collect. This sample yielded 5 drill cores, Par 1-3, and Perp 1-2. This sample was discussed with the mine team and the decision was made that it appeared to be coherent and representative. The representative nature was in terms of being composed of quartz, feldspar and mica, with a well defined foliation of 5 to 10 mm, something that is typically seen for the country rock. The sample did not appear to have any obvious discontinuities other than the foliation.

The second sample was also country rock, but came from K1072 ODS. This sample was made in to cut blocks for point load tests. This sample was very similar to the previous sample in terms of mineralogy, grain size, and structure. Therefore the decision was made that this was representative of the country rock.

The final sample that was collected was a sample of ore, the sample came from the underground, however, its origin could not be confirmed as it was collected from the oversized ore pile. This was due to it being unsafe to collect a sample in unsupported ground. This sample yielded two cores for both quartz breccia and massive sulphide. It is more difficult to determine specifically if a sample is representative for these materials as they represent two end members of a continuum. Based on a discussion at the mine as well as observations at the face, the author is of the opinion that the drill core samples, represent the two end members in terms of composition. The quartz breccia was composed of predominantly quartz in a matrix of sulphide. The massive sulphide was composed of sulphide minerals, with minor amounts of quartz. The grain size is a slightly different matter, as the massive sulphide was composed of grains of up to 50 mm, which was on the larger end of the spectrum. The quartz breccia sample showed a more typical grain size with grains of 1 to 10 mm, which were distributed throughout the sample. This was something that was observed very often within the mine.

5.1.2. Sample Preparation

This subsection will discuss the preparation of the samples for the different types of testing that was carried out within this thesis. These samples can further be subdivided into 3 sample sets based on the testing that was to be performed on them. The sets are as follows, irregular lumps (mine), cut blocks (TU Delft) and drill core (TU Delft).

The first sample set to be discussed is the irregular lumps, these samples were the field test samples. The samples were sorted when they came to the surface into 3 material types country rock, altered country rock and ore. The samples then had their dimensions recorded, and any samples that were undersized based on the limits set out in section 5.3 were discarded, any samples that were oversized were cut using a diamond saw. These sample were not dried, therefore the samples contained some amount of moisture.

Two of the laboratory samples collected at the mine and brought to TU Delft were used to generate drill cores. These were the samples collected from the K1084 raise and the oversized ore pile.

The sample from the K1084 raise yielded 5 drill cores of 40 mm in diameter. Three of these samples were drilled parallel to the foliation, and named Par 1-3. The other two were drilled perpendicular to foliation and named accordingly as Perp 1 and 2. The samples were cut and polished as to generate a two parrallel surfaces. The samples were then dried out in the oven for several day. The dimensions

and mass of the samples were then recorded, these results can be seen in Table 5.1. The accurate recording of mass and dimensions allows for the calculation of the density of the material, the average density is therefore 2.7 t/m^3.

The sample from the oversized ore pile as discussed previously contained both quartz breccia and massive sulphide. This sample yielded two drill cores from both materials, the two cores from the quartz breccia were both 40 mm in diameter, whereas the massive sulphide, had one of 30 mm and one of 40 mm in diameter. The difference in dimensions was due to not being able to successfully yield a core of 40 mm due to discontinuities within the sample. The samples were treated in the identical manner to the samples from the K1084 raise, and the dimensions and mass can be seen in Table 5.1. An average density of 2.7 t/m^3 was calculated for quartz breccia and 3.4 t/m^3 for the massive sulphide.

Table 5.1: Dimension and mass analysis for drill core samples.

Sample	Material	Diameter (mm)	Length (mm)	L/D	Volume (cm3)	Mass (g)	Density (t/m3)
Par 1	CR Schist	40	79.9	2.0	100.4	266.1	2.6
Par 2	CR Schist	40	81.2	2.0	102.0	270.9	2.7
Par 3	CR Schist	40	60.4	1.5	75.9	201.9	2.7
Perp 1	CR Schist	40	81.6	2.0	102.5	272.3	2.7
Perp 2	CR Schist	40	81.7	2.0	102.7	271.7	2.6
Ore 1	Ore (mostly quartz)	40	72.8	1.8	91.5	243.5	2.7
Ore 2	Ore (very sulphide rich)	40	50.0	1.3	62.8	205.2	3.3
Ore 3	Ore (very sulphide rich)	30	66.4	2.2	46.9	162.7	3.5
Ore 4	Ore (mostly quartz)	40	58.5	1.5	73.5	195.8	2.7

The final laboratory test sample set was prepared at TU Delft as cut blocks from the country rock sample collected from the K1072 ODS. The samples (Schist-B**X**) were cut with a diamond saw to meet the dimension requirements listed in section 5.3. The dimensions were then recorded, however the samples were not weighed, and sat for several weeks before preparation and testing, so it is was assumed that these samples were dry.

5.2. Equotip

This section will discuss the testing conducted using the Equotip equipment. The section will be composed of the background theory, methodology and results. This was conducted to approximate the UCS, as this is a technique that could be carried out in the field, with minimal sample preparation.

Equotip works on the basis of the Leeb's hardness test. This method uses a test device with a 3 mm diameter tungsten carbide spherical tip, which impacts the surface of the test material. The spherical tip travels through an electric coil and measures the velocity of impact (V_{Impact}) and the velocity of the rebound ($V_{Rebound}$) proportionally as induced voltages. The Leeb's hardness (L_D) is calculated as shown in Equation 5.1 (Corkum et al., 2018).

$$L_D = \frac{V_{Rebound}}{V_{Impact}} * 1000 \tag{5.1}$$

The work of Corkum et al. (2018) investigated the implications of sample dimensions and volumes on the Leeb's hardness results. This work was carried out with Wallace sandstone, a medium grained sandstone which is considered to be fully homogeneous. The result of this work led to the conclusion that Leeb's hardness becomes near constant at a length diameter ratio of greater than an 0.4. Further, the conclusion was drawn that Leeb's hardness becomes near constant at volumes greater than 90 cm^3.

The conversion of Leeb's hardness to UCS is done through the use of Equation 5.2, combined with the recommended fitting parameter coefficients shown in Table 5.2. These are the parameters recommended for the conversion of metamorphic rocks (Corkum et al., 2018).

$$\sigma_c = \alpha L_D^{\mathrm{B}} * 10^{-6} \tag{5.2}$$

Table 5.2: Fitting parameter coefficients selected for metamorphic rocks based on the work of (Corkum et al., 2018).

Coefficient	Value
α	0.3
β	2.98

5.2.1. Equotip Methodology

The equipment used for the testing was the Equotip from Proceq, which was calibrated to a known standard. Core samples were tested 10 times on the top and bottom surface. The surfaces were smooth and clean due to being prepared for UCS tests. Samples that were prepared for point load testing were tested on faces which had been sawn, this was only if the sample did not wobble whilst testing. Impact tests were conducted over cut surface of the samples in 10 locations. The Equotip was held on to the surface with 2 fingers and the spherical tip was released onto the surface as shown in Figure 5.1 and the Leeb's hardness result recorded (Corkum et al., 2018).

Figure 5.1: Left is the Equotip test on a drill core. Right is Equotip test on a cut block

5.2.2. Equotip Results

The first set of results that will be discussed are the drill cores, descriptions of these can be found in Table 5.1. The samples with the prefix Par were impacted in the direction parallel to the foliation and those with Perp were impacted perpendicular to foliation.

As mentioned in Corkum et al. (2018), limits exist for the dimensions and volume of the sample to generate an accurate measure of Leeb's hardness. All samples met the dimension requirement, however sample Par 3 and Ore 2 to 4 did not meet the volume requirement. These samples were still tested, but this was noted.

The results from the Equotip tests are presented in Table 5.3. The first results that are discussed are the samples with the Par prefix, these samples show the lowest amount of variation in Leeb's hardness. It should be noted that Par 3 did provide lower values that the other two samples, this may have been a consequence of not meeting the volume requirement. The difference is not significant, so the sample

was included in the all Par value. This generated an average Leeb's hardness for all Par of 776 HLD with a standard deviation of 36 HLD. Based on the formula and coefficients in Equation 5.2 and Table 5.2, the UCS is approximately 123 MPa.

Table 5.3: Results of the Equotip testing for the drill cores

Sample	Maximum (HLD)	Minimum (HLD)	Median (HLD)	Mean (HLD)	Standard Deviation (HLD)	Estimated UCS (MPa)
Par 1	859	743	792	790	31.0	129
Par 2	844	720	790	782	37.0	126
Par 3	810	700	762	757	31.9	114
Perp 1	770	421	679	658	100.1	75
Perp 2	840	405	730	712	103.6	95
Ore 1	898	694	842	821	63.8	145
Ore 2	911	544	819	783	101.0	126
Ore 3	897	497	830	777	117.0	123
Ore 4	901	707	840	823	49.9	146
All Par	859	700	775	776	35.5	123
All Perp	840	405	714	685	102.9	85
Combined	859	497	761	740	83.6	106

The Perp subset of samples are the next to be discussed. These samples showed a much higher degree of variation than the Par subset, as can be seen in Table 5.3. The combined data resulted in a mean Leeb's hardness of 685 HLD with a standard deviation of 103 HLD. This generated an approximate UCS of 85 MPa. A possible reason for the high degree of variability, could be the discontinuities that lie beneath the surface as Equotip is a rebound based test.

As mentioned in Table 5.1 sample Ore 1 and 4 are most similar in terms of material. These samples resulted in mean Leeb's hardness of 821 HLD and 823 HLD, however Ore 1 has a significantly higher standard deviation of 64 HLD compared to 36 HLD of Ore 4. This could have possibly been explained by the sample size, however, it was Ore 4 that did not meet the volume requirement. A more realistic explanation for the higher variation is differences in the mineral impacted. The average of these two samples generated an approximated UCS of 146 MPa.

The final subset of samples is Ore 2 and 3, as discussed in Table 5.1, both these samples are composed of the same material. These samples showed the highest variation of all of the samples with a standard deviation of 101 HLD and 117 HLD, as can be seen in Table 5.3. This can be explained by two reasons, firstly these samples were composed of different metallic sulphides as well as quartz with a larger grain size than seen in any other sample, secondly both samples had volumes that were significantly lower than the 90 cm^3 as can be seen in Table 5.1. The averages for the samples were similar with Leeb's hardnesses of 783 HLD and 777 HLD. The combination of these results generated an approximate UCS of 125 MPa.

A second Equotip experiment was conducted on cut block samples of the country rock from the K1072 ODS as mentioned in section 5.1. This was conducted as a confirmation that the samples that were used to correlate the I_{s50} to UCS results were comparable. These samples were compared by eye and showed similar mineral assemblages, and in similar abundances. It should be noted that sample B14 was the only sample not to meet the volume requirement. All of the samples met the dimension ratio requirement of 0.4.

The faces that were tested, were subdivided into 2 categories, parallel to foliation and perpendicular to foliation, much like the samples in the drill core Equotip experiment. The first set of data to be discussed is the parallel to foliation samples as seen in Table 5.4.

Table 5.4: Results of the Equotip testing for the parallel to foliation in the cut blocks

Sample	Count	Maximum (HLD)	Minimum (HLD)	Median (HLD)	Mean (HLD)	Standard Deviation (HLD)	UCS (MPa)
Schist-B1	30	811	658	772	769	38,3	120
Schist-B2	20	853	733	783	786	30,1	128
Schist-B3	10	842	638	747	731	58,3	103
Schist-B4	20	832	667	772	765	40,6	118
Schist-B6	10	757	642	720	715	33,8	96
Schist-B7	20	820	641	760	749	47,4	111
Schist-B8	10	839	750	817	806	31,7	137
Schist-B11	20	831	688	738	744	38,0	108
Schist-B12	20	846	715	798	791	37,3	130
Schist-B13	10	793	663	728	731	41,7	103
Schist-B14	10	846	706	782	775	42,7	122
Schist-B15	20	821	670	760	764	40,1	117
Total	200	853	638	768	763	46,0	117

The samples that were parallel to the foliation provided an average Leeb's hardness of 98% of the value recorded from the Par drill cores. Further, the variation increased when compared with the values recorded for the drill cores from a combined standard deviation of 35.5 to 46 HLD. This could be explained through three points:

- The increase in sample number increases the range of minerals tested.
- The surfaces were not as smooth as the samples for UCS testing as they had not been polished.
- There was a higher degree of mineral variation within the sample.

The results from the Equotip testing perpendicular to foliation samples is presented in the Table 5.5. The tests that were conducted perpendicular to the foliation resulted in a 20 % higher average Leeb's hardness as well as a lower standard deviation. This may be a result of the larger sample size from 40 points to 150. The drill core samples combined gave a Leeb's hardness of 685 HLD, whereas the blocks gave a result of 731 HLD. This may have been a result of the surface finish, the sample size, or discontinuities within the rock.

Table 5.5: Results of the Equotip testing for the perpendicular to foliation in the cut blocks

Sample	Count	Maximum (HLD)	Minimum (HLD)	Median (HLD)	Mean (HLD)	Standard Deviation (HLD)	UCS (MPa)
Schist-B2	20	856	589	756	753	55,7	112
Schist-B3	10	812	586	729	719	63,4	98
Schist-B4	10	821	606	712	718	72,5	97
Schist-B5	20	882	565	765	757	72,3	114
Schist-B7	10	821	562	792	764	73,8	117
Schist-B8	10	810	598	730	713	67,7	95
Schist-B10	10	834	675	752	759	49,4	115
Schist-B11	10	828	630	762	749	59,9	110
Schist-B12	20	816	590	718	726	57,7	101
Schist-B13	10	789	644	745	740	42,7	106
Schist-B14	10	808	553	672	674	77,8	80
Schist-B15	10	804	396	657	657	118,8	75
Total	150	882	396	746	731	75,1	103

5.3. Point Load Testing

UCS testing is near impossible whilst at the mine as it requires extensive sample preparation and equipment which is fairly cumbersome and expensive. This is the reason that point load testing was selected. This section will go on to discuss the work carried out using the point load testing equipment at the mine as well as TU Delft. The testing of point load strength at TU Delft was done to correlate the point load strength results with the UCS test results. The determination of point load strength index for rocks will be conducted in accordance with the procedure D5731-16 from American Society for Testing and Materials (ASTM) (ASTM, 2016).

Point load testing works on the principle that two conical platens are brought together on either side of a test material through the use of a hydraulic ram. The upper platen is fixed whist the lower is coupled to the hydraulic ram. As conical platens are used, the load is applied on a smaller surface area than a conventional UCS test, therefore a smaller load is then required to break the material.

The failure of samples must meet a specific failure type to be accepted for point load testing. These failures can be seen in Figure 5.2. If the sample is to fail in an incorrect manner, the result would not be representative of the intact rock. Incorrect failure would be attributed to failure at a specific point or discontinuity, as a result some tests results may have to be discredited.

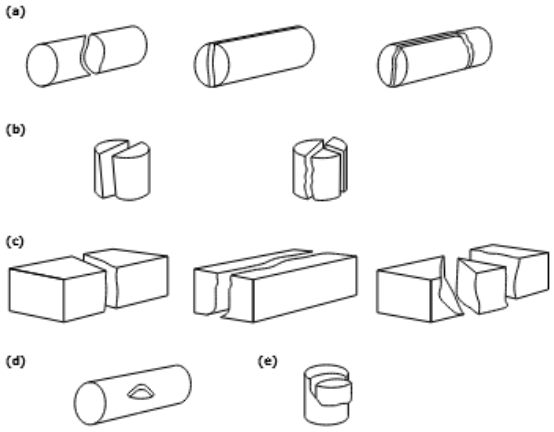

Figure 5.2: Samples that pass and fail for point load tests (ASTM, 2016). Samples a, b and c pass, where as samples d and e do not.

The load that is recorded by the test device, can then be converted through the following equations. Equation 5.3 is for the normalised width (W_N), this is calculated by averaging the top and bottom widths (W_1 and W_2) for the irregular lump, as shown in Figure 5.3. Specification limits for the samples are 30 - 85 mm. The shape is to be as near to cuboid shaped as possible, with a depth width ratio of 1/3 to 1, with a preference for 1 to 1. The length to the loading centre for all points should be greater than 0.5 of the width.

$$W_N = (W_1 + W_2)/2 \tag{5.3}$$

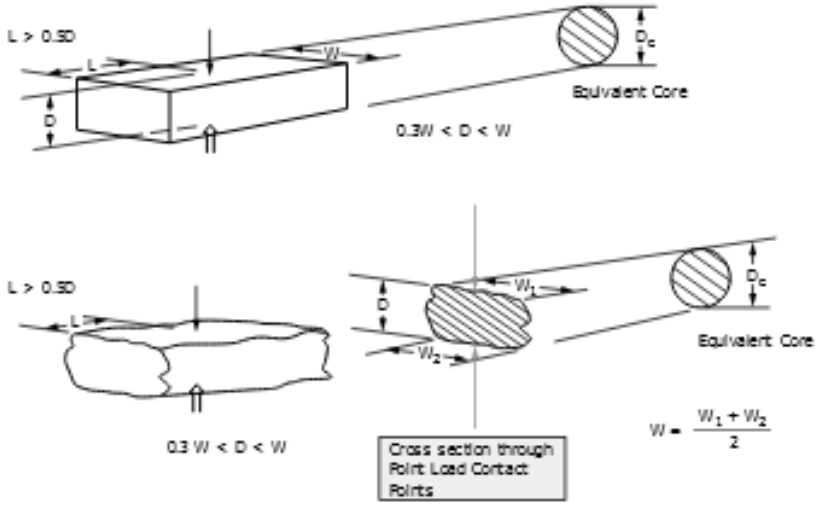

Figure 5.3: Point load dimensions for blocks and irregular lumps. (ASTM, 2016)

The surface area (S.A) is then calculated as shown in Figure 5.3, using Equation 5.4 with D being the sample depth.

$$S.A. = W_N * D \tag{5.4}$$

The diameter equivalent (D_e^2) is the diameter that an equivalent drill core sample would have as shown in Figure 5.3. The formula can be seen in Equation 5.5.

$$D_e = 2\sqrt{\frac{S.A}{\pi}} \tag{5.5}$$

The uncorrected point load strength (I_s) is then calculated as shown in Equation 5.6 using the equivalent diameter and the failure load (P).

$$I_s = \frac{P}{D_e^2} \tag{5.6}$$

The uncorrected point load strength index is adjusted for a size correction. This should be done through plotting the values of P and De on a log-log plot. A straight-line relation should be established to relate the two factors. The $I_{s(50)}$ value is then the corresponding value at De^2 = 2500 mm^2. This can only be done with a large data set. In this case, insufficient data is available, therefore a size correction factor (F) can be used instead, as calculated in Equation 5.7.

$$F = \frac{D_e}{50}^{0.45} \tag{5.7}$$

This then allows for the calculation of $I_{s(50)}$ which can be seen in Equation 5.8. $I_{s(50)}$ is the corrected point load strength for a 50 mm diameter equivalent core.

$$I_{s(50)} = F * I_s \tag{5.8}$$

A further calculation that can be done for the rocks within the Kearney vein system is the anisotropy index, this is defined as the ratio between the mean of the $I_{s(50)}$ in the parallel and perpendicular directions to the foliation. As a result of this the anisotropy can be quantified as shown in Table 5.6 (Tsidzi, 1990).

Table 5.6: Comparison of foliation and strength anisotropy index (I_a) as described in (Tsidzi, 1990).

Nature of rock	Strength anisotropy index (I_a)	Descriptive term
Very strongly foliated	>3.5	Very highly anisotropic
Strongly foliated	3.5-2.5	Highly anisotropic
Moderately foliated	2.5-1.5	Moderately anisotropic
Weakly foliated	1.5-1.1	Fairly anisotropic
Very weakly foliated or non-foliated	<1.1	Quasi-isotropic

UCS can be approximated by multiplying the point load strength index by a site-specific correlation factor (C). This is normally conducted by comparing UCS and corrected point load strength. This will only be done for similar material as the correlation factor may be different for ore and country rock.

The equation for the approximation of UCS is shown in Equation 5.9.

$$UCS = C * I_{s(50)} \tag{5.9}$$

5.3.1. Point Load Testing Methodology

As the point load testing was conducted in two locations, there was the use of two separate point load testing devices. The device used for the testing whist at the mine, was the digital point load tester from IMPACT Test Equipment, as can be seen in left of Figure 5.4, whist the testing within TU delft was conducted with an analogue point load tester from ELE, as can be seen in right. The resolution on data with the ELE point load tester is lower due to its analogue dial, with the data being measured to the nearest 0.5kN. When loading samples, it was noted that the ELE point load test equipment was measuring low, as the right dial did not move until the left dial read 2.5 kN, as a result the load results were adjusted accordingly.

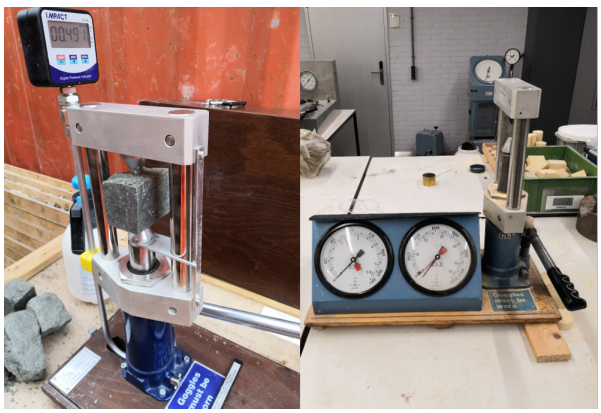

Figure 5.4: Left: Impact Digital Point Load Test equipment used at the mine. Right: ELE Analogue Point Load Test equipment used at the TU Delft

The dimensions of the sample as shown in Figure 5.3 were checked against the requirements and then recorded. The samples at the mine were then split into two categories, sub-parallel to foliation and sub-perpendicular to foliation. This allowed for a deviation of up to 10 °. Samples that did not fall into either of these categories were removed as they generated complexity that point load testing

was not accurate enough to resolve. The samples were then inserted into the point load tester and closed. This should be done at the smallest dimension in the central region. The load was then steadily increased until failure over a period of 10 to 60 seconds. The failure load was recorded, however the test can only be accepted if it matched the failure behaviour shown in Figure 5.2.

The nature of the country rock within the mine is schist. These schists behave anisotropically, thus have different strengths in different planes. This determines that testing must be carried out parallel and perpendicular to the foliation. However, the tests at TU Delft were only conducted perpendicular to foliation as they were intended to be used to correlate with UCS.

As discussed in subsection 5.1.2, the samples that were tested for point load at the mine contained some moisture as there was little time between collection and testing, the samples tested at TU Delft were completely dry when tested. This may have effected the results and will be discussed in more detail.

5.3.2. Point Load Results

This section will discuss the results of the point load tests carried out at the two location. The testing at the mine was more extensive than that conducted at TU Delft for correlation purposes. The testing at the mine covered the country rock, altered country rock and ore (quartz breccia), where as only country rock was tested at TU Delft.

Firstly the schistose material in the form of the country rock and altered country rock will be discussed. During the testing it was discovered that samples loaded along the foliation, failed as a result of indirect tension. As a result of this the samples therefore did not provide a representative strength for UCS. They however do allow for the calculation of $I_{s(50)}$ and the isotropic index of the rock.

Country Rock

The country rock consisted of 30 samples of which 16 were tested sub-parallel to foliation and 14 sub-perpendicular. The samples from the sub-parallel test were all successful and there were only 3 failed tests within the sub-perpendicular tests. These invalid tests were all as a result of preexisting fractures.

The results from the point load tests carried out perpendicular to foliation are shown in Figure 5.5. The results shows a large variation, which can be associated with inhomogeneities and discontinuities within the samples, as point load testing focused the load on a small region. This large amount of variation meant that it was not viable to use the linear regression technique to calculate the $I_{s(50)}$, thus the size correction factor technique for the average value was used. This yielded an $I_{s(50)}$ of 6.0 MPa with a standard deviation of 1.5 MPa.

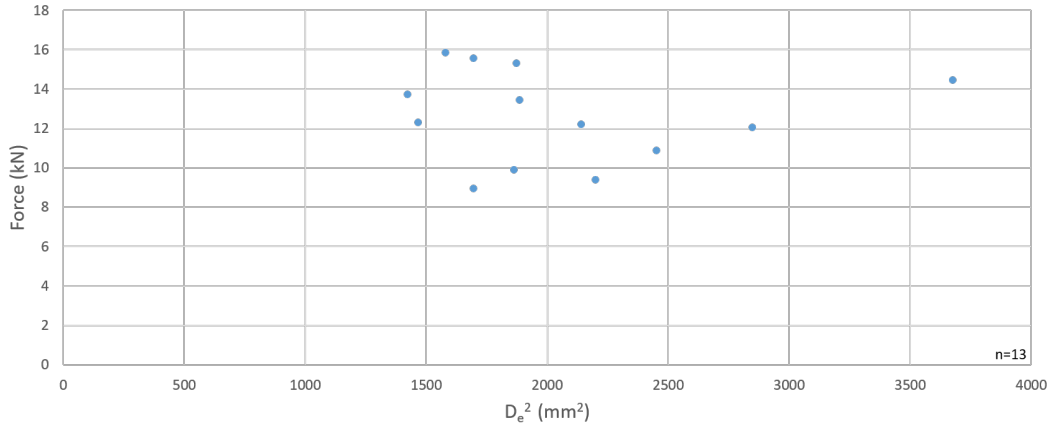

Figure 5.5: Results from point load test carried out perpendicular to foliation on country rock. n = 13.

Tests parallel to foliation were also carried out on the country rock material, generating the results shown in Figure 5.6. These results show a large degree of variation, much like the perpendicular results. As a result the $I_{s(50)}$ was calculated based the average corrected values, resulting in 1.8 MPa with a standard deviation of 0.7 MPa.

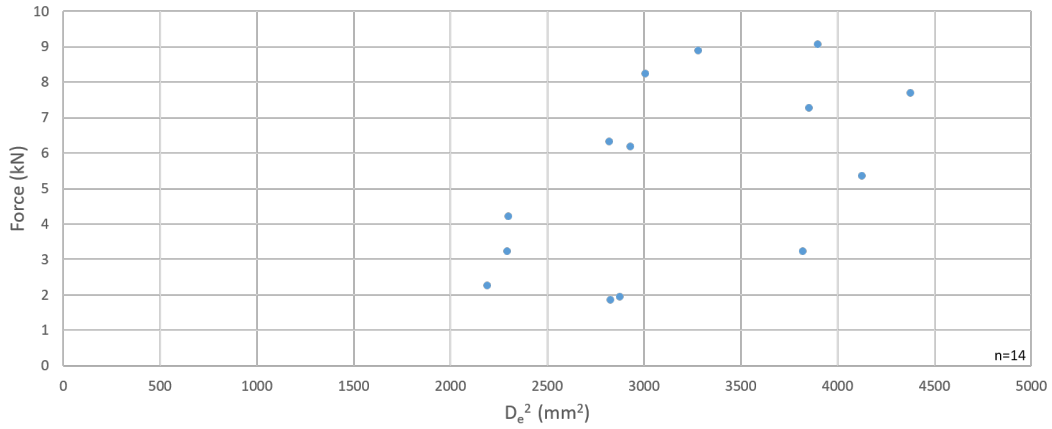

Figure 5.6: Results from point load test carried out parallel to foliation on country rock. n = 14.

Using the corrected average value for $I_{s(50)}$ for both sample sets allows for the calculation of the anisotropic behaviour of the samples. $I_{a(50)}$ = 3.3, this value when compared to the work of Tsidzi (1990) suggests that the rocks are highly anisotropic and thus strongly foliated, which was also observed from visual inspection.

Altered Country Rock

The next set of results is for the altered country rock, which constisted of 45 samples of which 28 were tested perpendicular to foliation and 17 were tested parallel to foliation. Of those 28 tested perpendicular to foliation, 5 samples failed along existing fractures and were therefore discarded.

The results for the altered country rock tested perpendicular to foliation are shown in Figure 5.7. The results show a large amount of variation, meaning that the method used must be the corrected average, which results in a corrected average $I_{s(50)}$ of 5.1 MPa with a standard deviation of 1.4 MPa.

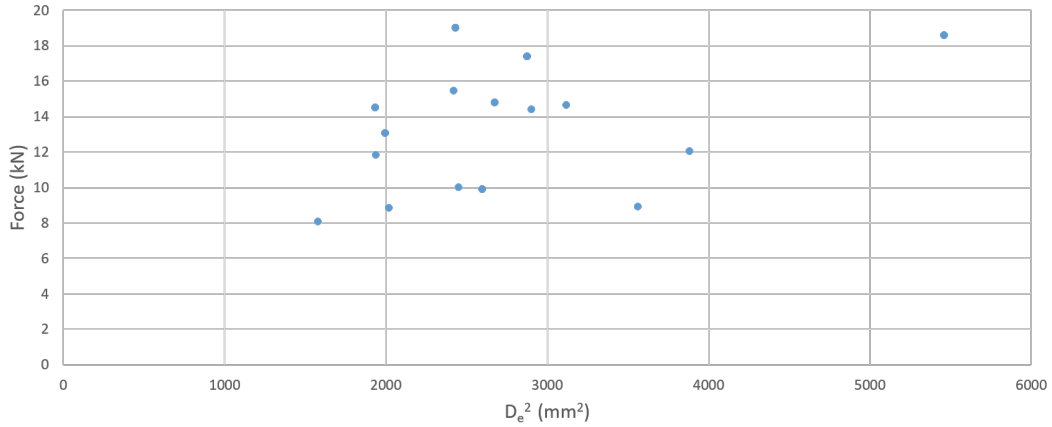

Figure 5.7: Results from point load test carried out perpendicular to foliation on altered country rock. n = 23.

The tests parallel to foliation were also carried out on the altered country rock. These results continue to show the trend of high variation. The corrected average $I_{s(50)}$ is 1.7 MPa with a standard deviation of 0.7 MPa.

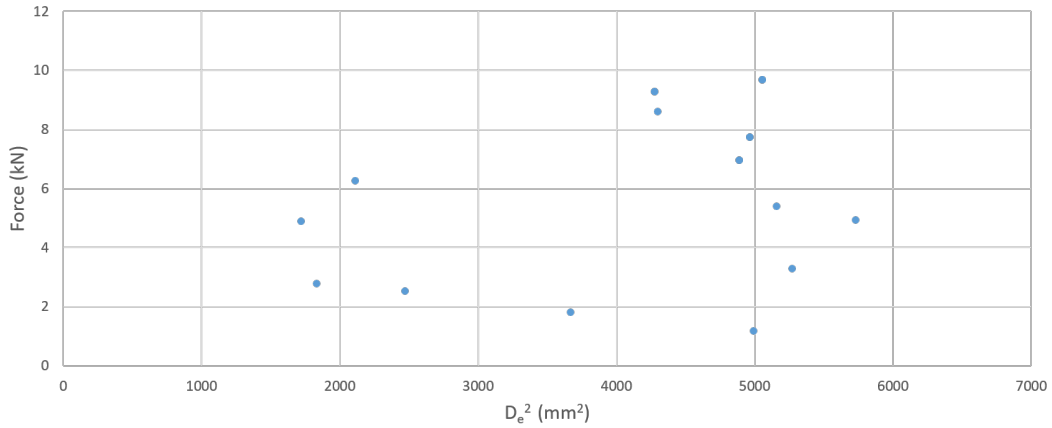

Figure 5.8: Results from point load test carried out parallel to foliation on altered country rock. n = 17.

The I_{a50}= 3.1 based on the results for the corrected average values for $I_{s(50)}$. This confirms the observations made by visual inspection, that the rock is highly anisotropic as shown by Table 5.6.

Ore

The final data set is the ore samples, these samples proved difficult to gain successful point load tests. This was due to the nature of the samples being quartz breccia, meaning that the rock is composed of broken particles in a matrix. This presents an issue as it may result in recording of the discontinuity strength rather than the intact rock strength.

The data presented is from the K1084 ODS and consisted of 42 samples of which 14 were not accepted due to existing failures within the samples. The results of the ore samples tested at the mine showed the highest correlation with the linear regression, resulting in a R^2 of 43%, there is however still a large amount of variation in the data as can be seen in Figure 5.9. The linear regression and corrected average, both result in an $I_{s(50)}$ of 5.0 MPa, with a standard deviation of 2.2 MPa.

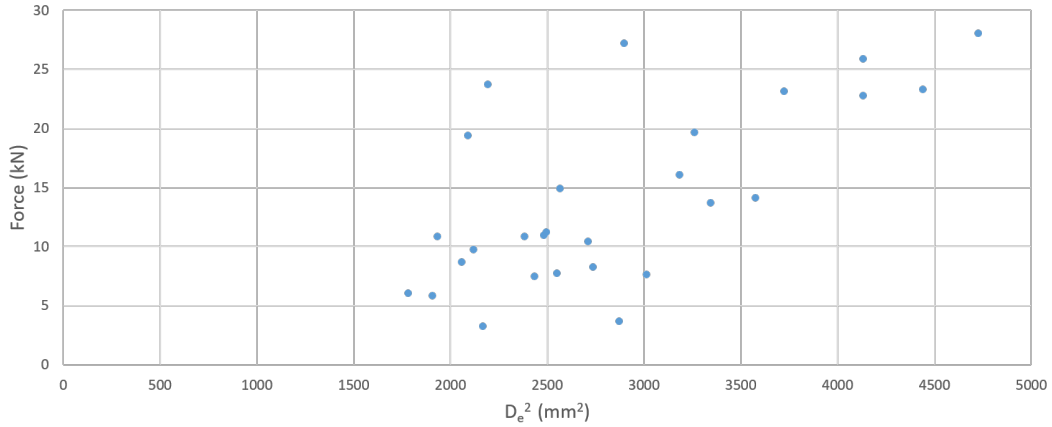

Figure 5.9: Results from point load test carried out on ore rock. n = 28.

TU Delft Testing

The sample set tested at TU Delft consisted of 16 samples of country rock from the same block, as mentioned in subsection 5.1.2, these were all cut blocks and were completely dry. Of these samples one failed to show the correct failure behaviour and two broke before testing. As mentioned previously that these tests were carried out only perpendicularly to foliation, in order to correlate with the UCS test results.

The linear regression for these samples shows the highest correlation for country rock samples, with a R^2 of 20%. It does still show a large variation as can be seen in Figure 5.10, as a result it should be determined based on the corrected average $I_{s(50)}$, which results in 6.6 MPa with a standard deviation of 1.96 MPa.

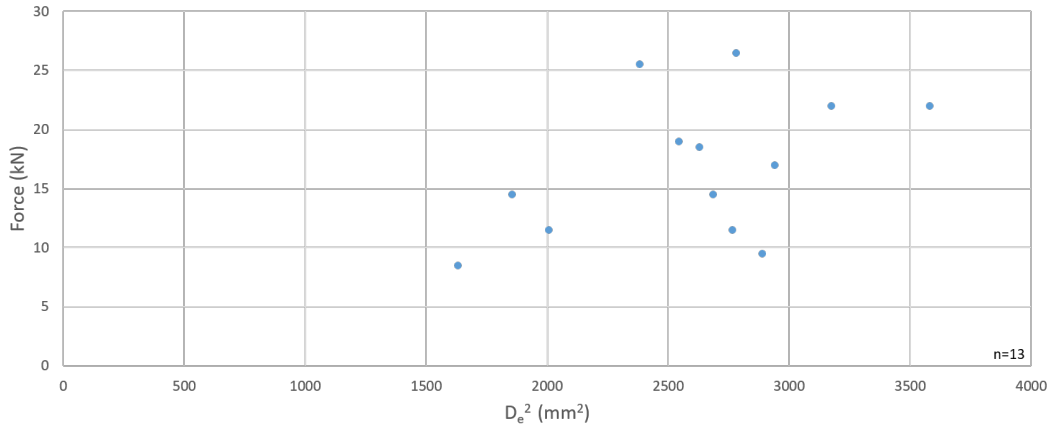

Figure 5.10: Results from point load test carried out perpendicular to foliation on country rock at the TU Delft. n = 28.

5.4. Acoustics

Acoustic emission is a non-destructive testing method, which can be used for determining the dynamic Young's modulus and the Poisson's ratio. This method may give an indication of material properties before destructive testing is conducted, thus may generate a usable result in case the UCS testing is unsuccessful. The test will further help to indicate the degree of anisotropy within the samples. The method work on the principle that waves are generate during a deformational event. The waves of interest are compressional wave (P wave) and shear wave (S wave), however surface waves are also generated. These waves have different velocities, dependent on the density, dynamic Young's Modulus and Poisson's ratio of the material.

The experiment works by inducing an elastic deformation from a transducer. The elastic energy from the deformation is then dissipated from the epicentre in the form of waves, as can be seen in Figure 5.11. As these waves pass through the material the P wave travels the fastest and arrives at the other transducer first, followed by the S wave and then the surface waves. The time for the waves to travel from one point to the other is recorded, and using the basic formula distance over time the velocity is recorded. These velocities will be known as V_p and V_s respectively.

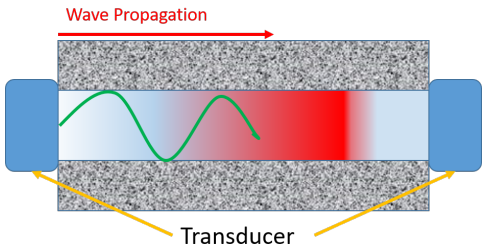

Figure 5.11: Shows the wave propagation through the sample of the P-wave (red) and the S wave (green).

The Poisson's ratio is a characteristic that can be determined independent of the material density. The Poisson's ratio is calculated as shown in Equation 5.10.

$$\nu = \frac{V_p^2 - 2V_s^2}{2(V_p^2 - V_s^2)} \tag{5.10}$$

The dynamic Young's Modulus can also be calculated, where the density of the material is known. The calculation for the dynamic Young's Modulus is shown in Equation 5.11

$$\mathrm{E} = V_s^2 \rho \frac{3V_p^2 - 4V_s^2}{(V_p^2 - V_s^2)} \tag{5.11}$$

The elastic rock properties which determine the P and S wave velocities are dependent on the mineralogy and structure of the material. This is particularly of interest for the experiments conducted as the samples are expected to contain micro discontinuities due to being situated near to a shear zone, and/or composed of schistose material. Another issue that might be experienced is interference, particularly as the distance between the two transducer decreases, as the time gap between the different wave arrivals is reduced.

It should be noted that the methodology for this experiment is D2845-08, which has been withdrawn by ASTM, due to no update being carried out in the last 8 years (ASTM, 2008). Within this paper, if the degree of velocity anisotropy is 2% or less, then the sample would be accepted for calculation of the dynamic Young's Modulus and Poisson's ratio. This means that the velocity recorded in the same orientation for different samples must have P and S wave velocities within 2% of each other. If this is not the case the samples can be suggested to be inhomogeneous or contain discontinuities.

The static and dynamic Young's Modulus are not equivalent due to the magnitude of their deformations, therefore some factor must be applied to correlate both values. The work of Brotons et al. (2016) determined three different relationships which can be used dependent on the information available for the samples. Only one of these equations was suitable for the data collected during this project and is shown in Equation 5.12.

$$E_{static} = 11.531 * \rho_{bulk}^{-0.457} * E_{dynamic}^{1.251} \tag{5.12}$$

5.4.1. Acoustics Method

The samples used were the drill core samples prepared for UCS, as can be seen in Table 5.1. The samples were put in a drill core holder, the transducers were then attached to the surface with conductive gel and held on with reasonable pressure using fingers.

The pre-amplified voltage during this experiment was 800mV which was then amplified by a factor of 100. A signal was generated which reset the timer for receiving oscilloscope, whilst inducing the deformation within the transducer. The oscilloscope then recorded the induced voltages within the receiving transducer. These results were then used to select the arrival time of the P and S waves respectively.

5.4.2. Acoustics Results

As discussed in the background section for acoustic emission it is pertinent to establish the degree of velocity anisotropy within the samples, as it needs to be less than 2 %. This test must be conducted before any calculation can be carried out. The comparison was carried out between sample set Par 1 and 2 and sample set Perp 1 and 2, as the waves would propagate through the same plane (parallel or

perpendicular to foliation). Par 3 was excluded due to its significantly shorter length, as this would lead to greater interference from the surface waves. The results of the experiment are shown in Table 5.7. The splitting of the samples will also be conducted for ore, as the samples represented two different rock types, therefore Ore 1 will be compared to Ore 4 and Ore 2 will be compared to Ore 3.

Table 5.7: Output data required to calculated the acoustic properties for samples Par 1 and 2, and Perp 1 and 2.

Sample	L/D	Density (t/m3)	P-Velocity (m/s)	S-Velocity (m/s)
Par 1	2,00	2,6	5623	3625
Par 2	2,03	2,7	5588	2925
Perp 1	2,04	2,7	4105	2753
Perp 2	2,04	2,6	4653	2949

Comparing samples Par 1 and 2, the P wave velocity is different by 0.6 %, however the S wave velocity difference is over 10 % which is greater than the 2 % limit. These two samples therefore can be described as anisotropic in terms of material properties. The comparison of Perp 1 and 2, showed a P wave velocity difference of over 11 % and an S wave velocity difference of over 6 %, which again means that this could not be used to calculate the elastic properties of the rock.

It is interesting to note that, when the P wave propagated along the foliation as in samples Par 1 and 2, it produced the lowest anisotropy by a factor of 10. However when the P wave propagate through the foliation in sample Perp 1 and 2, the anisotropy was significantly higher due to the changing mineral layers. The anisotropy that was observed in the S wave velocity for both sample sets, can be attributed to the changing of mineral layers.

The comparison of Ore 1 and 4 showed a result for the anisotropy of the P and S wave velocity that was larger than the 2 % required. This could be a result of the samples being significantly different in length or as a result varying discontinuities.

The samples Ore 2 and 3 showed good anisotropy for both velocities as can be seen in Table 5.8. This allowed for the calculation of dynamic Young's Modulus, Poisson's ratio and equivalent static Young's Modulus. These showed good anistropy due to the high ratio of metallic sulphide, which exhibited similar behaviour. The result generated an average static Young's Modulus of 50.8 GPa and a Poisson's ratio of 0.12.

Table 5.8: Output data and results from the accoustic testing on samples Ore 2 and Ore 3.

Sample	P-Velocity (m/s)	S-Velocity (m/s)	Dynamic Elastic Modulus (GPa)	Static Elastic Modulus (GPa)	Poissons' Ratio
Ore 2	5690	3771	97.9	49.6	0.13
Ore 3	5637	3619	104.3	51.9	0.11
Anisotropy	0.9 %	1.3%			

5.5. Uniaxial Compressive Strength

This section will discuss the background, test methodology and results for the UCS testing conducted at TU Delft. The testing was conducted following the protocol of D7012-14 (ASTM, 2014). The background to the concept of UCS, Young's Modulus and Poisson's ratio were discussed in the chapter 3.

The equipment at TU Delft is a axial strain controlled UCS test rig. This means that the axial strain is altered as the two flat platens move towards each other. The behaviour of rocks is that axial strain will induce stresses within the rock, which can be measured by the test rig as a load. The test rig at TU delft records the load, axial strain and radial strain. The radial strain is measured by a chain that encircles the core sample at approximately the mid-point of the core.

According to D7012-14 ASTM (2014), which states that the sample length to diameter ratio must be greater than 2:1, as ratios less than this may result in the over estimation of UCS. However in a previous iteration (D2938-86) there was an excepted formula as shown in Equation 5.13, for undersized samples where the UCS_{corr} is the corrected UCS, and the UCS_m is the UCS measured by the test rig (ASTM, 1992).

$$UCS_{corr} = \frac{UCS_m}{0.88 + 0.24(\frac{diameter}{length})} \tag{5.13}$$

However in the authors opinion this previously accepted formula is no longer validated by ASTM. In ASTM (2014) it continues to state that, “if it is necessary to test specimens not meeting the length to diameter ratio required due to a lack of available specimens, the report shall contain a note stating the non-conformance with this standard including a statement explaining that the result may differ from a test result that meets the requirement”. Further it states in the documentation that the diameter of core should be 10 times that of the largest mineral grain.

5.5.1. UCS Method

This subsection will discuss the methodology for the UCS tests conducted at TU Delft. The samples were prepared as 40mm drill cores, with the exception of one sample which was 30mm, as discussed in subsection 5.1.2. The samples were then cut and polished to provide a smooth surface for loading, as described in protocol D7012-14 (ASTM, 2014). It should be noted that the sample with the 30mm diameter was not tested for radial strain as it was not possible with the equipment set up.

Sample Par 3 did not meet the length having a length to diameter ratio of 1.5. Further Ore 1,2 and 4 did not meet the requirement with a length to diameter ratio of 1.82, 1.25 and 1.46 respectively. These tests were conducted as there was a lack of viable samples due to the limited amount of material that was transported to TU Delft. The direct effect of not meeting these requirements will be discussed in the result of each test. Further it should be noted that the core diameter should be 10 times the size of largest mineral grain, the sample Ore 1 to 4 did not meet this requirement.

The samples were placed in the UCS test rig between the platens. The radial strain chain was attached around the sample. The platens were then moved so that the sample was touching both. The axial strain was then increased on the sample and the load was recorded. The samples were loaded until there was an obvious event, such as a large increase in radial strain or catastrophic failure.

5.5.2. UCS Results

The results of the UCS tests conducted are documented within this sub section.

Firstly the samples of the country rock that were tested for UCS will be split into the two sets like all previous experiments, these sets are parallel and perpendicular to foliation. The first set to be presented is the perpendicular to foliation. A graphical representation of the output information from the UCS tests is shown in Figure 5.12. The areas of interest from the graph are the peak stress, and the linear portions of the two curves.

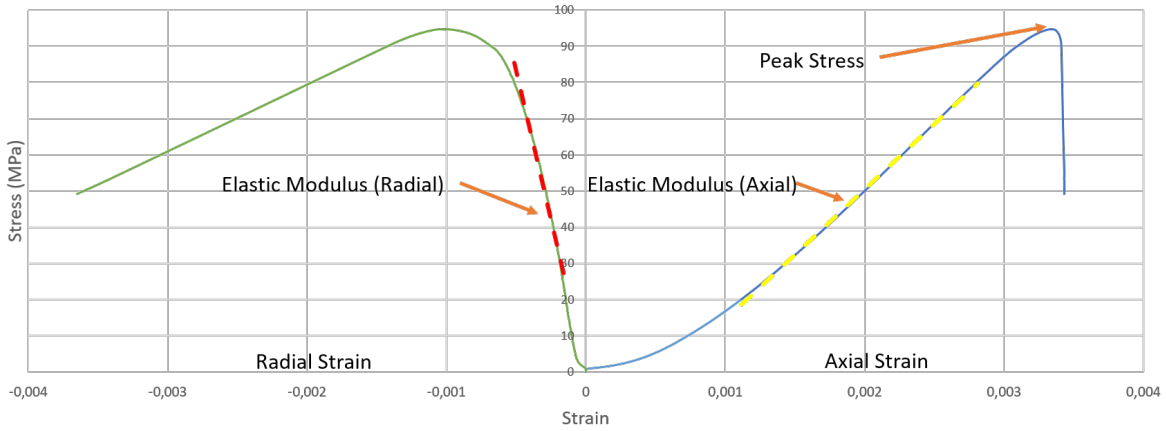

Figure 5.12: UCS test result from sample Perp 1, labelled with the key information.

The test results for the samples tested perpendicular to foliation are shown in Table 5.9. These results give an average UCS of 99 MPa with an Young's Modulus of 36.5 GPa and a Poisson's ratio of 0.22.

Table 5.9: UCS results for the test on Perp 1 and 2 as well as averages for both tests combined

Sample	UCS (MPa)	Young's modulus (Axial) (GPa)	Young's modulus (Radial) (GPa)	Poisson Ratio
Perp 1	95	36	164	0.22
Perp 2	103	37	166	0.22
Average	99	36.5	165	0.22

The same work was conducted on the samples parallel to foliation. The results are presented in Table 5.10. There are issues with the experiments conducted on these samples, firstly the radial strain chain did not provide valid data for the sample Par 1, also Par 3 did not meet the length requirement as mentioned previously. These tests were still included as they were inline with the other results. The results give an average UCS of 114 MPa, an Young's Modulus of 45 GPa and a Poisson's ratio of 0.19.

Table 5.10: UCS results for the test on Par 1-3 as well as averages for the combined tests

Sample	UCS (MPa)	Young's modulus (Axial) (GPa)	Young's modulus (Radial) (GPa)	Poisson Ratio
Par 1	117	45	N/A	N/A
Par 2	107	52	252	0.21
Par 3	114	38	216	0.18
Average	114	45	234	0.19

The next data set is the ore samples, the author has separated these into two sub sets. Ore 1 and 4 for the quartz breccia group and Ore 2 and 3 for the massive sulphides group.

The results for the quartz breccia are presented in Table 5.11. It should be noted that there was a discontinuity on the top surface of the sample Ore 1. This discontinuity was where the failure propagated from during the test, as a result the value of the UCS was significantly lower than the value for Ore 4. The author has determined that it is more realistic to discredit the UCS value for sample Ore 1 and take the UCS value from Ore 4 only. All other values were accepted from sample Ore 1.

Table 5.11: UCS results for the test on Ore 1 and 4, as well as average test results.

Sample	UCS (MPa)	Young's modulus (Axial) (GPa)	Young's modulus (Radial) (GPa)	Poisson Ratio
Ore 1	90	28,5	128	0,22
Ore 4	179	44,0	379	0,12
Average	134.5	36.5	253.5	0,17

The results from the massive sulphide UCS test are shown in Table 5.12. It should be noted that sample Ore 3 was 30mm in diameter, and the set up for radial strain did not allow this. Further the sample Ore 2 does not meet the length to diameter ratio.

As a precaution the author has made the decision to go with the result of the average of the two UCS and Young's Modulus, due to Ore 2 being too short in length thus providing an over estimation of UCS, and Ore 3 being of too small a diameter thus providing an underestimation. The resulting average UCS is 116.5 MPa, with an Young's Modulus of 47.5 GPa. As there was no Poisson's ratio recorded for Ore 3, the result is 0.12 as generated in Ore 2.

Table 5.12: UCS results for the test on Ore 2 and 3, as well as average test results.

Sample	UCS (Mpa)	Young's Modulus (Axial) (Gpa)	Young's Modulus (Radial) (GPa)	Poisson Ratio
Ore 2	130	35	288	0.12
Ore 3	103	60	N/A	N/A
Average	116.5	47.5	288	0.12

5.6. Summary of All Testing

A wide variety of testing was conducted within the laboratory with the aim of gathering information on the intact rock properties, as well as identifying some correlations between different data gathering techniques.

The experiments conducted with the Equotip, provide the author with a large number of results in a very quick and non-destructive manner, with a small amount of sample preparation. The difference between the results parallel and perpendicular to the foliation surprised the author, however it can be reasonably assumed that these are a result of the discontinuities with in the fabric perpendicular to the impact direction.

Point load testing aims to provide an estimation for the UCS, which can be conducted within the field. Further the test is also beneficial in the fact that the equipment is relatively inexpensive and requires little to no sample preparation. However, point load experiments raise some questions, the sample variation was very high and as a result it was not possible to correlate using a linear regression, which is considered best practice. The country rock tested at the mine and the country rock tested at TU Delft should have showed the same results for point load testing. This was not the case due to two possible reasons, the use of differing point load test equipment with different degrees of accuracy or a result of moisture contained within samples tested at the mine. It is of the authors opinion that the best option would be to try to generate a correlation between I_{s50} and UCS for the separate test rigs. This should also be the objective for the separate materials, as the ore will not have the same correlation factor as the country rock. As the altered country rock was not tested for UCS at TU Delft it can be assumed that the alteration of the rock has caused a strength reduction which can be directly determined from the ratio of I_{s50} for country rock and altered country rock. The tests conducted along foliation cannot be considered as viable as it represented indirect tensional strength. The point load test results also showed that there was a large amount of localised variation within the tested samples.

The acoustic emission tests were conducted as a non-destructive back up for the UCS tests. The acoustic emission tests were relatively unsuccessful as only 2 out 9 showed low enough velocity anisotropy. The successful test was for the massive sulphide samples of Ore 2 and 3. Further this testing provided an insight into the degree of discontinuities on the drill core sample scale, showing that there was a significant difference between samples. The final thought of the author is that this testing should not be repeated as it may not yield significantly more insight.

UCS testing requires a significant amount of sample preparation compared to point load testing, however, it does yield significantly more direct test results as well as more information. This testing is considerably more time consuming than the point load testing, hence there is a reduction in the number of samples. It does, however, yield the Young's Modulus and Poisson's ratio for the material tested. The UCS tests were successful for the most part, the only real issues were sample Ore 1 underperformed and failed due to an existing discontinuity, and the sample Par 1, failed to record a radial Young's Modulus. The result that the intact rock strength was stronger parallel to foliation was surprising as the author was expecting that the rock would be stronger perpendicular to foliation. The reason for these values being closer than expected can be suggested to be caused by discontinuities out with the foliation plane.

5.6.1. Comparison

This subsection will look at comparing the results of the different experiments. The results of the UCS and estimated UCS from the Equotip will be compared in order to determine if the constants within Corkum et al. (2018) were viable or whether site specific constants would provide a more accurate correlations. Secondly the comparison of the I_{s50} and the Equotip results was carried out to see if there was correlation between the data. Finally the site specific value for correlating the I_{s50} was identified by comparing the average of the point load sample set results at the mine and TU Delft to the results of the UCS tests.

The summary of the final results for UCS, or estimated UCS are shown in Table 5.13. The results show that Equotip overestimated the UCS of the drill cores of country rock tested parallel to foliation and the drill cores of massive sulphide, based on the coefficients of (Corkum et al., 2018). The overestimation was 9 % and 25 % respectively for the sample sets. The results for the other two sample sets showed the opposite issue with the Equotip underestimating the UCS. The underestimation was 14 % for the samples of country rock tested perpendicular to foliation and 30 % for quartz breccia.

Table 5.13: UCS summary results

Sample	UCS (MPa)	Equotip UCS [drill core] (MPa)	Equotip UCS [blocks] (MPa)	Is50 [mine] (MPa)	Is50 [Tu delft] (MPa)
Parallel Group	113	123	117	N/A	N/A
Perpendicular Group	99	85	103	5.98	6.58
Quartz Breccia	179	124.5	N/A	6.07*	N/A
Massive Sulphide	116.5	145.5	N/A	6.07*	N/A
Chlorite Schist	N/A	N/A	N/A	5.09	N/A

The sample set size was not large enough to draw a conclusion between the the UCS and the Equotip estimated UCS for any individual sample set. Therefore the sample sets of Par and Perp were combined and plotted against the individual UCS results, as can be seen in Figure 5.13. This resulted in an α of 0.16 and an β of 0.98. This has a R^2 of 81%, however this is only based on 5 points, therefore more research would be required to prove this relation with confidence. Until further site specific research is carried out the author is of the opinion that it is more reasonable to continue with the assumptions made by Corkum et al. (2018), due to their increased sample size.

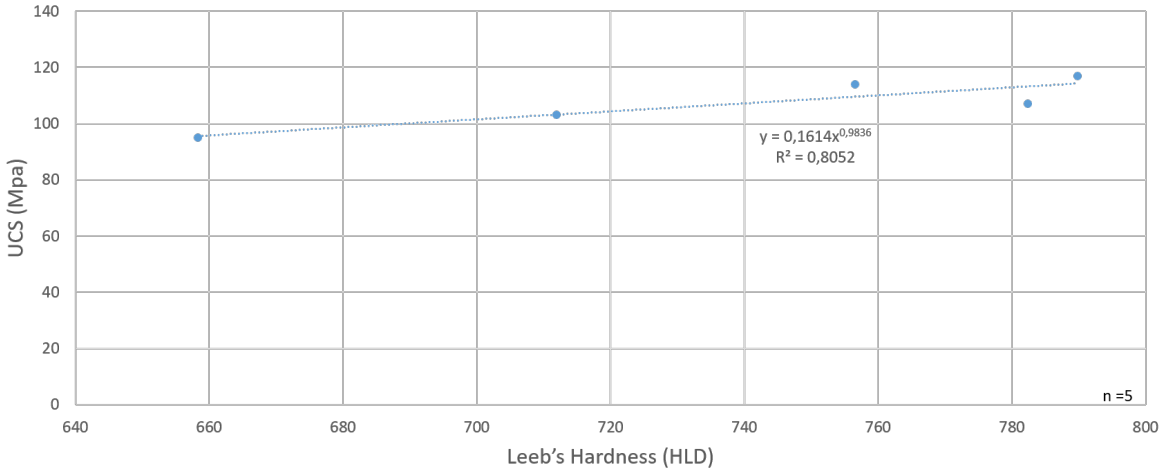

Figure 5.13: Leebs Hardness vs UCS for the samples Par 1 to 3 and Perp 1 and 2. n = 5

The Equotip result for the point load blocks was plotted against the corrected I_{s50} for each sample as can be seen in Figure 5.14. This produced a poor correlation with a R^2 of 6%, which can be contributed to a large amount of variation with the point load test results.

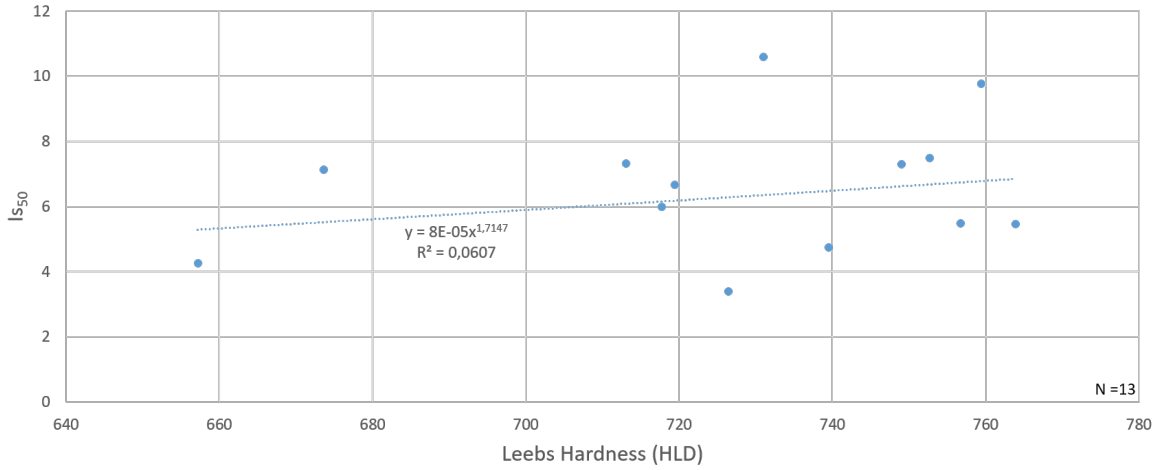

Figure 5.14: Leebs hardness vs I_{s50} for the cut block samples from the TU Delft. n = 13

Further to generate comparisons, it is noted that I_{s50} should be proportionally related to the UCS. As a result it is possible to present a hypothesised relationship of C = 16.5 for the mine point load test rig and C = 15 for TU Delft's point load test rig when comparing the country rock. It should be noted that the point load tests conducted on ore at the mine consisted of both quartz breccia and massive sulphide. The I_{s50} for ore was compared to average UCS of all the ore samples (137.5 MPa), which was felt to be representative of both quartz breccia and massive sulphide, this generated a K = 23.3 for ore material at the mine.

The comparison from country rock and altered country rock should be conducted, as mentioned above they are the same rock originally. The alteration process has led to a strength reduction. The strength reduction should be directly related to the ratio between their I_{s50}. It is of the authors opinion that the altered rock has 85% of the strength of the country rock based on their I_{s50}s.

The information gathered in this chapter for the material properties of the intact rocks coupled with the rock mass properties gathered in chapter 4, allow for the generation of an accurate numerical model which will be described in the chapter 6.

6

Numerical Modelling

This chapter will discuss the numerical modelling which is the key output for this thesis. This work will be split up into model set up, model scenarios and model results. The objective is to establish several scenarios based on the design constraints for the underground mine, in order to determine the most stable stoping order.

6.1. Numerical Modelling Background

Numerical modelling aims to reproduce 'real world behaviour' through computer simulations. 'Real world behaviour' or physical phenomena can be described in terms of partial differential equations. Finite element modelling works by discretising the problem space into elements. These elements are surfaces in 2D and volumes in 3D, which are composed of nodes and stress points. This project was conducted in Plaxis, thus a brief summary of the software will be presented.

Plaxis is a finite element package, developed in the 1980s, between TU Delft and Rijkswaterstaat, with the initial objective of developing an 'easy-to-use' 2D finite element code for the analysis of soft soil river embankments, in the Netherlands. In the preceding decade, the software was extended to incorporate most aspects of geotechnical engineering. The software is designed for the analysis of deformation, stability, dynamics and groundwater flow in geotechnical problems (Brinkgreve, Zampich, and Ragi Manoj, 2019).

The process of finite element modelling can be broken down to a 7 step process, as visualised by Figure 6.1. These steps will be explained subsequently.

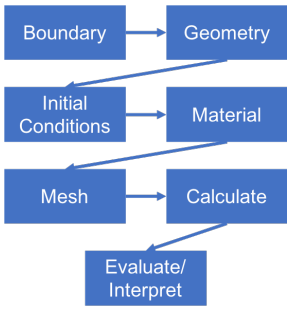

Figure 6.1: Flow diagram of the finite element modelling process.

The initial step is to set up the boundaries for the model. These boundaries are the sides of the block developed for the modelling. Special care should be made when establishing the boundaries as they should be far enough from the area of interest so as not to impact upon it, but they should not be too far away so as to induce much more calculation time.

The next step in the process seen in Figure 6.1 is to establish the geometry for the problem. This should also follow the precautions stated in the previous paragraph, but in terms of the simplification of geometry. For example the realistic case of a tunnel within a mine is that the tunnel will undulate on the axis perpendicular to that of the tunnels propagation. If this were to be modelled in a numerical modelling software, this would result in the generation of complex geometries which increases the number or complexity of elements.

Thirdly, in order to provide representative material behaviour for the rock mass and the cemented rock fill, a constitutive model for the behaviour of must be chosen. The properties required are dependent on the selected constitutive model. The decision was taken for the rock mass to be represented by the Hoek-Brown model and the cemented rock fill will be represented by the Mohr-Coulomb model. Both of these models are linearly elastic perfectly plastic. This means that the behaviour is linearly elastic following the materials Young's modulus until it reaches the failure point, where it then deforms constantly based on the stress applied. Within the Hoek-Brown model the behaviour for the Young's modulus is determined by the Hoek-Diderichs rock mass modulus. Whereas the Young's modulus is derived directly from the material testing for the Mohr-Coulomb model. The determination of the failure point for the rock mass will be described by the Hoek-Brown failure criterion and the cemented rock fill will be described by the Mohr-Coulomb failure envelope. The input data required for both of these constitutive models can be found in chapter 3, as well as a further explanation for how the intact rock is modified to replicate the rock mass by the Hoek-Brown model.

Forthly, is to introduce the initial conditions, which consist of the in situ stress of the material through the K0 procedure. This procedure is to generate the stress field based on the geostatic stress, coupled with the ratios of both in and out of plane horizontal forces. Further during this stage an initial loading conditions can be applied upon the boundaries of the materials.

The final step before calculating is the meshing procedure, which is carried out by the software, based on the input characteristic. This allows for the generation of more elements and nodes at areas of interest such as excavations. For example, this can be elements which are small enough to pick up on the behaviour or the lack of complex elements due to geometry. The mesh coarseness determines the number of generated elements, thus the finer the mesh the more elements and nodes. If a mesh is too course then the model results may be unrealistic, due to constraints imposed by the mesh. This will result in unrealistic smaller displacements, exaggerated bearing capacity and exaggerated safety factor. Whereas if the mesh is too fine then the calculation time tends to infinity. The nodes which are generated within the elements have degrees of freedom which correspond to discrete values of nodal displacements.

The calculation phase is mostly all controlled by Plaxis itself, but for the use of numerical modelling it is essential to understand the process. The process is broken down as follows;

1. The elemental stiffness matrices are based on the nodal coordinates and the material properties defined for the model.

2. A global stiffness matrix (K), is composed of all the individual elemental stiffness matrices within the model.

3. The boundary conditions are added to the global matrix.

4. The load vector (f) is composed of the loads within the model.

5. The unknown displacement components within the nodes are assembled in the vector (u).

$$\mathbf{f} = [k]\mathbf{u} \tag{6.1}$$

Important to note here is that the unknown displacements are solved iteratively because the local stress-strain relationship is non-linear, whereas the global system of equations that is being solved in every step (iteration) is a linear system (linearisation of the stress-strain relationship).

The final process of numerical modelling is the analysis of the models, which is different dependent on the specific model and goal. Within this thesis, displacements, relative shear stress, principal stresses and predicted failure points will be addressed. Additionally within this thesis, safety factor calculations were carried out which reduces the strength of the rock mass until global failure.

6.1.1. Safety Factor Analysis

This section will discuss the safety factor analysis that will be carried out during the model comparison phase of this thesis. The safety calculation runs on the principle of strength reduction. When a point in a Plaxis model reaches the failure criterion, the stresses beyond the failure envelope are then redistributed within the near field of that stress point. These stress redistributions can only be done when the surrounding points are not on the failure envelope. The safety factor calculation will continue to iterate through the strength reduction process until there are enough points on the failure envelope to generate a failure mechanism, as one failure point does not make a mine fail.

The safety factor calculation in Plaxis for the Hoek-Brown model is known as the strength factorisation, which is the reduction in the Hoek-Brown strength criterion. This leads to decreased stresses being required to reach the failure criterion (Benz et al., 2008).

$$\sigma_1 = \sigma_3 + \frac{\sigma_{ci}}{\eta}(m_b \frac{-\sigma_3}{\sigma_{ci}} + s)^a \tag{6.2}$$

6.2. Overall Model Set Up

Numerical modelling aims to replicate real world behaviour as already discussed, but within a mine there is no standard case for geometry, as it is extremely variable. Therefore a decision must be taken to determine what is of interest for modelling. The decision was made to produce a model in 2D, as it was felt that this would provide an accurate and representative result. The decision was made for two reasons, the first was that the excavations are laterally similar along their length and as the excavations will be 30 m long in the out of plane direction the 3D effect is expected to be reduced significantly. The second reason is that the calculation time will be reduced significantly, particularly as this is a complex scenario with multiple different phases of excavation and backfill. The limitations are however the lack of the 3D effect providing support to the excavation and the lack of out of plane shear stresses. The 3D however would give extra strength to the excavation, therefore the 2D case established is more conservative than reality.

This project is to look at the global stability, therefore it would be advisable to build a model based on the worst case scenario. The worst case scenario for this project would be the maximum number of drives and stopes, with the closest vicinity to each other, with the narrowest crown pillar. Before the worst case can be identified it is important to understand the constraints set within the project, these are as follows:

1. An accurate reflection of the pre-underground mining stress needs to be set up in advance, as a result geostatic stress needs to be determined for the model. As well as subsequent historic events which led to the pre-underground mining stress, such as the shearing of the ore body and the excavation of the open pit.

2. All development drives are omitted from the model as they are outwith the ore zone.

3. The supporting methods for drives are omitted in order to present a worse case for the mine.
4. The ore drive geometries must be those defined in section 2.3 of 3 m wide and 4 m high. This design specification is based on the block model and mining equipment.
5. Development of ore drives start at the top level and progress downwards.
6. The ore drive layouts must be the same as those defined by the mine plan, as they are based on the block model and will lead to the best recovery based on the current knowledge.
7. Stoping requires an open drive above and below the section identified to be stoped. This means that stoping can only progress in an upwards direction.
8. The stopes are limited by the side walls of the lower drive and base of the upper drive, with parallel stope sides connecting the two levels.
9. The stopes must be backfilled after excavation, meaning both the lower ore drive and stope are filled, based on the Avoca mining method.
10. Stoping will not occur above level K1084 to increase the region defined as the crown pillar, increasing the stability as discussed in section 2.3.
11. Division of excavations must be reflectable of reality i.e. drives and stopes.

The worst case scenario for the crown pillar would be the deepest point based on the digital elevation model for the open pit. This is due to it resulting in the narrowest crown pillar, which is a key component of support for the mine. As a result an open pit cross section was taken running east west at 371025 mN.

An analysis of the planned development was undertaken in order to find the region in which the drive geometries would present the worst case. The author identified a cross section at 371000 mN, which runs from east to west through the ore drives. This cross section was identified as it had the maximum number of ore drives. These drives for the most part will have stopes above them, which will have a combined effect on each other, which could lead to instability within the mine.

The model geometry is now developed based on what is considered to be the worst case. This allows the process of generating the model to begin. The first essential part of any numerical model is to define the boundaries of the model, these can be seen in Table 6.1. The boundary conditions are defined by 3 types: Normally fixed, fully fixed, and free. 'Normally fixed' means that the boundary is fixed in one axis, thus for X min and X max it is fixed in x direction. 'Fully fixed' means that it is fixed in all directions, thus cannot move. 'Free' means that it can move in all directions, however, it still requires a boundary condition. This boundary condition is that the force is equal to zero as there is no load on this region, as it is the top surface, and only air exists above it. The location of the boundaries, as shown in Table 6.1, were selected for a variety of reasons. Y max was selected as this was the highest localised point at the mine, where as Y min was selected to be 27 m below the lowest ore drive as the effect of excavations did not extend that far. The selection of both the X min and X max were determined in order to allow for the accurate calculation on the initial stress state, whilst not extending the model dramatically to increase modelling time.

Table 6.1: Plaxis 2D model boundary conditions

Boundaries		
Xmin	-35 m	Normally Fixed
Xmax	250 m	Normally Fixed
Ymin	-75 m	Fully Fixed
Ymax	160 m	Free

The next thing to establish is the geometry, as discussed above, two decisions have been made, these are the location of the pit cross section and the cross section of the ore drives. It is then important to define the stope geometry, as the drives are not all offset by the same distance. This leads to the

stopes having varying dips and/or orientations. This is more reflective of the reality of the ore body, as there does appear to be changes in dip based on the observations made in the block model. As stipulated in the requirements the stopes are designed by connecting the base of the upper drive to the arc of the lower drive.

With the model geometry defined it is essential to give each geometry the correct material type. As discussed in section 4.7, it was decided that the upper and lower part of the deposit would be defined separately to allow for strength reduction through the use of a lower GSI. The split of the deposit was determined to be at the base of the drive on the K1096 level. On top of this it was determined that the material that made up drives and stopes would be ore, and all material lying outside of this would be country rock. This information for boundaries, geometry and material allow for the generation of the model, which can be seen in Figure 6.2.

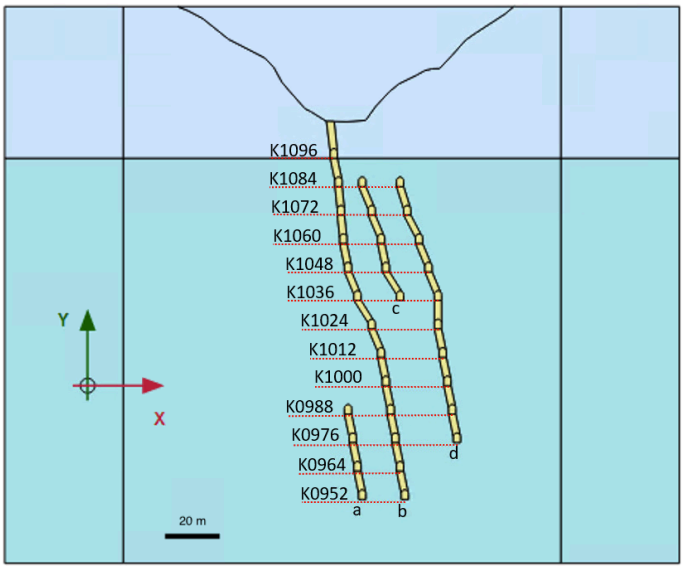

Figure 6.2: Model set up in 2D

The upper region of the resulting model represents the lower GSI value country rock and contains the open pit, the drive on the K1096 level, as well as the ore situated above it (Note that the ore did not receive a reduction in GSI. The lower block is composed of the country rock with the ore zones defined within it. These ore zones result in 3 drives for the K1084, K1072, K1060, K1048 and K1036 levels, which are all connected to each other. The middle drive is no longer present on the K1024 level, meaning that this only has 2 ore drives. This is continued for the next 2 levels to the K1000 level. At the K0988 level there is the occurrence of ore on the west of the main ore section, leading to 3 drives on the K0988 and K0976 levels. On the final 2 levels the ore is not present on the east of the main level meaning that there are only 2 ore drives. This means ascending from the base there are 2, 2, 3, 2, 2, 2, 2, 3, 3, 3, 3, 1 and 1 stope(s) for the subsequent levels. However, the final two of these will not be stoped as they are above the K1084 level.

The next step to modelling is to establish the material properties for the model however, this is something that will change with different scenarios, therefore it will be given its own subsection which will follow in section 6.3. Whist establishing the material properties it is essential to define the initial situation of the model. As discussed previously in section 2.2, it is believed that the stress ratio is 1:1:2, with the 2 value being along the axis of shearing.

Meshing was a set of processes which took multiple steps to establish an effective mesh. The best solution that was found in terms of modelling time and accuracy was a localised refinement within the ore volume of 0.05 and 0.25 for the pit surface. A localised coarsening of 1.5 in the regions x = -35 to 15 and x = 200 to 250, with an overall coarse mesh. This operation means that there is a reduction in the size of the element volumes meaning that the result in that region are more accurate in terms

of changes in stresses and deformations. The meshing process generated 11,433 15-node elements and 171,495 nodes, and the output mesh is shown in Figure 6.3. It is pertinent to note that the mesh is non-uniform and thus will lead to the increase in the number of stress points and nodes locally. This is pointed out in order to avoid confusion when addressing subsequent figures as it may look like there is higher concentrations of stresses, however in reality it is just an increase in the number of recorded points.

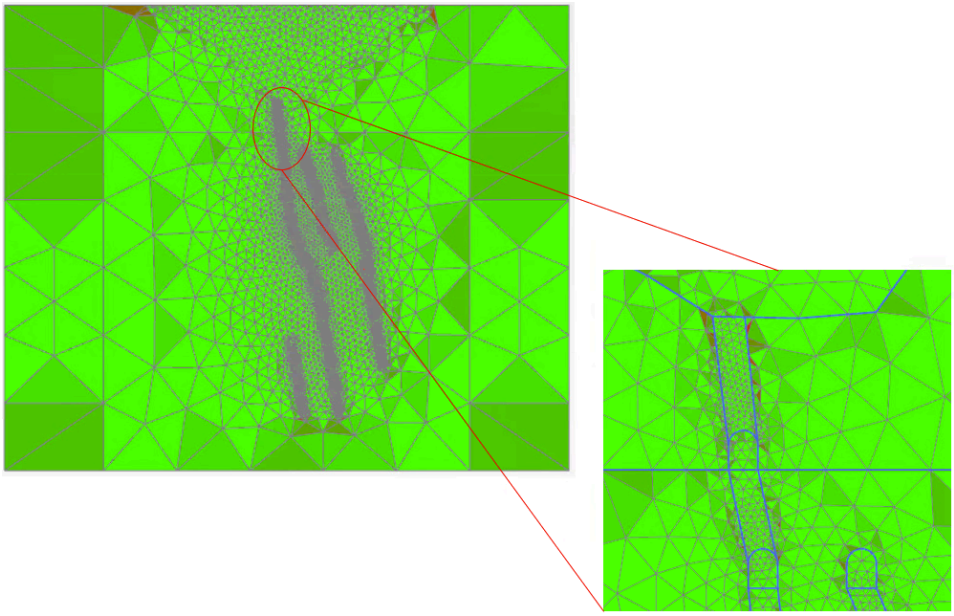

Figure 6.3: Model mesh output from Plaxis 2D

The decision to omit water was taken for several reasons, as discussed in section 4.5, due to the lack of knowledge about the water table and under the recommendations of the mine. As stated previously this may result in an underestimation of the stresses at depth as well as an over estimation in the rock strength.

6.3. Model Rock Characteristics

The results from the work carried out in chapter 4 and chapter 5 define the model parameters, which will be used in Plaxis to give realistic behaviour to the medium. The testing carried out was extensive, however, it is not realistic within this thesis to test every single scenario possible. As a result, the data must be refined to generate data that can be realistically used. This section will first discuss the rock mass and then go on to discuss the backfill.

6.3.1. Rock Properties

The model above is composed of 3 materials the upper country rock, lower country rock and the ore material as discussed in section 6.2. The decision was taken to reduce the model to 3 materials to reduce complexity, whilst trying to provide realistic behaviours. The nature of both country rock units is schist which generates a m_i of 12. The only difference between the upper and lower country rock is that the GSI for the upper region will be lower based on the observations made within chapter 4. This results in both a lower rock mass Young's modulus and Hoek-Brown failure criterion for the upper.

Within the country rock there is the issue that the material did not behave isotropically as the samples were tested in different orientation, thus it is essential to determine which orientation performs worse

in terms of stability. The data can be found in Table 6.2 and is based on the UCS test results for the country rock in parallel and perpendicular direction.

Table 6.2: Shows the two orientations of country rock based on the UCS test results

Sample	Density (t/m^3)	Young's Modulus (RM) (GPa)	Poisson Ratio	UCS (MPa)	Mi	GSI
Perpendicular						
Upper country	2.7	11.2	0.22	99	12	50
Lower country	2.7	14.9	0.22	99	12	55
Parallel						
Upper country	2.7	13.8	0.19	114	10	50
Lower country	2.7	18.4	0.19	114	10	55

The next material to be established is a realistic material for the ore region. Having previously discussed in subsection 4.4.3, if the material selected is massive sulphide or quartz breccia then the GSI will be 35. Based again on the chart in Figure A.3, the m_i will be 19 due to the nature of being breccia. To determine the material properties for the ore, it was decided to establish one unit based on the combined result of all of the UCS test results for the ore, as it was felt that units were too small to discretise into individual units. The parameters for the ore are shown in Table 6.3.

Table 6.3: Properties for ore based on field and experimental testing. * as ore 1 failed because of a chip, the value was excluded. The average of the other 3 samples was used and then reduced 5% as a safety precaution

Sample	Density (t/m^3)	Elastic Modulus (RM) (GPa)	Poisson's Ratio	UCS (MPa)	Mi	GSI
Ore	3.0	4.8	0.15	137.5*	19	35

The properties of UCS, GSI and m_i are used for the calculation of the Hoek-Brown failure criterion for the model. With all of these materials having different properties, it is interesting to establish how the failure criterion compare to each other, this can be seen in Figure 6.4. This shows that when the UCS is increased, i.e. when comparing the parallel and perpendicular results, the curve values are increased. It also shows that the lower the GSI, the lower the required stress to reach the failure criterion is. The resulting failure criterion for the ore shows a completely different profile to the other rocks as a result of the lower GSI and a higher UCS, and m_i.

The variation of material within the ore drives is unknown currently, making it difficult to determine a definitive geological model for the analysis. More understanding will be gained with the proper recording of future development. It should be noted that the rock characteristics may change for the same rock units with depth.

6.3.2. Backfill

The planned operation at the mine is to backfill all stopes with cemented rock fill once emptied. It is essential to estimate realistic behaviour for this backfill material. The strength of backfill is based on several characteristics, these are the aggregate or rock fill size and strength, and the cement blend. To find a solution the starting point should be trying to find a cemented rock fill with similar rock properties to the waste (country rock) at the mine. The work of Emad (2017) uses a case study backfill rock of mica schist with a UCS of 94 MPa and an intact rock Young's modulus of 48 GPa. These intact rock properties are similar to the country rock which is considered as waste for the Cavanacaw mine. As a result it can provide a good estimation for the backfill behaviour that can be achieved. The resulting properties for the Mohr-Coulomb model can be seen in Table 6.4 and are composed of aggregate of 3 to 21 cm, with no added fines, with a binder of type-10 Portland Cement and type-C fly ash in a 30:70 ratio. The use of the Mohr-Coulomb model is more appropriate here, as the backfill does not represent

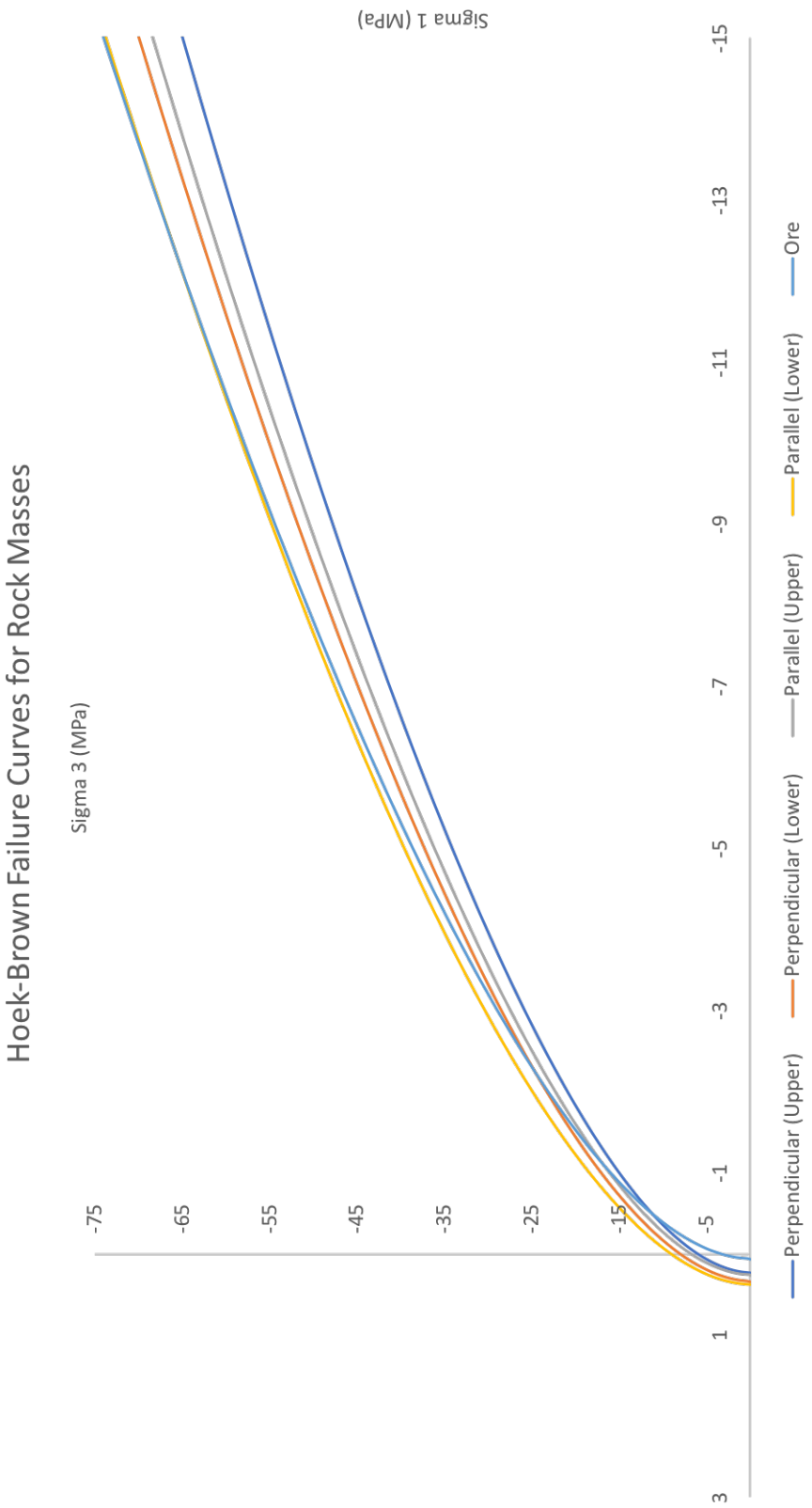

Figure 6.4: Hoek-Brown failure criterion curves for the model rock masses

a rock and the test results are representative of the backfill mass, and therefore do not need to be altered. It should be noted that this is an estimation of the backfill material and in reality a full technical analysis should be conducted before stoping is carried out, as well as continuous assessment of the backfilled stopes.

Table 6.4: Backfill characteristics

Material	σ_t (MPa)	E (GPa)	φ (°)	c (MPa)	v	Density (t/m^3)
Cemented Rock Fill	0.030	2.5	37.0	1.10	0.35	2.0

6.4. Model Scenarios

The proposed plan is to do a comparative analysis for different model scenarios. This is believed to offer the most effective insight into the data, as it is difficult to determine the true scenario for the rock mass with the limited information.

All of the models will operate with the same mine geometry that can be seen in Figure 6.2, the difference will be made in terms of the material characteristics that the models are made up of or the order in which excavations are carried out. This resulted in the generation of 4 models:

- Model A - bottom to top sublevel stoping with perpendicular country rock.
- Model B - bottom to top sublevel stoping with parallel country rock.
- Model C - middle to top, bottom to middle sublevel stoping with a sill pillar and worst country rock.
- Model D - Bottom to top sublevel stoping with a sill pillar and worst country rock.

As the thesis aims to look at predominantly the underground excavation is should be noted that displacements were reset to zero before starting underground excavations. This has no effect on the model other than allowing to distinguish the total displacement caused by the underground excavations.

6.4.1. Model A

Model A is the first model to be tested. This model uses perpendicular to foliation results for the country rock. The country rock is subdivided into upper and lower as discussed previously and seen in Table 6.2. The ore results are those shown in Table 6.3.

The excavation order for model A is as follows (stope locations can be found in Figure 6.2):

0. Generation of initial stress field (K0), non-excavated ground surface. (Phase Initial)
1. Excavate the open pit as a single phase. (Phase 1)
2. Excavate each level of ore drives from K1096 to K0952 as single phases. (Phase 2 - 14)
3. Excavate stope a on K0952 followed by backfilling as separate phases.(Phase 15 - 16)
4. Excavate stope b on K0952 followed by backfilling as separate phases. (Phase 17- 18)
5. Repeat previous two steps for K0964 level. (Phase 19-22)
6. Excavate and then backfill stopes in the order a-d-b for level K0976. (Phase 23 - 28)
7. Excavate and then backfill stopes d then b for level K0988. (Phase 29 - 32)

8. Repeat the above step for levels K1000, K1012 and K1024. (Phase 33 - 44)
9. Excavate and then backfill stopes in the order d-c-b for level K1036. (Phase 45 - 50)
10. Repeat above step for level K1048, K1060 and K1072. (Phase 51 - 68)
11. Extraction is complete.

The excavation pattern is set as above for several reasons, firstly it is deemed good practice to backfill before continuing with excavations in order to reduce the number of openings at one time, which increases the available supporting volume. Next, stopes in the ore section with the letter b are left until last on each level, as that region has the raise within it which leads to good ventilation and access to amenities.

6.4.2. Model B

Model B is established in order to compare the material properties from the test parallel and perpendicular to foliation for the country rock. The model was given the material properties for the parallel test results for the country rock, which can be found in Table 6.2. Characteristic for ore is as the previous model (A), as can be found in Table 6.3. An identical excavation order to that of Model A is used.

6.4.3. Model C

Model C is generated in order to compare the stoping order. The material properties used for the country rock will be dependent on least stable model between model A and B. The ore however will be the same as in Table 6.3.

The excavation order will be as follows (also using Figure 6.2):

0. Generation of initial stress field (K0), non-excavated ground surface. (Phase Initial)
1. Excavate the open pit as a single phase. (Phase 1)
2. Excavate each level of ore drives from K1096 to K1036 as single phases (Phase 2 - 7)
3. Excavate stope d on K1036 followed by backfilling as separate phases.(Phase 8 - 9)
4. Excavate stope c on K1036 followed by backfilling as separate phases. (Phase 10 - 11)
5. Excavate stope b on K1036 followed by backfilling as separate phases. (Phase 12- 13)
6. Repeat previous three steps for the K1048 level. (Phase 14-19)
7. Repeat the previous step for the K1060 and K1072 level. (Phase 20 - 31)
8. Excavate each level of ore drives from K1024 to K0952 as a single phase. (Phase 32 - 38)
9. Excavate stope a on K0952 followed by backfilling as separate phases.(Phase 39 - 40)
10. Excavate stope b on K0952 followed by backfilling as separate phases. (Phase 41- 42)
11. Repeat previous two steps for K0964 level. (Phase 43-46)
12. Excavate and then backfill stopes in the order a-d-b for level K0976. (Phase 47 - 52)
13. Excavate and then backfill stopes d then b for level K0988. (Phase 53 - 56)
14. Repeat the above step for levels K1000 and K1012. (Phase 57 - 64)
15. Extraction is complete.

Model C differs significantly from Model A and B, as it introduces a sill pillar composed the material that could be stoped between level K1024 and K1036. This is a result of constraint 7 set out for the model, where it stipulates an open drive above and below is required for an area to be stoped. Due to the new stoping order, the drives on the K1036 level are backfilled after the first 3 stoping and backfilling phases. The sill pillar material could be removed using a different mining method, such as blind stoping, at some point, but this is not part of this thesis.

6.4.4. Model D

The introduction of a sill pillar in Model C, means that a new model should be introduced which follows the stoping order of Model A and B but with a sill pillar. The sill pillar is left between levels K1024 and K1036, in order to replicate the conditions in Model C.

Thus the stoping pattern will be as follows (stope locations can be found in Figure 6.2):

0. Generation of initial stress field (K0), non-excavated ground surface. (Phase Initial)
1. Excavate the open pit as a single phase. (Phase 1)
2. Excavate each level of ore drives from K1096 to K0952 as single phases (Phase 2 - 14)
3. Excavate stope a on K0952 followed by backfilling as separate phases. (Phase 15 - 16)
4. Excavate stope b on K0952 followed by backfilling as separate phases. (Phase 17- 18)
5. Repeat previous two steps for K0964 level. (Phase 19-22)
6. Excavate and then backfill stopes a then d then b for level K0976. (Phase 23 - 28)
7. Excavate and then backfill stopes d then b for level K0988. (Phase 29 - 32)
8. Repeat the above step for levels K1000 and K1012. (Phase 33 - 40)
9. Excavate and then backfill stopes in the order d-c-b for level K1036. (Phase 41 - 46)
10. Repeat above step for level K1048, K1060 and K1072. (Phase 47 - 64)
11. Extraction is complete.

The material properties for the country rock will be the same as in model C, which is set to the worst performing material from models A and B. The ore properties will be the same as those found in Table 6.3.

6.5. Model Results

This section will look at the results for the models presented above. Firstly model A will be presented and discussed in order to generate an understanding for the different activities within the model. After this is presented a comparison will be made between Model A and B in order to determine whether the country rock tested parallel or perpendicular to foliation presents the worst case. As the worst case country rock is now established, alternate stoping orders can be analysed to determine if they increase the stability. This can be done by comparing model A or B with model C. Finally, dependent on the result a final comparison shall be made in order to determine the effect of the introduction of a sill pillar on the stability of Model A or B, or whether the alternative stoping order is better (Model C).

6.5.1. Model A

This subsection will look at the results of model A, specifically the fundamental components, these components are the initial stress generation, the excavation of the open pit, the excavation of drives, the excavation of the stopes and the backfill of stopes and drives. These individual components are combined in a sequence as stipulated in subsection 6.4.1. The initial step of analysis would be to look at the rock response as a result of each of the components. The next step will be to look at the combined result on a single level and multilevel scale to identify the impact of coupled excavations.

Pre-Underground Mining Stress State

Before moving forward with the analysis of the results from the underground excavations, it is important to check the results for the generation of the pre-underground mining stress field. This was a two part procedure, composed of the K0 procedure, which generated initial stress conditions on the non-excavated block, and then the excavation of the open pit.

Figure 6.5, shows the Cartesian stresses that can be observed at the stress points during the K0 procedure. These Cartesian stresses correlate directly to the principal stresses in this case. σ_y equates in this case to the geostatic stress caused by the overlying mass, which in turn allows for the generation of the complete stress state. As a result the stress state in terms of principal stresses is then $\sigma_1 = \sigma_z$, $\sigma_2 = \sigma_y$, and $\sigma_3 = \sigma_x$. As a result in Figure 6.5, the stress in and out of the plane is double that of the two other stresses.

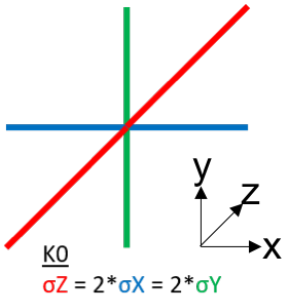

Figure 6.5: Composition of K0 stress field. σZ is into the plane and twice the magnitude of σX and σY. As a result σ1 is in and out of the plane σ2 is the horizontal stress and σ3 is the vertical stress.

The visualisation of the stress field can be done through the generation of a contour plot, as can be seen in Figure 6.6. This figure shows the gradient of σ1, σ2 and σ3 with depth. It shows that all σ's increase linearly as would be expected with geostatic stress. Further it shows the gradient of σ1 is twice that of σ2 and 3. This confirms the correct K0 procedure as this is the expected result for the region based on the current knowledge base.

The second step in generating the pre-underground mining stress state is to generate the open pit. This is an essential part of generating a realistic case for the mine, as it allows for the stresses associated with the elastic response of the rock to be generated, as discussed in subsection 3.1.1.

The principal stress are altered in terms of magnitude and orientations due to the excavations of the open pit. The change in magnitude is due to the removal of a load coupled with the shear stresses that form as a response to the slopes, where as the change in orientation is due to the shear stresses. A schematic of the change in orientation and magnitude can be seen in Figure 6.7. As a result of the removal of material, there is an increase in σ3 in the near field due to the lack of confining over burden, whereas there is a decrease in σ2 due to the geometry of the open pit generating compression from remaining material. It can further be seen that there is the rotation of σ2 and σ3 within the near field to the open pit. The rotation is such that σ2 in the near field has moved from a horizontal orientation to parallel to the excavation. σ3 is now orientated from the vertical to perpendicular to the excavation. σ1 is still perpendicular to the orientation of the cross section, and is relatively unaffected by the excavation.

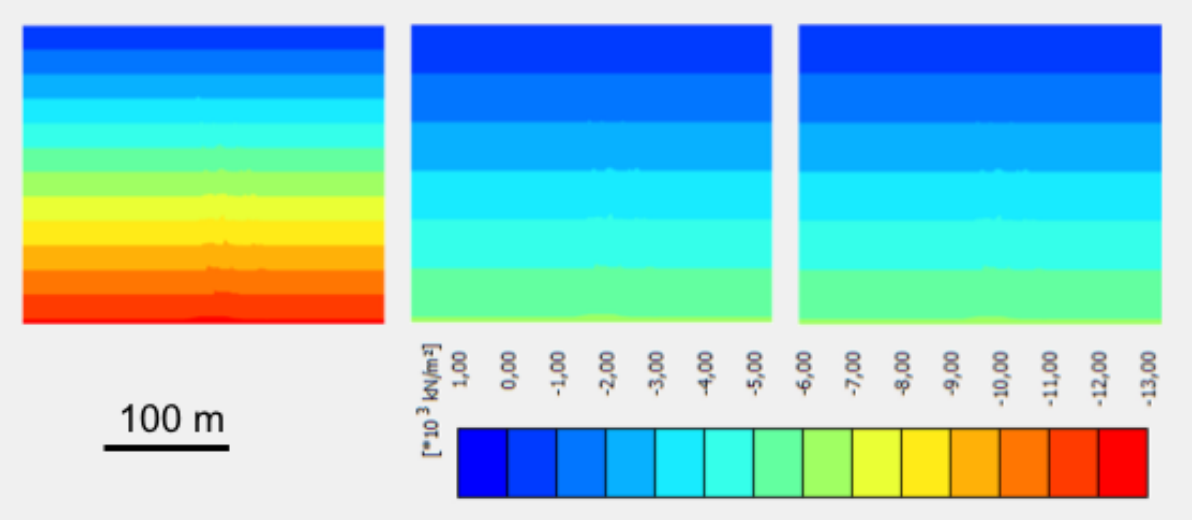

Figure 6.6: The results of the K0 procedure on the non-excavated block, left shows $\sigma 1$, centre is $\sigma 2$ and right is $\sigma 3$. The graphs show that all the σs increase linearly with depth, however $\sigma 1$ increases at twice the rate of the others.

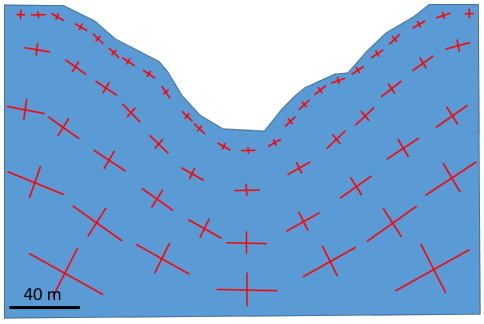

Figure 6.7: A Schematic of the redistributed stress field due to the excavation of the open pit. $\sigma 1$ is in the out of plane direction, $\sigma 2$ is rotated to be parallel to the pit excavation walls, and $\sigma 3$ is orientated so as to be perpendicular.

The total response in terms of displacements for the upper segment of the mine is shown below in Figure 6.8, the response is small in the region of a maximum of 7.2 mm. The response shows that it is predominantly in the vertical direction in the form of heave, however on the sloped sections there is a slight response towards the centre, which is to be expected due to the asymmetric removal of material.

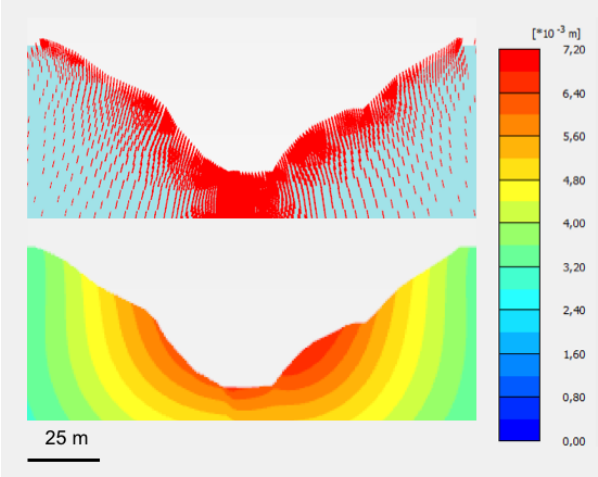

Figure 6.8: The top cross section shows the reaction displacement direction, post open pit removal. The lower cross section shows the magnitude of the norm of the total displacement vector.

The behaviour and reactions observed in both of these steps is what was expected in terms of an elastic response to the removal of material. As a result it allows for the modelling to progress to the next stage, which is the analysis of the underground excavations, starting with the drive excavations.

Ore Drive Excavation

The set up for the model is now done in terms of the stress field and the expected response has been observed, in turn allowing for the model to progress to the next phase. Firstly it is essential to establish if the response of the underground excavations are what should be expected. This will be done through the analysis of various scenarios in order to establish logic behind the results.

It may be misleading to conclude on individual $\sigma 1$, $\sigma 2$ or $\sigma 3$ plots without looking at the total picture (general principal stresses plot), since Plaxis orders principal stresses such that $\sigma 1$ is always the major principal stress and $\sigma 3$ is the minor principal stress. At some point, $\sigma 3$ may become the middle principal stress, etc., so if you conclude on 'the absence of $\sigma 2$', it might mean that $\sigma 2$ has become $\sigma 1$ or $\sigma 3$.

The result of phase 2 (first underground excavation) is shown in Figure 6.9, this shows the principal stress orientation around the underground excavation. Firstly there is the concentration and reorientation of $\sigma 1$ in the corners and the peak of the curved roof, which is something that is to expected. Next there is the bending of the $\sigma 2$ field around the excavation, in particular it is interesting to note the absence of $\sigma 2$ lines on the top ark of the curve. Finally $\sigma 3$ is bent to perpendicular to the excavation. $\sigma 2$ takes a dominant role here in the reorientation of the principal stress field, which is not necessarily the expected reaction when considering an underground excavation. It is known that one principal stress is always along the Z axis, due to no shear stress being out of the XY plane, it is then understood that throughout this phase there is points in which previous $\sigma 2$ may become $\sigma 1$ or $\sigma 3$. This is the case for all the different principal stresses. Possible explanations for this may be the initial stress conditions, the excavation of the open pit, or a combination of both.

To determine the causation for the stress field calculated for the excavation of K1096, three simple models were generated. These models were generated in order to establish the dominant causation for each stress field. These models will be K0 = 1:1:1, no pit; K0 = 1:1:2, no pit and; K0 = 1:1:1, pit and will only address this first excavation. Figure 6.10, shows the output models from these three scenarios. Comparing these scenarios, it is interesting that there is no scenario that matches perfectly that which is seen in Figure 6.9. The initial point of interest is that the $\sigma 1$ field is definitively dominated by the pre-mining stress field of K0 = 1:1:2, as can be seen in image 1 row 3. $\sigma 2$, is a more complicated question as it does not fit any of the models specifically, however it does appear to be a combination of both the K0 = 1:1:2 and the pit, as combining these two stress fields provides the best likeness. Finally $\sigma 3$, appears to be predominantly a result of the open pit, as the two outputs match very similarly. To conclude the results of the stress field generated through the first underground excavation is complex with both the pre-mining stress and the open pit excavation playing a role in the formed stress field. A further suggestion might be that this will change with depth, seeing as the impact from the open pit was restricted to its near field.

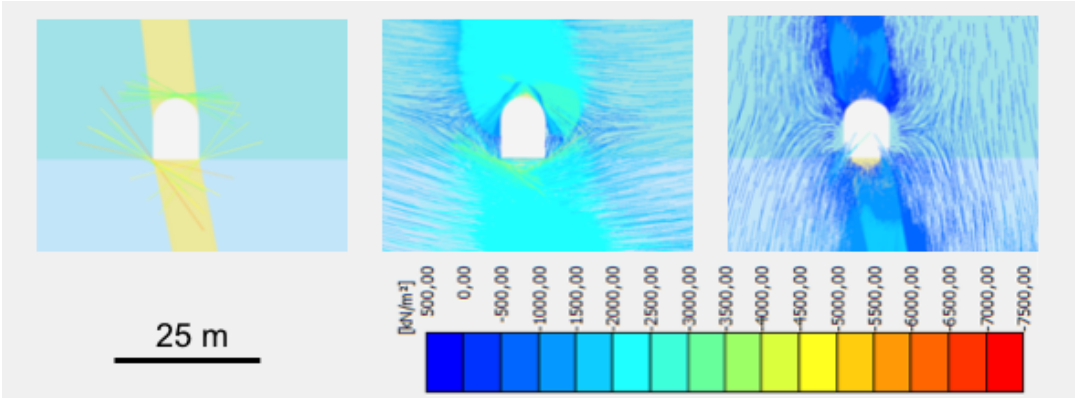

Figure 6.9: The stress field of the drive excavation at K1096. Left is $\sigma 1$, centre $\sigma 2$ and right is $\sigma 3$.

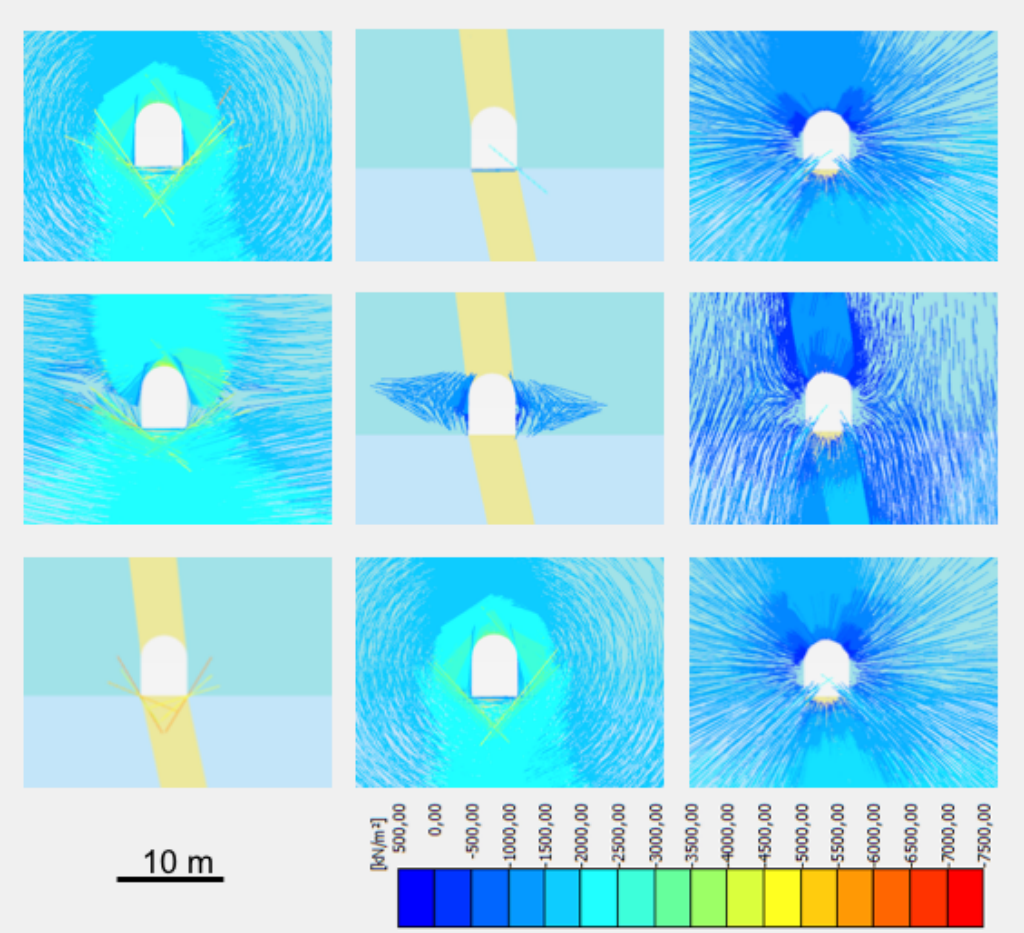

Figure 6.10: The different scenarios of which compose the stress field. Row 1 is K0 = 1:1:1 (no pit), row 2 is K0 = 1:1:2 (no pit), and row 3 is K0 = 1:1:1 (pit). Column 1 is $\sigma 1$, column 2 is $\sigma 2$, and column 3 is $\sigma 3$.

Before moving forward to look at the further stages of the model, the stress curve development should be addressed. This done be selecting multiple point around the region of interest, as shown in Figure 6.11. These points were selected as they show specific responses to the excavation. Stress point A, to show the region above the excavation. Stress point B was selected to show the effect on the immediate boundary of the excavation. Then stress point C was selected to show the boundary of the two material and the termination of the arc. Stress point D, was selected to show the stress in the supporting wall. Finally, stress point E and stress point F, were selected to show the resulting stress field in the corner and the floor of the excavation. These will be plotted for the $\sigma 1$ and $\sigma 3$, to determine the progressive stress pathway and how it compares to the failure criterion. As well as be plotted as the cartesian stresses in order to yield an indication to the stress rotation.

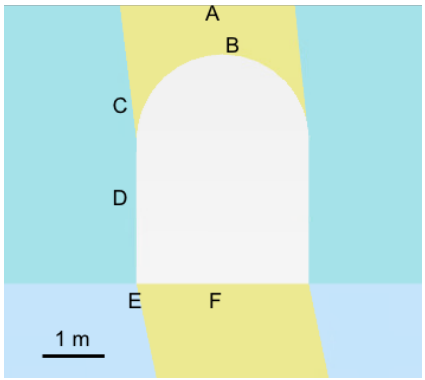

Figure 6.11: The selected location of stress point for analysis around the excavation on K1096 level.

The output graphs for the selected points are shown in Figure 6.12. The graphs all begin in approximately the same initial stress state, with very slight difference caused by slight changes in height. All six selected points show the same trend with the excavation of the open pit. The trends in the pathways can be described using simple terminology, which is mobilisation and demobilisation, these terms mean to go towards or away from the failure curve respectively. The trend for the open pit excavation is the mobilisation of $\sigma 3$, due to the reduction in the confinement. This deconfinement is associated with the reduction in the overlying mass. $\sigma 1$ also exhibits an increase in the stress value, however it is classed as demobilisation, as it moves the point away from the failure curve. The combined result of the pathway between the initial stress state and that at the end of the open pit excavation is mobilisation as a result of deconfinement.

The stress reaction to the phase 2 excavation is not the same at all the selected points like it was for the open pit excavation, thus they will be described individually. The reaction of the stress field in stress point A, which is approximately 1 m above the arch of the excavation, is that of mobilisation of both $\sigma 1$ and 3. This is reduced in comparison to points closer to the excavation due to the arching effect. The stress point B, also lies above the excavation, however it lies extremely near to the excavation surface where stresses are zero. The stress point shows a pathway during the excavation of mobilisation in both the $\sigma 1$ and $\sigma 3$ values, which in turn results in a net mobilisation. This mobilisation is caused by increased compression in $\sigma 1$ due to the arching effect and a lack of confinement, which reduces the compression in the $\sigma 3$ plane.

The next point to be considered is the corner point of the curve (stress point C), the response shows mobilisation in the $\sigma 3$ directions, with demobilisation in the $\sigma 1$ orientation. Due to the mobilisation of $\sigma 3$ being significantly larger than that of the demobilisation of $\sigma 1$, the net result is mobilisation of the point towards the failure criterion. The justification for this behaviour is the arching stress effect around an opening, and that this point lies near to the surface with a lack of confinement. Continuing round the excavation, the next point is stress point D, which represents the side wall of the excavation. The same behaviour as the previous point is experienced here, however due to being contained within a different medium, the point is further from the failure criterion.

Corners have been well documented to be a location of stress concentrations due to their abrupt change in geometry, the results for stress point E is no different. The stress pathway from the open pit to the underground excavation show a demobilisation of $\sigma 3$ and a mobilisation of $\sigma 1$, which lead to a net demobilisation. The values at this stress point all decrease due to the concentration of stresses.

The final point analysed is the floor of the excavations (stress point F), which shows the mobilisation of $\sigma 3$ and slight demobilisation of $\sigma 1$. This result does not only move towards the failure curve but reaches it, meaning that the point has reached the failure criterion. This results in floor heave due to a lack of confinement, due to the arching effects of the tunnel shape.

This data is incredibly useful, however a further visualisation of the proximity to failure can be had by looking at the relative shear stress. The relative shear stress is a measure of the proximity to the failure envelope for a given stress point. It is given by the ratio of mobilised shear stress, which is the maximum shear stress value for a given $\sigma 1$ and 3, and the maximum shear strength for a given $\sigma 3$. A relative shear stress ranges from 0 to 1, with a value of 1 representing a value which lies on the failure criterion.

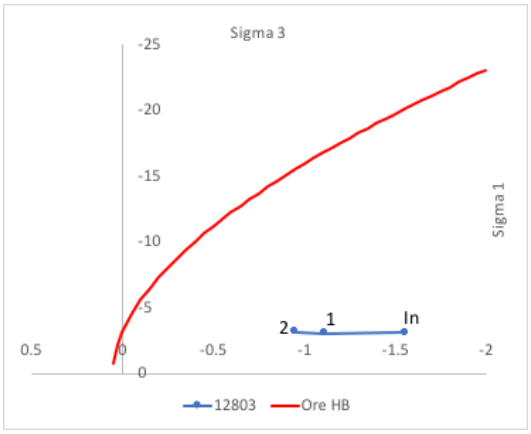

(a) Stress point A

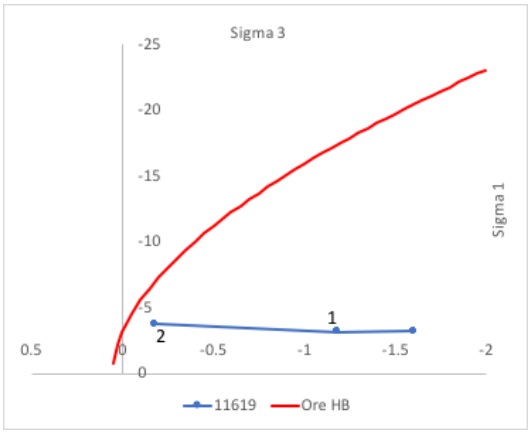

(b) Stress point B

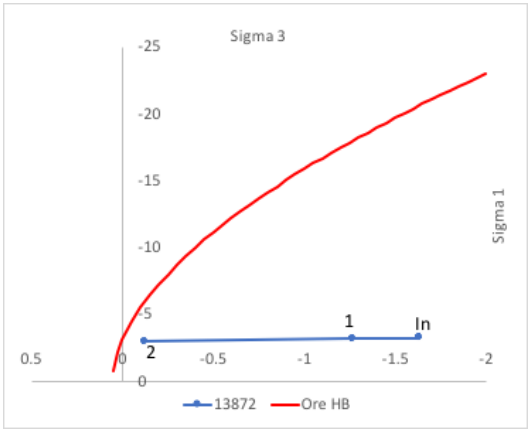

(c) Stress point C

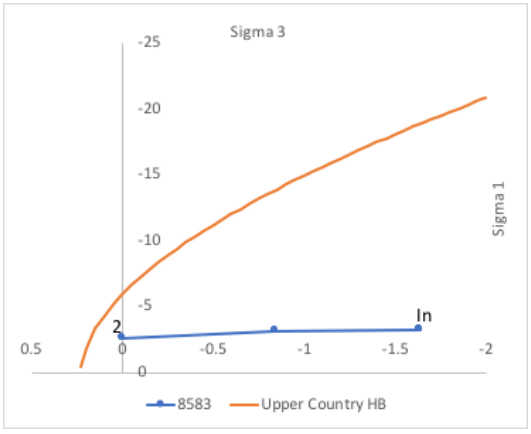

(d) Stress point D

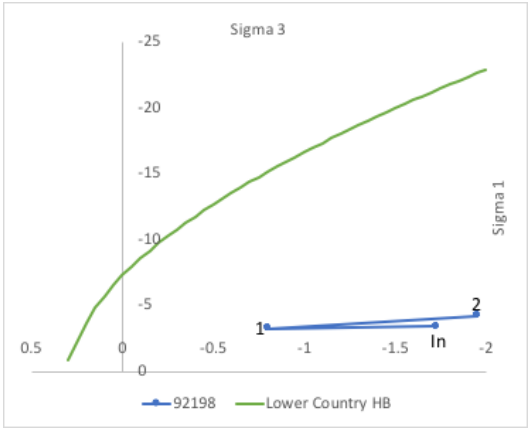

(e) Stress point E

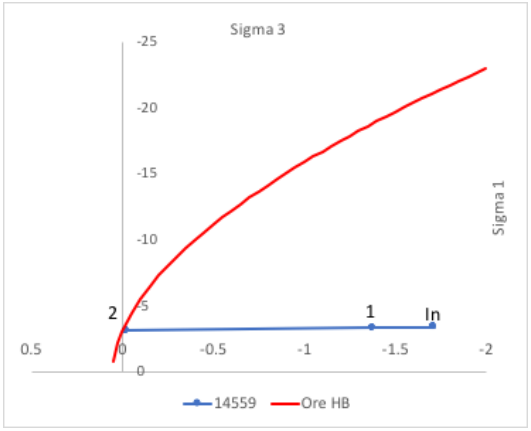

(f) Stress point F

Figure 6.12: Shows the graphs for the 6 selected points around the excavation. Note that the orientation of the principle stress axis are not the same for each graph. Note the axis are non-orthonormal.

Figure 6.13, shows the proximity to failure for the region around the excavation K1096. The trend that was seen in the individual points is also apparent, where the arch has concentric curves, that represent the redistribution of stress by an arch. The opposite can be seen in the floor where the arching effect is also present, however due to the geometry, there is a semi-circular volume, which represents the points in proximity to failure. The corner points in the bottom, show that they are further from the failure curve than the other points in the vicinity of the excavation. Finally it can be seen that there is an trend to towards the failure curve in the regions of the side walls.

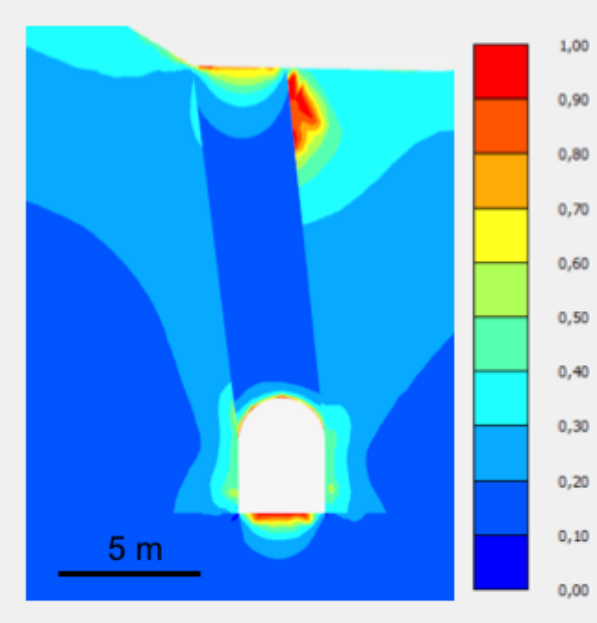

Figure 6.13: The relative shear stress for the tunnel excavation K1096. The values indicate the relative shear stress, which is the ratio between the mobilised shear stress and the maximum shear strength for a given point.

The final step before moving forward is to address the rotation of the stress field around the excavation. As Plaxis2D limits shear stresses to the XY plane, σZ is always equal to to one of the principal stresses. As a result of this it is possible to determine stress orientation in the XY plane for the minimum and maximum principal stress in that plane. The angle in which the stress field is orientated is defined by the end members shown in Figure 6.14.

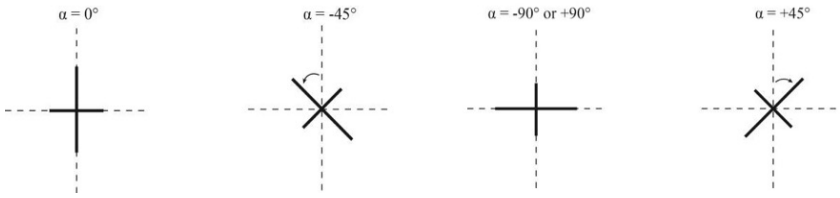

Figure 6.14: Principal stress orientation end members: clockwise rotation is positive and counter-clockwise rotation is negative (Plaxis bv, 2014)

As the principal stress orientations are defined, it is now possible to interpret, Figure 6.15. The figure shows that the major principal stress in the plane is orientated horizontal in the region above the excavation. When following the arc of the excavation, the major principal stress on the left side is rotated in an anticlockwise direction until reaching the side wall of the excavation, where the major stress is orientated vertically. This trend continues around the excavation, in an anticlockwise direction.

This however, only provides partial information, as it does not define which principal stresses lies within the plane. To counteract this it is possible to plot the Cartesian stress values for the initial phase and the two subsequent phases in order to determine which normal stress lies out of plane.

The determination of which principal stress lies out of the plane can be understood by looking at Figure 6.10. The absence of $\sigma 1$ within the majority of the first image shows that the orientation of $\sigma 1$ is predominantly in the out of plane direction. This means that the rotations presented in Figure 6.15 are predominantly $\sigma 2$ and 3 with the exception of the arch and the corners of the excavation, where $\sigma 1$ is present within the XY plane.

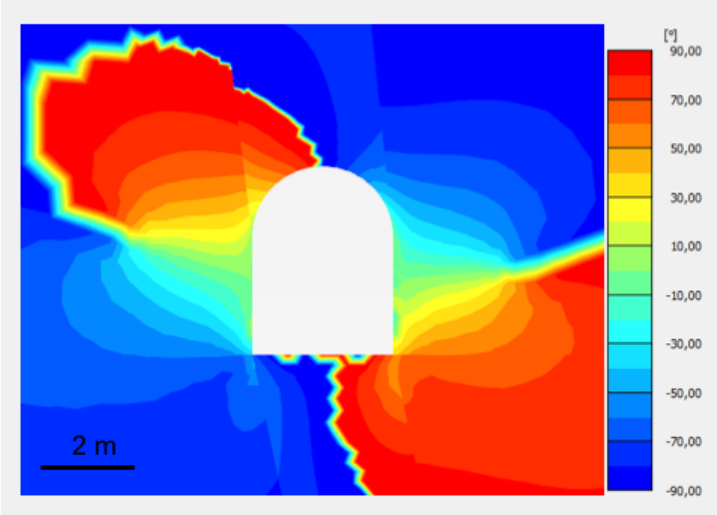

Figure 6.15: Phase 2 principal stress orientations around drive excavation. Note that this is a smooth and continuous stress distribution, and the stark transition from red to blue, is as a result of stress directions above 90 °turning to -90 °.

Having achieved a description of one drive excavation, the next step of importance is to look at the coupled effect of drive excavations. This can be done through the analysis of the excavations on the K1084 level. The stress fields can be seen in Figure 6.16 for both the levels K1096 and K1084. During the excavation of the K1084 drives it can be seen that around the excavation, the stress field behaves in the same way as the individual excavation, which was seen in Figure 6.9. The coupled effect is most obvious in the $\sigma 2$ field, with a figure of eight pattern of stress orientation around the drives next to each other. There is no significant change in the stress state due to the coupled excavations.

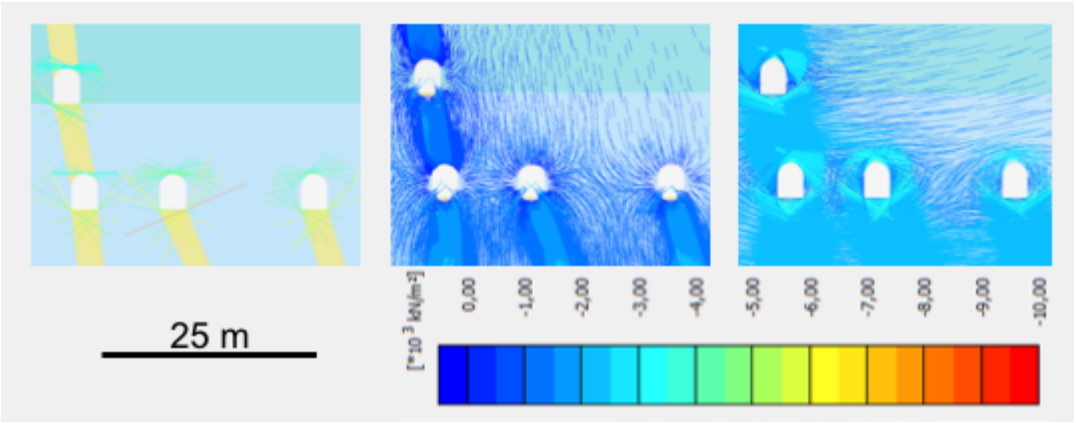

Figure 6.16: The stress field of the drive excavation at K1084. Left is $\sigma 1$, centre $\sigma 2$ and right is $\sigma 3$.

Progressing on from the stress field it is essential to determine where the points surrounding the excavation lie in terms of the failure criterion. The relative shear as seen in Figure 6.17 for the excavation of K1084 shows several interesting findings. The relative shear in excavation K1096 and K1084b are similar, although there is a slight difference. The country rock around the ore drive has a different GSI, and therefore K1096 has reduced country rock strength, leading to the different extent of relative shear stress. The drives c and d, also have different relative shear volumes, which can be explained by the material above the ore drives not being ore but country rock which has a higher strength for the given stresses.

The results show that the behaviour of the stress fields is extremely similar for the drive excavations between the first two levels. The next logical step would be to continue with depth to the final drive excavation in order to determine if the same results observed in the first two levels are repeated.

Figure 6.17: The relative shear stress for the tunnel excavation K1084.

The deepest drive excavation is the excavation of the K0952 level, with the resulting stress field being seen in Figure 6.18. The magnitude of the stresses in the points surrounding the excavation show a significant increase, which can be attributed to the increase in depth. Further it can be seen in particular within $\sigma 1$ that there is increased stress rotation in particular around the curved roof of the excavations.

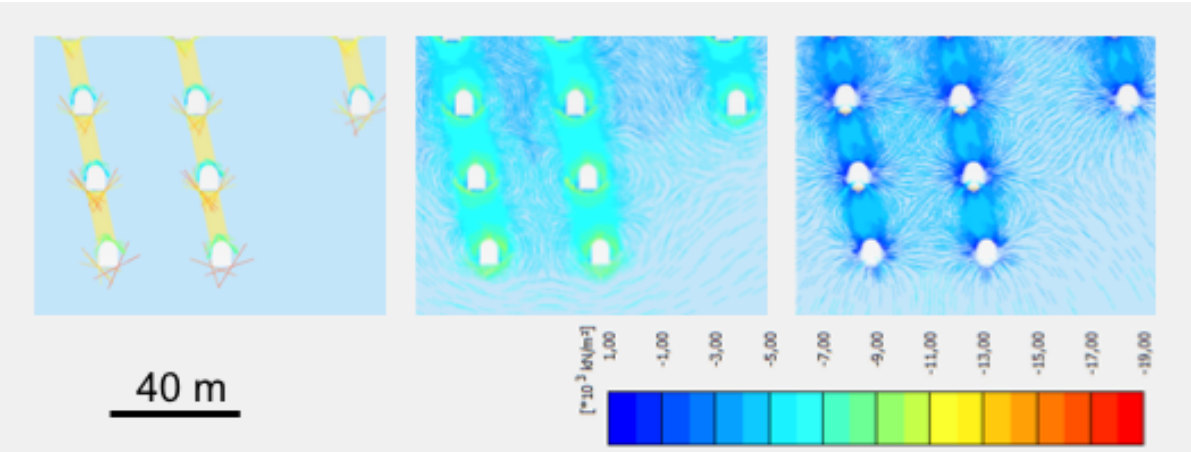

Figure 6.18: The stress field of the drive excavation at K1084. Left is $\sigma 1$, centre $\sigma 2$ and right is $\sigma 3$.

The increased stress magnitudes which are seen with the depth increase, do not necessarily mean that there will be more or less failure p. This is due to increased confinement of $\sigma 3$ which allows for increased shear strength.

To establish the result of these increased stresses with respect to failure, a visual comparison can be made with the relative shear stress shown in Figure 6.13 & Figure 6.17 with Figure 6.19. The first observation is that the volume around an individual excavation in the range of 90 to 100 % of the maximum shear stress is much higher. This indicates an increase in the probability of failure in the immediate vicinity. Further the zonation of $> 20\%$ is much more extensive at depth.

The concluding remarks for the drive development are; the behaviour of the rock reacted as predicted; the magnitude of stresses increase as you increase in depth, which is to be expected; the stress concentration due to excavations are concentrated around the opening, in particular the curved roof which helps to redistribute the stress, and the corners where the stress is strongly concentrated.

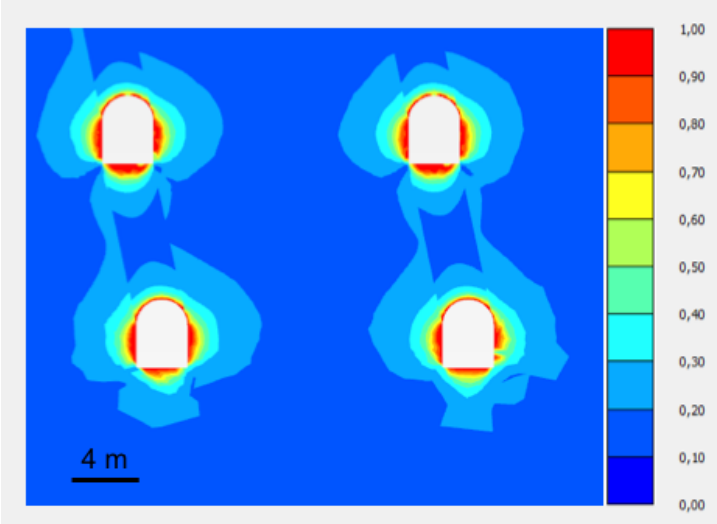

Figure 6.19: Relative shear stress around the excavation at the phase where K0952 drives are excavated.

Stope Extraction and Backfill

The excavation of K0952 marks the end of the development of the mine. The mine then moves into the main extraction phase, which consists of the stope extraction and backfilling. The excavations carried out during the subsequent phases, represent much larger singular volumes than the drive excavations. This implies that the stress magnitudes may be significantly higher due to the larger volumes. This subsection will look at the results of the singular extraction of a stope, its backfilling, and then the result of multiple stopes. Finally the complete development result will be addressed.

The stress response to excavation of stope K0952a is shown in Figure 6.20. It should be noted that the scale in this image is from 2,000 to -30,000 kN/m^2 rather than 1,000 to -19,000 kN/m^2, which was the scale for the previous figures.

The $\sigma 1$ for the excavation of a stope behaves in the same manner as a drive excavations, with the stress concentrations occurring around the arc of the upper tunnel and the corners of the lower tunnel, however with the added caveat of being significantly higher in magnitude. $\sigma 2$ values are re-orientated around the excavation, to run parallel to its walls. This stress response is different dependent on the location, there is a increase in the $\sigma 2$ in the side walls due to a lack of confinement, where as there is a decrease in the $\sigma 2$ in the roof due to the redistribution of stresses around the excavation. $\sigma 3$, also increases significantly due to the lack of confinement in the immediate stress field, and is rotated perpendicular to the excavation walls.

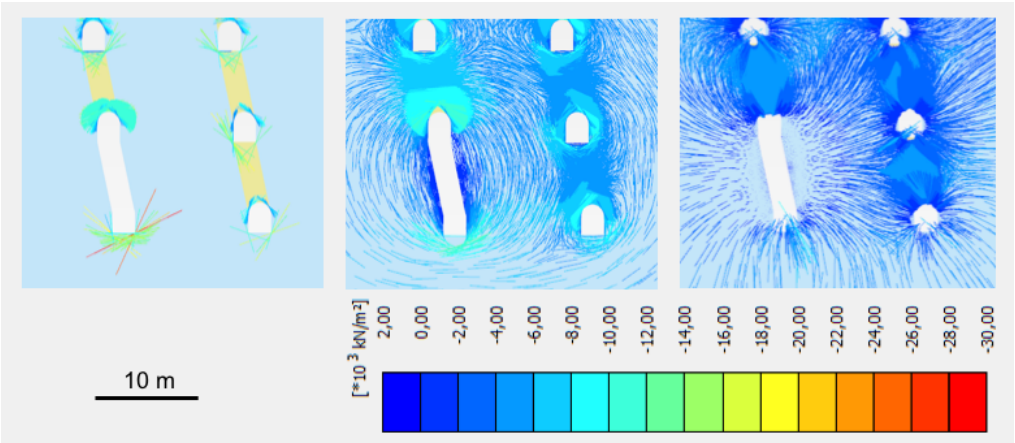

Figure 6.20: The stress field of the stope excavation of K0952 a. Left is $\sigma 1$, centre $\sigma 2$ and right is $\sigma 3$.

Much like the drive excavations it is pertinent to look at the stress field development of the region of the stopes before moving forward. Figure 6.21, shows the selected points that will be addressed to determine the stress field development. These points were selected in order to help indicate the different behaviours exhibited around the excavation.

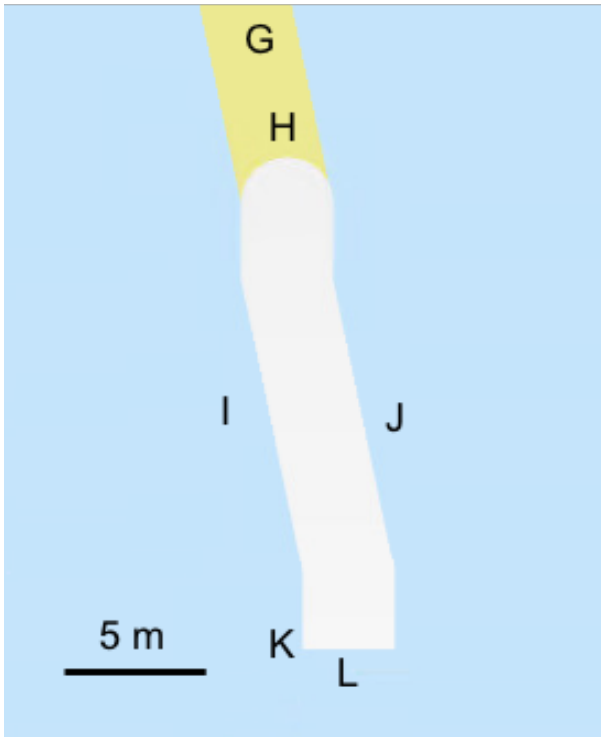

Figure 6.21: The selected stress points around the stope excavation K0952 a.

Figure 6.22a represents stress point G, a point above the arch of the drive K0964a. The initial stress state is $\sigma 1$ is twice that of $\sigma 3$, which was the desired behaviour. During the first excavation phase (open pit), there is the mobilisation of $\sigma 3$ and slight demobilisation of $\sigma 1$, which leads to a net mobilisation, due to the removal of mass. Phases 2-12 represent drive excavations above the point with increasing proximity to the point, however they only result in incremental changes in the stress field. These results are the mobilisation of $\sigma 3$ and slight demobilisation of $\sigma 1$. The progression does however lead to net mobilisation through this section. This increase in the $\sigma 3$ value can be associated with the reduction in overlying material through the excavation process. The stress change become significantly different at phase 13, which is the extraction of the drive 1 m bellow the point stress point G, at this point there is the same behaviour exhibited in Figure 6.12, where there is mobilisation of both the $\sigma 3$ and 1, which results in a net mobilisation. This can be contributed to the the arching effect of the curved roof. The next phase represents the excavation in the level bellow the point by 13 m. There is little change in the stress field at this point other than slight mobilisation of $\sigma 1$ and slight demobilisation of $\sigma 3$. The next step is to stope the material between the drives created in phase 13 and 14, this results in the mobilisation of $\sigma 1$ and the demobilisation of $\sigma 3$, for a net demobilisation, This result can be explained by the increase in arching effect within the material above the excavation. Phase 16 represents the backfilling of the stope, there are extremely small mobilisations in $\sigma 1$ and $\sigma 3$, however these represent less than 0.4% changes.

Point stress point H, shows the same pathway as stress point G, until the end of phase 12, where the result is significantly more extreme. At phase 13, there is the mobilisation of $\sigma 3$ and 1, which results in a net mobilisation. This mobilisation is significant, as it results in the stress point reaching the failure criterion. This replicates the behaviour seen in Figure 6.12f. The excavation in phase 14 results in the further mobilisation of $\sigma 3$, but with the demobilisation of $\sigma 1$. The net result is no change, due to the point lying on the failure criterion. The excavation of the stope, represented by phase 15, results in the

mobilisation of $\sigma 1$, and the demobilisation of $\sigma 3$, due to the aching effect. The net result is no change as the stress point still lies on the failure criterion. The backfilling (phase 16) results in the demobilisation of $\sigma 1$ and mobilisation of $\sigma 3$, which again leads to no net change as the point remains on the failure criterion.

Points stress point I and stress point J, represent points which lie on either side of stope K0952a, both points show the same behaviour, thus will be explained together. The behaviour is the same as described for stress point G until the end of phase 12. The behaviour at phase 13 is that of mobilisation of both $\sigma 1$ and 3, with a net result of mobilisation. Point stress point I, has a higher amount of mobilisation due to in higher proximity to the excavation. There is further mobilisation of $\sigma 1$ and 3 in phase 14. The stress field changes significantly during the excavation of the stope K0952a. At this point there is demobilisation of $\sigma 1$, coupled with a significant mobilisation in $\sigma 3$, which results in the mobilisation of the stress points, reaching the failure criterion. This is same behaviour seen in the side wall of the drive excavation, with arching effect and a lack of conferment. This is however upscaled due to the comparative size of the excavation. Once again there is very little change in the stress field during the backfilling procedure, thus there is no net mobilisation or demobilisation.

Point stress point K, represents the corner of the the drive K0952a, drive and stope. Again the trend is the same as in point stress point G until phase 12. At phase 13, the extraction of the K0964, there is little to no stress field change. The major stress change occurs at phase 14, where there is the excavation of the K0952 drives. The stress change is such that there is mobilisation of $\sigma 1$ and demobilisation of $\sigma 3$, which is associated with the concentration of stresses within the corner. This is the same trend that has been discussed in the previous drive excavations. This stress trend is continued during the stoping of K0952a in phase 15, as the point still represents the corner of the excavation. This trend results in net mobilisation of the stress point. The backfilling procedure (phase 16) results in the a net demobilisation, however this is a small change.

The final stress point to be addressed is stress point L, which represents the floor of both the drive and stope K0952a. The behaviour is the same as exhibited in point stress point G, stress point H, and stress point I up until the end of phase 13. The largest stress change occurs in phase 14, where there is mobilisation of $\sigma 3$ and slight demobilisation of $\sigma 1$. This results in net mobilisation to the extent in which the point lies on the failure envelope. This mobilisation, much like the behaviour in floors mentioned previously can be contributed to the lack of confinement. The excavation of the stope (phase 15), results in slight mobilisation. This mobilisation is as a result of demobilisation in $\sigma 3$ coupled with mobilisation in $\sigma 1$. The final phase is the backfilling (phase 16) which results in little change, however the change that occurs can be associated with the loading due to the introduction of material filling the stope.

After addressing specific points around the excavation, it is important to look at the general picture surrounding the excavation. Figure 6.23, shows the relative shear stress around the excavation of the stope. The first observation is that this is an upscaled version of the relative shear stress which was observed around the drive excavations, this is logical as it is just an elongated geometry of the drive. The volume of the relative shear contours does not change significantly in the roof or floor but it changes significantly in the side walls. The zone which represents 0.90-1.00, aligns as expected with the zonation of predicted failure points as shown in Figure 6.24.

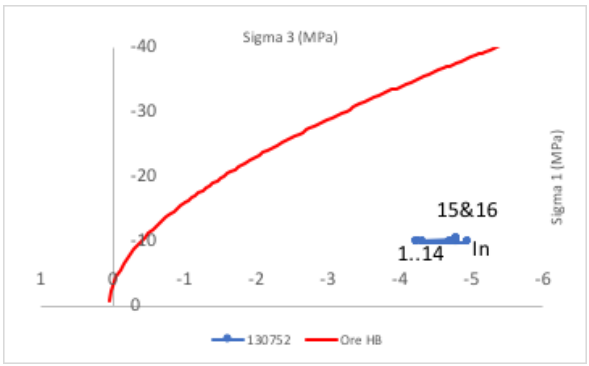

(a) Point stress point G

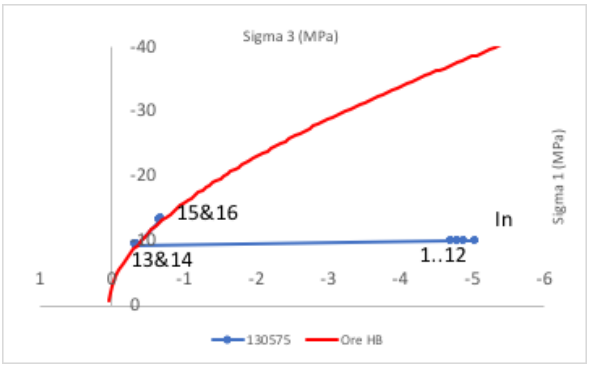

(b) Point stress point H

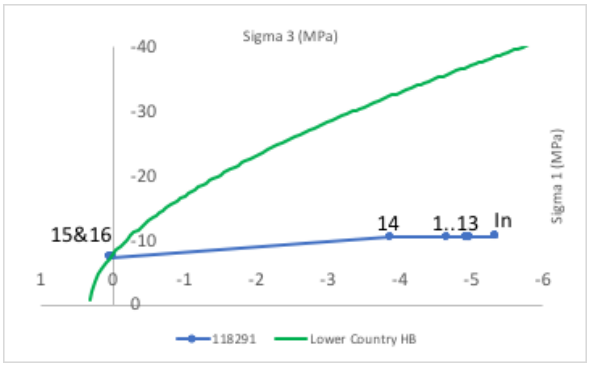

(c) Point stress point I

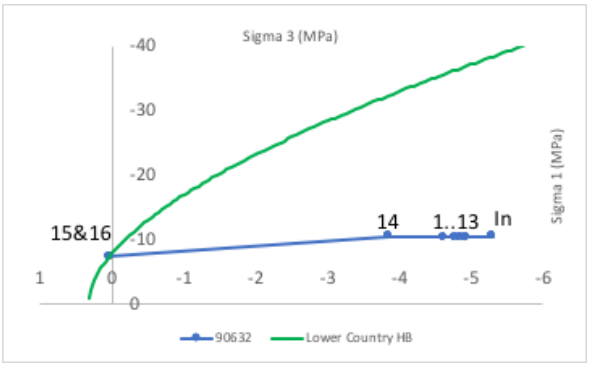

(d) Point stress point J

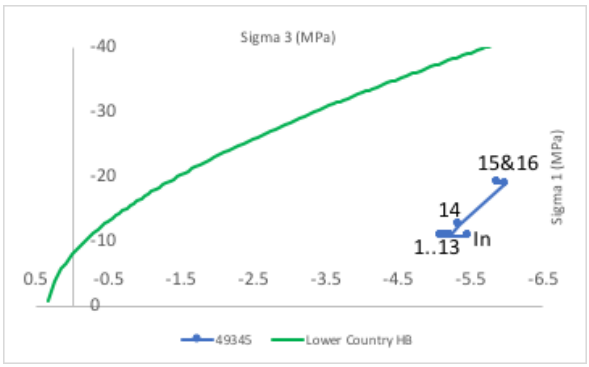

(e) Point stress point K

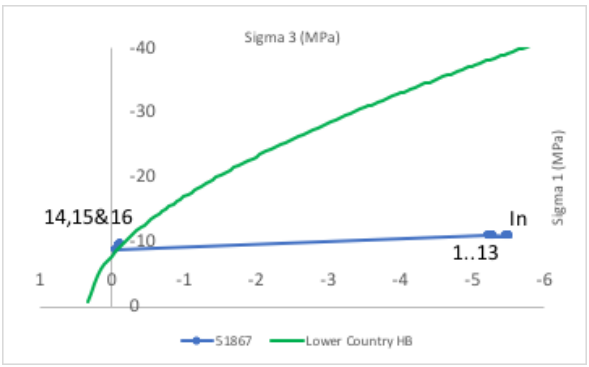

(f) Point stress point L

Figure 6.22: Shows the graphs for the 6 selected points around the excavation. Note axis are not orthonormal.

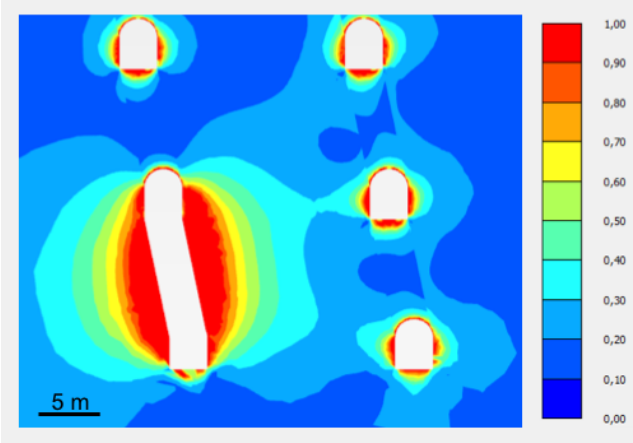

Figure 6.23: The relative shear stress around K0952 a at phase 15 (excavation).

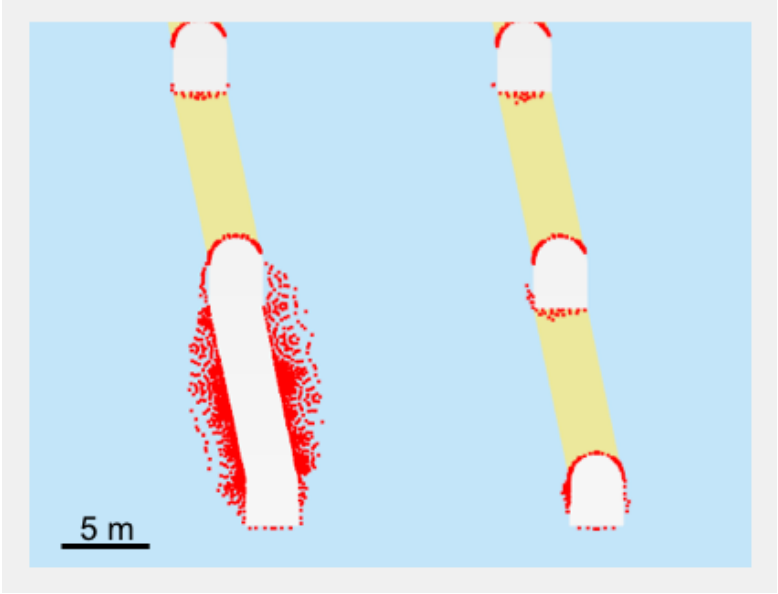

Figure 6.24: The predicted failure points around stope K0952 a at phase 15 (excavation).

The next step in the mining cycle is the backfilling of the stope, something which was eluded to in the discussion of the results from Figure 6.22. During the backfilling procedure, there is the addition of mass into the void. This mass will have an influence on the surrounding rock material, however this will be much of a much lower magnitude than an excavation. Backfill is not to redistribute the previously induced stresses, but to stabilise the walls by filling the void, as well as redistributing the induced stress caused by subsequent excavations.

The results discussed previously for the stress points shown in Figure 6.21, showed that there was very little change in the stress field during the back filling. The small change that was observed was as a result of the added mass of the backfill and settling of the stresses. The best method of confirmation of this result would be to look at the relative shear stress and compare it to the previous phase relative shear stress. The comparison of the relative shear stress for the stoped drive as shown in Figure 6.23, and the backfilled drive as shown in Figure 6.25, show identical relative shear patterns around the excavation. The only difference is the introduction of the backfilled material, which shows less than 10% relative shear stress. This suggest that backfill does not alter the stress field and behaves correctly.

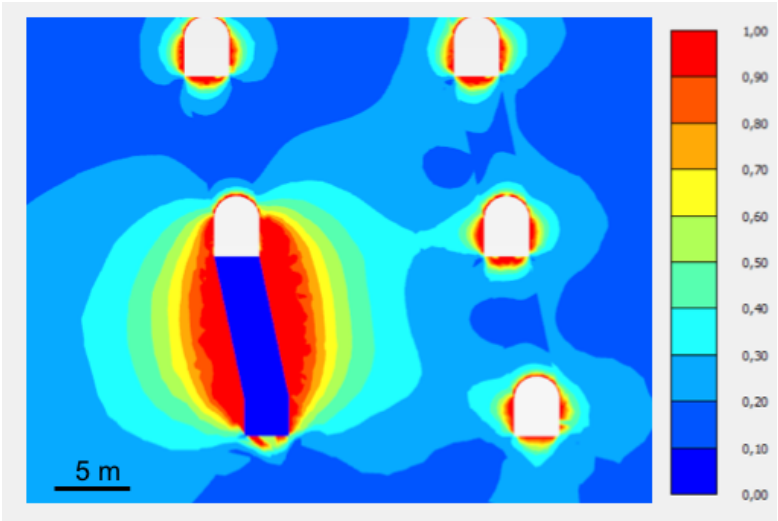

Figure 6.25: The relative shear stress around K0952 a at phase 16 (backfill).

The reason for backfilling of stopes is the supporting of a void by filling and the redistribution of subsequent extractions. Phase 17 is the proceeding phase to the backfilling of drive K0952a, which is the stoping of K0952b. The resulting stress field orientation is the same as was observed in the excavation of the stope K0952a, thus it would be superfluous to present this again. It is more useful to present the relative shear stress and predicted failure points in order to determine the proximity to failure.

Figure 6.26, shows the relative shear stress of the coupled excavation. The result of the two excavations is a hyperboloid geometry shape with the narrowest point halfway between the excavations. This suggest that there is an increase in the number of points close to failure which follow this pattern. Figure 6.27, does show this suggested behaviour.

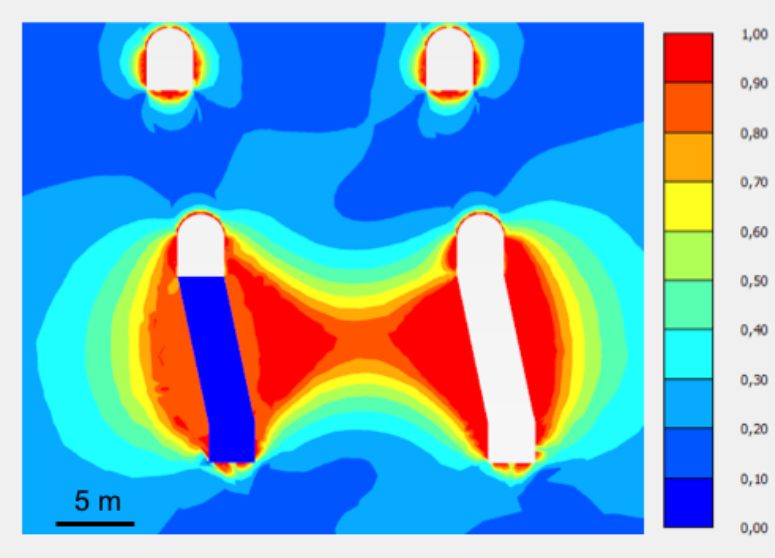

Figure 6.26: The relative shear stress for the K0952 level a at phase 17 (excavation).

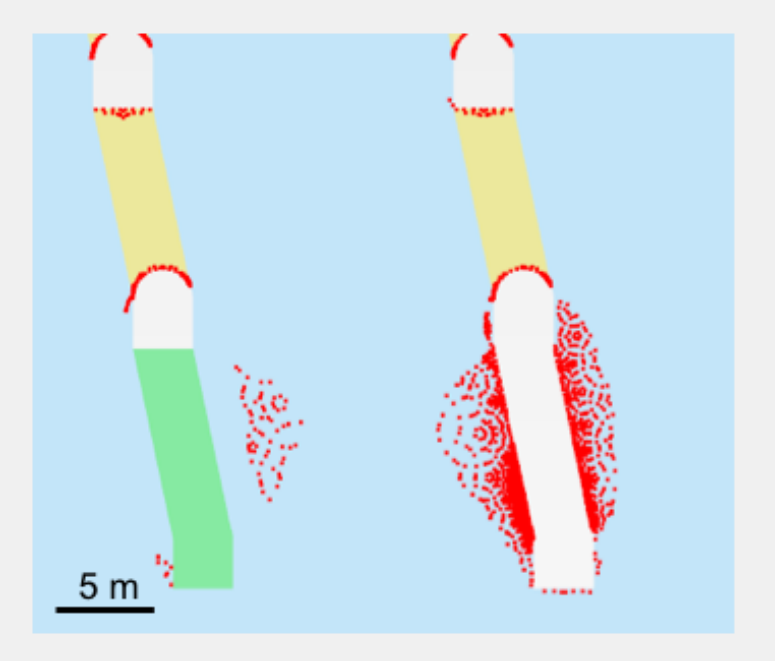

Figure 6.27: The predicted failure points for the K0952 level a at phase 17 (excavation).

The backfilling procedure that follows in phase 18, results in the same reaction discussed for phase 16, therefore it is superfluous to discuss this. The excavation of stope K0964a in phase 19, however shows the importance of backfilling. Figure 6.28, shows the stress field developed around the excavation. The key difference in the behaviour of the stress field is the stress behaviour within the backfilled material. The backfilled material is used to redistribute the stress field. There is a limited initial stress state in the backfill, therefore the extraction of the stope above results in a $\sigma 1$ orientation which would be expected by the arching effect. The $\sigma 3$ is orientated perpendicular to the excavation in the upper section of the backfill, which is related to the lack of confinement in the upper section of the backfill.

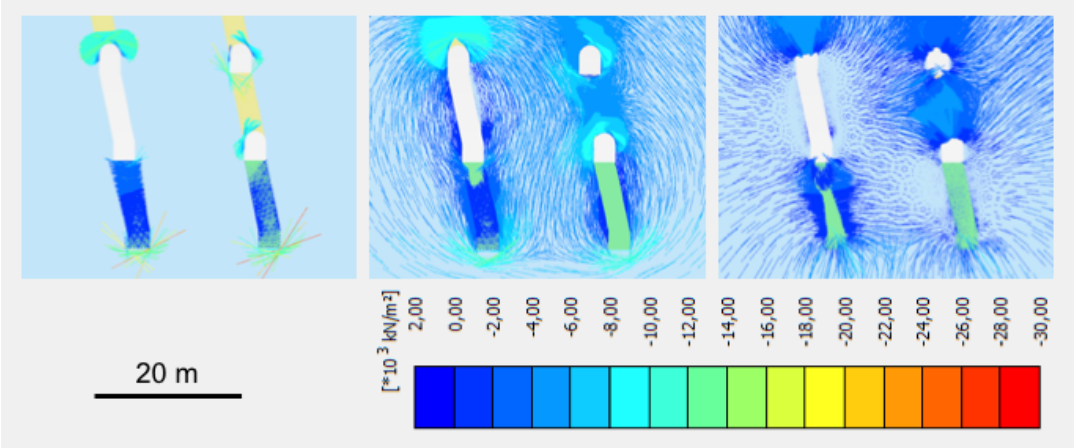

Figure 6.28: The stress field of the stope excavation of K0964 a. Left is $\sigma 1$, centre $\sigma 2$ and right is $\sigma 3$.

Despite the stress field generated within the back fill due to the arching effect, there is low risk of failure within this material, as shown by the relative shear stress in Figure 6.29. This shows the relatives shear stress as less than 0.30, which is an extremely low risk. An explanation for this behaviour could be that there is only limited stresses in the backfill when it is introduced and the induced stress only occur when the stope directly above is excavated.

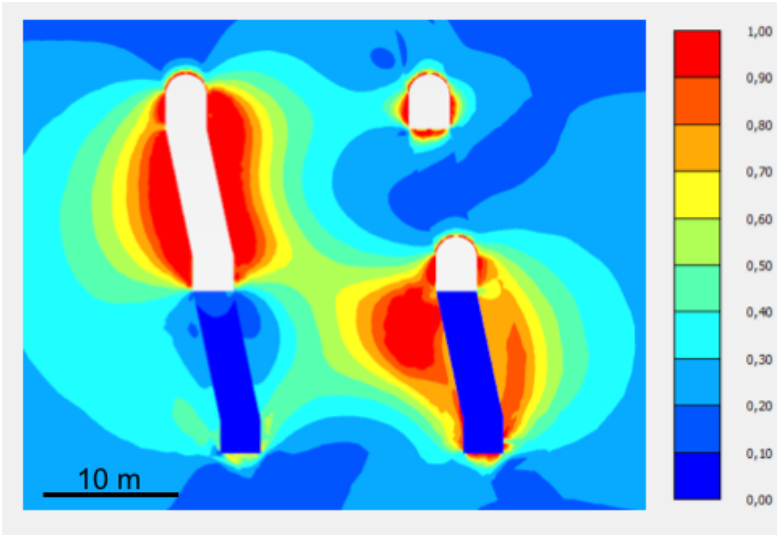

Figure 6.29: The relative shear stress for the K0952 and K0964 levels a at phase 19 (excavation).

A subsequent comment should be made about Figure 6.29, which is that the relative shear is reduced significantly around a previous excavation, when an excavation is carried out directly above it. This is evident when comparing Figure 6.29, 6.26, & 6.23, which clearly show the progression of relative shear through subsequent excavations.

This trend is continued throughout the model, as can be seen from the final stoping phase (phase 67), which is shown by Figure 6.30. This figure shows the relative shear stress being reduced through subsequent phases, with a final result of extremely localised zones of relatively high shear stress around the excavations that are left open.

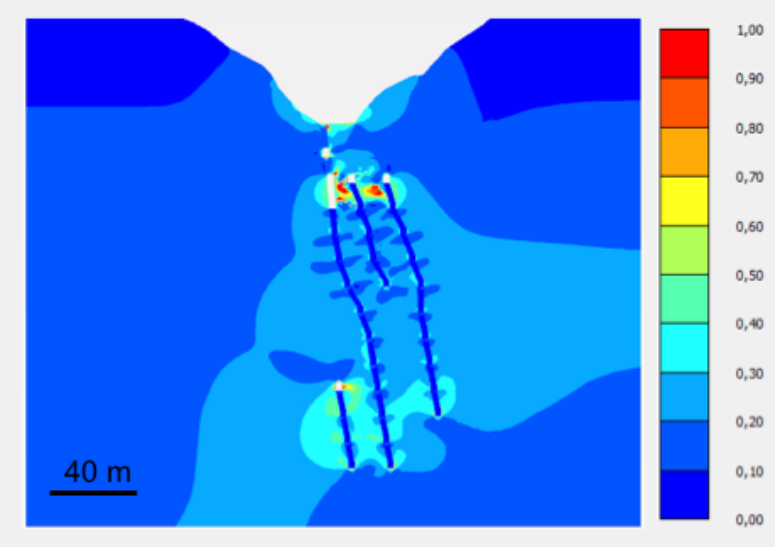

Figure 6.30: The relative shear stress for the full model at the final excavation (phase 67).

The final visualisation of the model is the total displacement of the underground excavation phases as shown in Figure 6.31. Note that the displacement effect was reset after the excavation of the open pit, in order to visualise the result for underground excavations. The results show that the displacements are higher in the footwall of the ore body, specifically where the highest angle of overhang occurs (K1012 and K1024).

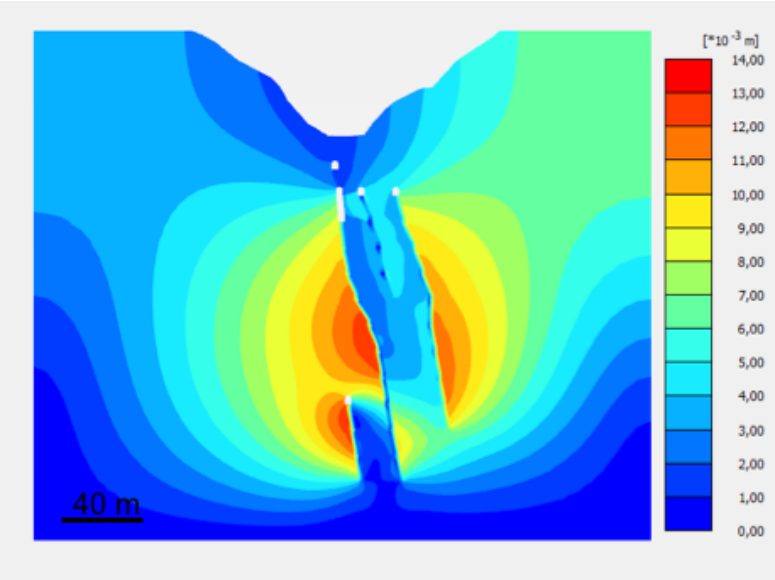

Figure 6.31: Total displacement result at phase 68.

6.6. Model Comparison

The overall goal of this research is to determine the most stable stoping order based on the requirements of the mine. This can be done through multiple different comparative approaches such as comparing results of the displacement, the area of high relative shear stress, the safety factor for the phases and the total model displacement. The difficulty comes when trying to generate an area for the high relative shear stress, as this cannot be directly output from the software. An alternative procedure would to evaluate the number of predicted failure points, as these represent a relative shear value of 1.00 which indicates instability. Combined with an analysis of the relative shear stress at specific phases to confirm the assumption that the greater the number of predicted failure points, the greater the region of high relative shear stress.

6.6.1. Model A vs Model B

As mentioned previously the objective of the comparison of model A and B, is to determine which rock properties present the worst case based on two end members. The worst case will then be used moving forward to determined the most stable stoping pattern. This subsection will look at comparing the total displacement, failure points and safety factor for the two models.

Displacement

It is possible to present the displacement resultants for the models, however this may be misleading, when comparing rock masses with different properties. As differing displacements will result from the same applied load, however it will be presented here to uphold the continuity within this report.

Figure 6.32, shows the total displacement for model A and model B. The models both show identical displacement patterns, as would be expected when comparing identical stoping order. However the magnitude of these displacements is significantly different. Model B shows lower displacements than that of model A throughout. This is backed up by model A having a maximum total displacement of 13.15 mm, compared to 11.22 mm for model B. However as stipulated previously this may be misleading, so it must be backed up with further justification (failure point and safety factor).

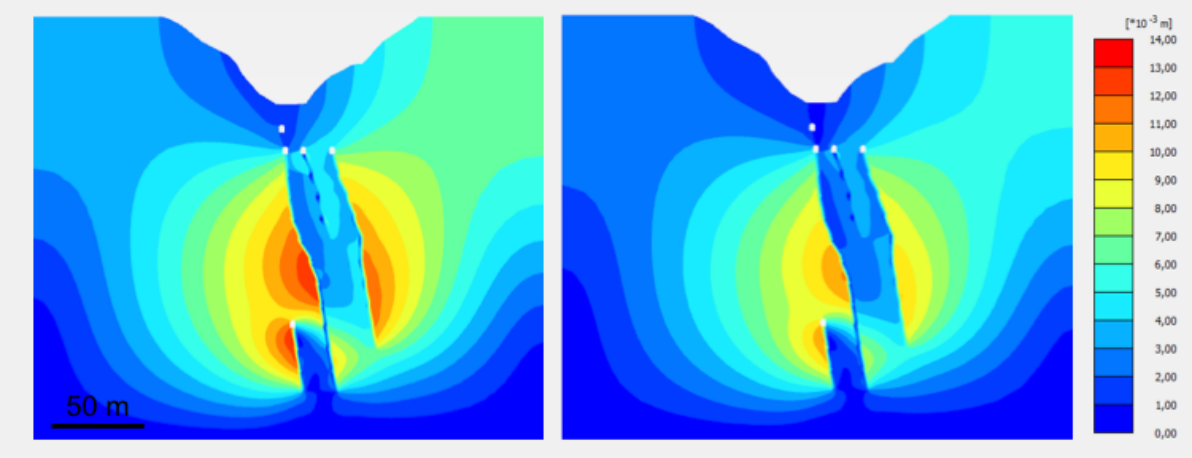

Figure 6.32: Comparison for the total phase displacement at the final phase. Left is model A and right is model B.

Failure Points

The analysis of predicted failure points is an excellent method for identifying which models are more stable. This is especially the case where two identical models exist with differing material properties, as is the case between model A and model B. The higher the number of predicted failure points gives

an indication of a higher probability of collapse. A caveat should be noted as mentioned previously, one failure point does not cause a collapse, so the concentration of failure points is more important to address.

When comparing the two models, it is possible to output a plot of the complete predicted failure history of the model. This can be seen in Figure 6.33, which shows that model A, exhibits a significantly higher number of predicted failure points. Both models, however indicate the same approximate predicted failure locations. This is to be expected as they have identical geometries and sequences, but different material properties. This however only presents part of the story as this is a step by step process, it is important to look at the evolution of the model over time (phases).

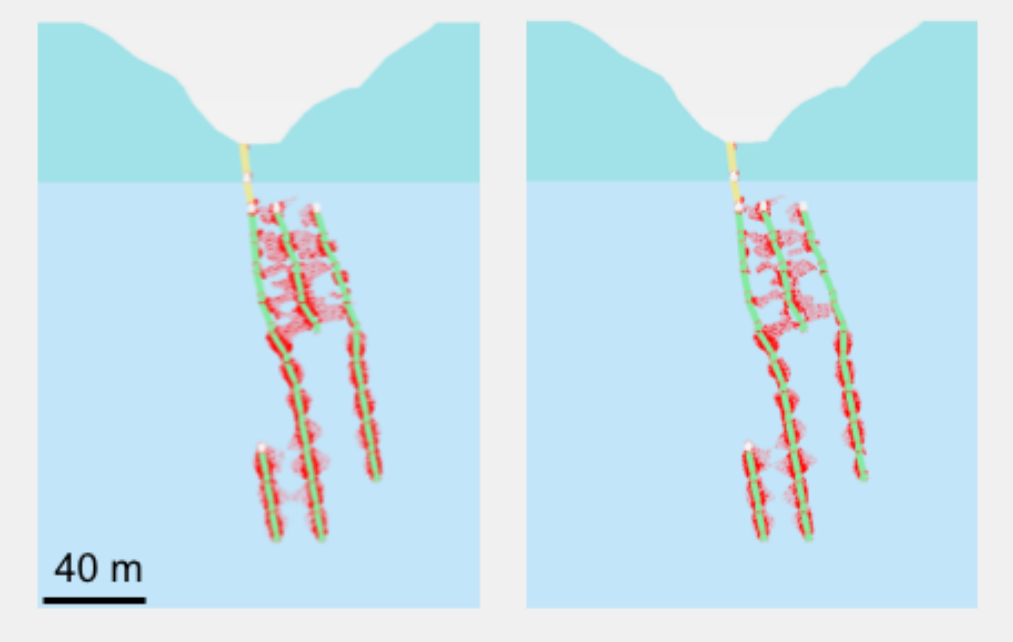

Figure 6.33: The output of failure point history for models A and B.

Figure 6.34, shows the cumulative predicted failure points evolving over time. The figure shows an increase over time which is expected. The graph shows that the majority of the predicted failure points occur within the stoping phase of the model, it also shows that backfilling causes little to no predicted failure points, which is to be expected. The number of predicted failure points does not show any real trend other than increasing over time. The models shall be dealt with separately here as they do not both show the same trends.

Model A, the first major inflection occurs at phase 15, which is attributed to the initiation of stoping, followed by no increase during the backfilling. This pattern is repeated 6 times, which is attributed to similar excavations carried out on the bottom three stoping levels. Phase 29 does not show the same inflection, however this can be attributed to being further from the previous excavation than the other phases. A new trend begins at phase 31, where there is a larger increase in predicted failure points as a result of two excavations being in closer proximity on a single level, this continues until phase 47. Phase 49 represents a third excavation on the K1048 level. This results in a smaller increase in the number of predicted failure points, due to the localised region containing points which are already predicted to be at failure. The jump in predicted failure points from this phase onward is larger when excavating the second of the three excavation on the level (phase 53 ,59, and 65), this may be as a result of the proximity of the first excavation on that level.

Model B, shows a different predicted failure point pattern than A, due to the different material properties. During the drive development there are almost the same number of predicted failure points (upto phase 14). At the beginning of the stoping operation, the pattern of predicted failure points is different. During

the first stope excavation there is less of an increase in predicted failure points than in model A. The first major change is not until phase 19, where there is only a small increase in predicted failure points. At phase 21 there is a large increase in the predicted failure points, which shows the materials are behaving differently, and can be associated with the proximity of the excavations. There then appears to be a similar increase as shown in phase 21 for each stope, except for phase 23 and phase 29, which show a smaller increase in the predicted failure points. This continues until phase 49, where the pattern is identical to that described in model A, however with a lower magnitude.

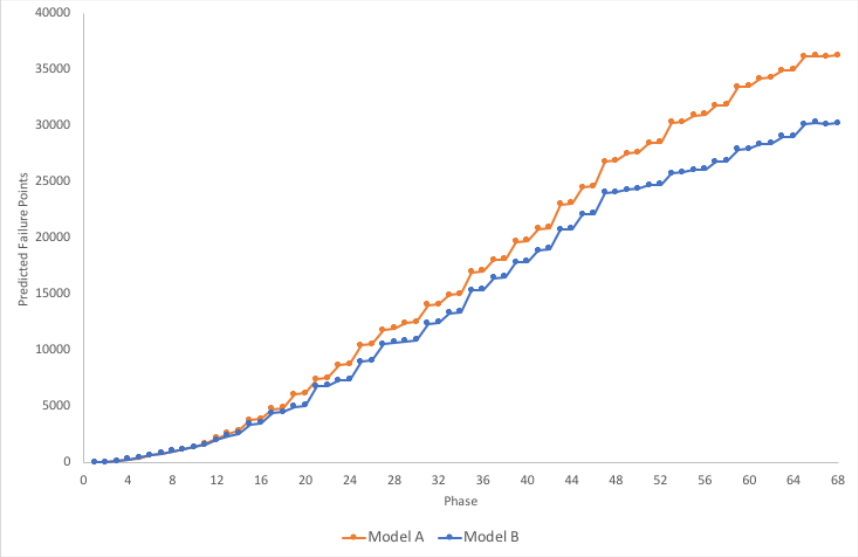

Figure 6.34: The cumulative predicted failure points for each phase for model A and B.

To confirm that model B is better than model A, the relative shear stress can be compared to see the points on the failure envelope and the points that are near to failure envelope. It is impractical to present all phases within this thesis, therefore 4 phases were selected in order to compare the behaviour of the predicted failure points to the volume of material at or near to the failure envelope. The phases selected were phase 15, 19, 23, and 53 as shown in Figure 6.35, based on the analysis of Figure 6.34.

Phase 15, is the first stoping phase, and the first location where a noticeable difference is present, as can be seen in Figure 6.34, this suggests that model A is more unstable. When comparing Figure 6.35a & Figure 6.35b, it can be observed that the volume of relative shear stress is higher for model A, however more significantly it can be seen that the area of relative shear stress above 0.95 is higher. These two observations suggest that model A is more unstable at this point.

Phase 19, was again selected as there was a significant difference between the two models, in the data shown in Figure 6.34. Once again comparing the two models as can be seen in Figure 6.35c & Figure 6.35d, it can be observed that model A, has a significantly higher proportion of material with a relative shear stress greater than 0.95.

Phase 21, was selected as it showed the opposite trend where there is a larger increase in the predicted failure points in model B, as can be seen in Figure 6.34. The figure shows a larger zone of relative shear stress for model A, which is observed in Figure 6.35. The increase in phase 21 can only be understood when looking at phase 19 (Figure 6.35d) and comparing it to phase 21 (Figure 6.35f). The area of relative shear stress greater than 0.95 has increased significantly in comparison to the increase observed between Figure 6.35c and Figure 6.35e.

The final phase that will be analysed is phase 53, as it is the phase that stands out when looking through the failure point history. In both model A and B, there is a rise in both curves as seen in Figure 6.34, however the increase is larger in model A. To confirm this the comparison can be made by addressing Figure 6.35g & Figure 6.35h, which shows there is a larger volume of material with a relative shear stress greater than 0.95 in model A.

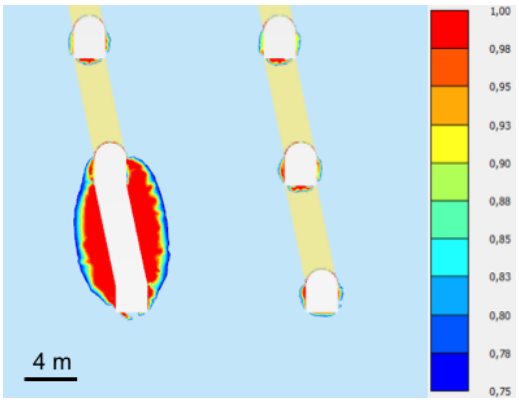

(a) Model A phase 15

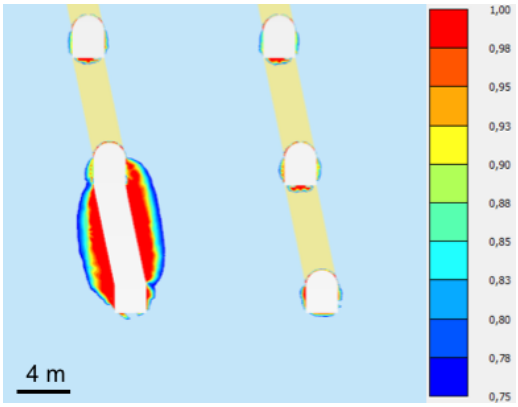

(b) Model B phase 15

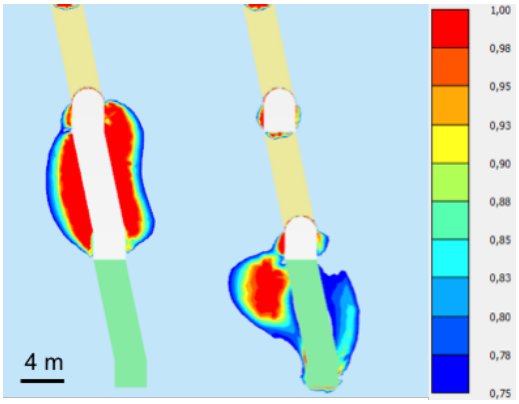

(c) Model A phase 19

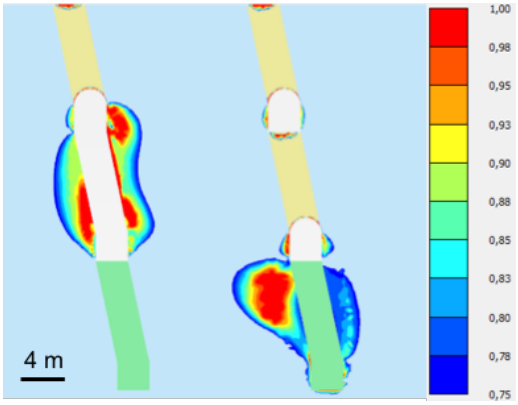

(d) Model B phase 19

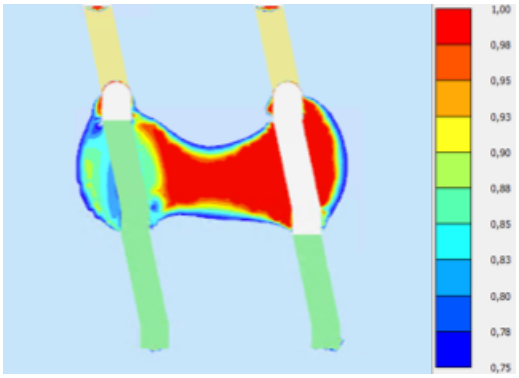

(e) Model A phase 21

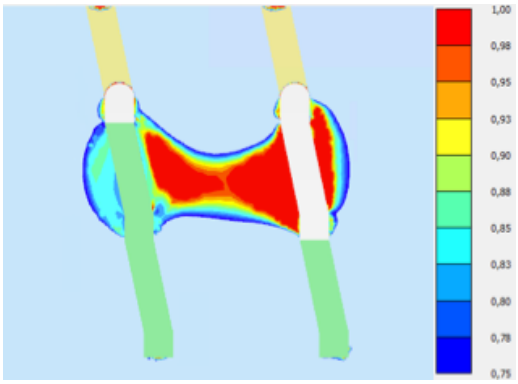

(f) Model B phase 21

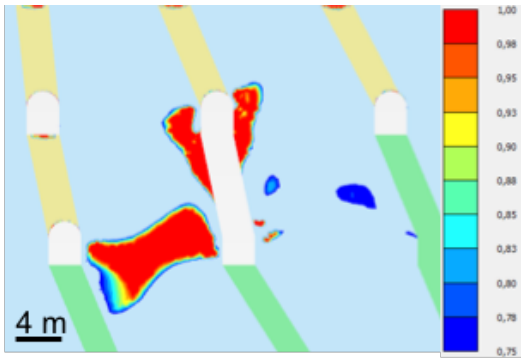

(g) Model A phase 53

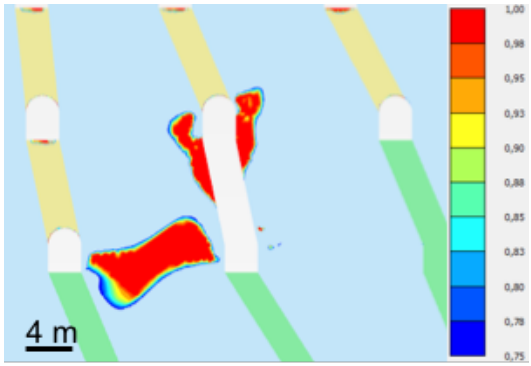

(h) Model B phase 53

Figure 6.35: The relative shear stress for selected phases, in order to compare model A against model B.

Safety Factor

The final piece of model comparison will be to compare the safety factor for both models, as this gives a representative value of safety for each phase. This will only be carried out for phases which contain excavations, and not for backfilling phases. This is for two reasons, firstly calculations took around 12 h per phase, and secondly backfilling phases should not reduce the safety factor, as the total excavated volume is reduced.

It should further be noted that the safety factor considered within this thesis is the overall safety factor rather than the local safety factor. This means that local failure mechanisms will not be addressed within this thesis, due to the time constraints. As a result the localised failure mechanisms may result in lower safety factors, however it is important to note that the model within this project will be conducted in the absence of excavation support (shotcrete and rock bolts), thus generating a lower localised safety factor.

The safety factor data is presented in Figure 6.36 for model A and B. The initial observation from the data is that model B, performs better in terms of safety factor for almost all phases.

The phase can be split into two sets, phase 1 to phase 14 and phase 15 to phase 67, which represent the drive excavations and stoping respectively. The trend for both models for the drive excavations is for the safety factor to decrease as the depth and excavated volume increase. This makes logical sense as the larger the excavated volume, the larger the region in which a failure mechanism can form around.

The behaviour becomes more difficult to describe for the stoping phase of the graph, as there is the coupled excavation effect and the reduction in the excavated volume due to backfilling. In terms of the safety factor for stoping the general trend is that the safety factor increases as the phases progress, however it is not always the case that the safety factor increases. The safety factor falls for phase 15 and 17, which is two excavations on the same level, the safety factor then increases in phase 19, which is stoping on the next level up. Once again stoping on the same level leads to a drop as seen in phase 21. This trend is then repeated in phase 23 to phase 27, which represent 3 stopes on the same level. The trend is not continued on the next level, where excavations are reduced back to two per level, however they are spaced further apart which might provide an explanation, as to why the trend is not repeated. The local fluctuation for the remaining section, appear to be as a result of the geometry or proximity of previous excavations, however there is no obvious trend apart from the increase in safety factor as the working depth is reduced. It should be noted that for model A there is an outlying data point for phase 55, which suggests a safety factor greater than expected. This data point has been included as it does not alter the final result.

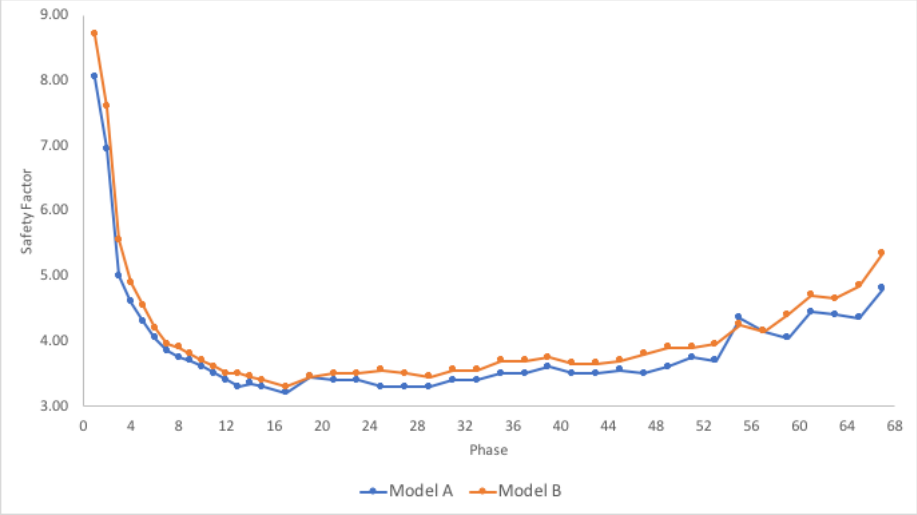

Figure 6.36: The progressive safety factor for model A and model B.

The statistics from the safety factor data, shows that model B preforms better, with a minimum safety factor of 3.30 compared to 3.20. Further the average for model B is 4.15 and model A is 3.95. These factors of safety suggest that the mine is globally stable, however there is still uncertainty within the model as it is a estimation based on limited input information.

Conclusion

The concluding remarks of this model comparison, is that Model B preforms better in all the categories. Firstly the displacements are lower in Model B, however as stated previously the caveat is that the two models have different material properties, thus behave differently. Comparing the predicted failure point history, it is proven that model B, exhibits less predicted failure points. This predicted failure point history coupled with the volume of material with a relative shear above 0.75, suggested that model B once again preformed better. The final piece of evidence that model B preformed better was the safety factor, where model B had a greater or equal safety factor for all bar one phase.

The objective of this comparison was to determine which of the country rock end members preformed worse for identical extraction sequences. The results confirm that model A, which was composed of the country rock tested perpendicular to foliation, performed worse. This means that model A proceeds to the next stage. The country rock properties for model C and D will also be generated from the country rock material tested perpendicular to foliation.

6.6.2. Model A vs Model C

The comparison of model A and C is not as simple as the previous case, this is due to the models having different stoping orders. The objective here is also different, as the previous comparison was to determine the worst case rock properties, something which is outwith the control of the mine. Where as here the aim is to progress with the best case in terms of stability, which is something that the mine has direct control over. This subsection will replicate the structure of the previous subsection in terms of comparing the displacement, predicted failure point progression, and the safety factor.

Displacements

As models A and C both have the same material properties it becomes valid to look at displacements as the material response is identical. This means that higher phase displacement could indicate higher localised stress imbalance, which in turn may suggest less stability.

The total displacement resultant is shown in Figure 6.37 for model A and C. The first observation to be made is that model A has a significantly larger region with higher resultant displacements, this is especially prevalent around levels K1000 to K1024, where there is the largest overhang. The maximum displacement value for model A is 13.15 mm where as for model C it is 13.08 mm, which is an increase of 0.5%. The key difference is caused by the stoping of the upper region first, as it breaks the pathway, meaning that the displacements from the base are not carried to the surface.

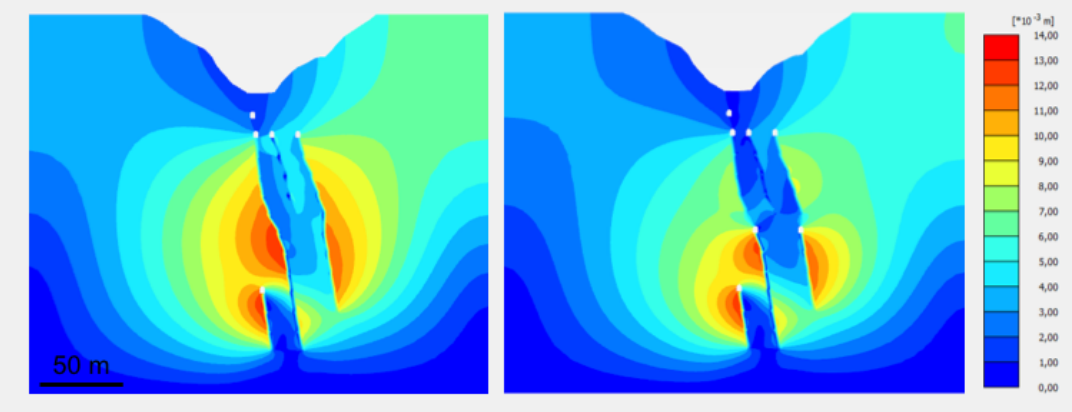

Figure 6.37: Total displacements at final phase. Left is model A, right is model C.

This resultant displacement map is the combined result of the phase displacements. It is useful to look at the phase displacement in this case as the material properties are identical therefore, higher displacements would be as a result of higher force unbalances.

The models have alternative stoping orders, and as a result the stoping excavations happen at alternative times. As a result of the alternative order, stoping occurs from phase 8 to 31 for model C. The displacements during excavation phases are significantly larger for model C between phase 8 to 14 as they represent stope extractions. The trend then switches and the excavations between phase 15 and 31 cause larger displacements in model A, as a result of being deeper. Between phase 32 and 38, the displacements are lower in model C as drive excavations are being produced. The displacements are higher in model A for phase 39 and 41 due to the coupled effect of continuous stoping. However this is reversed at phase 43 where the coupled effect and the depth of excavations become the key factor in terms of displacement. This trend continues until the end except for phase 49, which is an outlier.

The results show several key observations, the displacements in the lower section of the deposit are much higher than those in the upper, as a result of the increased in stresses. The next observation is that there is a coupled effect which leads on average to an increase in displacements, however if the depth decreases significantly then there is the possibility of reduction. The interesting statistics to look at for this case would be max phase displacement, which is for model C at 7.76 mm compared with 7.61 mm for model A. Which suggests that model A performs better, however when looking at the average data model A performs worse with an average of 2.61 mm compared to 2.42 mm.

The displacements as a result of these excavations are small, and do not suggest result that could be measured accurately in the field. Further the suggestion based on the data is that model C performs better, however more evidence is required to back this up.

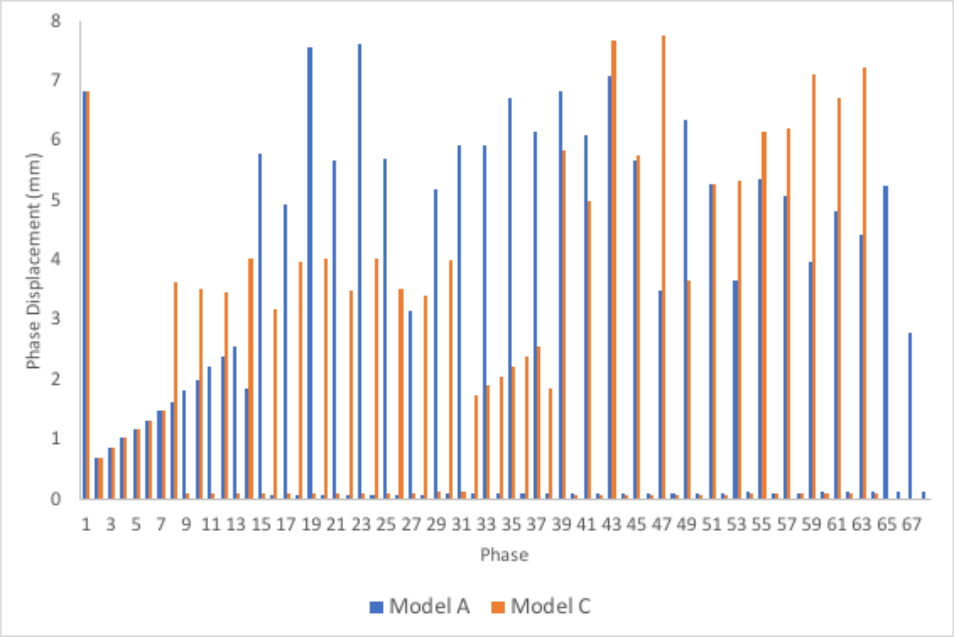

Figure 6.38: Phase displacements for excavation phases, model A vs model C.

Failure Points

The initial analysis of the predicted failure point history for model A and model C as shown in Figure 6.39, show starkly different predicted failure point patterns. Model A shows much more prevalent predicted failure points in the upper half of the deposit, where as model C shows more points in the lower half of the deposit, which would make sense based on the observations made about the displacement patterns. This is as a direct result of the stoping order being different, as model C stopes the lower section after the upper section. This leads to a reduction in the total number of predicted failure points from 36,281 to 27,405.

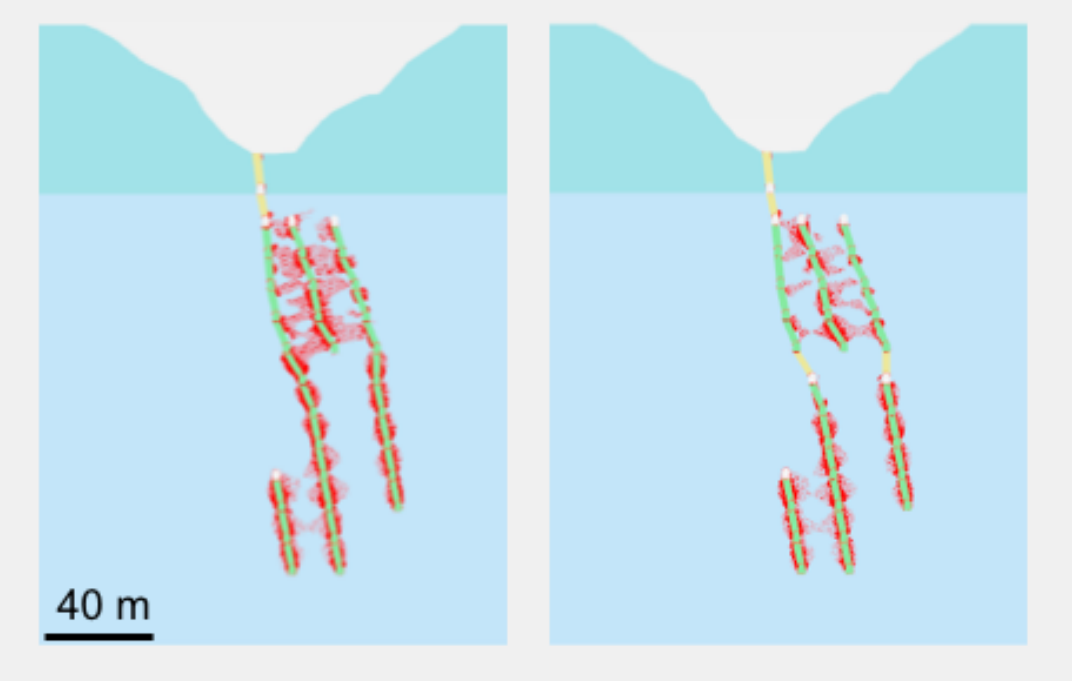

Figure 6.39: The output of the predicted failure point history for models A and C.

Before moving into the phase by phase analysis of the model, it is important to remember the description of both models and remember that model C has a sill pillar, comprised of the stopes K1024a&d. As a result of the sill pillar being left there is a reduction in the number of phases from 68 to 64.

The logic behind model A's cumulative predicted failure point pathway has been described above hence it would be redundant to describe this. Model C has an identical pathway to model A, until phase 8 where they deviate, as model C then progresses into a stoping pattern, where the number of predicted failure points increases. There is a larger increases in predicted failure points at phase 10 due to the proximity of the two excavations K1036 c&d. This trend then continues till phase 32, with very minor deviations except for phase 28. The larger increase at phase 28 can be associated with the proximity of excavations K1084 c&d. The generation of drives between phase 33 and 38 continues the trend of increasing in predicted failure points. At phase 39, the start of the second phase of stoping the increase in predicted failure points is larger than was previously observed. This pattern is then repeated until stoping is complete at phase 67, and can be associated with the increased depth.

Before moving forward it is important to compare like for like phases within the model, to determine the impact of the revised extraction sequence on individual excavations, in order to determine specific phases which lead to this change. Figure 6.41 shows that the stoping in the section below the sill pillar in model C predicts very similar predicted failure points, as identified in Figure 6.39. There is however a significant reduction in the number of predicted failure points in model C for the section above the sill pillar. The significant difference is the absence of the of phase 41 and 43 extractions and that the excavation in model A above the sill pillar result in more predicted failure points per excavation than model C. This increase can be suggested to be a result of the stresses being brought to surface as the excavations progress upwards.

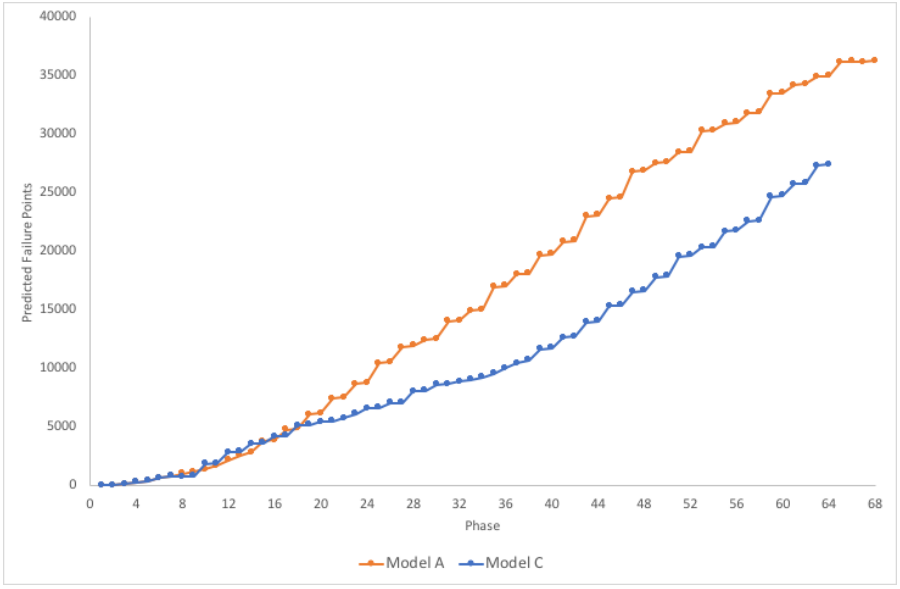

Figure 6.40: The cumulative predicted failure points for each phase for model A and C.

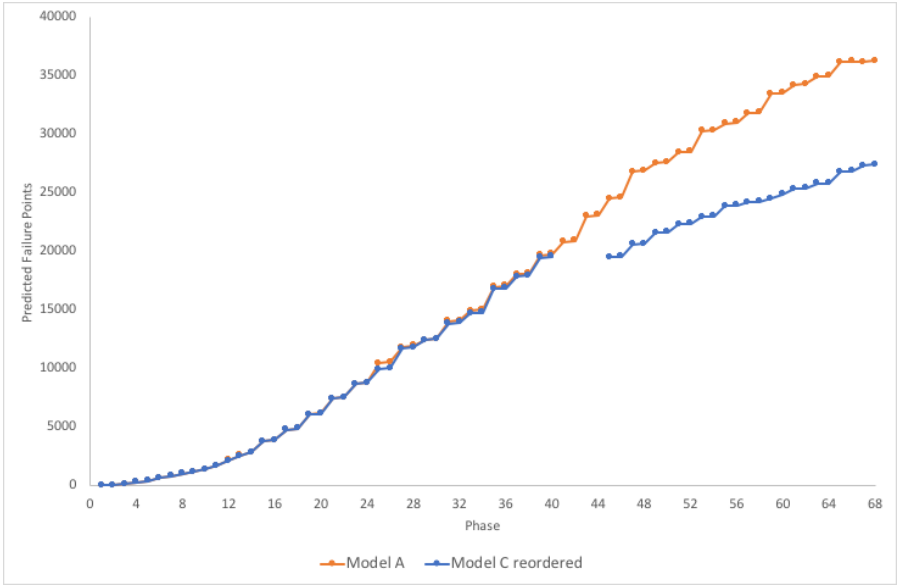

Figure 6.41: The matched cumulative predicted failure points for each phase for model A and C.

Safety Factor

The results thus far in the comparison of model A and C suggest that model C preforms better. Before this can be definitively proven, the safety factor analysis should be conducted.

It becomes redundant to re-evaluate the behaviour of the safety factor for model A, as it was carried out in the previous section, however it will be shown in Figure 6.42 for comparative purposes. The trend shown in model C for the first 7 phases is identical to that of model A. The safety factor is lower in phase 8, as it represents the excavation of a stope. From phase 10 onwards the general safety factor increases in model C, due to the decreasing of depth until phase 26. Phase 28, 30, and 32 represent the top level stope excavation, which is in close proximity to the weaker upper country rock, which could explain the decrease in safety factor. Phase 33 to phase 38 in model C represents the development of drives in the lower part of the deposit, which is an explanation for the reduction in safety factor. Phase 39, the safety factor once again drops, this is the first stoping phase at the base of the deposit. The value stays the same at phase 41, and then progressively increases to the final phase value due to the reduction in depth.

The comparison of the two models can be done through addressing two things, the minimum safety factor and the average safety factor. For both of these statistics, model C preforms better with a minimum safety factor of 3.50 compared to 3.20, and an average safety factor of 4.25 compared to 3.95. The only outlier point is phase 55 of model A, however this was still included as it does not have an effect on the overall result.

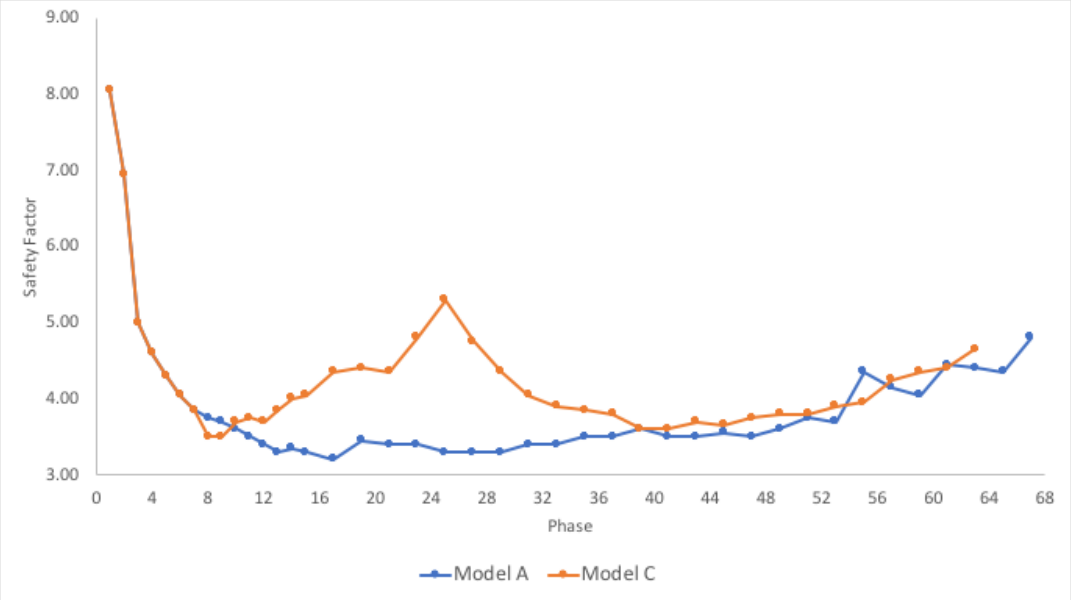

Figure 6.42: The progressive safety factor for model A and model C.

Conclusion

The result is apparent that model C performs better than model A, based on the analysis of the displacements, predicted failure points and safety factor. The logical reasoning behind this is that model C offers more support due to the introduction of the sill pillar. However, it is essential to check if the introduction of the sill pillar was the only reason for the increased stability or whether the alternative stoping order is a key factor. Therefore a comparison must be made with model D, in order to check whether the original stoping order with the introduction of a sill pillar is more stable than that of model C.

6.6.3. Model C vs Model D

As stated in conclusion to the previous subsection it is important to determine if the result of the increased stability is due to the introduction of the sill pillar only or if it was partially as a result of the new stoping order. It becomes essential to test this, hence the introduction of model D, which combines the stoping order of model A with the introduction of a sill pillar in a the same location as model C.

Displacements

The comparison of the resulting total displacements for model C and D, show that model C has a higher maximum total displacement of 13.08 mm, compared with the 12.89 mm seen in model D. This difference is extremely small less than 1.5 %. The stoping patterns are slightly different, with model C showing larger displacements in the lower half of the deposit when compared with model D, and model D showing larger displacements in the upper half of the deposit when compared to model C. This is as a result of the different stoping orders, where model C stopes the lower section second and model D stopes the upper section second.

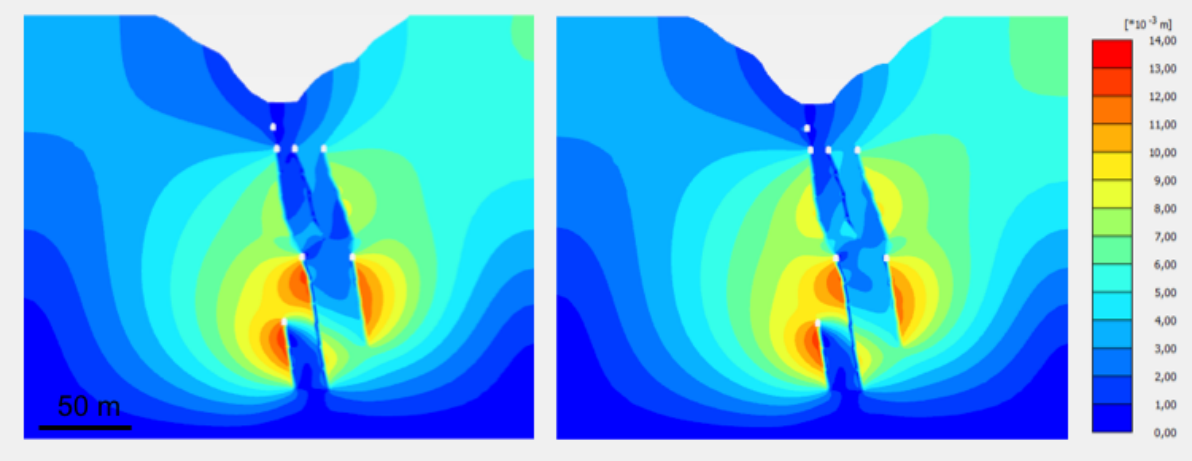

Figure 6.43: Total displacements at final phase. Left is model C, right is model D.

The splitting of the data into the phase displacements yields the same results as the the comparison between model A and C up until phase 41, as model D is identical to model A until this point. The section of interest is then from phase 41 onward, within this section model D preforms better than model C, with lower displacements for every phase other than phase 49. However like the previous comparison model D does perform better in terms of equivalent phase displacements for the upper part of the deposit.

Using only visual inspection of the graphs, it is difficult to distinguish which model preforms better. Therefore an analysis of the data must be carried out. The results show that model C has a higher maximum phase displacement of 7.76 mm compared to 7.61 mm for model D. However the average phase displacement is lower in model C with a value of 2.42 mm compared to 2.50 mm in model D. This suggest that model C preforms better on average, but the peak displacement could be an indicator of worse basal stability.

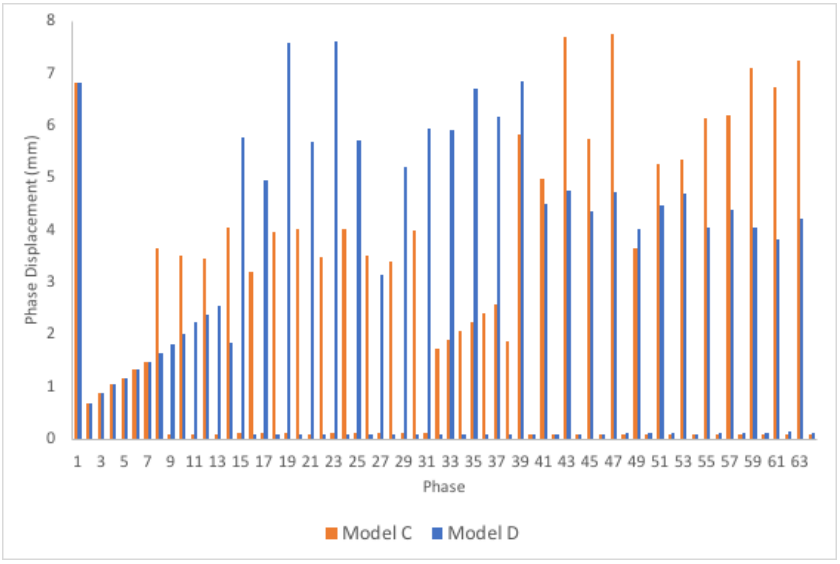

Figure 6.44: Phase displacements for excavation phases, model C vs model D

Predicted Failure

The result of the complete predicted failure history mimics that of the results of the comparison between model A and C, where model C shows more predicted failure points in the lower section. Overall model D has over 3000 more predicted failure points than model C, with the majority of these taking place in

the immediate vicinity of the sill pillar. This suggests that model C is more stable, however it is essential to also look at the phase data to understand this.

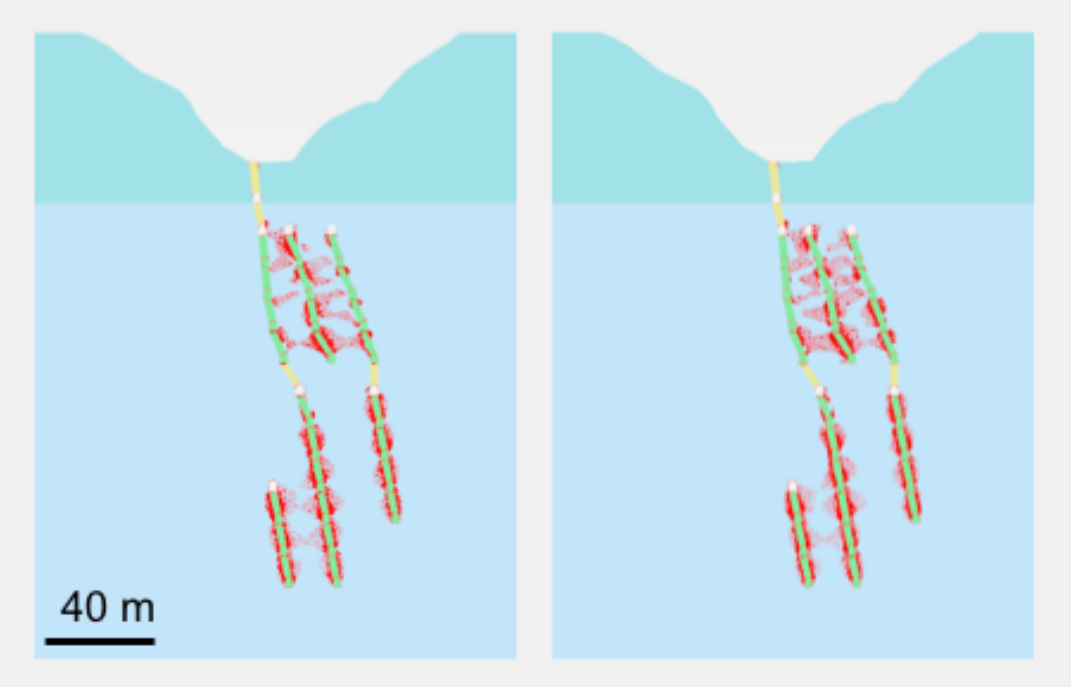

Figure 6.45: The output of failure point history for models C and D.

The next step is describe the predicted failure point evolution for model D from phase 41 onward, as it is identical to model A until this point. Model D shows an inclination in the curve of predicted failure points at phase 43, which can be associated with the proximity of stopes K1036c&d. The number of predicted failure points appears to continue to grow on the excavation phases until completion, with minor variation in the number of predicted failure points.

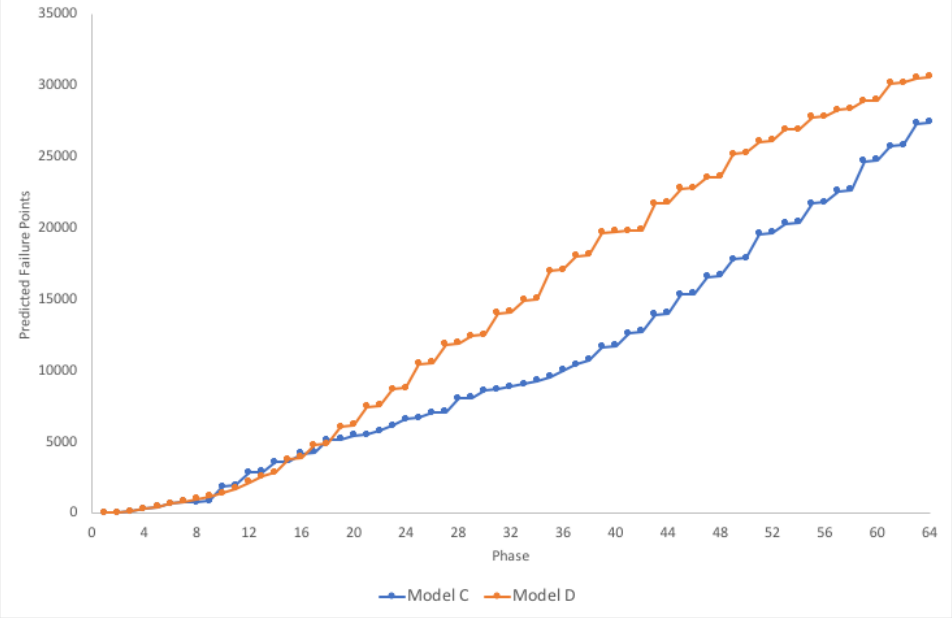

Figure 6.46: The cumulative predicted failure points for each phase for model C and D.

The final step here in the predicted failure point analysis is to compare like for like excavation, in order to determine any distinguishing factors. The progression suggests as was apparent in Figure 6.45, that

model C preforms comparably in terms of predicted failure points in the lower part of the deposit. It is not until phase 43 where there is a difference. The final result is that model C has less predicted failure points in the upper part of the deposit as can be seen from the curve from phase 43 onward and as a result it generates less predicted failure points.

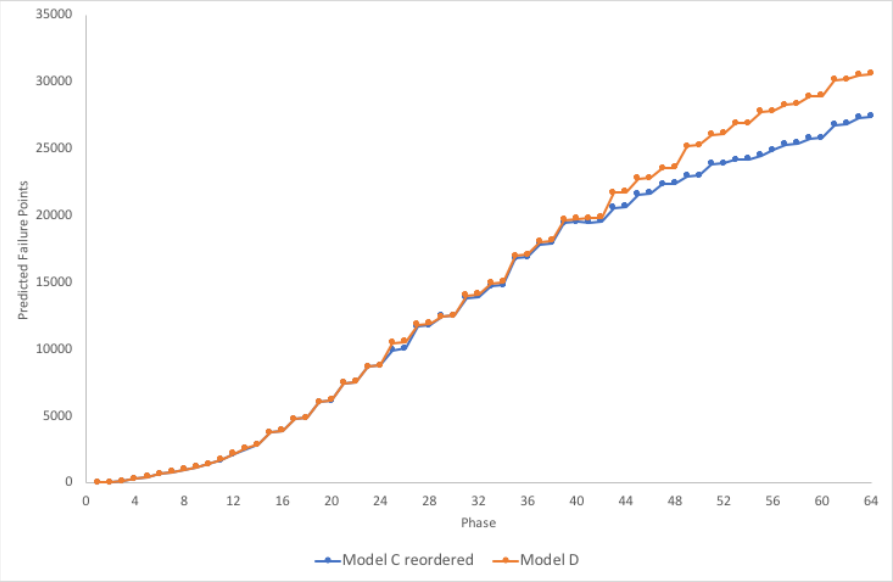

Figure 6.47: The matched cumulative predicted failure points for each phase for model C and D.

Safety Factor

The final factor to consider is the comparison for safety factor between model C and D as can be seen in Figure 6.48. The results in model D is identical to that of model A up until phase 41, thus the explanation to this point can be seen in the previous subsection. At phase 41 in model D, the overall trend until completion is positive, due to the reduction in the depth. There are however outliers in this trend, which are phases 51 and 55, which have higher safety factors than the other points. These values may be higher as result of being further from other excavations.

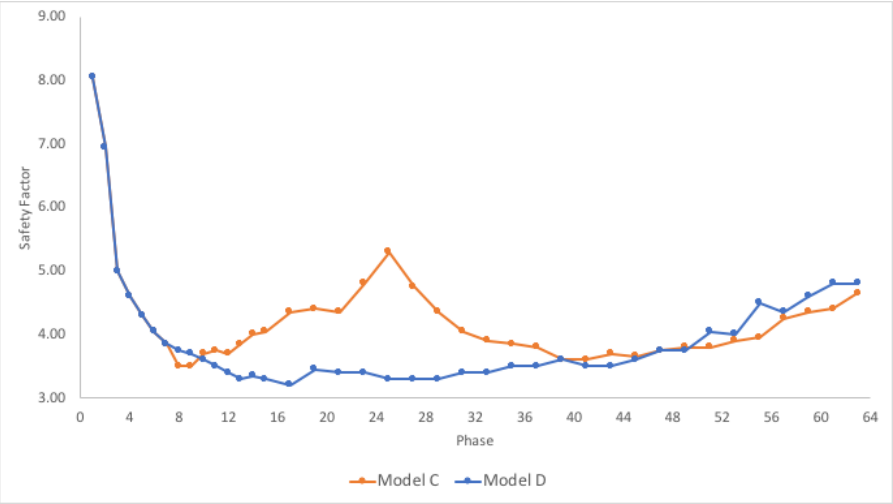

Figure 6.48: The progressive safety factor for model A and model C.

The next step is to address the statically data, which firstly shows that adding a sill pillar to model A to produce model D, does not increase the minimum safety factor as this happens at a phase 21, which

is before the pillar. Therefore model C preforms better in terms of minimum safety factor with a value of 3.50 compared to model 3.20. The average again shows that model C is better with an average of 4.25, compared to 3.95. It should be noted that the average for model D is an improvement over model A.

Conclusion

The models C & D are the final comparison that will be conducted within this thesis. Firstly the displacements provided an interesting insight due to the different displacement profiles, with model C having higher displacements at depth, where as model D had them in the upper part of the deposit. The results of the average maximum phase displacement was that model C preformed marginally better.

Secondly was the comparison of predicted failure points. The first observation was that model C had more predicted failure points at depth, where as model D had them in the upper region, which matches the observation in the displacement profiles. The final result was that model D had more predicted failure points.

Finally the result for the safety factor confirmed that model C was the best option due to having a higher minimum safety factor and a higher average safety factor for excavation phases.

The result that model C is the most stable case addressed is for a number of reason. The first reason is that the first excavation occurs at shallower depth than model A or D. This means that the principal stresses will be higher, therefore difference between σ_1 and σ_3 would be further from the failure criterion, as σ_1 does not change much in the region of the excavation. The second reason is that the overlying mass is reduced in model C, before excavating the lower levels, which leads to a reduction in vertical load on the lower excavations. Thirdly model C has less open volume in which failures can occur around, when the first stope is excavated, this means that the model has less of an ability to combine failure points to generate a complete failure. Forth is the number of excavations combined in a single continuous sequence is reduced as model C splits the deposit into top and bottom. This is due to there being increased relative shear around the excavation which is continued on the next excavation. The relative shear here is for the most part related to reduction in σ_3, due to the lack of confinement. The final reason is the introduction of the sill pillar, however this is not the major factor, as model C still performs better than model D.

The final comment to be made regarding that stability of the different scenarios is that the minimum global safety factor is greater than 3.2. In theory a safety factor of greater than 1.0 means that the excavation is considered stable, however if the rock strength was reduced it would then become unstable. The results suggest that a significant reduction in rock strength can occur before global failure occurs. It should however be noted that this is a much simplified case, and in reality the mine contains discontinuities and units which could not be modelled and would reduce the rock mass strength. Further the addition of ground water may lead to a reduction in the rock strength as well as changes in the effect stress at depth. The localised failures were not addressed within this thesis, but can be suggested to be lower based on the analysis of predicted failure points and relative shear area surrounding the stope excavation.

7

Summary

The aim of this thesis was to determine if the planned stoping order of bottom to top sublevel stoping was optimal in terms of overall stability. In order to reach this aim a pathway had to be followed as shown in Figure 1.2. This chapter will summarise and discuss the main findings made within this thesis.

The first step of the thesis was to conduct a conceptual study, in order to identify the available data for the geology and the mine. The Kearney ore deposit at Cavanacaw, is a shear hosted gold vein, where the gold is hosted within the matrix of sulphide minerals. The deposit was planned to be exploited through the modified Avoca method a form of sublevel stoping. The mine had previously been exploited through an open pit, and the underground operation is currently in the development phase. During the literature study, data was identified for the mine geological block model and material properties of the rocks within the mine. However the rock properties were only estimations based on visual inspection and were felt not to be accurate enough to generate the numerical model.

Additionally within the conceptual study, rock mechanics was addressed in order to identify methods in which the rock mass could be modelled. The relationships determined in Hoek and Brown (1980) and Hoek and Diederichs (2006), offered viable methods for modelling the rock mass based on several inputs. These inputs were the intact rock properties of UCS, Poisson's ratio and Young's Modulus, and the rock mass quantification of GSI, m_i, and disturbance factor. Further it was identified that the mine recorded rock mass quantification in the form of Q-values, which could be converted to GSI through the use of a correlation identified in Hoek, Carter, and Diederichs (2013). The information gathered with in the conceptual study allowed for the planning of a data collection campaign, which consisted of field and laboratory work.

The field campaign consisted of quantifying the geology into different units which could be modelled, as well as quantifying rock mass characteristics. The result of the field campaign was the identification of 7 rock types; country rock, altered country rock, mineralised country rock, massive sulphide, quartz breccia, and mineralised fault gouge. The mineralised material was limited to the shear zone which was identified during the conceptual study, this shear zone pinched and swelled along its strike. Between different levels there was the suggestion that the ore body dipped 17° to the north based on the geometric relations. There was also the successful conversion of Q-value to GSI(Q) using Hoek, Carter, and Diederichs (2013) for the country rock material, however this was unsuccessful for the ore drives. The ore drives could not be quantified in this way as the material was variable in each face. As a result the GSI was quantified for the geological units which made up the ore drive. The classification of the geology combined with the geological block model allowed for the identification of material that should be further tested to generate the intact rock properties.

The first step of the laboratory testing phase consisted of sampling. There were two techniques of sampling dependent on the test location. The first set of samples consisted irregular lumps of country

rock, altered country rock, and ore, which were point load tested at the mine. The second set consisted of three 40 cm blocks which were composed of country rock (2), and quartz breccia and massive sulphide (1). One of the country rock samples and the quartz breccia and massive sulphide were used to generate drill core. The second country rock was then used to generate cut blocks.

Equotip testing was carried out at TU Delft on the drill core and cut blocks. The point load test was carried out at the mine and TU Delft, all cut blocks and irregular lumps were tested in this way. Acoustic emission testing and UCS testing was carried out on only drill core.

The tests can be considered to have different success rates. Equotip provided a large amount of data which could be carried out with relative ease. The results did not correlate directly using the equations and coefficients suggested by Corkum et al. (2018) to the direct UCS test result. These values did provide reasonable estimation, and with further testing new site specific coefficients may have been able to be established. The point load test results brought several issues to light, firstly the samples tested at the mine were fresh and contained moisture, where as the samples at tested at TU Delft were dry. Secondly at the mine, the ore was represented by both quartz breccia and massive sulphide. The final issue was that the samples showed high anisotropy which meant that the recommended method of linear regression was not possible, thus the alternate method of using a correlation factor had to be used. With these result it was still possible to calculate a constant for the conversion of I^{s50}, which was 16.5 and 23.3 for schistose material and ore respectively. Further having data for country rock and altered country rock it was possible to determine a strength reduction factor for the altered country rock of 85 %. The acoustic emission testing was fairly unsuccessful, however did generate Young's modulus and Poisson's ratio for the massive sulphide material. The reason for the lack of success was that the samples had high levels of anisotropy due to the discontinuities within. The final test was UCS, this had issues one sample did not record the radial elastic modulus, and another failed early due to a chip in the corner.

The information gathered during the concept study, field campaign and laboratory testing was combined in order to build the numerical model. This allowed for the generation of the rock mass Young's modulus and the failure criterion. The numerical modelling within this thesis first looked at explaining a single model for bottom to top sublevel stoping. This generated an understanding of the behaviour of the rock mass in response to the excavations.

The main aim of the thesis was to conduct a model comparison between the different stoping sequences, however as there was two different country rock materials, the first comparison was to see which performed worse and represented the worse base case. The result was that samples tested perpendicular to foliation performed worse and therefore was used to populate the subsequent models. The next step was to compare model A with model C, which represented middle to top, bottom to middle sublevel stoping. The result was that model C was more stable due to a higher safety factor and a lower number of predicted failure points. Model D was introduced to determine if the improvement in stability was due to the introduction of the sill pillar or due to the new stoping order. The comparison between model C and D, resulted in model C still preforming better. This meant that the original stoping order of bottom to top sublevel stoping was not the optimum and a stoping order of middle to top, bottom to middle was more stable.

This result that model C was preferential in terms of stability over model A, has some implication in other factors which should be considered. Firstly model C offers a quicker return on investment, due to a reduced amount of development being required to start stoping. The second implication is negative, as there is a reduction in the total stoped volume due to the sill pillar. This however may be overcome through the use of blind stoping, this decision should be made before the first backfill phase of model C, in order to establish the correct support method.

8

Conclusion

The stoping order determined for a mine has implication in almost all results of the extraction process. These results are the stability, infrastructure cost, recovery and time to profit. This thesis focused on the stability however the final solution may have implications on the other aspects.

The aim of this thesis is to determine if the planned extraction sequence of bottom to top sublevel stoping (model A) was the optimum decision for the mine in terms of stability or whether an alternative approach within the constraints set by Galantas would yield greater stability.

In order to reach this aim several steps of progression had to be made as described in Figure 1.2. The research began with a literature study, which yielded insight into the geology and the Avoca mining method specific to the mine. Having generated insight into the mine geology, the geology was then refined into modelable domains, during a field campaign. These units were given rock mass characteristics (GSI and Q-values). In order to give the rock mass realistic properties, laboratory testing was conducted to generate intact rock properties. These intact rock properties were combined with the rock mass characteristics determined in the field and used to generate equivalent rock mass properties using Hoek and Brown (1980) and Hoek and Diederichs (2006). The final stage of the project was to build and analyse several numerical models based on the mine excavation plan and the determined rock mass properties, with different excavation pathways. The analysis looked at the total displacements, phase displacements, predicted failure points and safety factor.

8.1. Research Questions

Major Question: **Is bottom to top sublevel stoping the most stable excavation order or is an alternative method more stable?**

Bottom to top sublevel stoping is not the most stable in terms of overall stability. The alternative of middle to top bottom to middle sublevel stoping perform better in the number of predicted failure points as well as safety factor. The reduction in the number of predicted failure points is approximately 25 %. In terms of safety factor the minimum values improves from 3.20 to 3.50, further the average safety factor is improved from 3.95 to 4.25.

Sub Questions:

1. What alternative stoping orders are available meeting the mines requirements?

   The mines requirement was to use the Avoca mining method meaning that the progression of stoping must be upwards. The mine aimed to maximise the extraction which only allowed for the

generation of a single sill pillar. As a result the only stoping orders which were considered, were bottom to top sublevel stoping, bottom to top sublevel stoping with a sill pillar and middle to top bottom to middle sublevel stoping.

2. Can numerical analysis be used to determine the stability of different stoping orders?

   Numerical modelling offers a viable solution for looking at the stability of different stoping sequences, as it offers a method to replicate the behaviour exhibited by the rock mass. This is done through the use of constitutive models which can replicate the deformation response of the rock mass, as well as the failure criteria. As a result a solution is generated for the specific model, which leads to insight into the induced stresses, failures and displacement at a local and global scale. This is something that cannot be replicated in field for such a range of scenarios.

3. How can stability be evaluated through the results of the numerical analysis?

   Stability in the mine can be analysed through two major methods within this thesis. The first method of determining instability is to look at the safety factor, a method of reducing the strength of the rock mass. The lower the safety factor the closer that the model/phases is to failure. The second of these is the number of predicted failure points. In the specific case dealt with in this thesis, the higher number of predicted failure points is indicative of having a higher region of relative shear. This is due to the models having identical meshes and stope geometries.

4. Can 2D provide an adequate representation of the scenario or is 3D needed?

   There are several issues with modelling in 2D rather than 3D, however there are also some benefits. The issues are that there is a lack of shear stress in the out of plane direction. The second issue is the lack of the 3D effect, however for this specific case this may no be an issue as the excavation will be 30 m long in the out of plane direction, therefore reducing the the 3D effect. Further the excavation are near laterally similar for the mine, thus the effect along its length should be near identical. The benefit of 2D is that the model is much less complex, which means that the calculation time is significantly shorter. This is a particular issue when dealing with a complex scenario with multiple different excavation and backfill phases. Further the 2D model yields less information, therefore is easier to conduct relevant analysis on, and predict regions which would be of interest for further analysis in either 2 or 3D.

5. What failure mechanisms are relevant for this application?

   There are many failure mechanisms that are relevant for this project such as block falls, caving, buckling, rupturing and slabbing around the underground opening, these all represent localised failures except for caving which can represent both local and global. The modelling of these localised failures introduces discontinuities into the rock mass, which adds a significant level of complexity. Subsidence can be a result of the amalgamation of localised failures into a global failure, which can in turn result in the global failure of the open pit. The aim of this project is to look at global stability for the mine, so it is important to focus on the global failure mechanisms rather than those localised around the excavation. Reducing the complexity to address only plastic and elastic behaviour within the rock mass allows for the addressing of the global stability. This reduces the complexity of the model while indicating regions which should be addressed for further refinement to understand the localised failures.

6. What constitutive models are relevant for the project? Which will be chosen? What information is needed?

   In order to model the behaviour of the heterogeneous rock mass several constitutive models are viable. The constitutive models that are viable for this project are Mohr-Coulomb, Hoek-Brown, and the jointed rock model. Both the Mohr-Coulomb and Hoek-Brown are failure criteria, that are encapsulated in an isotropic linearly elastic perfectly plastic constitutive model. The jointed rock model is an anisotropic linearly elastic perfectly plastic constitutive model with different Coulomb failure criteria in predefined failure orientations. These models require different amounts and types of information in order to model the rock mass with equivalent properties. The limitation of the Mohr-Coulomb and jointed rock is that they require the properties of the rock mass to be known through testing. The Hoek-Brown method represent the rock mass properties through the

conversion of intact rock properties by the rock mass characteristics. All of these methods are widely used within the geotechnical industry and appear within reputable modelling softwares such as Plaxis, RS2 and Flac.

The decision was made to use the Hoek-Brown failure criterion with a rock mass stiffness represented by the Hoek-Diederichs rock mass stiffness due to its ability to replicate the rock mass behaviour through the use of intact rock properties and rock mass characteristics. This means that the testing can be conducted using uniaxial testing of the intact rock, with the rock mass being quantified by field observations.

The Mohr-Coulomb and jointed rock model, both require the rock mass to be tested this was something that was not viable due to the required triaxial tests, which cost significantly more than uniaxial tests. Further the samples tested need to be the rock mass rather than intact rock. This means that testing would need to be carried out on meter scale samples or in situ in order to take into account the discontinuities. This presents an issue with sample acquisition, transportation and cost of testing.

The information needed to generate a representative rock mass through the Hoek-Brown failure criterion with a rock mass stiffness represented by the Hoek-Diederichs rock mass stiffness is the rock mass characteristics and the intact rock properties. The rock mass characteristics consist of the GSI, the m_i and the disturbance factor. The properties of the intact rock that need to be known are the UCS, the Young's modulus, and the Poison's ratio.

7. What information is necessary to build an accurate numerical model?

   Several key components are needed in order to establish an accurate numerical model. First it is necessary to define boundaries for the model and conditions which will be exhibited at those boundaries. Secondly a representative geometry for the mine layout should be determined. Thirdly from the geometry, the determination of how the excavations will be divided should be established. Fourthly the material properties are needed, this includes the properties to populate the constitutive model as well as the density. The fifth element required is the initial conditions of the model. Finally a mesh for the finite element model should be established, which allows for accurate results whilst having a reasonable calculation time.

8. Which information is currently available and which information should be gathered in order to build a relevant numerical model?

   The mine design/mining method was determined by Galantas Gold prior to the commencing of this thesis. The extraction sequences were constrained by the mining method and mine layout and are presented in question 1. The information available for the rock mass characteristics at the mine were in the form of Q-value, which would subsequently need to be converted to GSI for use within the numerical model. Information was available for the intact rock properties of the mine, however this information was an estimate based on visual inspection of the rock. This was felt to lack adequate accuracy for the development of the numerical model.

   Therefore the plan of action going forward was to confirm the correlation between the Q-value and GSI previously determined by Hoek, Carter, and Diederichs (2013). This was carried out by calculating the Q-value and GSI at specific faces during the mine visit. The quantification of the intact rock properties was conducted through multiple forms of testing however the only results used were those of the direct test in the form of UCS testing.

   In order to present a realistic case in 2D, it is essential to build a geometry that represents a specific case within the mine. The geometry decided was chosen to represent a worst case example (i.e. narrowest crown pillar and largest number of excavations). Within the model, information is required to be established for the boundary conditions as well as the mesh. The determination of these conditions will be conducted through an iterative process, with the aim of identifying conditions which generate accurate results, whilst having reasonable computational time.

9. How does the rock mass character vary throughout the mine?

   The information currently gathered shows the host rock Q-value improves with progression down the decline, however there is still a large amount of variation within the Q-value due to localised variation within the host rock. There is an improvement in the Q-value for each ore drive with increasing depth, K1084 improved 42 % over K1092, and K1072 improved 12 % over K1084. The continuation of this trend may be possible, however as a safety precaution the values were not changed with the depth beyond what was known.

10. Is it viable to correlate Q-value to GSI, for the quantification of rock mass at the mine.

    The work of Hoek, Carter, and Diederichs (2013), related the Q-value to GSI. This relation was checked at the mine using results for Q-value and GSI for the several faces. The result of the relationship had a slightly different correlation of 0.749x + 14.017 compared to that of Hoek, Carter, and Diederichs (2013) which generated 0.890x + 1.679. The difference in correlation can be explained by the lack of range of the data from the mine, coupled with the limited sample size. The Hoek, Carter, and Diederichs (2013) relationship was still used to quantify the country rock for the mine as this method is a proven and scientifically accepted method.

    The method was not used for the quantification of the ore drives as they were composed of multiple different rock units with different rock mass properties in a small region. The decision was taken that it would be more representative to determine a rock mass for specific units within the ore drives. The GSI of these units were taken directly through the visual inspection of the units within the ore drives.

11. Can the combination of field observations and laboratory testing generate the necessary input to simulate a representative rock mass in a numerical model?

    The rock mass behaviour can be represented through the use of the linearly elastic perfectly plastic model with a Hoek-Brown failure criterion, with the rock mass Young's modulus represented by the Hoek-Diderichs equation. In order to use this constitutive model and empirical estimation of rock mass Young's modulus, information for both the rock mass properties and intact rock properties needs to be established accurately otherwise it will not represent the rock mass. The rock mass properties can only be considered representative if they represent the whole rock mass. It is more difficult to say if the intact rock properties are representative of the whole rock mass as they represent a small volume within the rock mass. However it is still important to determine if the intact rock properties, represent the intact rock properties within the whole rock mass.

    The rock mass characteristics used in this model represented a wide range of sample points within the mine. Further the values for the GSI was reduced in order to increase the margin of safety. The intact rock properties are more difficult to define as representative, as the samples equate to block of 0.008 m^3 in a volume of more than 500,000 m^3. To determine if these samples were representative a discussion was held with then mine to propose argumentation why the chosen samples were representative. The samples were considered representative based on having a typical mineralogy, grain size, and structure.

12. Is intact rock property testing at the mine sufficiently accurate to allow for the generation of an accurate numerical model, or can it be used as a long term proxy to confirm assumption made in this thesis?

    Within this thesis an extensive range of testing was carried out in order to determine the intact rock properties. These tests were Equotip, point load, acoustic emission and UCS. These tests required different levels of sample preparation and provided different information. The Equotip, provided an estimation for the UCS and could be conducted on cut surfaces at the mine. The point load test also provided an estimation of the UCS, and could also be conducted at the mine on irregular lumps, with little to no sample preparation. The acoustic emission testing gave an estimate for the Young's Modulus and Poisson's ratio, however this test required extensive sample preparation and could only be conducted in a laboratory. The UCS testing provided a direct result for the UCS, the Young's Modulus, and the Poisson's ratio. This result could only be conducted within a laboratory and requires extensive sample preparation. This shows that mine testing cannot provide enough information for the generation of the numerical model. The decision was made within this thesis to only use the UCS test results, as they were felt to be more

representative. The reason for this is that they are a direct result rather than an estimation based on empirical relationships.

The tests that can be carried out at the mine present useful insight with much less sample preparation. The point load testing despite having a large degree of variation could be continued to be carried out at the mine in order to confirm assumptions made about the rock with depth. Further the information yielded from the Equotip appeared to show the indication of a correlation, however there was not a large enough sample set to confirm this.

13. What are the major factors controlling the stress field around the underground excavations?

    The major controlling factor for the stress field is the depth. As depth increases the overlying material increases, therefore increasing the load. The initial stress field is set up through the use of the K0 procedure, which generates vertical stresses in equilibrium as a reaction to the rock mass weight. The set up at the mine is that the out of plane K0 is twice the vertical and horizontal in plane K0 due to the tectonic history.

    Another significant aspect to the pre-underground mining stress specific to the mine is the addition of the open pit. The introduction of the open pit increases the relative shear stress near to the surface due to the removal of the material. The effect of the open pit is lessened the further from the surface the location is. The change in the relative shear stress is caused by the change in the principle stresses. The excavation of the open pit leads to an increase in the σ_3, due to a reduction in the confining overburden, the change in the value for σ_1 is small hence why there is mobilisation in the shear stress.

14. Why is one stoping sequences more stable than another sequence?

    The result that middle to top bottom to middle sublevel stoping (model C) is the most stable case addressed is for a number of reason. The first reason is that the first excavation occurs at shallower depth than bottom to top sublevel stoping (model A). This means that the principal stresses will be higher, therefore difference between σ_1 and σ_3 would be further from the failure criterion, as σ_1 does not change much in the region of the excavation. The second reason is that the overlying mass is reduced in model C, before excavating the lower levels, which leads to a reduction in vertical load on the lower excavations. Thirdly model C has less open volume in which failures can occur around, when the first stope is excavated, this means that the model has less of an ability to combine failures to generate a complete failure. Forth is the number of excavations combined in a single continuous sequence is reduced as model C splits the deposit into top and bottom. This is due to there being increased relative shear around the excavation which is continued on the next excavation. The relative shear here is for the most part related to reduction in σ_3 due to the lack of confinement. The final reason is the introduction of the sill pillar, however this is not the major factor, as model C still performs better than bottom to top sublevel stoping with a sill pillar (model D).

9

Limitation & Recommendations

The recommendations for this project extend through out this thesis. This is due to every section having its limitations that could not be overcome due to the available information and time frame for this project. The limitations are as follows:

- Only a limited number of stoping sequences were addressed within this thesis, due to constraints determined by the mine. Alternative options may offer increased stability that were not considered within the project.
- Lack of information with depth, in terms of the geology, the rock mass properties, the rock mass characteristics and the intact rock.
- The geotechnical information within the model was as a result of an empirical relationship developed in Hoek, Carter, and Diederichs, 2013, rather than specific observations for GSI.
- The sample size for intact rock properties was very small, the samples were felt to be representative, however this is difficult to say with full certainty.
- The known geology for the ore drives is more complex than the simplification presented within this model.
- The model is done in the absence of water, due to a lack of data about the behaviour of water within the mine. The limited data suggested only limited ingress based on the current developments. This absence of water may lead to an overestimation of the rock mass strength as well as an overestimation of the effective stresses in the subsurface.
- The absence of supporting methods other than backfill. This means that the results are conservative for the stability of the excavation.
- The model was conducted in 2D rather than 3D, in order to reduce the complexity and computational cost, however this results in a loss of the shear stress in the out of plane direction as well as reduces the underground failure mechanisms observable. Further the focus of the project was on the global failure and due to time the localised failure mechanisms were not analysed in detail.
- The rock mass was treated as isotropic within the numerical model, however in reality the behaviour is anisotropic.
- Only elastic and plastic behaviour was observed within the model reducing the underground failure mechanisms that could be observed.

- The backfill material was taken purely from literature, as it was not with the scope of this thesis to determine it. Thus it is not known whether this is a viable solution based on the material available at the mine.
- This project only looks at stability, in reality there are several key factors that make up the decision for mining method and stope sequence.

These limitation within this work could not be resolved with the information or time available. It is important to be able to reflect on the work and develop a plan going forwards that may allow for the rectifying of these deficiencies and presenting a more accurate case.

The recommendations for the thesis going forwards will be:

- The recording of the geological information should be continued as is the current procedure at the mine. This information should be used to refine and develop a more accurate model of the ore body, which will in turn refine the mining design and method. This will also allow for the addressing of new scenarios that are viable for the mine.
- The recording of rock mass characteristics at the mine is through Q-values, this method is extremely useful, however does not take all of the available rock mass characteristics into account. The recommendation is therefore that the mine should move to a more thorough method of recording the rock mass characteristics. An example of this method can be found at $http : //rockmass.net/files/Q - RMR - RMi_v3.xls$, and will allow for the generation of the RMR, Rock Mass Index (RMi), Q-value and GSI in a similar amount of time to recording the Q-values.
- In order to compensate for the limited number of samples used to build the numerical model, it would be useful to conduct another laboratory testing campaign. This campaign should be conducted in order to better correlate the test results which can be conducted on site (point load and equotip), with the direct results of UCS tests. These tests could be conducted for a more diverse range of materials from the mine, allowing for the discretising of a more refined geology. Further it would allow for the daily indication of intact rock properties, which useful for the addressing of stability.
- The model was limited by the lack of water within it. This is something that should be rectified moving forward by a survey of where the water table is, as well as looking at the water ingress throughout the mine and identifying where the water ingress moves from seeping to pressurised.
- The lack modelling in 3D is something that was essential in order to complete the project in a timely manner. However the recommendation is not to conduct a 3D analysis but as only global stability was addressed within this thesis, it would be much more fruitful to address the localised failures around the excavations in 2D. The inclusion of support methods of shotcrete and rock bolts would lead to a more realistic result, something that was also not addressed within this thesis.
- A complete study as to the technical viability of the backfill material should be conducted. This thesis made an approximation based on limited data. In reality it is essential to understand the backfill, in order to accurately predict its support capacity and behaviour. This should be conducted in advance of stoping as well as continuously monitored through the backfilling phase.
- Modelling an anisotropic rock mass was not possible based on the information available when developing the numerical model. The suggestion would be to gather information so as the jointed rock model could be used, however this is difficult due to needing to know the rock mass properties directly. There are some estimation methods for the conversion of Hoek-Brown to Mohr-Coulomb, which may offer a solution to this.
- A study of the scenarios presented within this thesis should be analysed in terms of the time value of money and the total recovered value. An initial suggestion can be hypothesised here that the time to profitability may be reduced by going with model C, as the excavations of stopes happens half way through the development phase, however there is the loss of the material from one level within the mine.

Bibliography

ACA Howe, 2008. *Technical report on the Omagh gold project, Counties Tyrone and Fermanagh, Northern Ireland* [Online]. Omagh: Galantas Gold Corporation. Available from: https://www.sedar.com/GetFile.do?lang=EN&docClass=24&issuerNo=00003744&issuerType=03&projectNo=01281716&docId=2241917 [Accessed May 15, 2019].

Arthurs, J.W., 1976. The geology and metalliferous mineral potential of the Sperrin Mountains area. *Special Report to the Geological Survey of Northern Ireland*. Belfast: Geological Survey of Northern Ireland, pp.119–148.

ASTM, 1992. *ASTM-D2938-86 Standard test method for unconfined compressive strength of intact rock core specimens*. Annual Book of ASTM Standards, Vol. 04.08, pp. 390–391. West Conshohocken, PA: ASTM International.

ASTM, 2008. *ASTM-D2845-08 Standard test method for laboratory determination of pulse velocities and ultrasonic elastic constants of rock* [Online]. West Conshohocken, PA: ASTM International. Available from: https://doi.org/10.1520/D2845-08 [Accessed June 11, 2019].

ASTM, 2014. *ASTM-D7012-14 Standard test methods for compressive strength and elastic moduli of intact rock core specimens under varying states of stress and temperatures* [Online]. West Conshohocken, PA: ASTM International. Available from: https://doi.org/10.1520/D7012-14E01 [Accessed June 12, 2019].

ASTM, 2016. *ASTM-D5731-16 Standard test method for determination of the point load strength index of rock and application to rock strength classifications* [Online]. West Conshohocken, PA: ASTM International. Available from: https://doi.org/10.1520/D5731-16 [Accessed May 12, 2019].

Barton, N., Lien, R., and Lunde, J., 1974. Engineering classification of rock masses for the design of tunnel support. *Rock Mechanics*, Vol. 6, pp.189–236.

Benz, T., Schwab, R., Kauther, R.A., and Vermeer, P.A., 2008. A Hoek–Brown criterion with intrinsic material strength factorization. *International Journal of Rock Mechanics and Mining Sciences*, Vol. 45(2), pp.210–222.

Bieniawski, Z.T., 1974. Geomechanics classification of rock masses and its application in tunnelling. *Proceedings 3rd International Congress on Rock Mechanics, Denver*. Vol. 2. Washington: National Academy of Sciences, pp.27–32.

Bieniawski, Z.T., 1989. *Engineering rock mass classifications: a complete manual for engineers and geologists in mining, civil, and petroleum engineering*. New York: John Wiley & Sons.

Boate, G., Hartlib, S., and Boate, A., 1657. *Irelands naturall history (sic)*. London: Samuell Hartlib.

Brady, B.H.G. and Brown, E.T., 2007. *Rock mechanics: for underground mining*. 3rd ed. Dordrecht: Springer.

Brinkgreve, R.B.J., Zampich, L.M., and Ragi Manoj, N., 2019. *PLAXIS Connect Edition v20 (user manual)*. Delft: Plaxis bv.

Brotons, V., Tomás, R., Ivorra, S., Grediaga, A., Martínez-Martínez, J., Benavente, D., and Gómez-Heras, M., 2016. Improved correlation between the static and dynamic elastic modulus of different types of rocks. *Materials and Structures*, Vol. 49(8), pp.3021–3037.

Bullock, R.L., 2011. Comparison of underground mining methods. In: P. Darling, ed. *SME mining engineering handbook*. 3rd ed. Vol. 1. Englewood, CO: Society for Mining, Metallurgy and Exploration (SME), pp.385–404.

Burke, J., 2017. *Cavanacaw mine ground control management plan*. Internal Galantas Gold Corporation report. Confidential. Unpublished.

Cliff D, C. and Wolfenden, M., 1992. The Lack gold deposit, Northern Ireland. In: A. Bowden A, G. Earls, G. O'Connor P, and F. Pyne J, eds. *The Irish Minerals Industry 1980-1990*. Dublin: Irish Association for Economic Geology, pp.65–75.

Clifford J, A., Earls, G., Meldrum A, H., and Moore, N., 1992. Gold in the Sperrin Mountains, Northern Ireland: an exploration case history. In: A. Bowden A, G. Earls, G. O'Connor P, and F. Pyne J, eds. *The Irish Minerals Industry 1980-1990*. Dublin: Irish Association for Economic Geology, pp.77–87.

Corkum A, G., Asiri, Y., El Naggar, H., and Kinakin, D., 2018. The Leeb hardness test for rock: an updated methodology and UCS correlation. *Rock Mechanics and Rock Engineering*, Vol. 51(3), pp.665–675.

Deere D, U. and Deere D, W., 1964. Technical description of rock cores. *Rock Mechanics Engineering Geology*, Vol. 1, pp.16–22.

Earls, G., Clifford J, A., and Meldrum A, H., 1989. Curraghinalt gold deposit, County Tyrone, Northern Ireland. *Applied Earth Science: Transactions of the Institution of Mining and Metallurgy: Section B*, Vol. 98, pp.50–51.

Emad, M.Z., 2017. Numerical modelling approach for mine backfill. *Sādhanā*, Vol. 42(9), pp.1595–1604.

Google Maps, 2015. *Map of Ireland 54°45'29.11"n, 5°52'74.36"w, elevation 237039 m, satellite image* [Online]. Available from: `https://www.google.co.uk/maps` [Accessed August 1, 2019].

Grimstad, E. and Barton, N., 1993. Updating the Q-system for NMT. In: R. Kompen, O.A. Opsahl, and K. Berg, eds. *Proceedings of the international symposium on sprayed concrete-modern use of wet mix sprayed concrete for underground support, Fagernes, Norway*. Oslo: Norwegian Concrete Association, pp.46–66.

Hoek, E., 1994. Strength of rock and rock masses. *Journal of International Society for Rock Mechanics*, Vol. 2(2), pp.4–16.

Hoek, E., 2001. Rock mass properties for underground mines. In: W.A. Hustrulid and R.L. Bullock, eds. *Underground mining methods: engineering fundamentals and international case studies*. Littleton, CO: Society for Mining, Metallurgy, and Exploration (SME), pp.467–474.

Hoek, E. and Brown, E.T., 1980. *Underground excavations in rock*. 1st ed. Boca Raton, FL: CRC Press.

Hoek, E. and Brown, E.T., 1997. Practical estimates of rock mass strength. *International Journal of Rock Mechanics and Mining Sciences*, Vol. 34(8), pp.1165–1186.

Hoek, E. and Brown, E.T., 2019. The Hoek–Brown failure criterion and GSI–2018 edition. *Journal of Rock Mechanics and Geotechnical Engineering*, Vol. 11(3), pp.445–463.

Hoek, E., Carter, T.G., and Diederichs, M.S., 2013. Quantification of the geological strength index chart. In: L. Pyrak-Nolte, ed. *Proceedings of the 47th US Rock Mechanics/Geomechanics Symposium, San Fransisco*. Alexandria, VA: American Rock Mechanics Association, pp.1757–1764.

Hoek, E. and Diederichs, M.S., 2006. Empirical estimation of rock mass modulus. *International Journal of Rock Mechanics and Mining Sciences*, Vol. 43(2), pp.203–215.

Hoek, E. and Marinos, P., 2000. Predicting tunnel squeezing problems in weak heterogeneous rock masses. *Tunnels and Tunnelling International*, Vol. 32(11), pp.45–51.

Hoek, E. and Marinos, P., 2007. A brief history of the development of the Hoek–Brown failure criterion. *Soils and Rocks*, Vol. 30(2), pp.85–92.

Hollis, S.P., Roberts, S., Earls, G., Herrington, R., Cooper, M.R., Piercey, S.J., Archibald, S.M., and Moloney, M., 2014. Petrochemistry and hydrothermal alteration within the Tyrone Igneous Complex, Northern Ireland: implications for VMS mineralization in the British and Irish Caledonides. *Mineralium Deposita*, Vol. 49(5), pp.575–593.

Lusty Paul A, J., Gunn A, G., McDonnell P, M., Chacksfield B, C., Cooper M, R., and Earls, G., 2009. Gold potential of the Dalradian rocks of north-west Northern Ireland: prospectivity analysis using Tellus data. *Applied Earth Science: Transactions of the Institution of Mining and Metallurgy: Section B*, Vol. 118(3-4), pp.162–177.

Marinos, P. and Hoek, E., 2000. GSI: a geologically friendly tool for rock mass strength estimation. *GeoEng 2000 Conference, Melbourne*. Lisbon: International Society for Rock Mechanics and Rock Engineering, pp.1422–1442.

Marinos, P., Marinos, V., and Hoek, E., 2007. Geological strength index (GSI): a characterization tool for assessing engineering properties for rock masses. In: C. Mark, R. Pakalnis, and R.J. Tuchman, eds. *Proceedings of the international workshop on rock mass classifications in underground mining, Vancover*. Pittsburgh: National Institute of Occupational Safety and Health, pp.87–94.

Marshall, N. and Brown, M., 2011. *Omagh Gold Mine, Omagh, Northern Ireland - conceptual underground geotechnical design criteria*. Internal Galantas Gold Corporation report. Confidential. Unpublished.

McFarlane, J., Cooper M, R., and Chew D, M., 2009. New geological and geophysical insights into the Dalradian Lack Inlier, Northern Ireland: implications for lithostratigraphy and gold mineralisation. *Irish Association for Economic Geology Annual Review 2009*, pp.57–59.

McFarlane, J., Attwood, C., and Hardie, N., 2009. *Cavanacaw geotechnical assessment 2009*. Internal Galantas Gold Corporation report. Confidential. Unpublished.

Norwegian Geotechnical Institute, 2015. *Using the Q-system (handbook)* [Online]. Oslo: Norwegian Geotechnical Institute. Available from: `https://www.ngi.no/eng/content/download/4014/431191/version/1/inLanguage/nor-NO/file/Handbook%5C%20The%5C%20Q-system%5C%20mai%5C%202015%5C%20nettutg.pdf` [Accessed May 15, 2019].

Palmstrom, A. and Stille, H., 2007. Ground behaviour and rock engineering tools for underground excavations. *Tunnelling and Underground Space Technology*, Vol. 22(4), pp.363–376.

Parnell, J., Earls, G., Wilkinson, J.J., Hutton, D.H.W., Boyce, A.J., Fallick, A.E., Ellam, R.M., Gleeson, S.A., Moles, N.R., Carey, P.F., and Legg, I., 2000. Regional fluid flow and gold mineralization in the Dalradian of the Sperrin Mountains, Northern Ireland. *Economic Geology*, Vol. 95(7), pp.1389–1416.

Phelps, R., Coulter, S., Mawson, M., and Harris, G., 2014. *Resource estimate, preliminary economic assessment and detailed feasibility study on the Omagh gold project County Tyrone, Northern Ireland* [Online]. Omagh: Galantas Gold Corporation. Available from: `https://www.sedar.com/GetFile.do?lang=EN&docClass=24&issuerNo=00003744&issuerType=03&projectNo=02236647&docId=3605794` [Accessed May 6, 2019].

Potvin, Y., 1988. *Empirical open stope design in Canada*. Thesis (P.H.D.). University of British Columbia.

RailSystem, 2019. *Drill and blast method, image* [Online]. Available from: `http://www.railsystem.net/drill-and-blast-method` [Accessed June 14, 2019].

Stöckhert, F., 2015. *Fracture mechanics applied to hydraulic fracturing in laboratory experiments*. Thesis (P.H.D.). Ruhr-Universität Bochum.

Strachan, R.A., Smith, M., Harris, A.L., Fettes, D.J., and Trewin, N.H., 2002. The Northern Highland and Grampian terranes. In: N.H. Trewin, ed. *The Geology of Scotland*. 4th ed. London: The Geological Society, pp.91–147.

Tanner, G.P.W., 2014. Structural controls and origin of gold–silver mineralization in the Grampian Terrane of Scotland and Ireland. *Geological Magazine*, Vol. 151(6), pp.1072–1094.

Tsidzi, K.E.N., 1990. The influence of foliation on point load strength anisotropy of foliated rocks. *Engineering Geology*, Vol. 29(1), pp.49–58.

Weijermars, R., 1997. *Principles of rock mechanics*. Amsterdam: Alboran Science Publishing.

Woodham, C., Finlay, S., and Holman, R., 1989. Gold exploration in the Dalradian of Northern Ireland. *Applied Earth Science: Transactions of the Institution of Mining and Metallurgy: Section B*, Vol. 98, pp.63–65.

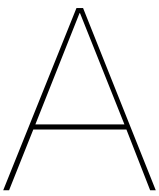

Appendix

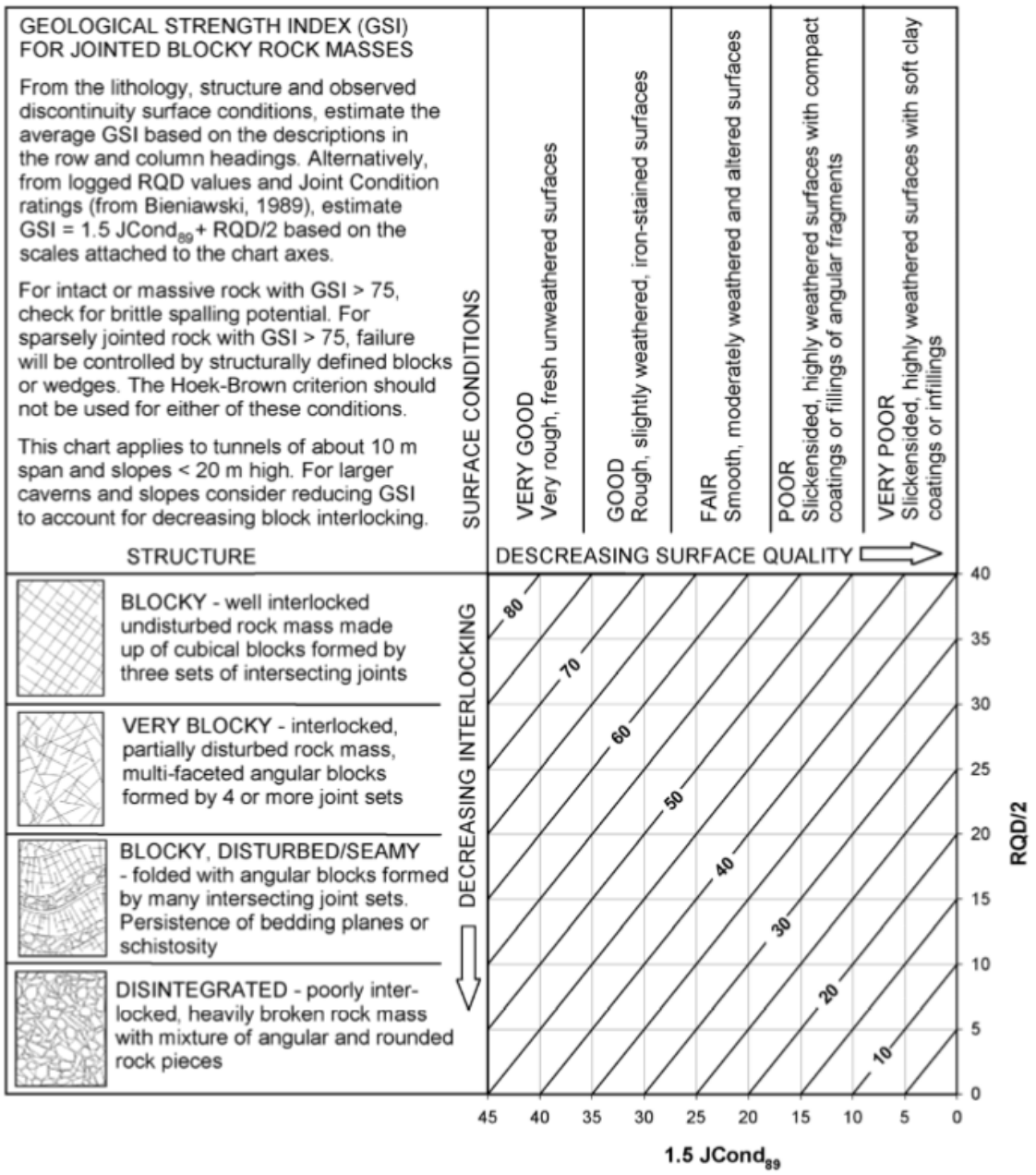

Figure A.1: Geological Strength Index (GSI) Graph (Hoek and Brown, 1997).

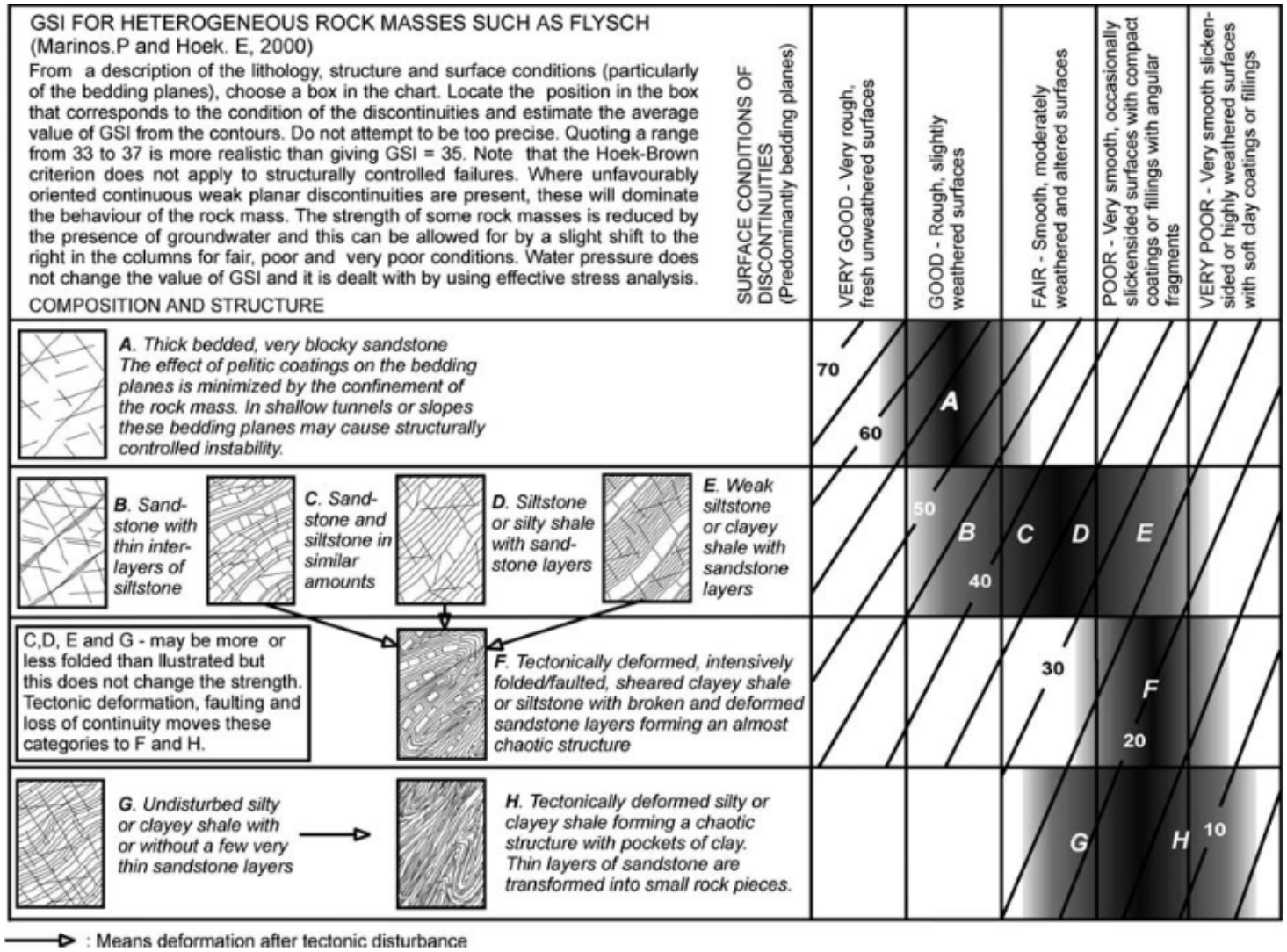

Figure A.2: Geological Strength Index (GSI) Graph (Flysch) (Marinos and Hoek, 2000)

Rock type	Class	Group	Texture			
			Coarse	Medium	Fine	Very fine
SEDIMENTARY	Clastic		Conglomerates (21 ± 3) Breccias (19 ± 5)	Sandstones 17 ± 4	Siltstones 7 ± 2 Greywackes (18 ± 3)	Claystones 4 ± 2 Shales (6 ± 2) Marls (7 ± 2)
	Non-Clastic	Carbonates	Crystalline Limestone (12 ± 3)	Sparitic Limestones (10 ± 2)	Micritic Limestones (9 ± 2)	Dolomites (9 ± 3)
		Evaporites		Gypsum 8 ± 2	Anhydrite 12 ± 2	
		Organic				Chalk 7 ± 2
METAMORPHIC	Non Foliated		Marble 9 ± 3	Hornfels (19 ± 4) Metasandstone (19 ± 3)	Quartzites 20 ± 3	
	Slightly foliated		Migmatite (29 ± 3)	Amphibolites 26 ± 6		
	Foliated*		Gneiss 28 ± 5	Schists 12 ± 3	Phyllites (7 ± 3)	Slates 7 ± 4
IGNEOUS	Plutonic	Light	Granite 32 ± 3	Diorite 25 ± 5 Granodiorite (29 ± 3)		
		Dark	Gabbro 27 ± 3 Norite 20 ± 5	Dolerite (16 ± 5)		
	Hypabyssal		Porphyries (20 ± 5)		Diabase (15 ± 5)	Peridotite (25 ± 5)
	Volcanic	Lava		Rhyolite (25 ± 5) Andesite 25 ± 5	Dacite (25 ± 3) Basalt (25 ± 5)	Obsidian (19 ± 3)
		Pyroclastic	Agglomerate (19 ± 3)	Breccia (19 ± 5)	Tuff (13 ± 5)	

* These values are for intact rock specimens tested normal to bedding or foliation. The value of m_i will be significantly different if failure occurs along a weakness plane.

Figure A.3: Hoek-Brown Material Constant as presented in Hoek (2001).